MODELING OF MIXED-CONVECTION LAMINAR FILM CONDENSATION FROM MIXTURES OF A VAPOR AND A LIGHTER NONCONDENSABLE GAS

by Vlajko Srzić

A Thesis Presented to The University of Manitoba in

Partial Fulfillment of the Requirements for the degree

Master of Science in Mechanical Engineering

Winnipeg, Manitoba, Canada

July, 1997

THE UNIVERSITY OF MANITOBA

FACULTY OF GRADUATE STUDIES

COPYRIGHT PERMISSION

MODELING OF MIXED-CONVECTION LAMINAR FILM CONDENSATION FROM MIXTURES OF A VAPOR AND A LIGHTER NONCONDENSABLE GAS

BY

VLAJKO SRZIĆ

A Thesis submitted to the Faculty of Graduate Studies of the University of Manitoba in partial fulfillment of the requirements of the degree of

MASTER OF SCIENCE

ABSTRACT

The effects of a lighter noncondensable gas on laminar film condensation from moving vapor-gas mixtures was investigated. Condensation occurred on the top of an isothermal flat plate with an arbitrary inclination. The liquid film and the mixture boundary layers were described with the conservation equations for mass, momentum, energy, and gas species (for the mixture boundary layer only). A finite volume method was applied on a staggered grid in the numerical solution domain. The properties for both liquid and mixture were evaluated at the local temperature. The solution procedure was terminated either when the separation criteria were met or when the flow reached the transition to turbulence. The main objectives of the study were to investigate the mixture boundary layer separation distance and the reduction in heat transfer to the wall due to the presence of a lighter noncondensable gas.

Three vapor-gas combinations were studied: steam-hydrogen, Freon12-air, and mercury-air. Applying two simple collapsing procedures, a set of graphs is presented for each vapor-gas combination which can be used to estimate the separation length for a given set of input parameters. It was found that the reduction of gas concentration toward zero caused an increase in the separation distance for steam-hydrogen and Freon12-air but a decrease in the mercury-air case. The reduction in the separation distance for mercury-air mixture at low values of the gas concentration was found to be caused by a relatively large

magnitude of an inertia term in the mixture momentum equation. For higher values of the gas concentration, the magnitude of the inertia terms become small compared to the buoyant force term. Therefore, for high gas concentration, the separation location increases for all three vapor-gas combinations, because in that region the dominant buoyant force decreases.

For each mixture and for a given free stream temperature, the variation of Nusselt number (normalized by the square root of the local Reynolds number) along the plate is also presented for different values of gas concentration and wall temperature. For higher gas concentration the effect of the buoyant force on the Nusselt number is manifested in a maximum value of the Nusselt number, after which the magnitude of the Nusselt number decreases. A comparison of the effect of a lighter and heavier gas on the rate of heat transfer was presented for steam-air and steam-hydrogen mixtures for both horizontal and vertical plates. A calculation showed that in both cases the inhibiting effects of hydrogen are more pronounced compared to air. The effect of the buoyant force also becomes evident in the vicinity of the separation point, where the rate of heat transfer for steam-hydrogen decreased faster than that for steam-air.

ACKNOWLEDGMENTS

The author expresses his gratitude to Dr. S.J. Ormiston and Dr. H.M. Soliman for their invaluable help during the work on this thesis. The financial support in the form of a research assistantship provided by the advisors is also greatly appreciated.

TABLE OF CONTENTS

Title *Page*

ABSTRACT ii

ACKNOWLEDGMENTS iv

TABLE OF CONTENTS v

LIST OF FIGURES viii

LIST OF TABLES xiv

NOMENCLATURE xv

Chapter 1 INTRODUCTION 1

Chapter 2 LITERATURE REVIEW 3

2.1 Condensation of Moving Pure Vapors 4

2.2 Condensation of Moving Vapor-Gas Mixtures 9

2.3 Analytical Models of Boundary Layer Separation 15

2.4 Summary of the Review 19

Chapter 3 STATEMENT OF THE PROBLEM 22

3.1 The Physical Model 22

3.2 The Analytical Model 24

3.3 Definition of the Separation Condition 27

Chapter 4 SOLUTION PROCEDURE 33

4.1 Coordinate Transformation 33

4.2 Discretization 34

4.2.1 Discretized Equations 36

4.2.2 Calculation of the Interface Parameters 47

4.3 Program Description and Solution Procedure 48

Chapter 5 CONVERGENCE AND VALIDATION OF RESULTS 55

5.1 Grid Resolution 55

5.2 Convergence of Results 58

5.3 Comparison with Previous Work 61

Chapter 6 RESULTS AND DISCUSSION 71

6.1 Derivation of Dimensionless Separation Length 72

6.2 Steam-Hydrogen Mixtures 74

6.2.1 Separation Results for Steam-Hydrogen Mixtures 74

6.2.2 Heat Transfer Results for Steam-Hydrogen Mixtures 83

6.3 Comparison of the Heat Transfer Rates for Steam-Air and Steam-Hydrogen 85

6.4 Freon12-Air Mixtures 87

6.4.1 Separation Results for Freon12-Air Mixtures 88

6.4.2 Heat Transfer Results for Freon12-Air Mixtures 91

6.5 Mercury-Air Mixtures 93

6.5.1 Separation Results for Mercury -Air Mixtures 93

6.5.2 Velocity, Temperature and Gas Concentration Profiles 100

6.5.3 Heat Transfer Results for Mercury -Air Mixtures 101

Chapter 7 CONCLUDING REMARKS 166

7.1 Overview 166

7.2 Observations Regarding the Steam-Hydrogen Mixture 168

7.3 Observations Regarding the Freon12-Air Mixture 169

7.4 Observations Regarding the Mercury-Air Mixture 170

7.5 Recommendations 170

REFERENCES 172

APPENDIX A: Transport and Thermal Properties 175

A.1 Introduction 176

A.2 Water Properties 177

A.3 Air Properties 183

A.4 Mercury Properties 185

A.5 Freon12 Properties 193

A.6 Hydrogen Properties 200

A.7 Mixture Properties 203

APPENDIX B: Discretization and Solution of the Interface Boundary Equations 207

APPENDIX C: Initial Solution Field for the Second Station 213

LIST OF FIGURES

Figure	*Title*	*Page*
Figure 3.1	Physical model	30
Figure 3.2	Schematic representation of u-velocity profiles for a) $u_i < u_\infty$ and $\left(\frac{\partial u}{\partial y}\right)_{y=\delta} \leq 0$ and b) $u_i > u_\infty$ and $\left(\frac{\partial u}{\partial y}\right)_{y=\delta} \leq 0$	31
Figure 3.3	Schematic representation of u-velocity profiles at the separation point	32
Figure 4.1	Computational grid in (x,y) coordinate system	51
Figure 4.2	Computational grid in transformed coordinate system (χ, η) with locations for u, T, W = o; $\dot{m}_n$ = ➔ and $\dot{m}_e$ = ⬇	52
Figure 4.3	Structure of the program	53
Figure 4.4	Flow chart of the subroutine PROCESS	54
Figure 5.1	Sample of the mixture boundary layer thicknesses for steam-hydrogen mixtures	65
Figure 5.2	Comparison with Denny and Jusionis (1972) for Freon12-air mixtures, T_{wall} = 299.82 K	66
Figure 5.3	Comparison with Turner et al. (1973) for mercury-air mixtures at ΔT = 5.55 K	67
Figure 5.4	Comparison with Turner et al. (1973) for mercury-air mixtures at ΔT = 16.67 K	68
Figure 5.5	Comparison with Siddique et al. (1989) for steam-hydrogen mixtures at T_∞ = 373.15 K	69
Figure 5.6	Comparison with Siddique et al. (1989) for steam-hydrogen mixtures at T_∞ = 398.15 K	70
Figure 6.1	Effect of θ and u_∞ on x_{sep} for a mercury-air mixture at T_∞ = 666.67 K	103

Figure 6.2 Effect of W_∞ and u_∞ on $x_{sep}g^*$ for a mercury-air mixture at T_∞ = 666.67 K 104

Figure 6.3 Effect of W_∞ and u_∞ on the dimensionless separation length for a mercury-air mixture at T_∞ = 666.67 K 105

Figure 6.4 Dimensionless separation length for a steam-hydrogen mixture, T_∞ = 353.15 K 106

Figure 6.5 Dimensionless separation length for a steam-hydrogen mixture, T_∞ = 373.15 K 107

Figure 6.6 Dimensionless separation length for a steam-hydrogen mixture, T_∞ = 393.15 K 108

Figure 6.7 Variation of $\rho_i u_i \left(\frac{\partial u}{\partial x}\right)_i$ along the vertical plate for different values of W_∞ for a steam-hydrogen mixture at T_∞ = 353.15 K, ΔT = 15 K and u_∞ = 0.05 m/s 109

Figure 6.8 Variation of $\rho_i v_i \left(\frac{\partial u}{\partial y}\right)_i$ along the vertical plate for different values of W_∞ for a steam-hydrogen mixture at T_∞ = 353.15 K, ΔT = 15 K and u_∞ = 0.05 m/s 110

Figure 6.9 Variation of $g(\rho_i - \rho_\infty)$ along the vertical plate for different values of W_∞ for a steam-hydrogen mixture at T_∞ = 353.15 K, ΔT = 15 K and u_∞ = 0.05 m/s 111

Figure 6.10 Variation of $\mu_i \left(\frac{\partial^2 u}{\partial y^2}\right)_i$ along the vertical plate for different values of W_∞ for a steam-hydrogen mixture at T_∞ = 353.15 K, ΔT = 15 K and u_∞ = 0.05 m/s 112

Figure 6.11 Variation of x^*_{sep}, $\mu_i \left(\frac{\partial^2 u}{\partial y^2}\right)_i$ and $(\rho_\infty - \rho_i)$ with W_∞ for a steam-hydrogen mixture at T_∞ = 353.15 K, ΔT = 15 K and u_∞ = 0.05 m/s on a vertical plate 113

Figure 6.12 Value of $x^*_{sep}Ja^m$ for a steam-hydrogen mixtures 114

Figure 6.13 Value of the exponent m for a steam-hydrogen mixture 115

Figure 6.14 Comparison of approximate x^*_{sep} and numerically obtained x^*_{sep} for a steam-hydrogen mixture 116

Figure 6.15 Effect of W_∞ on Nu_x / $Re_x^{1/2}$ for a steam-hydrogen mixture at T_∞ = 393.15 K and T_{wall} = 373.15 K..... 117

Figure 6.16 Effect of $(T_\infty - T_{wall})$ on Nu_x / $Re_x^{1/2}$ for a steam-hydrogen mixture at T_∞ = 393.15 K and W_∞ = 0.01..... 118

Figure 6.17 Dimensionless liquid film thickness for a steam-hydrogen mixture at T_∞ = 393.15 K and T_{wall} = 373.15 K..... 119

Figure 6.18 Interfacial gas concentration for a steam-hydrogen mixture at T_∞ = 393.15 K and T_{wall} = 373.15 K..... 120

Figure 6.19 Values of Re_δ / $Re_x^{1/2}$ for a steam-hydrogen mixture at T_∞ = 393.15 K and T_{wall} = 373.15 K..... 121

Figure 6.20 Comparison of the rate of heat transfer for steam-air and steam-hydrogen mixtures at T_∞ = 373.15 K and W_∞ = 0.03..... 122

Figure 6.21 Values of $\frac{dq}{dx}$ along the plate for pure steam, steam-air and steam-hydrogen mixtures at T_∞ = 373.15 K and W_∞ = 0.03..... 123

Figure 6.22 Dimensionless separation length for a Freon12 - air mixture at T_∞ = 288.15 K..... 124

Figure 6.23 Dimensionless separation length for a Freon12 - air mixture at T_∞ = 315.15 K..... 125

Figure 6.24 Dimensionless separation length for a Freon12 - air mixture at T_∞ = 333.15 K..... 126

Figure 6.25 Variation of $\rho_i u_i \left(\frac{\partial u}{\partial x}\right)_i$ along the vertical plate for different values of W_∞ for a Freon12-air mixture at T_∞ = 288.15 K, ΔT = 5 K and u_∞ = 0.05 m/s..... 127

Figure 6.26 Variation of $\rho_i v_i \left(\frac{\partial u}{\partial y}\right)_i$ along the vertical plate for different values of W_∞ for a Freon12-air mixture at $T_\infty = 288.15$ K, $\Delta T = 5$ K and $u_\infty = 0.05$ m/s 128

Figure 6.27 Variation of $g(\rho_i - \rho_\infty)$ along the vertical plate for different values of W_∞ for a Freon12-air mixture at $T_\infty = 288.15$ K, $\Delta T = 5$ K and $u_\infty = 0.05$ m/s 129

Figure 6.28 Variation of $\mu_i \left(\frac{\partial^2 u}{\partial y^2}\right)_i$ along the vertical plate for different values of W_∞ for a Freon12-air mixture at $T_\infty = 288.15$ K, $\Delta T = 5$ K and $u_\infty = 0.05$ m/s 130

Figure 6.29 Variation of x^*_{sep}, $\mu_i \left(\frac{\partial^2 u}{\partial y^2}\right)_i$ and $(\rho_\infty - \rho_i)$ with W_∞ for a Freon12-air mixture at $T_\infty = 288.15$ K, $\Delta T = 5$ K and $u_\infty = 0.05$ m/s 131

Figure 6.30 Value of $x^*_{sep} Ja^m$ for a Freon12-air mixtures 132

Figure 6.31 Value of the exponent m for a Freon12-air mixtures 133

Figure 6.32 Comparison of approximate x^*_{sep} and numerically obtained x^*_{sep} for Freon12-air mixture 134

Figure 6.33 Effect of W_∞ on $Nu_x / \mathrm{Re}_x^{1/2}$ for a Freon12-air mixture at $T_\infty = 315.15$ K and $T_{wall} = 285.15$ K 135

Figure 6.34 Effect of $(T_\infty - T_{wall})$ on $Nu_x / \mathrm{Re}_x^{1/2}$ for a Freon12-air mixture at $T_\infty = 315.15$ K and $W_\infty = 0.01$ 136

Figure 6.35 Dimensionless liquid film thickness for a Freon12-air mixture at $T_\infty = 315.15$ K and $T_{wall} = 285.15$ K 137

Figure 6.36 Interfacial gas concentration for a Freon12-air mixture at $T_\infty = 315.15$ K and $T_{wall} = 285.15$ K 138

Figure 6.37 Interfacial gas concentration for a Freon12-air mixture at $T_\infty = 315.15$ K and $W_\infty = 0.01$ 139

Figure 6.38 Value of Re_δ / $Re_x^{1/2}$ for a Freon12-air mixture at T_∞ = 315.15 K and T_{wall} = 285.15 K 140

Figure 6.39 Dimensionless separation length for a mercury-air mixture at T_∞ = 666.67 K 141

Figure 6.40 Dimensionless separation length for a mercury-air mixture at T_∞ = 750 K 142

Figure 6.41 Dimensionless separation length for a mercury-air mixture at T_∞ = 880 K 143

Figure 6.42 The liquid film thickness for a mercury-air mixture at T_∞ = 666.67 K 144

Figure 6.43 Interface velocity for a mercury-air mixture at T_∞ = 666.67 K 145

Figure 6.44 The mass flux at the interface for a mercury-air mixture at T_∞ = 666.67 K 146

Figure 6.45 Gas concentration at the interface for a mercury-air mixture at T_∞ = 666.67 K 147

Figure 6.46 Interface temperature for a mercury-air mixture at T_∞ = 666.67 K 148

Figure 6.47 The normalized wall heat flux for a mercury-air mixture at T_∞ = 666.67 K 149

Figure 6.48 Variation of $\rho_i u_i \left(\frac{\partial u}{\partial x}\right)_i$ along the vertical plate for different values of W_∞ for a mercury-air mixture at T_∞ = 880 K, ΔT = 30 K and u_∞ = 0.03 m/s 150

Figure 6.49 Variation of $\rho_i v_i \left(\frac{\partial u}{\partial y}\right)_i$ along the vertical plate for different values of W_∞ for a mercury-air mixture at T_∞ = 880 K, ΔT = 30 K and u_∞ = 0.03 m/s 151

Figure 6.50 Variation of $g(\rho_i - \rho_\infty)$ along the vertical plate for different values of W_∞ for a mercury-air mixture at T_∞ = 880 K, ΔT = 30 K and u_∞ = 0.03 m/s 152

Figure 6.51 Variation of $\mu_i\left(\frac{\partial^2 u}{\partial y^2}\right)_i$ along the vertical plate for different values of W_∞ for a mercury-air mixture at $T_\infty = 880$ K, $\Delta T = 30$ K and $u_\infty = 0.03$ m/s 153

Figure 6.52 Variation of x^*_{sep}, $\mu_i\left(\frac{\partial^2 u}{\partial y^2}\right)_i$ and $(\rho_\infty - \rho_i)$ with W_∞ for a mercury-air mixture mixture at $T_\infty = 880$ K, $\Delta T = 30$ K and $u_\infty = 0.03$ m/s 154

Figure 6.53 Variation of $x^*_{sep} Ja^m$ with W_∞ for a mercury-air mixture 155

Figure 6.54 Value of the exponent m for mercury-air mixture 156

Figure 6.55 Comparison of approximate x^*_{sep} and numerically obtained x^*_{sep} for a mercury-air mixture 157

Figure 6.56 Velocity profiles along the plate for a mercury-air mixture at $T_\infty = 666.67$ K 158

Figure 6.57 Temperature profiles along the plate for a mercury-air mixture at $T_\infty = 666.67$ K 159

Figure 6.58 Concentration profiles along the plate for a mercury-air mixture at $T_\infty = 666.67$ K 160

Figure 6.59 Effect of W_∞ on Nu_x / $\mathrm{Re}_x^{1/2}$ for a mercury-air mixture at $T_\infty = 666.67$ K and $T_{wall} = 636.67$ K 161

Figure 6.60 Effect of $(T_\infty - T_{wall})$ on Nu_x / $\mathrm{Re}_x^{1/2}$ for a mercury-air mixture at $T_\infty = 666.67$ K and $W_\infty = 0.01$ 162

Figure 6.61 Dimensionless liquid film thickness for a mercury-air mixture at $T_\infty = 666.67$ K and $T_{wall} = 636.67$ K 163

Figure 6.62 Interfacial gas concentration for a mercury-air mixture at $T_\infty = 666.67$ K and $T_{wall} = 636.67$ K 164

Figure 6.63 Value of Re_δ / $\mathrm{Re}_x^{1/2}$ for a mercury-air mixture at $T_\infty = 666.67$ K and $T_{wall} = 636.67$ K 165

LIST OF TABLES

Table	*Title*	*Page*
Table 5.1	Convergence table for steam-hydrogen at $T_{\infty} = 393$ K and $T_{wall} = 363.15$ K	60
Table A.1	Saturated water vapor properties	179
Table A.2	Saturated liquid water properties	182
Table A.3	Saturated pressure of mercury	187
Table A.4	Latent heat of vaporization of mercury	189
Table A.5	Saturated pressure of Freon12	195
Table A.6	Latent heat of vaporization of Freon12	196

NOMENCLATURE

C_P specific heat, J/(kg·K)

D diffusion coefficient, m^2/s

Fr_x Froude number $= \dfrac{u_\infty^2}{gx\cos\theta}$

g gravitational acceleration, m/s^2

g^* component of gravity in the flow direction $= g\cos\theta$, m/s^2

g_{mx} local mass-transfer coefficient $= -\dfrac{\rho D}{W_i - W_\infty}\dfrac{\partial W}{\partial y}$

Gr Grashof number

h_{fg} latent heat of vaporization, J/kg

h_x local heat transfer coefficient $= q/\Delta T$, $W/(m^2K)$

i nodal index

j nodal index

Ja Jakob number $= c_p\,\Delta T/h_{fg}$

k thermal conductivity, W/(m·K)

l plate length, m

m number of nodes in the χ direction; collapsing exponent (see Equation (6.6))

$\dot{m}_i''$ mass flux at the interface, $kg/(s\cdot m^2)$

$\dot{m}$ mass flow rate per unit depth, kg/(s·m)

M molecular weight, kg/kmol

n number of nodes in the η direction within the liquid film

nv number of nodes in the η direction within the mixture layer

Nu_x local Nusselt number = $h_x\, x/k_L$

P Pressure, Pa

Pe Peclet number = $\frac{\dot{m}\delta\Delta\eta_+ c_P}{k\Delta\chi}, \frac{\dot{m}\delta\Delta\eta_+}{\mu\Delta\chi}, \frac{\dot{m}\delta\Delta\eta_+}{\rho D\Delta\chi}$

Pr Prandtl number = $\mu\, c_P/k$

q local wall heat flux, W/m^2

R $\left[\rho_L\mu_L/\rho\mu\right]^{1/2}$

$\overline{\mathrm{R}}$ universal gas constant = 8.3144 kJ/kmol·K

Re_δ film Reynolds number = $4\Gamma/\mu_L$

Re_x local Reynolds number = $\rho_L x u_\infty/\mu_L$

Sc Schmidt number = $\mu/(\rho D)$, evaluated at mixture properties

Sh_x local Sherwood number = $\frac{g_{mx}x}{\rho D}$

T temperature, K

ΔT overall temperature difference = $(T_\infty - T_{wall})$, K

u velocity component in the x direction, m/s

v velocity component in the y direction, m/s

W noncondensable gas mass fraction

x coordinate direction along the plate, m

x^* dimensionless coordinate along the plate = $\frac{gx\cos\theta}{u_\infty^2}$

y coordinate direction normal to the plate, m

Greek Symbols

α weight coefficient used to evaluate the face temperature; coefficient used to evaluate the face temperature

Γ condensate flow rate per unit width of film, kg/(m·s)

δ liquid film or boundary layer thickness, m

δ_m mean film thickness within a control volume $= \frac{\delta_e + \delta_w}{2}$, m

δ^* dimensionless film thickness $= \delta\sqrt{\frac{g\cos\alpha}{u_\infty \nu_L}}$

ϕ general variable used to represent u_L, T_L, u, T, or W

η coordinate used in the transformation, $\eta = y/\delta$

$\Delta\eta$ size of a control volume in the η direction

$\Delta\eta_+$ distance between control volumes (i,j+1) and (i,j) in the η direction

$\Delta\eta_-$ distance between control volumes (i,j) and (i,j-1) in the η direction

θ angle of plate inclination, measured from the vertical downward direction, radians

Λ pressure gradient parameter (see page 19)

μ viscosity, N·s/m^2

ν kinematic viscosity $= \mu/\rho$, m^2/s

ρ density, kg/m^3

σ condensation coefficient

τ shear stress, N/m^2

χ coordinate used in the transformation $\chi = x$

$\Delta\chi$ size of a control volume in the χ direction

Ω transpiration parameter (see page 18)

Subscripts

E control volume at (i+1,j)

e east face of the control volume at (i, j)

g noncondensable gas

i at the interface

iter iteration number

L liquid

0 zero gas concentration, i.e., at $W_{-} = 0$

P control volume at (i,j)

m mean value over length of plate

N control volume at (i, j+1)

Nu Nusselt's solution

n north face of the control volume at (i, j)

r used to denote reference temperature

S control volume at (i,j-1)

s south face of the control volume at (i, j)

sat saturation conditions

sep separation point

v vapor

W control volume at (i-1,j)

w	west face of the control volume at (i, j)
wall	at the wall
x	local value at axial location x
∞	at the free stream

Chapter 1

INTRODUCTION

The work presented in this thesis is a numerical study of laminar film condensation of a vapor in the presence of a noncondensable gas. The phenomenon of condensation was investigated by many authors because of its importance in industry. Typical industrial applications of condensation can be found in power plants (fossil and nuclear), the refrigeration industry, the aerospace industry, and so on. The most notable application is in the nuclear industry where, in the case of an accident, the reactor pressure can be reduced by means of condensation. However, if a noncondensable gas is mixed with vapor, it reduces the rate of condensation and consequently the rate of heat transfer, which are undesirable effects. Also, during the condensation process in other industrial applications, mixtures of vapor and gases are more often encountered than a pure vapor.

Since the presence of gases in vapor affects the condensation process, numerous analytical, experimental and numerical studies have been conducted in order to investigate all effects related to this problem. A review of the previous work showed that a considerable effort was on the topics of pure vapor condensation and on condensation of vapor in the presence of a heavier noncondensable gas. Condensation in the presence of lighter gases, however, did not receive as much attention as condensation in the presence of heavier gases. Indeed, very few publications were found in which condensation of a vapor-lighter gas mixture was considered. One possible reason for such a shortage of

analysis lies in the complexity of the process, which complicates the solution procedure. The complexity of the physical processes is reflected in the presence of the unfavorable buoyant force which acts against the flow direction and often causes the mixture boundary layer to separate. A comprehensive analysis of this complex problem therefore requires a comprehensive mathematical model, which can only be solved numerically.

Because (a) the condensation of a vapor-lighter gas mixture is important in industry, (b) understanding of the fundamental physical phenomena is also important, and (c) there is not much previous work related to this problem, this thesis was focused on the effects of a lighter gas on the laminar film mixed convection condensation. The solution procedure was entirely based on a numerical approach, and the results are presented in graphical form. In the analysis, an emphasis was put on two segments: the mixture boundary layer separation and the reduction in heat transfer to the wall due to the presence of gases. The former phenomenon is important because the entire model is valid only up to the separation location, while the latter phenomenon is important because of its application to the design of condensation systems. Results were obtained for three vapor-gas combinations: steam-hydrogen, Freon12-air and mercury-air. These three vapor-gas combinations were chosen to obtain three different ratios of molecular weights. Using the results obtained for all three mixtures it was possible to estimate the separation location for a specified range of input parameters. Also, the results show the change of heat transfer to the wall and comparison of heavier/lighter gas effects on the rate of heat transfer during condensation.

Chapter 2

LITERATURE REVIEW

Among the numerous publications related to laminar film condensation, the focus of this review is on condensation of moving pure vapors and condensation of moving vapor-gas mixtures. Recognizing the specific features of condensation of a vapor mixed with a lighter gas, described in the INTRODUCTION, the review also includes some publications related to the analytical methods for the prediction of boundary layer separation.

Review of the condensation of a moving pure vapor is included because it can be considered as a limiting case of the condensation of a vapor with a very small gas concentration. In addition, condensation of pure vapors gives the highest rate of heat transfer to the wall, which is used for comparison with the heat transfer rate obtained during the condensation of the vapor-gas mixture. In the part of the review that covers condensation of moving vapor-gas mixtures, more publications will be related to mixtures of a vapor and a heavier gas because very little of the previous work has focused on the condensation of a vapor-lighter gas mixture. The last part of the literature review is related to the topic of boundary layer separation because of some similarities between laminar film condensation of a vapor-lighter gas mixture and the flow stagnation over a moving plate with suction. None of the presented segments of literature can entirely cover all the features of the problem of condensation of vapor with a lighter gas. Furthermore,

the review of the analytical methods for boundary layer separation is added although the approach in the present work is entirely numerical. The reason for such a compilation of literature lies in the fact that all described phenomena are related to some aspects of vapor condensation in the presence of a light gas and it helps to better understand the nature of the problem considered in this work.

2.1 Condensation of Moving Pure Vapors

A comprehensive review of the literature in this area was given by Rose (1988). The starting point for all research in the condensation of moving pure vapors was the classical Nusselt (1916) work, with emphasis on the interfacial shear force at the vapor-liquid interface. In the derivation of simplified formulae for interfacial shear stress and heat transfer rate, authors frequently used assumptions such as neglecting effects of inertia and convection in the condensate film, and in some cases neglecting the liquid film surface velocity.

Rohsenow et al. (1956) assumed constant liquid properties and a linear temperature distribution across the film. They also neglected the inertia terms in the liquid momentum equation. From a simple force balance on a liquid slice across the flow and energy balance at the interface, a correlation between shear stress at the interface and film thickness was obtained. An expression for the mean heat transfer coefficient along the plate was also developed. In the same work, the analysis was extended to turbulent flow and an

expression for the film Reynolds number was derived to define the transition from laminar to turbulent flow.

The approach by Cess (1960) considered both momentum balances in the liquid and vapor as well as continuity of the interface velocity, with shear stress and mass flow at the interface as the boundary conditions. He solved the forced-convection condensation problem on a horizontal plate using a similarity transformation and a series solution method. Neglecting higher order terms he implicitly neglected acceleration effects and thermal convection within the liquid film. His work resulted in a relationship that gives the value of interfacial shear stress for two cases: the zero condensation rate limit, $\frac{RJa_L}{\mathrm{Pr}_L} \to 0$, and the infinite condensation rate limit, $\frac{RJa_L}{\mathrm{Pr}_L} \to \infty$. Later works showed that the actual shear stress at the interface is larger than the shear stress predicted by Cess. The heat transfer results were presented as a curve of $Nu_x \, \mathrm{Re}_x^{-1/2}$ vs. $\frac{RJa_L}{\mathrm{Pr}_L}$. Since the properties in the model were assumed to be constant, the results suggest that $Nu_x \, \mathrm{Re}_x^{-1/2}$ is constant along the plate. For both limiting cases mentioned earlier, closed form expressions for $Nu_x \, \mathrm{Re}_x^{-1/2}$ were given.

Analysis of laminar film condensation on a horizontal plate was also done by Koh (1962). He used the same set of governing equations as Cess did, transformed them into a set of ordinary differential equations which he solved numerically. Unlike Cess, he did not

neglect liquid film surface velocity. Results showed that $Nu_x \, \mathrm{Re}_x^{-1/2}$ depends on R *and* $\frac{Ja_L}{\mathrm{Pr}_L}$ for small values of Pr_L and that energy transferred by convection in the liquid film is negligibly small. Also, the presentation of results in this form suggests, like in Cess's paper, that $Nu_x \, \mathrm{Re}_x^{-1/2}$ is constant along the plate. For higher values of Prandtl number (Pr_L>10) it was found that energy transferred by convection in the liquid film is of significant importance and that the curve of $Nu_x \, \mathrm{Re}_x^{-1/2}$ has a minimum value when plotted against $\frac{Ja_L}{\mathrm{Pr}_L}$. A comparison of results with those obtained by Cess shows good agreement for small values of Pr_L, but for higher values of Pr_L there is some discrepancy, which confirms the importance of the energy convection in the liquid film for this case.

Shekriladze and Gomelauri (1966) neglected inertia and convection effects in the liquid film in their analysis of the flow along vertical and horizontal plates. They introduced an additional simplification using $\tau_i = \dot{m}_i^{"}(u_\infty - u_i)$ as the approximation for shear stress at the interface. The heat transfer coefficient for horizontal plates was given as a function of $\frac{Ja_L}{\mathrm{Pr}_L}$ and $\frac{\rho_L h_{fg} u_\infty k_L}{\Delta T \, x}$(or $\frac{\rho_L h_{fg} u_\infty k_L}{\Delta T \, L}$ for the average heat transfer coefficient). In order to include effects of inertia forces in the liquid film, a correction factor for the heat transfer coefficient was introduced. This factor shows that the effect of the inertia forces is negligible for non-metallic liquids ($\frac{Ja_L}{\mathrm{Pr}_L}$<0.1). Similar relationships for the local and average heat coefficients were developed for vertical plates. The results obtained for

horizontal plates approached the results obtained by Cess, for the case $\frac{Ja_L}{Pr_L} << 1$, which justifies neglecting liquid surface velocity.

Denny and Mills (1969) used a numerical approach to solve the finite difference formulation of the conservation equations for the boundary layer flow. For shear stress at the interface they used an asymptotic solution of the vapor boundary layer, which states that "the local shear stress is identically equal to the momentum given up by the condensing vapor." In the paper they investigated effects of "forced vapor flow, variable wall temperature and variable fluid properties". Ten fluids were used in the investigation. Results include graphical comparisons of the heat transfer coefficient for three substances that undergo a flow with the same characteristics. Also, an analytically derived expression for the heat transfer coefficient on a non-isothermal wall was compared to that obtained from the numerical solution. The purpose of the comparison was to investigate the influence of the reference temperature used in the simplified analysis. The reference temperature was defined using a weighting parameter, $T_r = T_{wall} + \alpha(T_\infty - T_{wall})$, and comparison of results was given for two values of α : 0.4 and 0.345. The relative error obtained in the comparison is in the range -3% to 2% and depends on the value of $(T_\infty - T_{wall})$.

A solution that included both the vapor and liquid boundary layers was given by Fujii and Uehara (1972). Their analysis followed Jacobs (1966) with a correction for the velocity at

the free stream. The model ensured the same velocity for the two boundary layers at the interface, as well as continuity of the shear stress at the interface. Assuming a parabolic velocity profile in the vapor, they used an integral method to calculate the liquid film thickness and surface velocity. Along with the numerical results, they gave an approximate expression for the mean Nusselt number Nu_m as a function of $R, \mathrm{Re}_l, \frac{L^3 g}{\nu_L^2}$ and $\frac{Ja_L}{\mathrm{Pr}_L}$. Generally, it was found that the approximate expression for the mean Nusselt number was in good agreement with the experimental data reported by several authors, except for the cases where $Nu_m > 2 \times 10^4$.

Rose (1989) proposed a new approximate formula for the parameter $Nu_x \, \mathrm{Re}_x^{-1/2}$ applicable to condensation over horizontal plates. The independent parameters included in the analysis are: $\frac{Ja_L}{\mathrm{Pr}_L}$ and R. The formula for zero condensation rate ($\frac{RJa_L}{\mathrm{Pr}_L} \to 0$) approaches the formula obtained by Cess (1960), while for very high condensation rate ($\frac{RJa_L}{\mathrm{Pr}_L} \to \infty$), it approaches the results obtained by Shekriladze and Gomelauri (1966). Comparison with the solution of Koh (1962) showed good agreement for lower values of Prandtl number.

2.2 Condensation of Moving Vapor-Gas Mixtures

Sparrow et al. (1967) solved a forced-convection condensation problem on a horizontal plate using both analytical and numerical approaches. In their work, the inertia forces in the liquid film were neglected and the temperature profile across the film was assumed to be linear. They neglected the energy equation for the mixture, assuming that the amount of energy transferred by convection and conduction at the interface is very small compared to that released as latent heat. Continuity of the shear stress was enforced at the interface, and the streamwise velocity at the interface was assumed to be zero because $u_i << u_\infty$. Using similarity transformations, the simplified set of partial differential equations was transformed into a set of ordinary differential equations, and then solved numerically and by an integral method. Steam-air was used as the vapor-gas combination. Heat transfer results were presented in terms of q / q_{Nu} vs. ΔT, which suggests that q / q_{Nu} is constant along a horizontal plate for a forced-convection condensation in the presence of a noncondensable gas. From the comparison with the results reported by Minkowycz and Sparrow (1966), it was observed that the presence of noncondensable gases in the condensation from a quiescent mixture on a vertical plate significantly decreases heat transfer compared to the forced-convection condensation case. Also, it was concluded that "the interfacial resistance has a negligible effect on forced-convection condensation" for a steam-air mixture.

A complete numerical treatment of the mixture boundary layer equations that describe a moving steam-air mixture along a vertical surface, was performed by Denny et al. (1971). They used the finite-difference method to solve the set of parabolic differential equations in the mixture, and a simplified Nusselt analysis to solve the liquid film layer. Properties in the liquid film layer were evaluated at the reference temperature $T_r = T_{wall} + 0.33(T_i + T_{wall})$, and properties in the mixture were evaluated at the local temperature. Heat transfer results were obtained for a steam-air mixture, and presented as diagrams of q / q_{Nu} versus x. Effects of different values of T_∞, W_∞, u_∞, and $(T_\infty - T_{wall})$ on q / q_{Nu} were investigated. It was noticed that q / q_{Nu} increases with increasing u_∞ and decreases along the plate. Also, for large u_∞, it was found that the effect of interfacial velocity and natural convection can be neglected. In most cases for $T_\infty = 373K$, increasing $(T_\infty - T_{wall})$ decreases q / q_{Nu} except in two limiting cases: for high u_∞ (3 m/s) and low W_∞ (0.001), and for low u_∞ (0.03 m/s) and high W_∞ (0.1).

A numerical procedure was also used by Denny and Jusionis (1972) in the investigation of the effect of a noncondensable gas (air) on the condensation of six different vapors on a vertical plate. Four vapors(Freon12, ethanol, butanol, and carbon tetrachloride) had molecular weights greater than air, and one of the vapors considered was Freon12. The heat transfer results were reported in the form of q / q_{Nu} versus x for $u_\infty = 0.305$ and 3.05 m/s, and for $W_\infty = 0.001$ and 0.01. The free stream temperature was varied from 305.37 to 322.15 K, while the plate temperature was kept at 299.82 K. Using numerical results, a

semi-empirical method was developed for the prediction of the heat flux, temperature at the interface, and the mass transfer conductance.

The effect of a noncondensable gas on the condensation of liquid metals was investigated by Turner et al. (1973). The model they used included the full set of differential equations for the mixture boundary layer, while the Nusselt analysis was used for the liquid film. At the interface, continuity of velocity and shear stress were applied. It was assumed that thermodynamic equilibrium does not always exist, so an interfacial resistance equation was used as an additional condition at the interface. The solution procedure required solving a set of equations for the interface in order to obtain the interface conditions. They then solved the set of partial differential equations for the mixture boundary layer by a fully implicit finite-difference method. The results were presented in terms of q / q_{Nu} versus x for mercury-air and sodium-argon mixtures. At low free stream velocities in the mercury-air mixture, the adverse buoyancy effect was found to be so pronounced that at some point along the plate the mixture boundary layer separated. The simplified formula by Acrivos (1958) for the separation distance was compared with the numerical results. The difference between the approximate and the exact (numerical) solution values for x_{sep} was attributed to neglecting the effect of suction in the approximate formula. At low pressures, the interfacial resistance was found to change the form of the q / q_{Nu} curve, so that a maximum value existed at some finite distance along the plate and q / q_{Nu} approached zero as x approached zero.

Rutunaprakarn and Chen (1975) considered quiescent condensation of a Freon12-N_2 mixture on a vertical plate. Although this paper considered quiescent condensation, it is included in the review because it involved vapor-lighter gas mixture. The basis for the work was a similarity transformation applied to the set of partial differential equations for liquid and vapor. The assumptions and the set of equations that were used are the same as in Minkowycz and Sparrow (1966). At the interface they used continuity of velocity, mass flow, and shear stress. The system of ordinary differential equations was solved numerically for free stream gas concentration in the range 10^{-4} to 5×10^{-4}. The main restriction in the analysis is that the similarity solution is only applicable to the cases where the bulk concentration of the lighter gas is very small (approximately 10^{-4}). Results were given in the form of Nu_x / $Nu_{x,Nu}$, where $Nu_{x,Nu}$ is the Nusselt number obtained for the pure vapor using Nusselt's solution. Velocity and concentration profiles were given as well as comparison with profiles obtained for a steam-air mixture. The conclusions were: 1) Larger shear force at the interface, caused by the buoyant effect, may introduce instability in both vapor layer and at the interface, and 2) Very small gas concentration in the vapor may cause "considerable reduction in heat transfer."

Work done by Lucas (1976) considered mixed-convection condensation of vapor mixtures, instead of vapor-gas combinations. For the condensate film, Nusselt's assumptions were used, while standard boundary-layer assumptions for the vapor layer were introduced. At the interface, continuity of velocity, temperature, shear stress, and

mass flow were enforced. The system of equations was solved numerically and by two integral methods. Numerical solution of the vapor boundary layer equations was based on a finite difference method, while the liquid film equations were solved analytically using the results obtained from the numerical solution. In the integral solutions, the same profiles were assumed for temperature and concentration. He also assumed negligible effect of thermodynamic coupling by thermal diffusion, and very small influence of heat transfer in the vapor. The two integral formulations differ only in the assumed velocity profiles. Both formulations result in three first order ordinary differential equations. Results were presented in the form of graphs of $Nu_x \, \mathrm{Re}_x^{-1/2}$ and $\frac{T_i - T_{wall}}{T_\infty - T_{wall}}$ versus $gx \,/\, u_\infty^{\,2}$. An emphasis was placed on a comparison between the sets of results obtained by the two integral methods. Generally, good agreement was obtained, and it was pointed out that the use of an integral approach leads to considerable savings in computational time.

Rose (1980) gave an expression that relates the condensation rate to the free stream and liquid film surface conditions. The new expression is an extension of the author's earlier work and was based on the replacement of Nusselt and Prandtl numbers by Sherwood and Schmidt numbers, respectively. The final result gave a relationship between Sc, Re, Sh, and $W_\infty \,/\, W_i$ and is valid for both limiting cases: zero and infinite condensation rates. Good agreement was obtained in a comparison with experimental data.

Siddique et al. (1989) analyzed the effect of hydrogen on forced-convection steam condensation over a horizontal flat plate. In the analysis they neglected liquid inertia and liquid energy convection. In addition, they assumed zero vapor-gas mixture velocity at the interface, and constant mixture properties evaluated at the interface temperature. The Schmidt number was calculated at the average values of the properties in the free stream and at the interface. In the analysis similarity transformations were used that yielded a system of ordinary differential equations which was solved iteratively. The investigation was focused on the effect of the free stream temperature, gas concentration, and wall sub-cooling on the condensation rate, as well as on the effect of the sensible heat on the overall heat transfer. The results were given in the form of q / q_0 versus x, where q_0 is the heat flux at zero gas concentration. Results obtained at $T_\infty = 100^0 C$ showed steadily decreasing heat transfer with increasing W_∞ for fixed wall sub-cooling level $(T_\infty - T_{wall})$. They observed that for values of $(T_\infty - T_{wall})$ up to $20^0 C$ the values of q / q_0 "is insensitive to the subcooling at all mass fractions of the noncondensable gas". A comparison of the heat transfer for steam-hydrogen and steam-air showed that "hydrogen has more inhibiting effect on the heat transfer" than air. That was attributed to the greater number of moles of the hydrogen in the mixture for the same free stream gas concentration. The authors showed that the contribution of the sensible heat transfer to the total heat transfer is not negligible, particularly at high gas concentration values.

A numerical solution of the complete model for laminar film condensation was done by Chin (1995). He investigated the effects of the inertia terms in the liquid momentum equation and the energy convection terms in the liquid energy equation. Three vapor-gas combinations were used in his work providing the range of Pr_L from 0.006 to 1000. He found that the effect of the inertia term is significant in the case of pure sodium condensation while in other cases the effect of the inertia term is negligible. Also, he found that the presence of a small amount of a noncondensable gas ($W_\infty = 10^{-3}$) in the sodium reduced this effect. The effect of the energy terms in the liquid energy equation was found to be insignificant for steam-air mixtures. This effect resulted in the underprediction of Nusselt number for glycerin-bromine mixtures. For sodium-argon mixtures, neglecting the energy convection terms resulted in the underprediction of Nusselt number for low values of x^* while, for higher values of x^*, the effect was an overprediction of Nu_x.

2.3 Analytical Models of Boundary Layer Separation

This segment of the literature review deals with work in boundary layer separation during single-phase flow over the exterior of surfaces. Two important phenomena that occur in laminar film condensation of a mixture of a vapor and a lighter gas are suction at the liquid-mixture interface and motion of the liquid film layer along the plate. Because these two phenomena can affect the mixture boundary layer separation, this segment of the

literature review gives special attention to the analytical boundary layer models that include them. A review of some analytical methods for the prediction of boundary layer separation was given by Chang (1970). The first approximate solution for the prediction of separation location was given by Pohlhausen (1921) and is referred to as the Pohlhausen-von Karman method. Although the method predicts the separation location for the flow without suction over fixed boundary, it is important because it forms the basis for numerous integral methods that were developed later. The method uses a fourth order polynomial approximation of the velocity profile. The characteristic parameter that results from the chosen profile is the shape factor $\Lambda = \frac{\delta^2}{\nu}\frac{du_\infty}{dx}$. At the separation location, which is characterized by $\left(\frac{\partial u}{\partial y}\right)_{y=0} = 0$, this parameter was found to be $\Lambda = -12$. The Pohlhausen-von Karman method is very simple and it gives approximately 30 per cent error for the separation location when compared to the numerical solution, which is assumed to be exact.

The Pohlhausen-von Karman method was used by Acrivos (1958) to calculate the shear stress and the rate of heat transfer in external flows for mixed convection condition. In his model, the effects of suction or a moving boundary were not considered; however, the temperature-induced buoyant force was included. Fourth and third order polynomial approximations were used for the velocity and temperature profiles, respectively. Results obtained from solving the momentum and energy integral equations were presented in graphical form as a function of the Prandtl number, and the significance of the parameter

Gr / Re_x^2 was emphasized. A plot of separation distance versus Prandtl number was given for the cooling problems with negative $u_\infty \frac{du_\infty}{dx}$ and for Prandtl numbers in the range $4<Pr<100$. Generally, it was concluded that cooling at the wall "hastens the appearance of the separation point," while heating stabilizes it.

Launder (1964) gave an interesting extension to the Pohlhausen-von Karman method, under the same flow conditions. He split the velocity profile into two curves, providing continuity of the velocity and its first and second derivatives at the interface between the two curves. For the case of retarded flow, overall good accuracy was obtained.

Another refinement of the Pohlhausen-von Karman method was applied by Zien (1971). The basis of the refinement was Volkov's (1965) idea to integrate the momentum equation twice, using a simple velocity profile. The method is also referred to as the double integral method. Zien applied the method to calculate the skin friction on a fixed porous plate assuming the existence of suction or blowing velocity. Calculations were done for linear and fourth order polynomial velocity profiles and for uniform suction or blowing. Results were given in the form of graphs of the friction coefficient versus a blowing parameter. They were compared to exact results obtained from the Blasius solution with suction and blowing, and with results obtained by using the same velocity profiles and the usual Pohlhausen-von Karman method. Overall results showed very good agreement with the exact solution in both cases, which justified application of the double integral method for the boundary layer with mass transfer at the wall. The advantage of this method is in the

simplicity of the calculation (results are in closed form), and very small sensitivity of the results to the chosen velocity profile.

The same technique was applied by Zien (1976) in an analysis of heat transfer in transpired boundary layers. The main purpose of the analysis was to demonstrate the effectiveness of the integral methods. Two temperature profiles were used to investigate the effects of the profiles on the heat transfer coefficient. Again, good agreement was obtained compared to the exact numerical solution.

Thomas and Amminger (1988) developed a one-parameter polynomial type integral method which gives an error of 10 to 15 per cent near the separation point. The method is applicable for the cases with suction or blowing and for a fixed wall boundary. The starting point for the analysis was an approximation of the distribution in shear stress. Integration of the Newton law of viscous stress with an assumed shear stress profile gave velocity profiles which are a function of the standard pressure gradient parameter $\Lambda = \frac{\delta^2}{\nu}\frac{du_\infty}{dx}$ and the transpiration parameter $\Omega = -\frac{v_0\delta}{\nu}$, where v_0 is the suction or blowing velocity. Using those velocity profiles, approximate integral solutions were obtained for similar and nonsimilar flows with transpiration and an adverse pressure gradient. Results were compared with numerical solutions and with the Pohlhausen-von Karman integral solution. Following the same approach, Thomas and Amminger (1990) developed a two-parameter integral method for a transpired thermal boundary layer. The

error in the heat transfer coefficient near separation ranges between 10 and 20 per cent compared to the numerical solution.

Another demonstration of the effectiveness of the double integral method was presented by Sucec (1995). He studied a steady laminar two-dimensional flow with constant properties. An important aspect of his derivation was the selection of a low order velocity profile that does not satisfy the boundary condition $\nu \frac{\partial^2 u}{\partial y^2} = -u_\infty \frac{du_\infty}{dx}$ at $y = 0$. The author made a comparison of the separation point location with the exact values for sixteen different free stream velocity variations. The maximum error was 3.4 per cent compared to the numerical results obtained for the stagnation type of flow.

2.4 Summary of the Review

As the review shows, among the numerous publications on laminar film condensation, only three papers considered effect of a lighter gas on condensation on a flat plate. Conclusions from all three papers can be summarized as: (a) the presence of a lighter gas in the vapor causes mixture boundary layer separation, (b) a small amount of a lighter gas can considerably reduce the rate of the heat transfer for the condensation of a vapor-gas mixture, and (c) lighter gas has more pronounced inhibiting effect on the heat transfer than heavier gas.

A review of the literature on boundary layer separation shows that very good methods were developed to predict the location of the separation point, but only for simple flows. No analytical approach was found that would consider both suction velocity and an accelerating boundary. An important assumption made by Sparrow et al. (1967) was that the streamwise velocity component at the interface can be neglected. This assumption can simplify calculation of the velocity profile in the mixture. However, this is valid only if $u_\infty >> u_i$. The work of Turner et al. (1973) showed that separation occurred with low values of u_∞. With high u_∞, the liquid film layer can reach turbulent flow before the separation occurs, so the approximation made by Sparrow et al.(1967) is not necessarily justified in attempts to get an analytical form for the separation point location.

In the case of condensation of vapor with a noncondensable gas, the suction velocity highly depends on the gas concentration at the interface, which is not known *a priori*. Determination of the gas fraction at the interface, for example, can be done following Sparrow et al. (1967). Their method was based on numerical integration of ordinary differential equations, and it is restricted to certain values of Schmidt number and by other assumptions that were made in the model. A consequence of increased gas concentration near the interface is a change in the density across the mixture layer. Separation theory only considers a change in the density due to a temperature gradient.

The work related to the condensation of a vapor-lighter gas mixture and a brief review of achievements in the analytical prediction of the boundary layer separation suggest that the

most appropriate approach to the problem is a numerical solution method, which will be applied in this work.

Chapter 3

STATEMENT OF THE PROBLEM

3.1 The Physical Model

The effect of a lighter noncondensable gas on laminar mixed-convection film condensation on the top of a flat, isothermal plate with arbitrary inclination was investigated in this work. The physical model is depicted in Figure 3.1.

In the model, the plate is assumed to have a large width (normal to the page). The liquid condensate film flows over the plate and adjacent to the liquid film is the mixture boundary layer which extends into the free stream flow, where there are uniform flow conditions and properties. The mixture consists of a vapor and a noncondensable gas whose molecular weight is lower than that of the vapor. The coordinate system is Cartesian with the origin located at the leading edge of the plate and the x axis directed along the plate. Since the plate has a large width, the flow in the liquid film and in the mixture layer is two-dimensional. The gravity force is acting in the vertical downward direction which is at an angle θ from the x axis. In the model, it is assumed that the total pressure is uniform everywhere and can be expressed as the sum of the vapor partial pressure and the partial pressure of the gas. Ideal gas behavior is also assumed for the gas and the vapor.

During condensation, the build up of noncondensable gas near the liquid-mixture interface creates a gas concentration gradient across the mixture boundary layer. The gas concentration is shown in Figure 3.1 as $W(x, y)$ to indicate that it is a function of x and y coordinates. The concentration gradient is maximum at the interface and decreases toward the free stream, where the gradient becomes equal to zero. The increase of gas concentration near the interface raises the partial pressure of the gas and decreases the partial pressure of the vapor. Consequently, the saturation temperature at the interface is lower than the free stream temperature, and heat transfer toward the plate is reduced compared with the case of pure condensation. The concentration and temperature gradients across the mixture layer change the density within the mixture boundary layer. The difference between the local mixture density and the free stream density creates a buoyant force which acts opposite to the flow direction. This means that the buoyant force slows the mixture layer and separation of the layer occurs at some distance along the plate if the free stream velocity is relatively small. The result of the mixture layer deceleration is a further decrease in heat transfer.

The effect of the lighter gas will be investigated on three vapor-gas combinations: steam-hydrogen, Freon12-air, and mercury-air. The transport and physical properties of all vapors and gases used in this study are given in Appendix A. In this work, the focus will be on the mixture boundary layer separation and on the effects of the gas on the heat transfer along the plate.

3.2 The Analytical Model

The analytical model includes the continuity, momentum, and energy equations for both the liquid film and the mixture layer as well as the gas conservation equation for the mixture layer. An appropriate set of boundary conditions is established at the wall, at the free stream and at the liquid film surface.

The system of equations for laminar, incompressible flow is:

- **Liquid Continuity Equation**

$$\frac{\partial}{\partial x}(\rho_L u_L) + \frac{\partial}{\partial y}(\rho_L v_L) = 0 \tag{3.1}$$

- **Liquid Momentum Equation**

$$\frac{\partial}{\partial x}(\rho_L u_L u_L) + \frac{\partial}{\partial y}(\rho_L u_L v_L) = \frac{\partial}{\partial y}\left(\mu_L \frac{\partial u_L}{\partial y}\right) + g(\rho_L - \rho_\infty)\cos\theta \tag{3.2}$$

- **Liquid Energy Equation**

$$\frac{\partial}{\partial x}(\rho_L u_L C_{P_L} T_L) + \frac{\partial}{\partial y}(\rho_L v_L C_{P_L} T_L) = \frac{\partial}{\partial y}\left(k_L \frac{\partial T_L}{\partial y}\right) \tag{3.3}$$

- **Mixture Continuity Equation**

$$\frac{\partial}{\partial x}(\rho u) + \frac{\partial}{\partial y}(\rho v) = 0 \tag{3.4}$$

- **Mixture Momentum Equation**

$$\frac{\partial}{\partial x}(\rho u u) + \frac{\partial}{\partial y}(\rho u v) = \frac{\partial}{\partial y}\left(\mu \frac{\partial u}{\partial y}\right) + g(\rho - \rho_\infty)\cos\theta \tag{3.5}$$

- **Mixture Energy Equation**

$$\frac{\partial}{\partial x}(\rho u C_P T) + \frac{\partial}{\partial y}(\rho v C_P T) = \frac{\partial}{\partial y}\left(k \frac{\partial T}{\partial y}\right) + \frac{\partial}{\partial y}\left(\rho D(C_{P_g} - C_{P_v}) \frac{\partial W}{\partial y} T\right) \tag{3.6}$$

- **Mixture Mass Diffusion Equation**

$$\frac{\partial}{\partial x}(\rho u W) + \frac{\partial}{\partial y}(\rho v W) = \frac{\partial}{\partial y}\left(\rho D \frac{\partial W}{\partial y}\right) \tag{3.7}$$

The boundary conditions that can be applied are:

- **At the plate surface** $(y = 0)$

$$u_L = 0 \tag{3.8}$$

$$v_L = 0 \tag{3.9}$$

$$T_L = T_{wall} \tag{3.10}$$

- **At the free stream** $(y \rightarrow \infty)$

$$u = u_\infty \tag{3.11}$$

$$T = T_\infty \tag{3.12}$$

$$W = W_\infty \tag{3.13}$$

- **At the liquid film surface** $(y = \delta)$

$$u_L = u \tag{3.14}$$

$$\mu_L \frac{\partial u_L}{\partial y} = \mu \frac{\partial u}{\partial y} \tag{3.15}$$

$$\dot{m}_i'' = \rho_L u_L \frac{d\delta}{dx} - \rho_L v_L = \rho u \frac{d\delta}{dx} - \rho v \tag{3.16}$$

$$\dot{m}_i'' W + \rho D \frac{\partial W}{\partial y} = 0 \tag{3.17}$$

$$\dot{m}_i'' = \frac{\sigma}{1 - 0.5\sigma} \frac{1}{\sqrt{2\pi R T_i}} \left[P_v - P_{sat}(T_i) \right] \tag{3.18}$$

$$k_L \frac{\partial T_L}{\partial y} = k \frac{\partial T}{\partial y} + \dot{m}_i'' h_{fg} \tag{3.19}$$

$$\dot{m}_i'' = \frac{d}{dx} \int_0^\delta \rho u dy \tag{3.20}$$

In the model, the transport and thermodynamic properties are evaluated at the local conditions. Also, it is assumed that thermodynamic equilibrium at the liquid-mixture interface does not always exist, and that interfacial resistance may have a significant influence. In most vapor-gas combinations, the interfacial resistance does not have a significant role, but in the condensation of liquid metals at low pressure it can considerably reduce the mass transfer through the interface and consequently it reduces heat transfer (Turner et al., 1973).

The general form of the interfacial resistance equation includes both surface temperature, T_i, and temperature of the molecules that are striking the surface, T_v, in the form

$$\dot{m}_i'' = \frac{\sigma}{1 - 0.5\sigma} \left[\frac{P_v}{\sqrt{2\pi R T_v}} - \frac{P_i}{\sqrt{2\pi R T_i}} \right] \tag{3.21}$$

This temperature difference is defined as a temperature jump, and in most applications this difference is negligible (Mills, 1992). In this work it will be assumed that $T_v \approx T_i$ so that the interfacial mass flow is proportional to the difference of the partial pressure of the

mixture at the interface P_v, and saturation pressure P_{sat}, calculated from the liquid surface temperature T_i. The coefficient σ in Equation (3.18) is referred to as the condensation coefficient and in this work it is taken to be unity (Turner et al., 1973). At high vapor pressure, the interfacial resistance is negligible in most cases, and the saturation temperature at the partial pressure of the vapor at the interface can be used as the interface temperature boundary condition.

To obtain the liquid film thickness δ, the liquid surface temperature T_i, and mass flux at the interface $\dot{m}_i''$, Equations (3.18), (3.19) and (3.20) were solved simultaneously.

3.3 Definition of the Separation Condition

An important phenomenon that occurs during condensation of a vapor-gas mixture involving a lighter gas is mixture boundary layer separation. Generally, boundary layer separation occurs when the normal velocity gradient at the surface is equal to zero. During laminar film condensation, a build up of the gas concentration near the film surface creates a buoyant force that acts against the flow direction. The magnitude of the buoyant force is maximum at the liquid-mixture interface and decreases toward the free stream flow where it becomes equal to zero. The result of the buoyant force is to change the mixture velocity profile so that at some location along the plate the velocity profile has a characteristic "S" shape, as shown in Figure 3.2(a). The velocity profile has zero gradients at the interface and free stream, and an inflection point somewhere in between.

As the vapor component condenses on the cold plate, a liquid film is formed on the plate and it accelerates along the plate due to the gravity force. At the location along the plate where mixture velocity gradient becomes zero at the interface, liquid surface velocity u_i has a value that is generally different from the free stream velocity. Two possible forms of velocity development are illustrated in Figure 3.2. The velocity profile across the liquid film and mixture boundary layer at two locations along the plate is shown in Figure 3.2(a) for one of these two possible forms. At the location x_1, two conditions are satisfied: $u_i < u_\infty$ and $\left(\frac{\partial u}{\partial y}\right)_{y=\delta} = 0$. If the velocity profile continues to develop, then it would look as shown at the location x_2. It can be observed that the velocity gradient at the interface is negative and that there exists a region near the interface where the mixture velocity is negative relative to the interface velocity, while $(u_\infty - u_i)$ is positive. This velocity profile implies a reverse flow relative to the interface, and because of that the situation at the location x_1 is classified as the boundary layer separation. Figure 3.2(b) depicts the case when the velocity gradient at the interface is zero at the location x_1 and negative at the location x_2, while in both cases the interface velocity is greater than the free stream velocity. This situation was encountered during condensation of pure vapors or mixtures of a vapor and a heavier gas. The situation at location x_2 shows that the mixture velocity is negative relative to the interface velocity while $(u_\infty - u_i)$ is negative and therefore, there is no reverse flow and the liquid is only dragging the mixture. Because of that, conditions at the location x_1 were not classified as separation. Based on

this discussion, the separation conditions are defined as: $u_i < u_\infty$ and $\left(\frac{\partial u}{\partial y}\right)_{y=\delta} = 0$, and the distance along the plate where separation occurs is defined as x_{sep}. The velocity profile for the case of separation is shown in Figure 3.3.

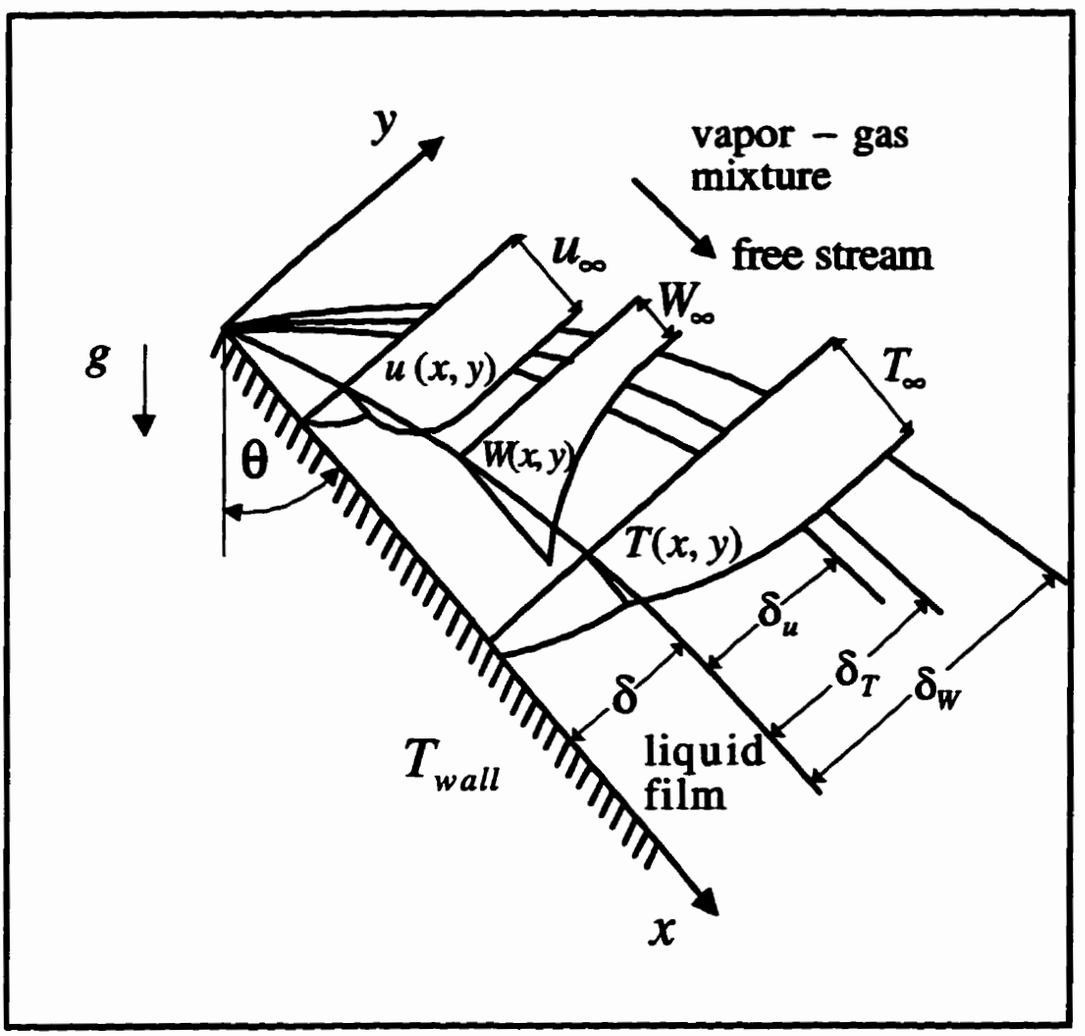

Figure 3.1: Physical model

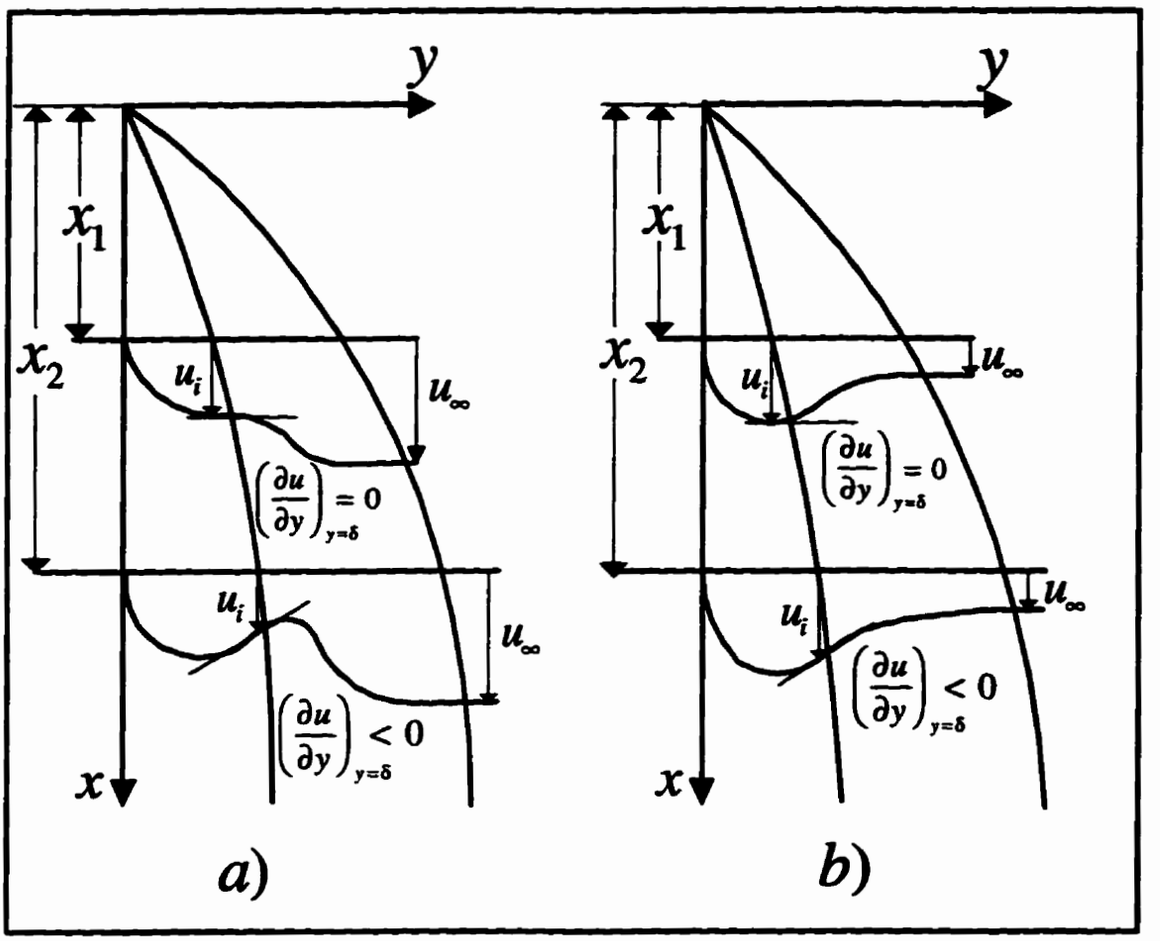

Figure 3.2: Schematic representation of u-velocity profiles for a) $u_i < u_\infty$ *and* $\left(\frac{\partial u}{\partial y}\right)_{y=\delta} \leq 0$ and b) $u_i > u_\infty$ *and* $\left(\frac{\partial u}{\partial y}\right)_{y=\delta} \leq 0$

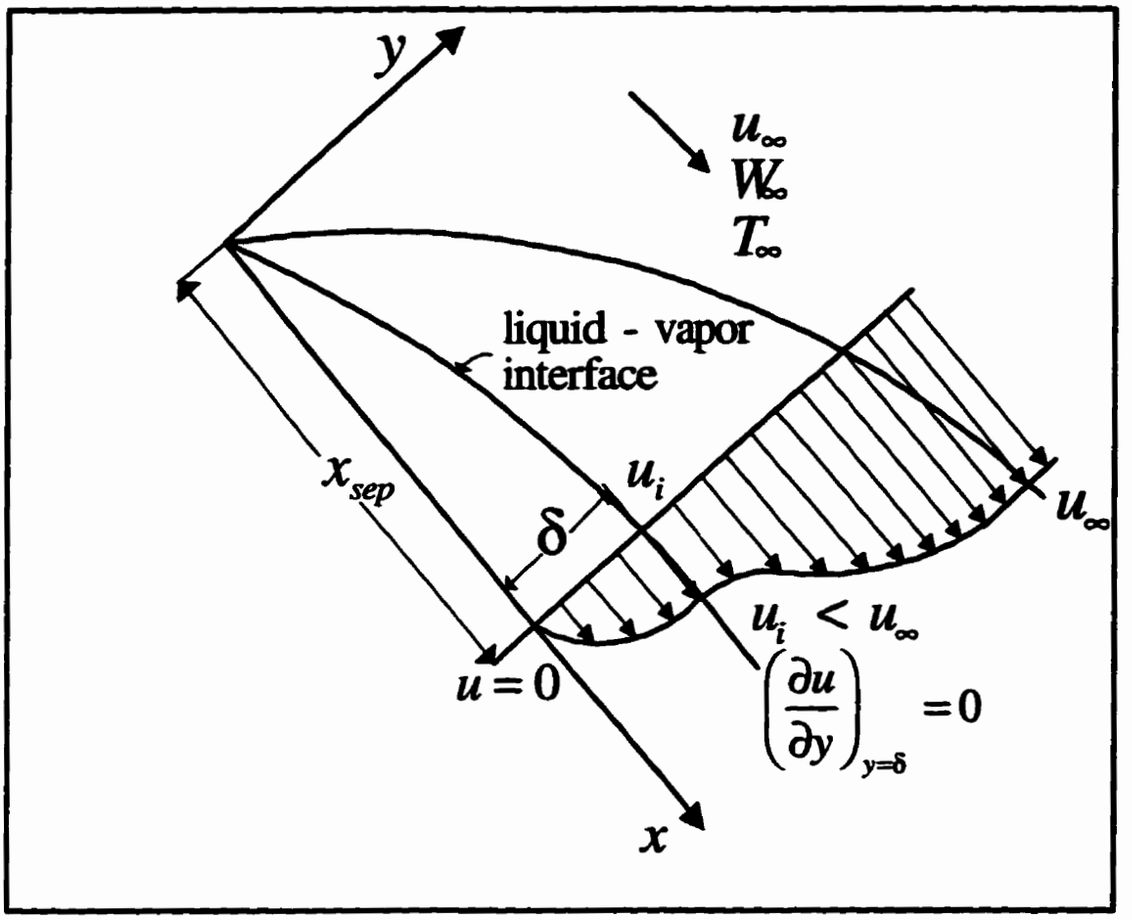

Figure 3.3: Schematic representation of u-velocity profile at the separation point

Chapter 4

SOLUTION PROCEDURE

4.1 Coordinate Transformation

The set of governing differential equations given by Equations (3.1) to (3.7) was written in the x-y coordinate system, and non-orthogonal (quadrilateral) control volumes were used to match the liquid and mixture flow regions. Using the coordinate transformation:

$$x = \chi \tag{4.1}$$

and

$$y = \delta\,\eta, \tag{4.2}$$

the set of the governing equations was written in $\chi - \eta$ coordinate system, in which the control volumes were orthogonal. Also, using the same coordinate transformations the set of boundary conditions [Equations (3.8)-(3.20)] was transformed into the $\chi - \eta$ coordinate system. The solution domain and the grid in the two different coordinate systems are shown in Figures 4.1 and 4.2. The number of control volumes across the liquid film, across the mixture boundary layer and along the plate were defined as input parameters. The liquid film surface was used as a boundary between the grid in the liquid (uniformly-spaced in the η direction within the liquid film) and the expanding grid in the η direction within the mixture layer. The spacing in the χ direction was either uniform or expanding for both the liquid film and the mixture layers.

4.2 Discretization

The governing system of equations in the $\chi - \eta$ coordinate system was discretized using a finite volume method (Patankar, 1980). Each equation in the system was integrated over a rectangular control volume, and the appropriate boundary conditions were applied. In the discretization procedure, full upwind differencing was used in the χ direction, while the exponential differencing scheme (Patankar, 1980) was used in the η direction. Since the shear stress at the interface and the interface velocity must be the same for the liquid film and the mixture layer, the discretized u-momentum equations were solved simultaneously for both regions. The velocity components in the transverse direction, v_L and v, were replaced by the mass flows $\dot{m}_L$ and $\dot{m}$, which were calculated from the discretized continuity equations. The procedure was to first calculate the mass flow rates using an initial guess for u_L and u, and then to solve the discretized momentum equations using the guessed mass flow rates. The mass flow rates were then updated using the velocities obtained from the solution of the momentum equations. The gas conservation equation and energy equations were solved separately using the mass flow rates calculated from the momentum equations. The energy equations were solved separately because the temperature at the interface was calculated using the boundary conditions equations. A control volume with zero thickness was used at the wall, at the outer edge of the mixture boundary layer and at the liquid-mixture interface in order to apply the boundary conditions. After applying the boundary conditions in discretized form, a system of algebraic equations was solved for each of the following variables: u and u_L, T_L, T and

W. Because the equation set is parabolic, the solution was carried out at each station (constant χ location) and the solution was marched down the plate using the solution from the previous station as the upstream condition. The solution procedure was repeated at each station until convergence of all variables was obtained. This iteration accounts for non-linearity and inter-equation couplings. The convergence criteria are based on a relative error, which was defined as follows:

$$error_1 = \left| \frac{\phi_{iter} - \phi_{iter-1}}{\phi_{iter}} \right| \tag{4.3a}$$

$$error_2 = \left| \frac{\phi_{iter} - \phi_{iter-1}}{\phi_{max} - \phi_{min}} \right| \tag{4.3b}$$

After each iteration, both errors were calculated in the η direction for: δ, u_L, u, w, T_L, and T at all mesh points. The lower error between $error_1$ and $error_2$ must be lower than a specified error criterion for all solution fields. In the case of a very small value of the denominator in Equations (4.3a) and (4.3b), the errors become large. Since both equations are equally acceptable as the convergence criterion, the lower error was chosen in order to reduce the number of iterations necessary to obtain converged solution fields. Thus, the convergence criterion was expressed as:

$$\min(error_1, error_2) < \text{concri}, \tag{4.4}$$

where concri stands for convergence criterion, which was specified as an input parameter. More details about coordinate transformation and discretization can be found in Chin (1995). Only the final form of the discretized equations is presented here.

4.2.1 Discretized Equations

- **Liquid Continuity**

For $j_L = 1$:

$$\dot{m}_{L,n}(i,1) = 0.0 \tag{4.5}$$

For $2 \le j_L \le n-1$:

$$\dot{m}_{L,n}(i, j_L) = \dot{m}_{L,w}(i, j_L) - \dot{m}_{L,e}(i, j_L) + \dot{m}_{L,s}(i, j_L) \tag{4.6}$$

- **Mixture Continuity**

At $j = 1$:

$$\dot{m}_n(i, j=1) = \dot{m}_{L,n}(i, j_L = n-1) \tag{4.7}$$

For $2 \le j \le nv - 1$:

$$\dot{m}_n(i, j) = \dot{m}_w(i, j) - \dot{m}_e(i, j) + \dot{m}_s(i, j) \tag{4.8}$$

$$\dot{m}_{L,s}(i, j_L) = \dot{m}_{L,n}(i, j_L - 1) \tag{4.9}$$

The general form of the momentum, energy and diffusion equations can be written in the form:

$$a_P(i, j)\phi(i, j) = a_N(i, j)\phi(i, j+1) + a_S(i, j)\phi(i, j-1) + b_P(i, j) \tag{4.10}$$

with ϕ as a general variable that represents u_L, T_L, u, T, or W. Coefficients $a_P, a_N, a_S, and\ b_P$ are given below.

- **Liquid and Mixture Momentum Equations**

At $j_L = 1$:

$$\left.\begin{aligned} a_P(i, j_L = 1) &= 1.0 \\ a_N(i, j_L = 1) &= 0.0 \\ a_S(i, j_L = 1) &= 0.0 \\ b_P(i, j_L = 1) &= 0.0 \end{aligned}\right\} \tag{4.11}$$

At $j_L = 2$:

$$a_N(i, j_L) = \dot{m}_{L,n}(i, j_L)\left[\frac{1}{\exp(Pe_{L,n}) - 1}\right] \tag{4.12}$$

$$Pe_{L,n} = \frac{\dot{m}_{L,n}(i, j_L)\delta_m(i)\Delta\eta_{L,+}(j_L)}{\mu_{L,n}(i, j_L)\Delta\chi(i)} \tag{4.13}$$

$$a_S(i, j_L) = \frac{\mu_{L,n}(i, j_L{-}1)\Delta\chi(i)}{\delta_m(i)\Delta\eta_{L,+}(j_L{-}1)} + \dot{m}_{L,s}(i, j_L) \tag{4.14}$$

$$a_P(i, j_L) = \dot{m}_{L,w}(i, j_L) + a_N(i, j_L) + a_S(i, j_L) \tag{4.15}$$

$$\begin{aligned} b_P(i, j_L) = {} & \dot{m}_{L,w}(i, j_L)u_L(i{-}1, j_L) + \\ & g[\rho_L(i, j_L) - \rho(i, nv)]\cos\theta\delta_m(i)\Delta\chi(i)\Delta\eta_L(j_L) \end{aligned} \tag{4.16}$$

For $3 \le j_L \le n - 2$:

$$a_N(i, j_L) = \dot{m}_{L,n}(i, j_L)\left[\frac{1}{\exp(Pe_{L,n}) - 1}\right] \tag{4.17}$$

$$Pe_{L,n} = \frac{\dot{m}_{L,n}(i, j_L)\delta_m(i)\Delta\eta_{L,+}(j_L)}{\mu_{L,n}(i, j_L)\Delta\chi(i)} \tag{4.18}$$

$$a_S(i, j_L) = \dot{m}_{L,n}(i, j_L{-}1)\left[\frac{\exp(Pe_{L,s})}{\exp(Pe_{L,s}) - 1}\right] \tag{4.19}$$

$$Pe_{L,s} = \frac{\dot{m}_{L,n}(i, j_L-1)\delta_m(i)\Delta\eta_{L,+}(j_L-1)}{\mu_{L,n}(i, j_L-1)\Delta\chi(i)} \tag{4.20}$$

$$a_P(i, j_L) = \dot{m}_{L,w}(i, j_L) + a_N(i, j_L) + a_S(i, j_L) \tag{4.21}$$

$$b_P(i, j_L) = \dot{m}_{L,w}(i, j_L)u_L(i-1, j_L) + g[\rho_L(i, j_L) - \rho(i, nv)]\cos\theta\delta_m(i)\Delta\chi(i)\Delta\eta_L(j_L) \tag{4.22}$$

At $j_L = n - 1$:

$$a_N(i, j_L) = \frac{\mu_{L,n}(i, j_L)\Delta\chi(i)}{\delta_m(i)\Delta\eta_{L,+}(j_L)} - \dot{m}_{L,n}(i, j_L) \tag{4.23}$$

$$a_S(i, j_L) = \dot{m}_{L,n}(i, j_L-1)\left[\frac{\exp(Pe_{L,s})}{\exp(Pe_{L,s}) - 1}\right] \tag{4.24}$$

$$Pe_{L,s} = \frac{\dot{m}_{L,n}(i, j_L-1)\delta_m(i)\Delta\eta_{L,+}(j_L-1)}{\mu_{L,n}(i, j_L-1)\Delta\chi(i)} \tag{4.25}$$

$$a_P(i, j_L) = \dot{m}_{L,w}(i, j_L) + a_N(i, j_L) + a_S(i, j_L) \tag{4.26}$$

$$b_P(i, j_L) = \dot{m}_{L,w}(i, j_L)u_L(i-1, j_L) + g[\rho_L(i, j_L) - \rho(i, nv)]\cos\theta\delta_m(i)\Delta\chi(i)\Delta\eta_L(j_L) \tag{4.27}$$

At $j_L = n$ and $j = 1$:

$$a_N(i, n) = \frac{\mu_n(i,1)\Delta\chi(i)}{\delta_m(i)\Delta\eta_+(1)} \tag{4.28}$$

$$a_S(i, n) = \frac{\mu_{L,n}(i, n-1)\Delta\chi(i)}{\delta_m(i)\Delta\eta_{L,+}(n-1)} \tag{4.29}$$

$$a_P(i, n) = a_N(i, n) + a_S(i, n) \tag{4.30}$$

$$b_P(i, n) = 0 \tag{4.31}$$

At $j = 2$:

$$a_N(i, j) = \dot{m}_n(i, j)\left[\frac{1}{\exp(Pe_n) - 1}\right] \tag{4.32}$$

$$Pe_n = \frac{\dot{m}_n(i, j)\delta_m(i)\Delta\eta_+(j)}{\mu_n(i, j)\Delta\chi(i)} \tag{4.33}$$

$$a_S(i, j) = \frac{\mu_n(i, j-1)\Delta\chi(i)}{\delta_m(i)\Delta\eta_+(j-1)} + \dot{m}_s(i, j) \tag{4.34}$$

$$a_P(i, j) = \dot{m}_w(i, j) + a_N(i, j) + a_S(i, j) \tag{4.35}$$

$$b_P(i, j) = \dot{m}_w(i, j)u(i-1, j) + g[\rho(i, j) - \rho(i, nv)]\cos\theta\delta_m(i)\Delta\chi(i)\Delta\eta(j) \tag{4.36}$$

For $3 \le j \le nv - 2$:

$$a_N(i, j) = \dot{m}_n(i, j)\left[\frac{1}{\exp(Pe_n) - 1}\right] \tag{4.37}$$

$$Pe_n = \frac{\dot{m}_n(i, j)\delta_m(i)\Delta\eta_+(j)}{\mu_n(i, j)\Delta\chi(i)} \tag{4.38}$$

$$a_S(i, j) = \dot{m}_n(i, j-1)\left[\frac{\exp(Pe_s)}{\exp(Pe_s) - 1}\right] \tag{4.39}$$

$$Pe_s = \frac{\dot{m}_n(i, j-1)\delta_m(i)\Delta\eta_+(j-1)}{\mu_n(i, j-1)\Delta\chi(i)} \tag{4.40}$$

$$a_P(i, j) = \dot{m}_w(i, j) + a_N(i, j) + a_S(i, j) \tag{4.41}$$

$$b_P(i, j) = \dot{m}_w(i, j)u(i-1, j) + g[\rho(i, j) - \rho(i, nv)]\cos\theta\delta_m(i)\Delta\chi(i)\Delta\eta(j) \tag{4.42}$$

At $j = nv - 1$:

$$a_N(i, j) = \frac{\mu_n(i, j)\Delta\chi(i)}{\delta_m(i)\Delta\eta_+(j_L)} - \dot{m}_n(i, j) \tag{4.43}$$

$$a_S(i, j) = \dot{m}_n(i, j\text{–}1)\left[\frac{\exp(Pe_s)}{\exp(Pe_s) - 1}\right] \tag{4.44}$$

$$Pe_s = \frac{\dot{m}_n(i, j\text{–}1)\delta_m(i)\Delta\eta_+(j\text{–}1)}{\mu_n(i, j\text{–}1)\Delta\chi(i)} \tag{4.45}$$

$$a_P(i, j) = \dot{m}_w(i, j) + a_N(i, j) + a_S(i, j) \tag{4.46}$$

$$b_P(i, j) = \dot{m}_w(i, j)u(i\text{–}1, j) + g[\rho(i, j) - \rho(i, nv)]\cos\theta\delta_m(i)\Delta\chi(i)\Delta\eta(j) \tag{4.47}$$

At $j = nv$:

$$\left.\begin{aligned} a_P(i, nv) &= 1.0 \\ a_N(i, nv) &= 0.0 \\ a_S(i, nv) &= 0.0 \\ b_P(i, nv) &= u_\infty \end{aligned}\right\} \tag{4.48}$$

- **Liquid Energy Equations**

At $j_L = 1$:

$$\left.\begin{aligned} a_P(i,1) &= 1.0 \\ a_N(i,1) &= 0.0 \\ a_S(i,1) &= 0.0 \\ b_P(i,1) &= T_{wall} \end{aligned}\right\} \tag{4.49}$$

At $j_L = 2$:

$$a_N(i, j_L) = \dot{m}_{L,n}(i, j_L)c_{P_{L,n}}(i, j_L)\left[\frac{1}{\exp(Pe_{L,n}) - 1}\right] \tag{4.50}$$

$$Pe_{L,n} = \frac{\dot{m}_{L,n}(i, j_L)\delta_m(i)\Delta\eta_{L,+}(j_L)c_{P_{L,n}}(i, j_L)}{k_{L,n}(i, j_L)\Delta\chi(i)} \tag{4.51}$$

$$a_S(i, j_L) = \left[\frac{k_{L,n}(i, j_L-1)\Delta\chi(i)}{c_{P_{L,n}}(i, j_L-1)\delta_m(i)\Delta\eta_{L,+}(j_L-1)} + \dot{m}_{L,s}(i, j_L) \right] c_{P_{L,n}}(i, j_L-1) \tag{4.52}$$

$$a_P(i, j_L) = \dot{m}_{L,e}(i, j_L)c_{P_{L,e}}(i, j_L) + \dot{m}_{L,n}(i, j_L)c_{P_{L,n}}(i, j_L) - \dot{m}_{L,n}(i, j_L-1)c_{P_{L,n}}(i, j_L-1) + a_N(i, j_L) + a_S(i, j_L) \tag{4.53}$$

$$b_P(i, j_L) = \dot{m}_{L,w}(i, j_L)c_{P_{L,w}}(i, j_L)T_L(i-1, j_L) \tag{4.54}$$

For $3 \le j_L \le n-2$:

$$a_N(i, j_L) = \dot{m}_{L,n}(i, j_L)c_{P_{L,n}}(i, j_L)\left[\frac{1}{\exp(Pe_{L,n}) - 1} \right] \tag{4.55}$$

$$Pe_{L,n} = \frac{\dot{m}_{L,n}(i, j_L)\delta_m(i)\Delta\eta_{L,+}(j_L)c_{P_{L,n}}(i, j_L)}{k_{L,n}(i, j_L)\Delta\chi(i)} \tag{4.56}$$

$$a_S(i, j_L) = \dot{m}_{L,n}(i, j_L-1)c_{P_{L,n}}(i, j_L-1)\left[\frac{\exp(Pe_{L,s})}{\exp(Pe_{L,s}) - 1} \right] \tag{4.57}$$

$$Pe_{L,s} = \frac{\dot{m}_{L,n}(i, j_L-1)\delta_m(i)\Delta\eta_{L,+}(j_L-1)c_{P_{L,n}}(i, j_L-1)}{k_{L,n}(i, j_L-1)\Delta\chi(i)} \tag{4.58}$$

$$a_P(i, j_L) = \dot{m}_{L,e}(i, j_L)c_{P_{L,e}}(i, j_L) + \dot{m}_{L,n}(i, j_L)c_{P_{L,n}}(i, j_L) - \dot{m}_{L,n}(i, j_L-1)c_{P_{L,n}}(i, j_L-1) + a_N(i, j_L) + a_S(i, j_L) \tag{4.59}$$

$$b_P(i, j_L) = \dot{m}_{L,w}(i, j_L)c_{P_{L,w}}(i, j_L)T_L(i-1, j_L) \tag{4.60}$$

At $j_L = n-1$:

$$a_N(i, j_L) = c_{P_{L,n}}(i, j_L)\left[\frac{k_{L,n}(i, j_L)\Delta\chi(i)}{c_{P_{L,n}}(i, j_L)\delta_m(i)\Delta\eta_{L,+}(j_L)} - \dot{m}_{L,s}(i, j_L) \right] \tag{4.61}$$

$$a_S(i, j_L) = \dot{m}_{L,n}(i, j_L-1)c_{P_{L,s}}(i, j_L-1)\left[\frac{\exp(Pe_{L,s})}{\exp(Pe_{L,s}) - 1}\right] \tag{4.62}$$

$$Pe_{L,s} = \frac{\dot{m}_{L,n}(i, j_L-1)\delta_m(i)\Delta\eta_{L,+}(j_L-1)c_{P_{L,s}}(i, j_L-1)}{k_{L,n}(i, j_L-1)\Delta\chi(i)} \tag{4.63}$$

$$\begin{aligned} a_P(i, j_L) = {} & \dot{m}_{L,e}(i, j_L)c_{P_{L,e}}(i, j_L) + \dot{m}_{L,n}(i, j_L)c_{P_{L,n}}(i, j_L) - \\ & \dot{m}_{L,n}(i, j_L-1)c_{P_{L,s}}(i, j_L-1) + a_N(i, j_L) + a_S(i, j_L) \end{aligned} \tag{4.64}$$

$$b_P(i, j_L) = \dot{m}_{L,w}(i, j_L)c_{P_{L,w}}(i, j_L)T_L(i-1, j_L) \tag{4.65}$$

At $j_L = n - 1$:

$$\left.\begin{aligned} a_P(i, n) &= 1.0 \\ a_N(i, n) &= 0.0 \\ a_S(i, n) &= 0.0 \\ b_P(i, n) &= T_i \end{aligned}\right\} \tag{4.66}$$

- **Mixture Energy Equations**

At $j = 1$:

$$\left.\begin{aligned} a_P(i,1) &= 1.0 \\ a_N(i,1) &= 0.0 \\ a_S(i,1) &= 0.0 \\ b_P(i,1) &= T_i \end{aligned}\right\} \tag{4.67}$$

At $j = 2$:

$$a_N(i, j) = \dot{m}_n(i, j)c_{P_n}(i, j)\left[\frac{1}{\exp(Pe_n) - 1}\right] \tag{4.68}$$

$$Pe_n = \frac{\dot{m}_n(i, j)\delta_m(i)\Delta\eta_+(j)c_{P_n}(i, j)}{k_n(i, j)\Delta\chi(i)} \tag{4.69}$$

$$a_S(i,j) = c_{P_a}(i,j-1)\left[\frac{k_n(i,j-1)\Delta\chi(i)}{c_{P_a}(i,j-1)\delta_m(i)\Delta\eta_+(j-1)} + \dot{m}_s(i,j)\right] \tag{4.70}$$

$$a_P(i,j) = \dot{m}_e(i,j)c_{P_e}(i,j) + \dot{m}_n(i,j)c_{P_a}(i,j) - \dot{m}_n(i,j-1)c_{P_a}(i,j-1) + a_N(i,j) + a_S(i,j) \tag{4.71}$$

$$b_P(i,j) = \dot{m}_w(i,j)c_{P_w}(i,j)T(i-1,j) + \frac{1}{\delta_m}\Delta\chi(i)\left\{\rho_n(i,j)D_n(i,j)\left[c_{P_{s,a}}(i,j)-c_{P_{v,a}}(i,j)\right]T_n\left(\frac{\partial W}{\partial\eta}\right)_n - \rho_n(i,j-1)D_n(i,j-1)\left[c_{P_{s,a}}(i,j-1)-c_{P_{v,a}}(i,j-1)\right]T_s\left(\frac{\partial W}{\partial\eta}\right)_s\right\} \tag{4.72}$$

$$T_n = T(i,j) + \alpha_n\left[T(i,j+1) - T(i,j)\right] \tag{4.73}$$

$$T_s = T(i,j-1) + \alpha_s\left[T(i,j) - T(i,j-1)\right] \tag{4.74}$$

$$\left(\frac{\partial W}{\partial\eta}\right)_n = \frac{W(i,j+1) - W(i,j)}{\Delta\eta_+(j)} \tag{4.75}$$

$$\left(\frac{\partial W}{\partial\eta}\right)_s = \frac{W(i,j) - W(i,j-1)}{\Delta\eta_+(j-1)} \tag{4.76}$$

For $3 \le j \le nv - 2$:

$$a_N(i,j) = \dot{m}_n(i,j)c_{P_a}(i,j)\left[\frac{1}{\exp(Pe_n) - 1}\right] \tag{4.77}$$

$$Pe_n = \frac{\dot{m}_n(i,j)\delta_m(i)\Delta\eta_+(j)c_{P_a}(i,j)}{k_n(i,j)\Delta\chi(i)} \tag{4.78}$$

$$a_S(i,j) = \dot{m}_n(i,j-1)c_{P_a}(i,j-1)\left[\frac{\exp(Pe_s)}{\exp(Pe_s) - 1}\right] \tag{4.79}$$

$$Pe_s = \frac{\dot{m}_n(i, j-1)\delta_m(i)\Delta\eta_+(j-1)c_{P_s}(i, j-1)}{k_n(i, j-1)\Delta\chi(i)} \tag{4.80}$$

$$a_P(i, j) = \dot{m}_e(i, j)c_{P_e}(i, j) + \dot{m}_n(i, j)c_{P_n}(i, j) - \dot{m}_n(i, j-1)c_{P_s}(i, j-1) + a_N(i, j) + a_S(i, j) \tag{4.81}$$

$$b_P(i, j) = \dot{m}_w(i, j)c_{P_w}(i, j)T(i-1, j) + \frac{1}{\delta_m}\Delta\chi(i)\left\{\rho_n(i, j)D_n(i, j)\left[c_{P_{g,n}}(i, j) - c_{P_{v,n}}(i, j)\right]T_n\left(\frac{\partial W}{\partial \eta}\right)_n - \rho_n(i, j-1)D_n(i, j-1)\left[c_{P_{g,n}}(i, j-1) - c_{P_{v,n}}(i, j-1)\right]T_s\left(\frac{\partial W}{\partial \eta}\right)_s\right\} \tag{4.82}$$

$$T_n = T(i, j) + \alpha_n\left[T(i, j+1) - T(i, j)\right] \tag{4.83}$$

$$T_s = T(i, j-1) + \alpha_s\left[T(i, j) - T(i, j-1)\right] \tag{4.84}$$

$$\left(\frac{\partial W}{\partial \eta}\right)_n = \frac{W(i, j+1) - W(i, j)}{\Delta\eta_+(j)} \tag{4.85}$$

$$\left(\frac{\partial W}{\partial \eta}\right)_s = \frac{W(i, j) - W(i, j-1)}{\Delta\eta_+(j-1)} \tag{4.86}$$

At $j = nv - 1$:

$$a_N(i, j) = c_{P_n}(i, j)\left[\frac{k_n(i, j_L)\Delta\chi(i)}{c_{P_n}(i, j)\delta_m(i)\Delta\eta_+(j)} - \dot{m}_n(i, j)\right] \tag{4.87}$$

$$a_S(i, j) = \dot{m}_n(i, j-1)c_{P_n}(i, j-1)\left[\frac{\exp(Pe_s)}{\exp(Pe_s) - 1}\right] \tag{4.88}$$

$$Pe_s = \frac{\dot{m}_n(i, j-1)\delta_m(i)\Delta\eta_+(j-1)c_{P_n}(i, j-1)}{k_n(i, j-1)\Delta\chi(i)} \tag{4.89}$$

$$a_P(i,j) = \dot{m}_e(i,j)c_{P_e}(i,j) + \dot{m}_n(i,j)c_{P_n}(i,j) - \dot{m}_n(i,j-1)c_{P_n}(i,j-1) + a_N(i,j) + a_S(i,j) \tag{4.90}$$

$$b_P(i,j) = \dot{m}_w(i,j)c_{P_w}(i,j)T(i-1,j) + \frac{1}{\delta_m}\Delta\chi(i)\left\{\rho_n(i,j)D_n(i,j)\left[c_{P_{g,n}}(i,j) - c_{P_{v,n}}(i,j)\right]T_n\left(\frac{\partial W}{\partial \eta}\right)_n - \rho_n(i,j-1)D_n(i,j-1)\left[c_{P_{g,n}}(i,j-1) - c_{P_{v,n}}(i,j-1)\right]T_s\left(\frac{\partial W}{\partial \eta}\right)_s\right\} \tag{4.91}$$

$$T_n = T(i,j) + \alpha_n\left[T(i,j+1) - T(i,j)\right] \tag{4.92}$$

$$T_s = T(i,j-1) + \alpha_s\left[T(i,j) - T(i,j-1)\right] \tag{4.93}$$

$$\left(\frac{\partial W}{\partial \eta}\right)_n = \frac{W(i,j+1) - W(i,j)}{\Delta\eta_+(j)} \tag{4.94}$$

$$\left(\frac{\partial W}{\partial \eta}\right)_s = \frac{W(i,j) - W(i,j-1)}{\Delta\eta_+(j-1)} \tag{4.95}$$

At $j = nv$:

$$\left.\begin{aligned} a_P(i,nv) &= 1.0 \\ a_N(i,nv) &= 0.0 \\ a_S(i,nv) &= 0.0 \\ b_P(i,nv) &= T_\infty \end{aligned}\right\} \tag{4.96}$$

Mixture Diffusion Equations

At $j = 1$:

$$a_N(i,1) = \frac{\rho_n(i,1)D_n(i,1)\Delta\chi(i)}{\delta_m(i)\Delta\eta_+(1)} \tag{4.97}$$

$$a_S(i,1) = 0.0 \tag{4.98}$$

$$a_P(i,1) = \dot{m}_n(i,1) + a_N(i,1) \tag{4.99}$$

$$b_P(i,n) = 0 \tag{4.100}$$

At $j = 2$:

$$a_N(i,2) = \dot{m}_n(i,2)\left[\frac{1}{\exp[Pe_n(i,2)] - 1}\right] \tag{4.101}$$

$$Pe_n = \frac{\dot{m}_n(i,2)\delta_m(i)\Delta\eta_+(2)}{\rho_n(i,2)D_n(i,2)\Delta\chi(i)} \tag{4.102}$$

$$a_S(i,2) = 0.0 \tag{4.103}$$

$$a_P(i,2) = \dot{m}_e(i,2) + \dot{m}_n(i,2) + a_N(i,2) \tag{4.104}$$

$$b_P(i,2) = \dot{m}_w(i,2)W(i-1,2) \tag{4.105}$$

For $3 \le j \le nv - 2$:

$$a_N(i,j) = \dot{m}_n(i,j)\left[\frac{1}{\exp(Pe_n) - 1}\right] \tag{4.106}$$

$$Pe_n = \frac{\dot{m}_n(i,j)\delta_m(i)\Delta\eta_+(j)}{\rho_n(i,j)D_n(i,j)\Delta\chi(i)} \tag{4.107}$$

$$a_S(i,j) = \dot{m}_n(i,j-1)\left[\frac{\exp(Pe_s)}{\exp(Pe_s) - 1}\right] \tag{4.108}$$

$$Pe_s = \frac{\dot{m}_n(i,j-1)\delta_m(i)\Delta\eta_+(j-1)}{\rho_n(i,j-1)D_n(i,j-1)\Delta\chi(i)} \tag{4.109}$$

$$a_P(i,j) = \dot{m}_w(i,j) + a_N(i,j) + a_S(i,j) \tag{4.110}$$

$$b_P(i,j) = \dot{m}_w(i,j)W(i-1,j) \tag{4.111}$$

At $j = nv - 1$:

$$a_N(i, j) = \frac{\rho_n(i, j)D_n(i, j)\Delta\chi(i)}{\delta_m(i)\Delta\eta_+(j_L)} - \dot{m}_n(i, j) \tag{4.112}$$

$$a_S(i, j) = \dot{m}_n(i, j-1)\left[\frac{\exp(Pe_s)}{\exp(Pe_s) - 1}\right] \tag{4.113}$$

$$Pe_s = \frac{\dot{m}_n(i, j-1)\delta_m(i)\Delta\eta_+(j-1)}{\rho_n(i, j-1)D_n(i, j-1)\Delta\chi(i)} \tag{4.114}$$

$$a_P(i, j) = \dot{m}_w(i, j) + a_N(i, j) + a_S(i, j) \tag{4.115}$$

$$b_P(i, j) = \dot{m}_w(i, j)W(i-1, j) \tag{4.116}$$

At $j = nv$:

$$\left.\begin{aligned} a_P(i, nv) &= 1.0 \\ a_N(i, nv) &= 0.0 \\ a_S(i, nv) &= 0.0 \\ b_P(i, nv) &= W_\infty \end{aligned}\right\} \tag{4.117}$$

4.2.2 Calculation of the Interface Parameters

The values of $\delta, T_i,$ *and* $\dot{m}_i^{"}$ were calculated from Equations (3.18) to (3.20). To solve this set of equations the system was reduced to one implicit equation with T_i as the unknown and a Newton-Raphson root search method was used. Details of the solution procedure can be found in Appendix B. If the assumption about negligible interfacial resistance is justified, the film layer thickness can be calculated from Equation (3.19), and the interface temperature can be taken as:

$$T_i = T_{sat}(W_i, W_\infty, T_\infty, M_v, M_g) \tag{4.118}$$

In this case, the liquid film thickness can be calculated from:

$$\delta(i) = \frac{-b + \sqrt{b^2 - 4ac}}{2a}, \tag{4.119}$$

where

$$a = h_{fg}(i)\sum_{j_L=1}^{n} \rho_L(i, j_L)u_L(i, j_L)\Delta\eta(j_L) \tag{4.120}$$

$$b = \delta(i-1)h_{fg}(i)\left\{\sum_{j_L=1}^{n} \rho_L(i, j_L)u_L(i, j_L)\Delta\eta(j_L) - \sum_{j_L=1}^{n} \frac{\dot{m}_{L,w}(i, j_L)}{\delta(i-1)}\right\} \tag{4.121}$$

$$c = -\delta^2(i-1)h_{fg}(i)\sum_{j_L=1}^{n} \frac{\dot{m}_{L,w}(i, j_L)}{\delta(i-1)} - 2\Delta\chi(i)k_L(i, n-1)\left\{\frac{T_L(i, n) - T_L(i, n-1)}{\Delta\eta_+(n-1)}\right\} + 2\Delta\chi(i)k(i,1)\left\{\frac{T(i,2) - T(i,1)}{\Delta\eta_+(1)}\right\} \tag{4.122}$$

More details about derivation of Equations (4.119)-(4.122) can be found in Chin (1995).

4.3 Program Description and Solution Procedure

As previously mentioned, the set of discretized equations was solved at each χ station (i = constant) using data obtained from the previous station or data defined as initial conditions. At the beginning of the plate, or at the first station, the velocity and

concentration profiles were taken to be zero. Across the liquid layer, temperature was assumed to be uniform and equal to T_{wall}, and across the mixture layer temperature was equal to T_{∞}.

For the second station, a guess for the initial solution fields was obtained from the classical Nusselt theory with interfacial resistance (Mills, 1992), as described in Appendix C. At the subsequent stations, the initial guesses for the solution fields were taken as the converged field values at the previous station.

The program structure is shown in Figure 4.3. The main part of the program consists of one subroutine which calls three other subroutines. The first subroutine performs pre-processing, the second one performs all the flow and heat transfer computations, and the third one does post-processing. In the subroutine PROCESS all necessary calculations were performed. All discretized equations, except the u-momentum equations, were solved separately, and a separate subroutine to solve each discretization equation was called from PROCESS. Figure 4.4 shows a flow chart for the subroutine PROCESS, emphasizing only the most important steps.

The flow chart in Figure 4.4 shows three major loops. The first loop checks overall convergence, the second checks the separation conditions, and the third is used to refine the step after separation occurred. The refinement of the step is used to improve accuracy in calculation of x_{sep}, and it is applied on the station that precedes separation. Once the

separation location is reached during calculation, the step was refined dividing by a factor ten or twenty, all profiles were taken to be as they were at the previous station, and calculation continued until the separation was reached again. After separation is reached for the second time, the calculation stopped.

The structure of the program is the same for all three vapor-gas combinations. The sets of subroutines that are used to calculate properties for different gases and vapors have the same names and lists of variables in order to provide compatibility with the main part of the program. This organization of the program facilitates modifications for other vapor-gas combinations.

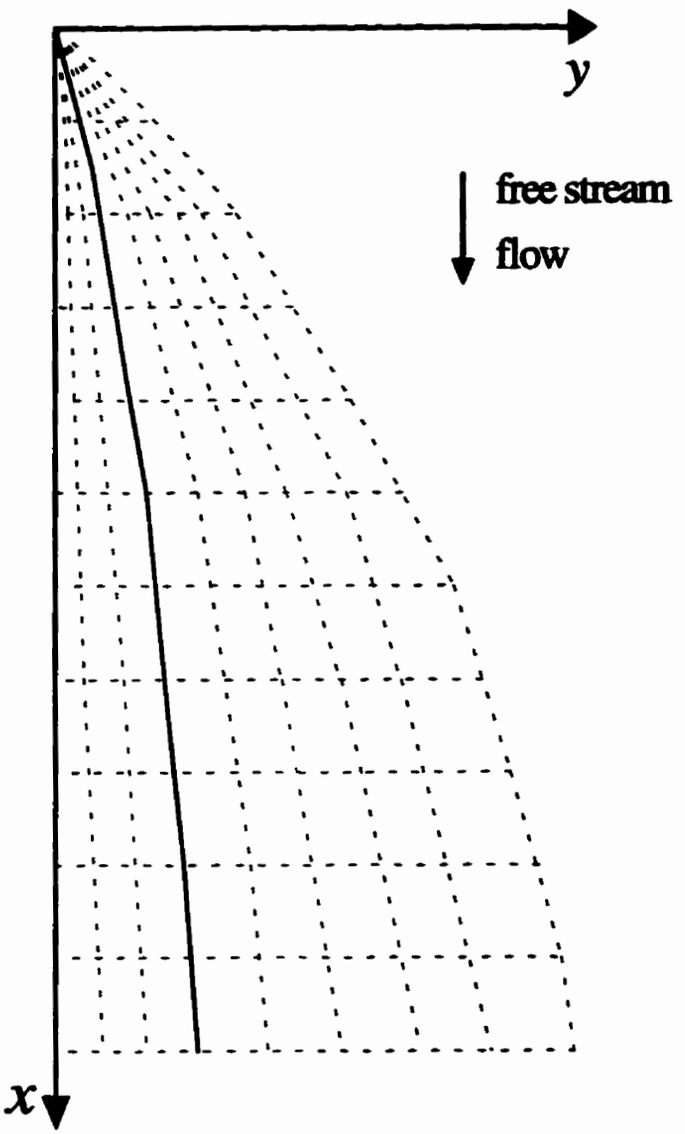

Figure 4.1: Computational grid in (x, y) coordinate system

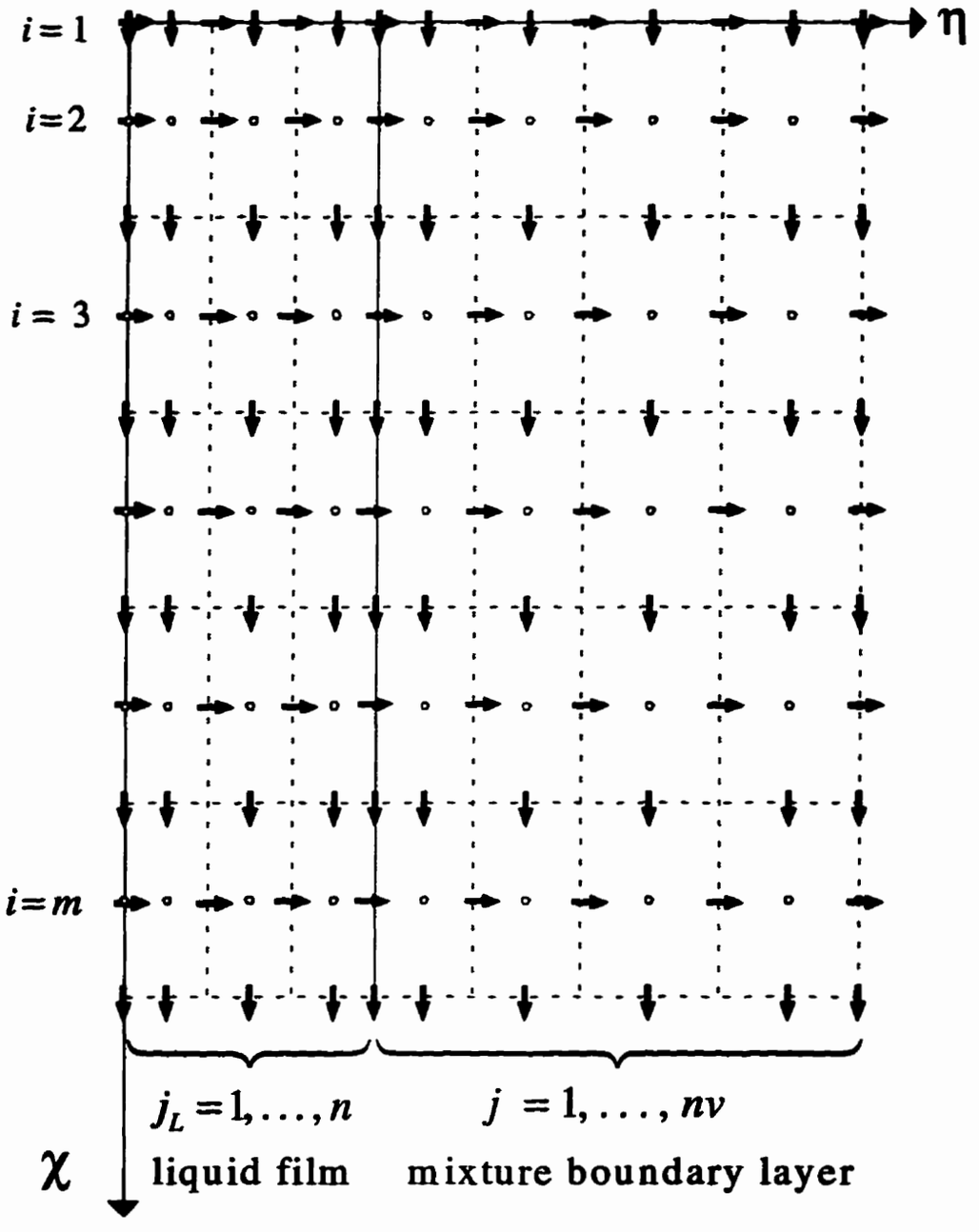

Figure 4.2: Computational grid in transformed coordinate system (χ, η) with locations for u,T,W = ○ ; $\dot{m}_n$ = → and $\dot{m}_e$ = ↓

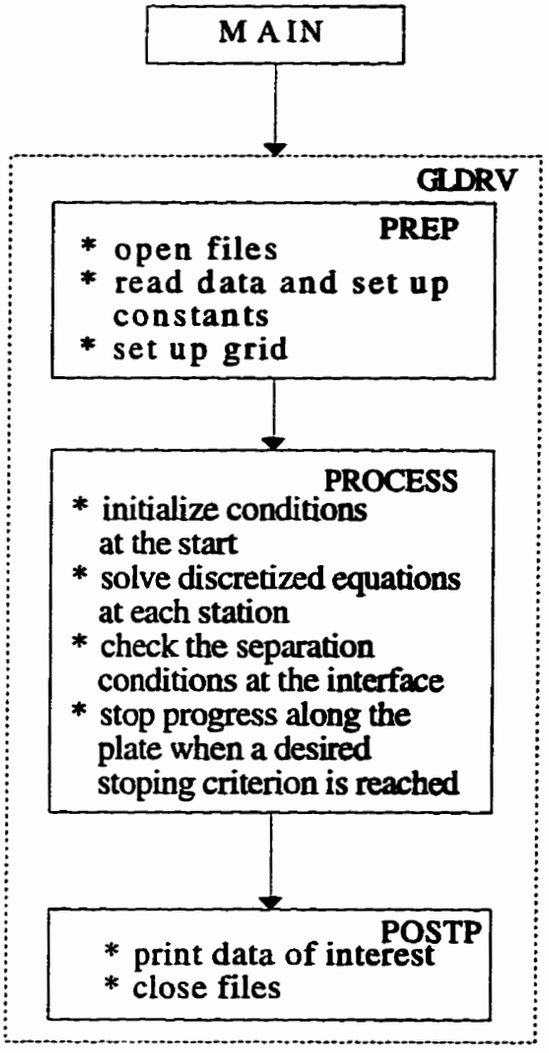

Figure 4.3: Structure of the program

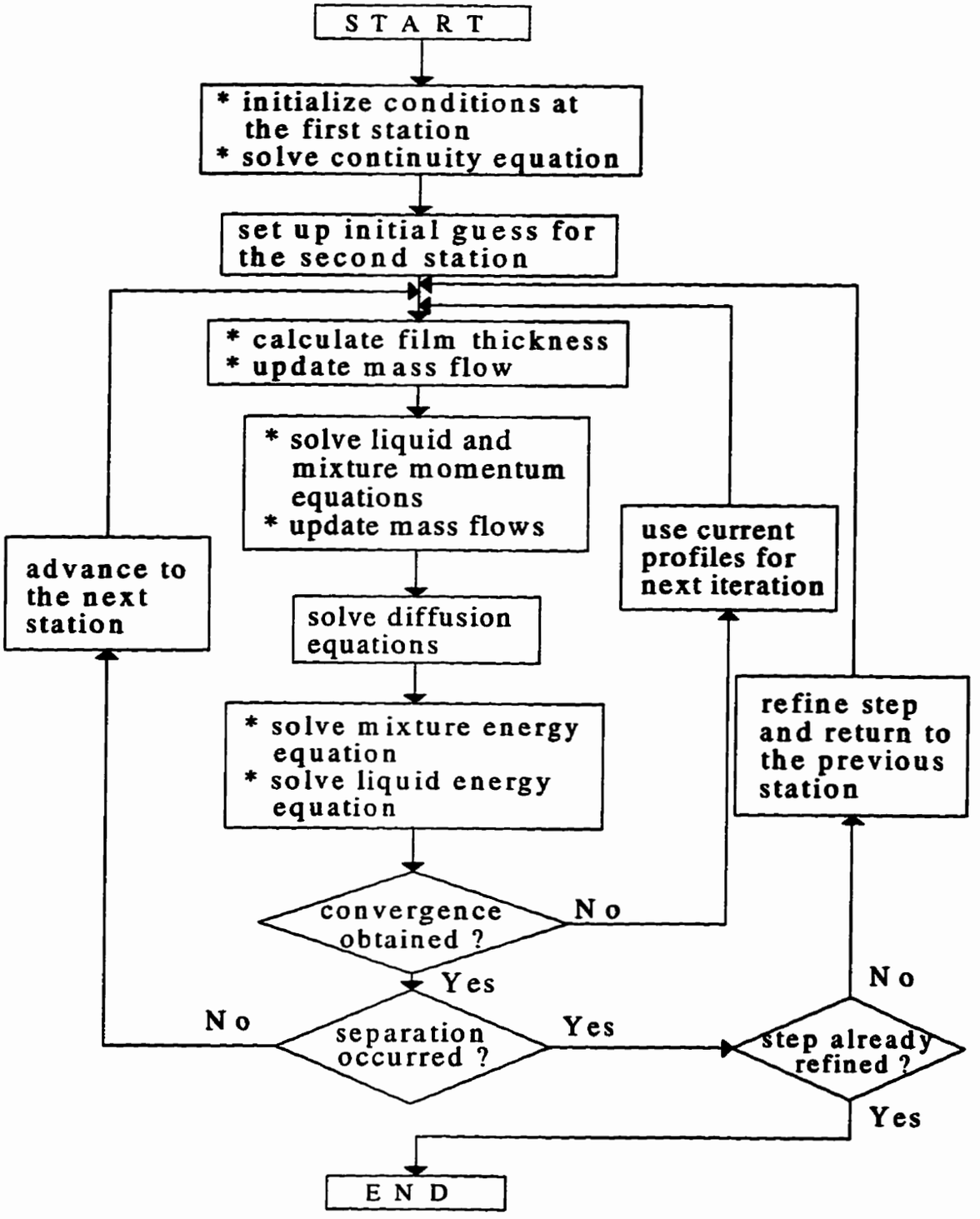

Figure 4.4: Flow chart of the subroutine **PROCESS**

Chapter 5

CONVERGENCE AND VALIDATION OF RESULTS

This chapter covers two steps in the verification of the computer code: tests of the convergence of the results and comparisons with the results published by other authors. Convergence of the results assumes not only that the results can be obtained within a certain tolerance, but also grid independence of the results. Since grid resolution is very important in the solution procedure, the first section of this chapter describes some aspects of choosing the proper grid parameters. The following section gives some results obtained with different grids and the effects of grid refinement on the rate of heat transfer and the separation distance. The last section of the chapter compares results obtained by other authors with the results obtained using the current model. It was mentioned in Chapter 2 that the available results for condensation of a moving vapor in the presence of a lighter gas were found in three references, so all three were used in the comparisons. An extensive comparison of the model in the case of condensation of vapor with a heavier gas can be found in Chin (1995).

5.1 Grid Resolution

The solution domain was divided along the χ axis into m stations, and across the liquid film and mixture layers into n and nv control volumes, respectively. Two factors influenced the choice of m, n, and nv: the separation distance, and the mixture boundary

layer thickness. Since the separation location depends highly on the input parameters, particularly on u_∞ and W_∞, the number of control volumes in the χ direction between zero and the separation point must be sufficient to maintain the accuracy of the calculation. The number of control volumes in the χ direction used in this work varied between 300 and 400 for all inlet conditions. In order to maintain this number of control volumes, the size of control volume in the χ direction was adjusted for each new set of input data, but in all cases a uniform step size was used in the calculation. Location on the plate where separation occurred was not known *a priori*, so usually one run of the program was necessary to find out an approximate x_{sep}, and then the step size was adjusted and the calculation was repeated. This procedure was necessary when input parameters were changed substantially from one run to another. If the input parameters were changed gradually, the step size was estimated based on the step size used in previous calculation.

Other important parameters that can affect the results are the number of control volumes in the η direction, and the mixture boundary layer thickness. The mixture boundary layer contains three layers: hydrodynamic, thermal and concentration layers. Each layer has its own thickness, and the ratios among these thicknesses depend on Prandtl and Schmidt numbers. The mixture boundary layer thickness, which was selected larger than any of the three layers, is an input parameter which defines the solution domain. The three boundary layers and the overall mixture boundary layer are shown in Figure 5.1. The overall mixture boundary layer thickness should not be too large because it would then require

more control volumes than necessary. The number of control volumes across the liquid film was usually n = 40 with a uniform distribution of nodes, and the number of control volumes in the mixture typically varied between 40 and 180 with an expanding distribution of nodes. During the solution procedure, the thickness of each layer was calculated and verified against the overall mixture boundary layer thickness to ensure that $\delta_{mixture}$ is sufficiently large.

Boundary layer thicknesses within the mixture layer were calculated using the following expressions:

$$\frac{\delta_u}{\delta} = \eta - 1 \text{ at } \frac{u - u_i}{u_\infty - u_i} = 0.99 \tag{5.1}$$

$$\frac{\delta_W}{\delta} = \eta - 1 \text{ at } \frac{W - W_i}{W_\infty - W_i} = 0.99 \tag{5.2}$$

$$\frac{\delta_T}{\delta} = \eta - 1 \text{ at } \frac{T - T_i}{T_\infty - T_i} = 0.99 \tag{5.3}$$

where δ_u, δ_W and δ_T are the hydrodynamic, concentration, and thermal boundary layer thicknesses, respectively, and δ is the liquid film thickness.

The purpose of adjusting the grid resolution at each new set of input parameters was not only to keep the accuracy of calculation , but also to reduce the computational time. For example, if gas concentration and free stream velocity were relatively small, and the total mixture layer thickness was selected large, then a large amount of computer time will be spent without any improvement in accuracy. In that case many control volumes would be

in the free stream where field values are not changing. Since the results presented in this work were obtained by running the program numerous times, it was important to reduce unnecessary calculation as much as possible.

5.2. Convergence of Results

Convergence of results was verified by changing the grid parameters. The parameters that were varied are: n, nv, m, factornv, factorm, and concri. Factorm defines the rate of expansion of the grid in the χ direction, and factornv is the grid expansion factor across the mixture boundary layer. An example of the convergence of the results is given in Table 5.1. Presented results were obtained for the steam-hydrogen vapor-gas combination. The results are divided in two groups: the results obtained with convergence criterion concri $=10^{-7}$, and the results obtained using concri $=10^{-6}$. Convergence criterion concri corresponds to the maximum relative error, given either by Equation(4.3) or Equation(4.4), and it is an input parameter.

Convergence tests were performed by changing one of the grid parameters while the others were kept constant, and by calculating the relative difference in x_{sep} and the heat flux at the wall, q_{wall}, compared to their values from the previous set of parameters. As an example, for concri $=10^{-7}$, changing n from 40 to 60 does not affect the location of separation (uniform step size and the change of profiles is too small to affect x_{sep}), and the

relative change in q_{wall} is 0.003%. However, increasing nv from 40 to 80, and from 80 to 120 gives differences in x_{sep} of 0.336 and 0.061%, respectively, and differences in q_{wall} of 0.218 and 0.026%, respectively. Therefore, refinement of the grid within the mixture layer strongly affects the convergence of x_{sep} and q_{wall}. Reduction of the relative error can also be obtained by increasing the number of axial stations, m. Increasing m from 200 to 300 produces a relative change in x_{sep} of 0.096% and in q_{wall} of 0.056%. Further tests showed that increasing m from 300 to 400 reduces changes in x_{sep} and q_{wall} to 0.048% and 0.005%, respectively.

Since the separation location depends on the step size, a uniform step was used in this work. If an expanding grid was used with factorm = 100, then x_{sep} and q_{wall} would change by 0.288% and 0.09%, respectively, compared to the results for uniform spacing. It is expected that a higher value of factorm should produce a greater difference in x_{sep} because the step size near the separation location will be greater. Consequently, the deviation in x_{sep} will also be greater. Increasing factornv from 100 to 1000 produced 0.015% difference in x_{sep}, and 0.006% difference in q_{wall}. A similar set of verifications was done for concri of 10^{-6}, and the results show the convergence of the relative error of x_{sep} and q_{wall} when the grid is refined.

The typical parameters used in the calculations were: m varied between 300 and 400, n = 40, nv varied between 40 and 80, concri = 10^{-7}, factornv = 100, and factorm = 1.

Steam-Hydrogen $T_\infty = 393K \quad T_w = 363.15K \quad W_\infty = 0.01 \quad u_\infty = 0.1\frac{m}{s} \quad g = 9.81\frac{m}{s^2}$									
"relxd" 1.0		"relxu" 0.4		"relxt" 0.9		"relxw" 0.2		"yvapor" 700	
concri	n	nv	m	factor nv	factor m	xsep×10³ [m]	qwall×10⁻⁵ [W/m^2]	% xsep	% qwall
10e-7	40	80	400	100	1	4.103383	1.193161	-	-
10e-7	60	80	400	100	1	4.103383	1.193201	0	0.003
10e-7	40	40	400	100	1	4.089599	1.190555	-	-
10e-7	40	80	400	100	1	4.103383	1.163201	0.336	0.222
10e-7	40	120	400	100	1	4.105890	1.193469	0.061	0.022
10e-7	40	80	200	100	1	4.109296	1.192554	-	-
10e-7	40	80	300	100	1	4.105351	1.193225	0.096	0.056
10e-7	40	80	400	100	1	4.103383	1.193161	0.048	0.005
10e-7	40	80	400	100	1	4.103383	1.193161	-	-
10e-7	40	80	400	100	100	4.091568	1.194312	0.288	0.096
10e-7	40	80	400	100	1	4.103383	1.193161	-	-
10e-7	40	80	400	1000	1	4.102757	1.192934	0.015	0.019
10e-6	40	40	400	100	1	4.085840	1.189795	-	-
10e-6	40	80	400	100	1	4.099624	1.192574	0.336	0.233
10e-6	40	100	400	100	1	4.101504	1.192901	0.046	0.027
10e-6	40	80	300	100	1	4.102007	1.193043	-	-
10e-6	40	80	400	100	1	4.099624	1.192574	0.058	0.039
10e-6	40	80	500	100	1	4.097695	1.192314	0.047	0.022
10e-6	40	80	400	100	1	4.099624	1.192574	-	-
10e-6	40	80	400	100	100	4.091568	1.192998	0.197	0.036

Table 5.1: Convergence table for steam-hydrogen at T_∞=393K and T_{wall}=363.15K

5.3 Comparison with Previous Work

Results for the condensation of a moving vapor in the presence of a lighter gas were given by: Denny and Jusionis (1972), Turner et al. (1973), and by Siddique et al. (1989). Denny and Jusionis (1972) analyzed the effect of a noncondensable gas on laminar film condensation on a vertical plate. The governing system of equations for the mixture boundary layer consisted of the mass, momentum, energy and species conservation equations. The inertia effect and energy convection were neglected in the liquid film. In addition, they evaluated liquid properties at the reference temperature $T_r = T_{wall} + 0.33(T_i - T_{wall})$. The governing system of equations was solved by the finite difference method. Comparisons are presented in Figure 5.2 for Freon12-air mixtures at different conditions. It must be noted that the curves of $\frac{q}{q_{Nu}}$ corresponding to the present results extend only up to $x = x_{sep}$. In the paper by Denny and Jusionis, all the results were given up to $x = 0.183\,m$, and no separation conditions were reported. The comparison shows good agreement between the two models. For example, at $T_\infty = 310.93\,K$ the relative error between the two curves varies from 1.38 to 1.72%, at $T_\infty = 305.37\,K$ the error is in the range of 2 to 2.9%, and at $T_\infty = 322.04\,K$ the error is in the range of 2.3 to 3%. Possible reasons for this difference lie in the different solution methods and in the use of the reference temperature for the evaluation of the liquid properties.

Turner et al. (1973) reported values of q / q_{Nu} for mercury-air mixtures at a low free stream velocity on a vertical plate. They neglected the inertia and the energy convection terms in the governing equations of the liquid film. Also, they included an interfacial resistance equation at the interfacial boundary condition. Results were also reported for the distance on the x axis (along the plate) where separation of the mixture boundary layer occurred. Results were obtained at $T_\infty = 666.67$ K and $u_\infty = 0.3048$ m/s for two values of ΔT: for $\Delta T = 5.55$ K, which are given in Figure 5.3, and for $\Delta T = 16.67$ K, which are given in Figure 5.4. In each case, a comparison was made for $W_\infty = 0.01$ and $W_\infty = 0.03$.

From Figures 5.3 and 5.4 it can be seen that the difference between the heat transfer results obtained by Turner et al. and those obtained in the present work varies from 8.3% to 47%. Similar differences in the heat transfer results between the model of Turner et al. and the present model were encountered by Chin (1995) for sodium-argon mixtures. The difference occurred in the region where the interfacial resistance has no significant effect. In the results given by Turner et al. the separation location was given within a range which is equal to the integration step, so the location of the separation point cannot be precisely determined. The range of difference for the separation point between Turner et al. and the present model varies from 7.5% to 46%. It can be noted that the axial step size used in the work done by Turner et al. was relatively large compared to the total integration range; the number of axial stations they used varied from 6 to 10. This small number of

steps may be a reason for the high relative difference between their model and the present work. Another possible reason for the difference may lie in the way the interfacial boundary conditions were prescribed. In the model by Turner et al., the system of equations which was solved for the interfacial boundary conditions included two additional equations: the equation for the velocity profile in the liquid film (obtained by integration of the liquid momentum equation using Nusselt's assumptions) and the equation which defines gas impermeability condition [Equation (3.17)]. In the present model, the interfacial velocity was obtained by solving the liquid and mixture momentum equations while Equation (3.17) was implemented as the boundary condition for the gas conservation equation.

The comparisons with Siddique et al. (1989) are shown in Figures 5.5 and 5.6. Siddique et al. calculated the rate of heat transfer for the condensation of moving steam-hydrogen mixtures over a horizontal flat plate. In the model, they assumed constant properties which were evaluated at the interface temperature. They also used the equation proposed by Rose (1980) that correlates the nondimensional condensation mass flux to the Schmidt number and the mass fraction of the noncondensable gas. The equation proposed by Rose was compared with the present model by Chin (1995). That comparison showed that the difference between the present model and Rose's equation is 6% for a steam-air mixture at $T_\infty = 400$ K and $\Delta T = 20$ K, and becomes higher for higher values of ΔT. The present comparisons with Siddique et al. were done at $T_\infty = 373.15$ K and $T_\infty = 398.15$ K for three

values of W_∞: 0.005, 0.05, and 0.1. Heat transfer rate at the wall was normalized by the value of the heat transfer rate for the case of pure vapor condensation. The results in Figure 5.5 show good agreement, particularly in the case of $W_\infty = 0.005$, where the two sets of results are almost identical. At $T_\infty = 398.15$ K and $W_\infty = 0.005$, the difference is within 6% for all tested values of ΔT. For the higher values of W_∞, good agreement was obtained for ΔT up to approximately 20 K. As ΔT increases above 20 K, however, the deviation between the present model and Siddique et al. increases. There are two possible sources for the higher differences at higher ΔT and W_∞. One source is using constant properties and a constant average value of Schmidt number in the analysis by Siddique et al.(1989). The calculation of Schmidt number at $T_\infty = 398.15$ K, $\Delta T = 10$ K, and $W_\infty = 0.005$ gives Sc = 0.174 at the interface and 0.168 at the free stream. As the gas concentration increases, the difference in Schmidt number also increases. For $\Delta T = 10$ K and $W_\infty = 0.1$, Sc at the interface is 0.353. and at free stream, Sc is 0.298. This difference is more pronounced for higher values of ΔT. At $\Delta T = 70$ K and $W_\infty = 0.1$, Schmidt numbers at the interface and at the free stream are 0.778 and 0.298, respectively. For this case, the relative difference in q / q_0 obtained using the two models is maximum. Another possible source for the difference at larger ΔT and W_∞ is the use of the formula proposed by Rose (1980).

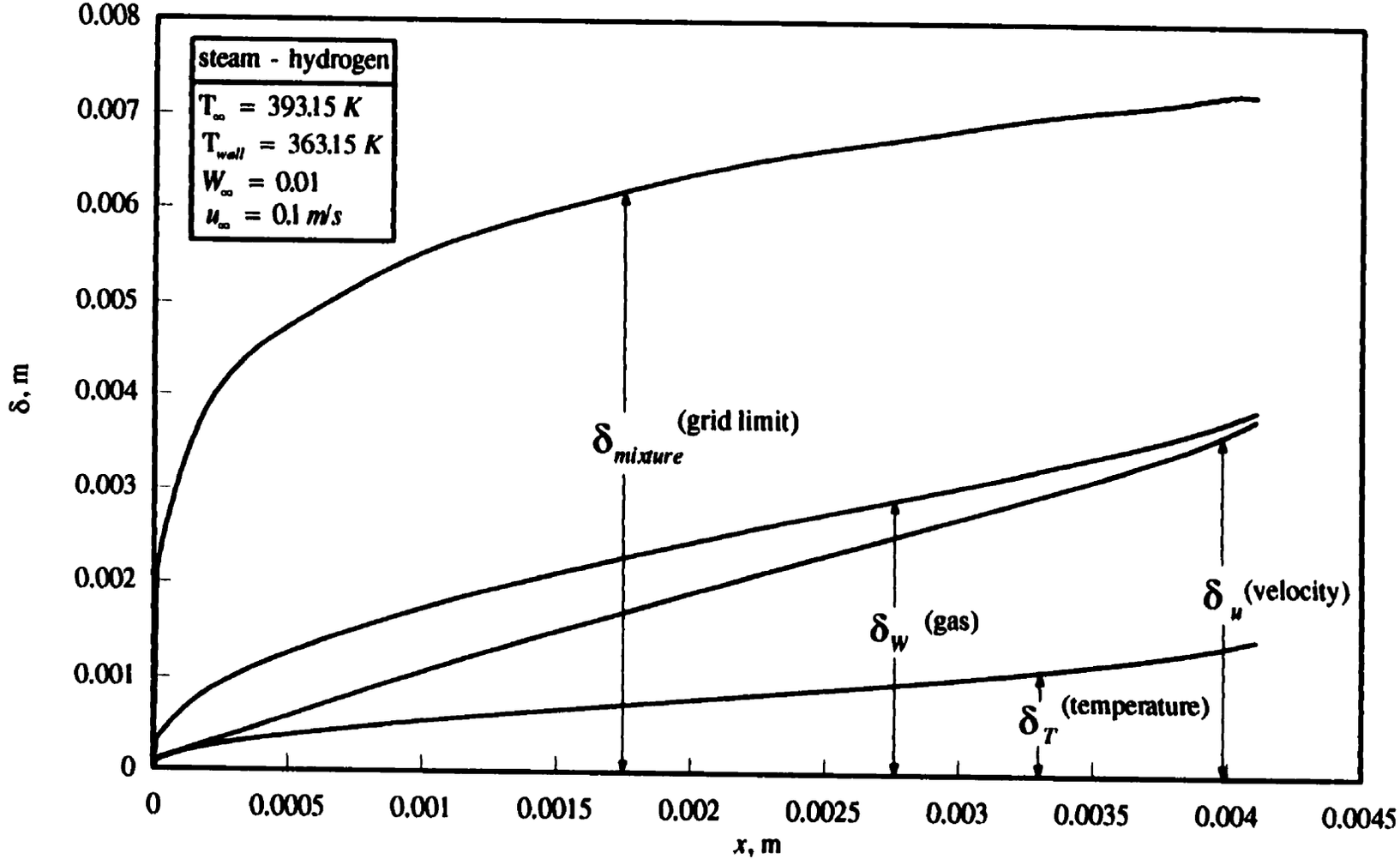

Figure 5.1: Sample of the mixture boundary layer thicknesses for steam-hydrogen mixtures

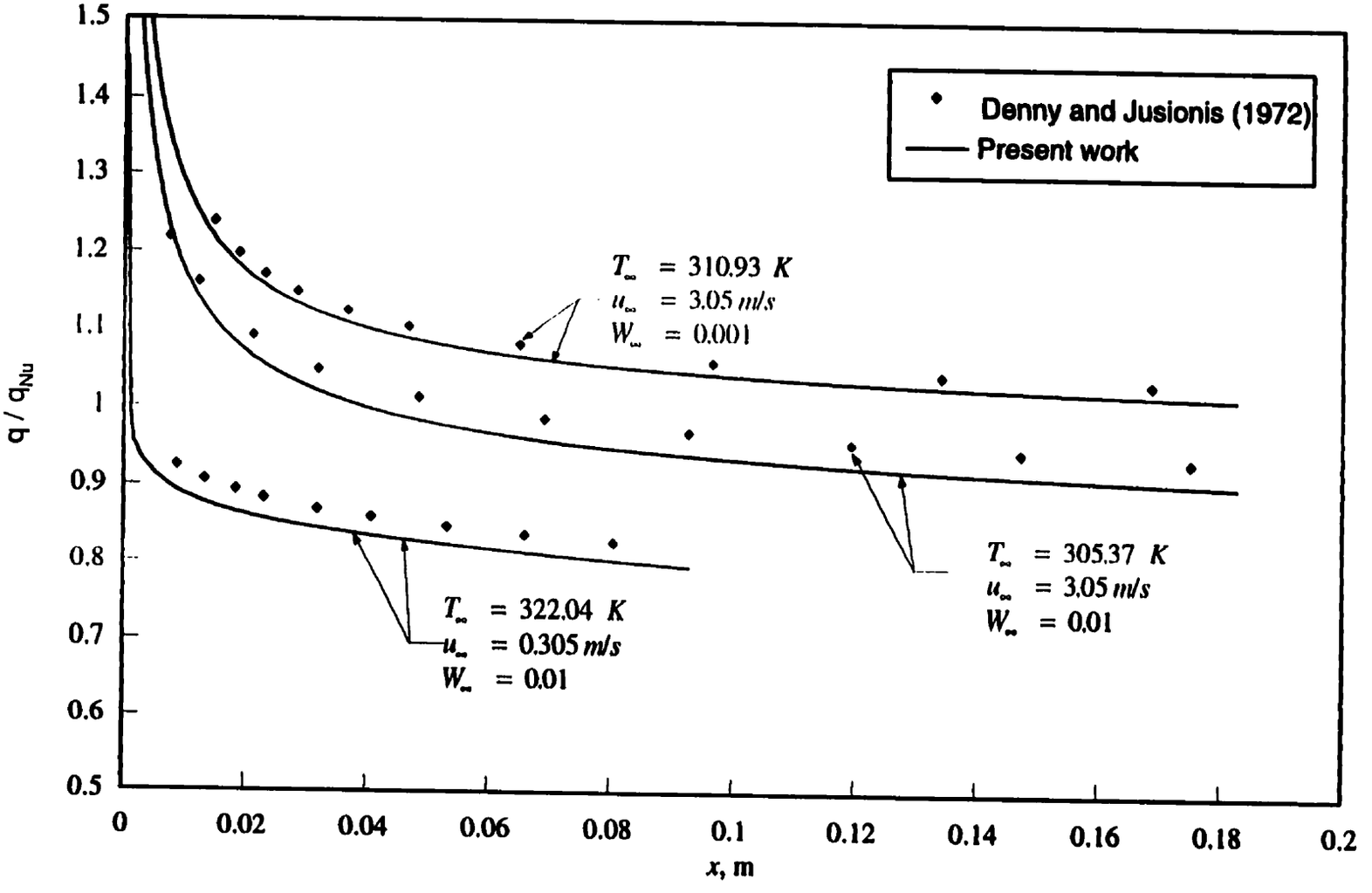

Figure 5.2: Comparison with Denny and Jusionis (1972) for Freon12 - air mixtures, T_{wall} = 299.82K

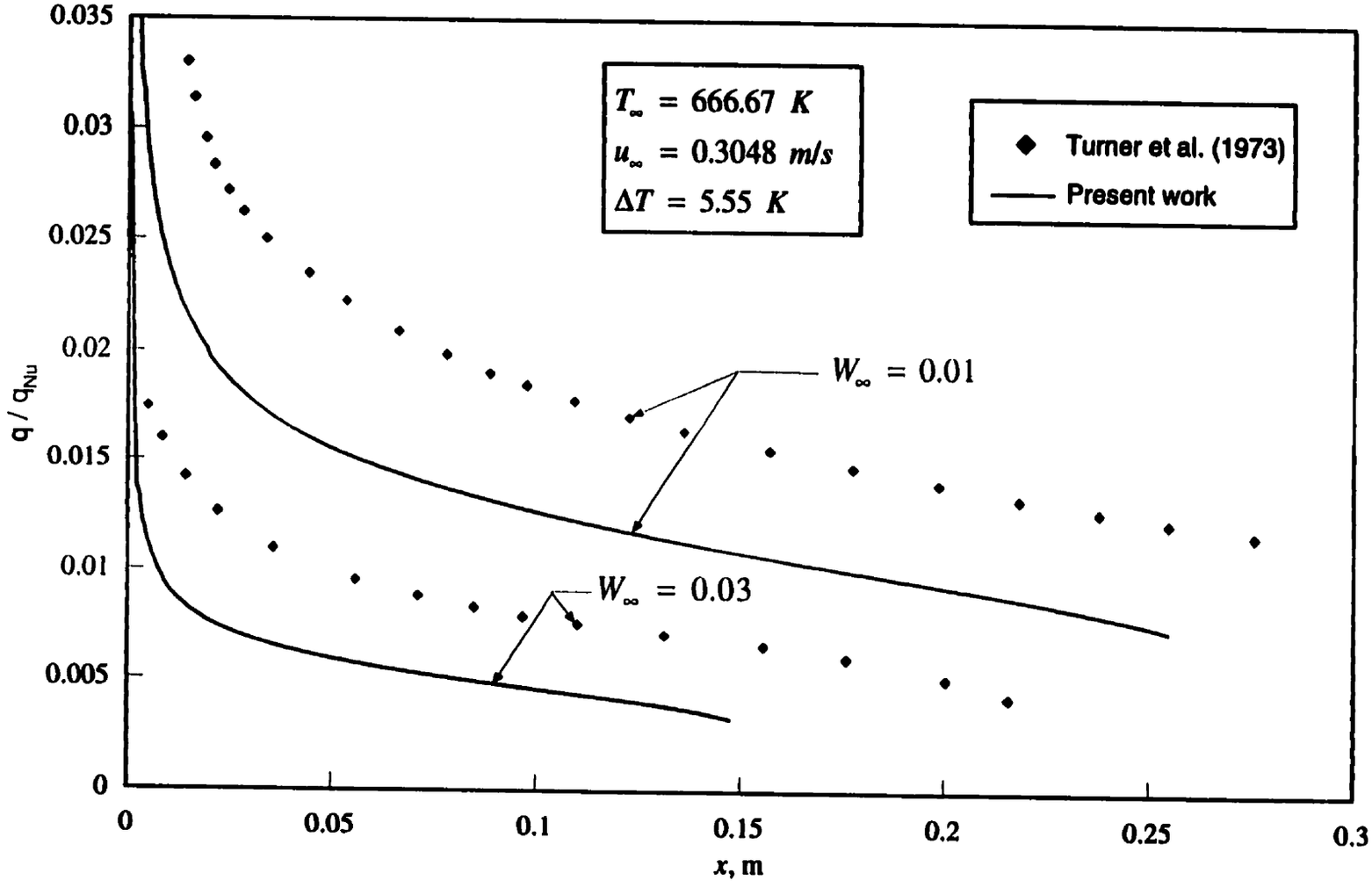

Figure 5.3: Comparison with Turner et al. (1973) for mercury - air mixtures at $\Delta T = 5.55K$

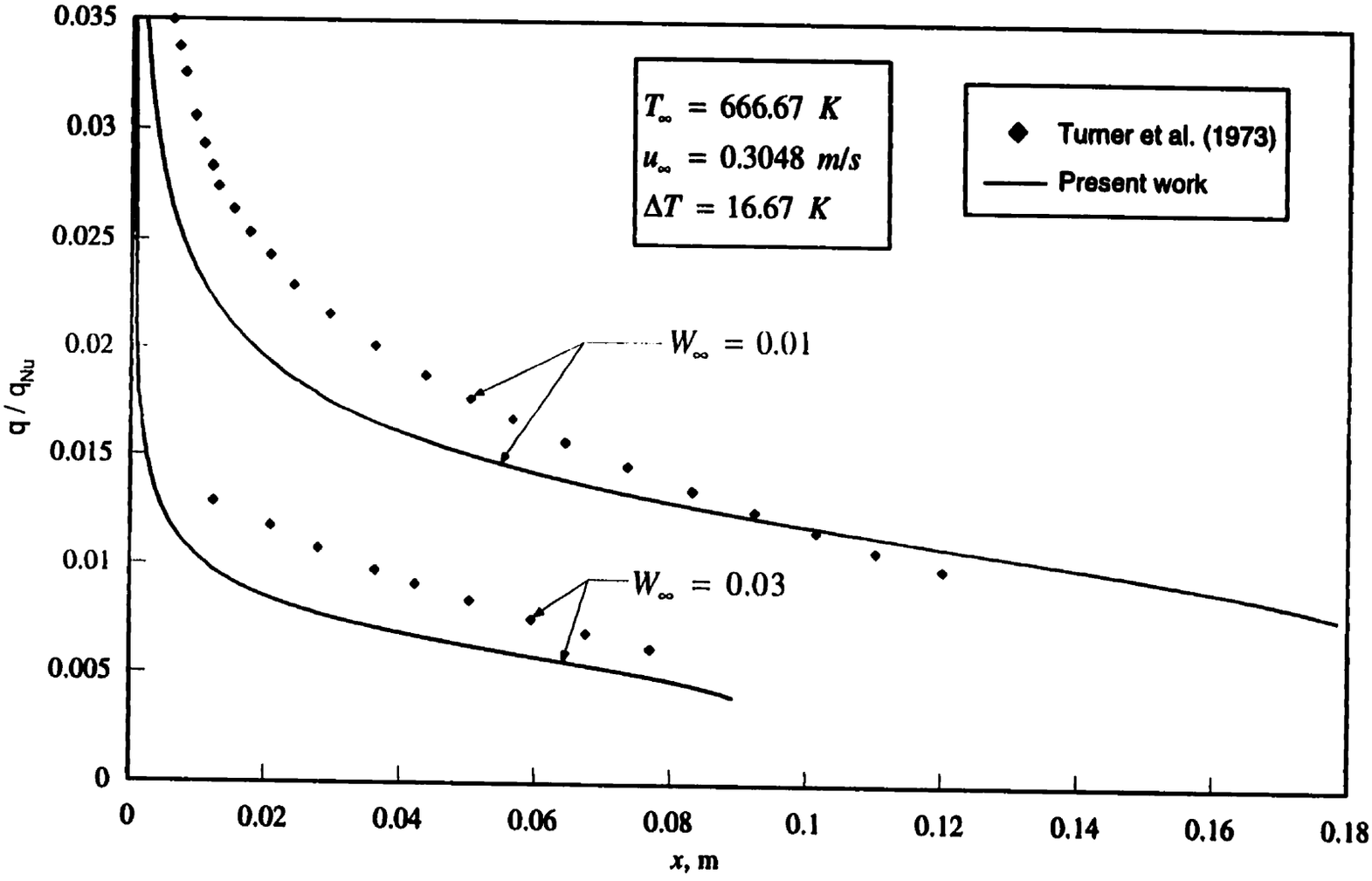

Figure 5.4: Comparison with Turner et al. (1973) for mercury - air mixtures at $\Delta T = 16.67K$

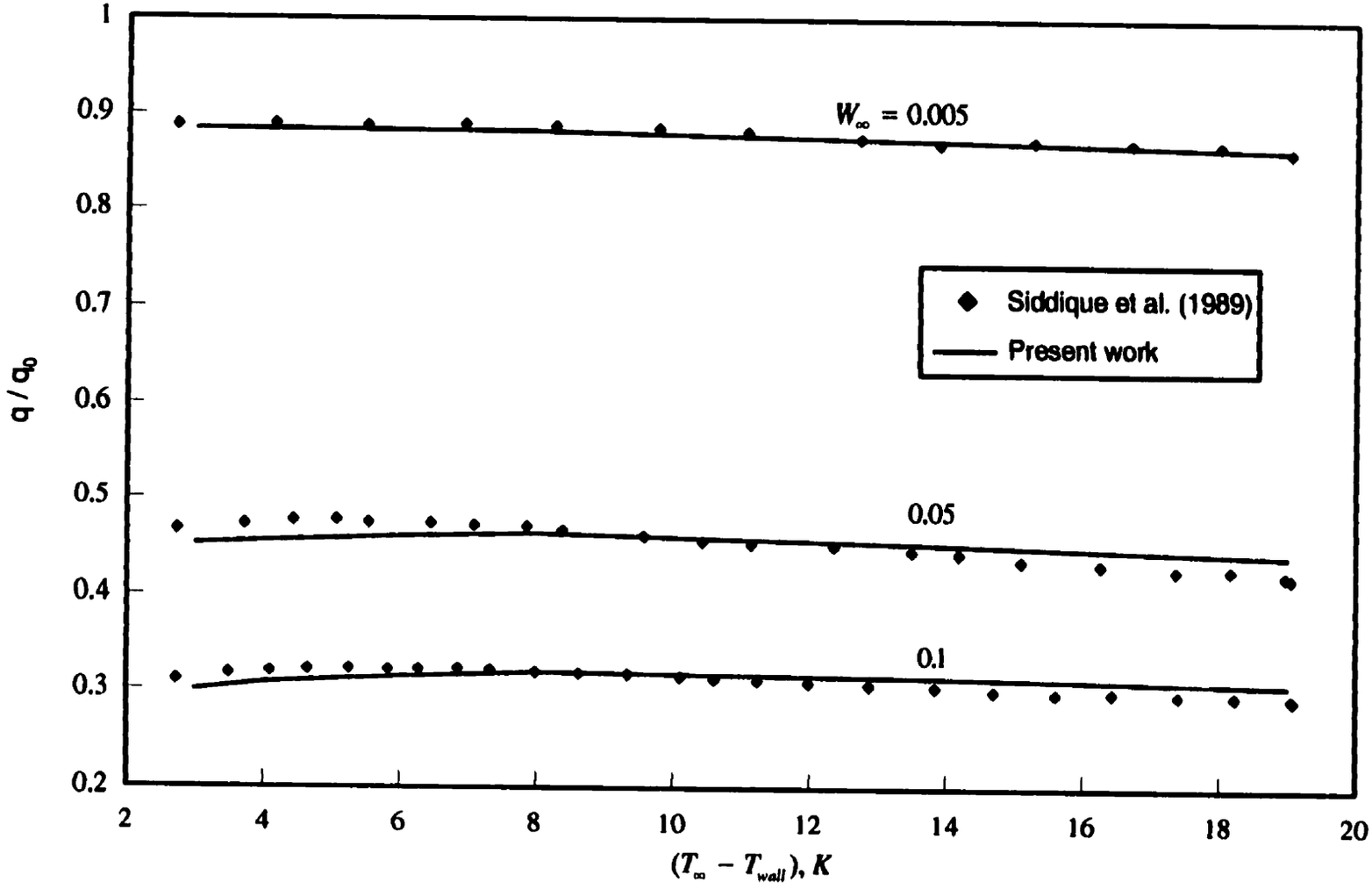

Figure 5.5: Comparison with Siddique et al. (1989) for steam - hydrogen mixtures at T_∞ = 373.15 K

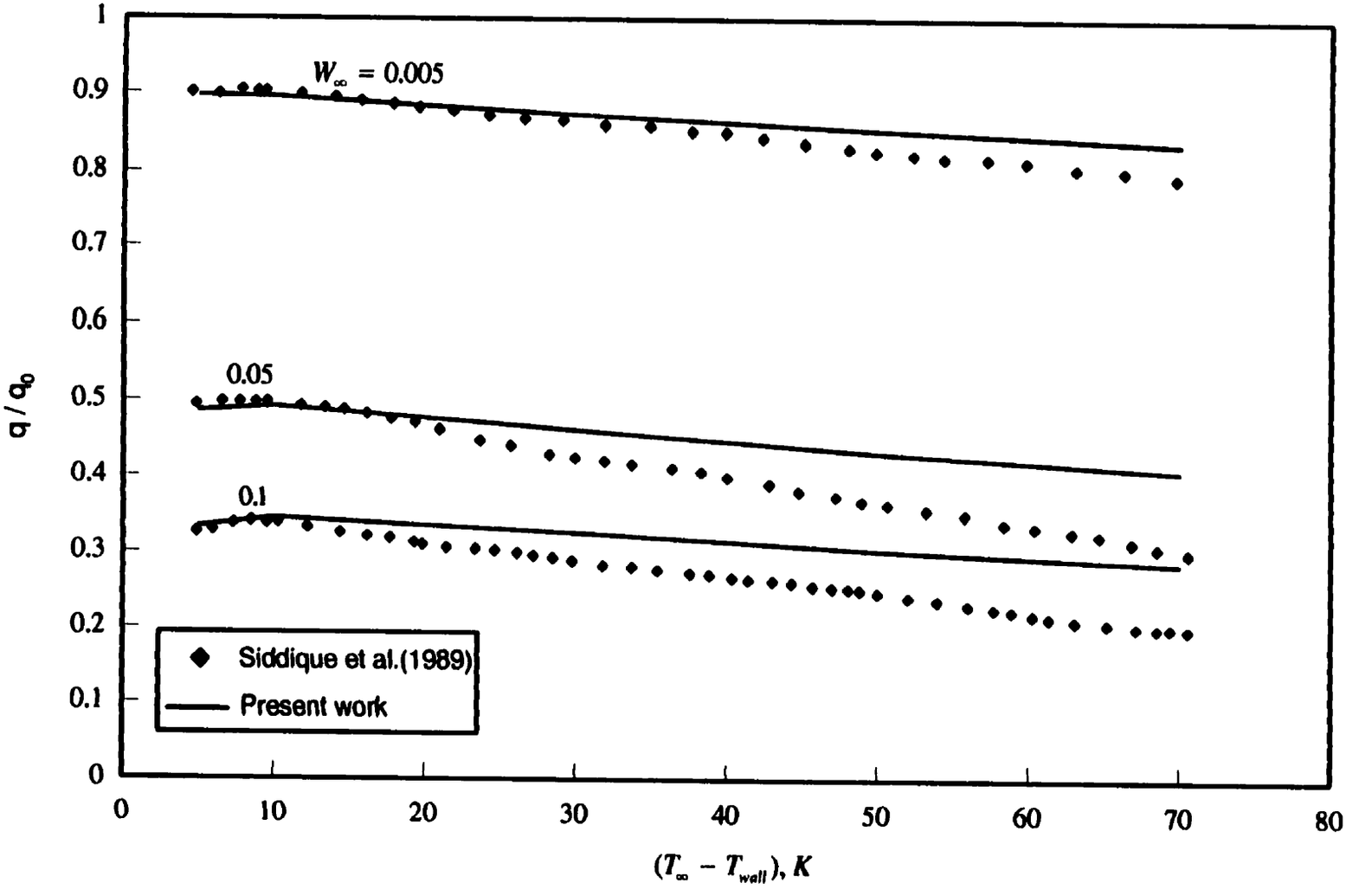

Figure 5.6: Comparison with Siddique et al. (1989) for steam - hydrogen mixtures at T_∞ = 398.15 K

Chapter 6

RESULTS AND DISCUSSION

Results in this work were obtained for three vapor-gas combinations: steam - hydrogen, mercury - air, and Freon12 - air. Generally, the results are divided into two groups: the first group is related to the mixture boundary layer separation, and the second group is related to the heat transfer results. The objective in the first set of results is to provide a simple form that can be used to estimate the separation location for each of the vapor-gas combinations, and in the second set of results the objective is to show the effect of the lighter gases on the rate of heat transfer. All the results are presented in graphical form because derivation of analytical closed form expressions is extremely difficult. The results are often presented in nondimensional form using parameters that allow a concise presentation. Also, all the results presented are valid only for laminar flow. A film Reynolds number less than 30 was the criterion used to define if the flow was laminar. The film Reynolds number was defined in the standard way as:

$$\mathrm{Re}_{\delta} = \frac{4\Gamma}{\mu_L}, \tag{6.1}$$

where

$$\Gamma = \int_0^{\delta} \rho_L u_L dy \tag{6.2}$$

Liquid viscosity and density were evaluated at the reference temperature

$$T_r = T_{wall} + 0.31(T_{\infty} - T_{wall}) \tag{6.3}$$

Because all calculations were stopped when the two criteria for the mixture boundary layer separation were met, each curve has a different ending point on the x-axis. The vapor-gas mixtures were chosen to obtain three different ratios of molecular weights. The molecular weight ratios are steam-hydrogen: $M_v/M_g = 9$; mercury-air: $M_v/M_g = 6.935$; and Freon12-air: $M_v/M_g = 4.174$.

6.1 Derivation of Dimensionless Separation Length

It was observed that combining certain parameters into dimensionless groups and plotting them can simplify a diagram and can eliminate the effect of some parameters. For example, plotting of $Nu_x / \mathrm{Re}_x^{1/2}$ versus $\frac{1}{Fr_x}$ for given T_∞, ΔT, and W_∞ can be used for all values of x, θ, and u_∞ (Chin, 1995), providing that the flow is laminar. A similar approach was used in plotting the boundary layer separation results. The procedure used is now described for a mercury-air mixture at $T_\infty = 666.67$ K and $\Delta T = 5.55$ K, and then used for all the following results presented in this thesis.

Figure 6.1 shows the separation distance along the plate versus free stream velocity. The free stream gas concentration is $W_\infty = 0.03$. The parameter that defines each curve is the component of the gravitational acceleration in the direction of the flow, so the effect of the plate inclination is included. From the figure we can see that increasing the free stream velocity and/or increasing θ, increases x_{sep}. As u_∞ approaches zero, x_{sep} also

approaches zero. The same set of results was repeated for other free stream conditions and the trend was found to be the same.

Elimination of the plate inclination was accomplished by multiplying x_{sep} by $g\cos\theta$. The same set of results from Figure 6.1 is plotted in Figure 6.2 along with another set with $W_\infty = 0.01$. For $W_\infty = 0.03$, the plot of $x_{sep} g\cos\theta$ shows that the three curves from Figure 6.1 collapsed into one curve in Figure 6.2. The same behavior was obtained for $W_\infty = 0.01$. The third step in reducing the number of independent parameters was to divide $x_{sep} g\cos\theta$ by u_∞^2. Figure 6.3 shows the dimensionless separation length, x^*_{sep} $\left(\text{or}\dfrac{1}{(Fr_x)_{sep}}\right)$, plotted versus u_∞ for two values of W_∞. In both cases, the result is a horizontal line, which suggests that for constant T_∞, T_{wall}, and W_∞, only one parameter is necessary to define the separation length. Also, it can be observed that in this particular case x^*_{sep} decreases when W_∞ increases.

It is important to point out the limiting cases for the parameters that are important in the collapsing procedure. These parameters are θ and u_∞. It was assumed that T_∞ and ΔT are constant for the situations described in Figures 6.1 to 6.3 and any limitations of those parameters are related to the defined temperature range for the P-T (saturation pressure - temperature) curve and properties. The inclination of the plate in general varies between 0^0 and 90^0, which corresponds to a vertical and a horizontal plate, respectively. Condensation on the horizontal plate is not important in the investigation of separation

effect because the buoyant force does not affect the flow in the direction of the plate so that separation does not occur. Consequently, the results shown in Figure 6.3 do not include angle of inclination 90^0 (the case of a horizontal plate).

The upper limit for the free stream velocity is restricted by the requirement of laminar flow. Since the present model applies to laminar film condensation, u_∞ was increased until $Re_\delta = 30$. For relatively high free stream velocities, the calculation procedure was usually terminated before separation occurred because $Re_\delta = 30$ was reached.

6.2 Steam-Hydrogen Mixtures

Results for steam-hydrogen are divided into two groups: the first group is related to the mixture boundary layer separation and the second shows the change in heat transfer due to presence of a lighter noncondensable gas.

6.2.1 Separation Results for Steam-Hydrogen Mixtures

Results were obtained for three free stream temperatures: $T_\infty = 353.15$ K, $T_\infty = 373.15$ K and $T_\infty = 393.15$ K. Those temperatures correspond to the total system pressure (with zero gas concentration) of 0.5 bar, 1 bar and 2 bar. If the gas concentration increases, then the total system pressure also increases with a rate that depends on the value of the free stream temperature. At each free stream temperature, the separation results were

obtained for three values of ΔT and for free stream gas concentration variation from 10^{-5} to 0.6. For $T_\infty = 353.15$ K and $T_\infty = 393.15$ K the values of ΔT were $\Delta T = 5$K, 15 K and 30 K, while for $T_\infty = 373.15$ K values of ΔT were 3 K, 15 K and 30 K. Following the procedure described in Section 6.1 for fixed T_∞ and for each ΔT, curves of x^*_{sep} versus W_∞ were plotted. For all three free stream temperatures, the results are shown in Figures 6.4 to 6.6. From those figures it can be seen that all the curves follow the same trend, which strongly depends on the value of W_∞. This trend shows that increasing W_∞ from the lowest value decreases x^*_{sep} until it reaches a minimum value, after which x^*_{sep} gradually increases. The lower limit used for W_∞ is 10^{-5}, and any additional reduction of W_∞ does not change the shape of the curves presented. The analysis was extended to very small values W_∞ (order of 10^{-7}) and it was found that x^*_{sep} does not have any unexpected change in behavior.

An explanation for this variation of x^*_{sep} can be found following the approach of Schlichting (1979). In that approach, the mixture continuity equation [Equation (3.4)] was subtracted from the mixture momentum [Equation (3.5)], and then the momentum equation was reduced to:

$$\rho u \frac{\partial u}{\partial x} + \rho v \frac{\partial u}{\partial y} = \frac{\partial}{\partial y}\left(\mu \frac{\partial u}{\partial y}\right) + g(\rho - \rho_\infty) \qquad (6.4)$$

The momentum equation can be written along the stream line at the interface between the liquid and mixture. Assuming constant viscosity and regrouping yields:

$$\underset{4}{\mu_i\left(\frac{\partial^2 u}{\partial y^2}\right)_i} = \underset{1}{\rho_i u_i\left(\frac{\partial u}{\partial x}\right)_i} + \underset{2}{\rho_i v_i\left(\frac{\partial u}{\partial y}\right)_i} - \underset{3}{g(\rho_i - \rho_\infty)} \qquad (6.5)$$

Terms 1,2 and 3 in Equation(6.5) correspond to acceleration of the interface, suction at the interface and buoyancy, respectively. All these three forces influence the value of x_{sep}. Using the finite difference approximation for the u-velocity derivatives, it is possible to calculate each term in Equation (6.5) and monitor how each term changes along the plate for different values of W_∞. Since the solution of the governing set of equations was based on a finite volume method, a calculation of terms 1, 2, 3, and 4 via a different approach (finite difference) would not exactly satisfy Equation (6.5). The finite difference calculation will, however, show qualitatively the rate of change of each term and the ratios between terms. The differences between this problem and the problem described by Schlichting are: the mixture boundary is not fixed (which introduces another inertia term - term 1), the suction velocity is not constant, and the existence of the buoyant term 3 (which varies along the plate) instead of a constant adverse pressure gradient. It should be emphasized that $(\rho_i - \rho_\infty)$ was always less than or equal to zero. The change of terms 1, 2, 3 and 4 in Equation (6.5) is plotted in Figures 6.7 to 6.10. The results were given for a steam-hydrogen mixture at T_∞= 353.15 K, T_{wall}= 338.15 K, u_∞= 0.03 m/s, and $\theta = 0$. The gas concentration was varied from 0 to 0.6.

Figure 6.7 shows the change of $\rho_i u_i \left(\frac{\partial u}{\partial x}\right)_i$ (term 1 in Equation (6.5)). It is evident that each curve in the figure has different length or different separation location. An important observation is that this term is always positive, which means that it increases the curvature of the velocity profile at the interface. From the figure it can be seen that the magnitude of this term is not large. For example, for $W_- = 0$ the magnitude is 0.018 while for $W_- = 0.6$ it drops below 10^{-4}. Also each curve has a negative slope which means that term 1 gradually decreases along the plate in this case. The magnitude and the rate of change of $\rho_i u_i \left(\frac{\partial u}{\partial x}\right)_i$ suggest that this inertia term does not contribute much to the effective adverse pressure gradient, which can be considered as equivalent to the right hand side terms of Equation (6.5).

Figure 6.8 shows the change of $\rho_i v_i \left(\frac{\partial u}{\partial y}\right)_i$ (term 2 in Equation (6.5)). This figure was not plotted in full scale because some cases have a very large change in magnitude along the plate (on the order of 10^4). Therefore, the vertical scale was adjusted so that only the region around zero is shown, and that is the reason why the curves for W_- close to zero look like straight lines. The figure shows that this term is always negative and it reduces the curvature of the velocity profile at the interface (it reduces the effective adverse pressure gradient). However, it is not constant along the plate; it approaches zero as the

velocity gradient decreases at the interface. The velocity gradient at the interface decreases to zero for any W_- because of either the moving boundary (which is the liquid film surface) or because of upward buoyancy force. In any case, this term is larger in the magnitude than the inertia term (term 1) along the plate except in the vicinity of the separation point where term 2 becomes zero.

The change of term 3 in the Equation (6.5) is shown in Figure 6.9. An important observation related to this figure is that increasing W_- from zero to approximately 0.1 increases the magnitude of $g(\rho_i - \rho_-)$ while increasing W_- from 0.1 to 0.6 decreases $g(\rho_i - \rho_-)$. This can be easily explained by the fact that the density difference $(\rho_i - \rho_-)$ has two limiting cases. The first one is pure vapor ,$W_-= 0$; in this case $(\rho - \rho_-) = 0$. The second limiting case is $W_- \rightarrow 1$, or the limiting case of pure gas for which the density difference again approaches zero. Between those two limiting cases, $|\rho_i - \rho_-|$ increases, reaches a maximum, and then decreases.

Figure 6.10 shows the change of $\mu_i\left(\frac{\partial^2 u}{\partial y^2}\right)_i$ calculated using the finite difference approximation involving three velocities at control volumes next to the interface. It can be immediately observed that the shape of the curves is similar to those plotted for term 2, but all curves are shifted up on the ordinate axis. The similarity of curves with those in

Figure 6.8 is explained by the relatively higher magnitude of term 2. Because the curvature of the velocity profile at the interface is defined by the change of $\mu_i\left(\frac{\partial^2 u}{\partial y^2}\right)_i$, the magnitude of that term is expected to be an indicator of x^*_{sep} variations. That term depends on the rate of change of term 1, term 2 and term 3 in the momentum equation (Equation (6.5)). Near the separation location, however, term 2 approaches zero and the value of $\mu_i\left(\frac{\partial^2 u}{\partial y^2}\right)_i$ is determined by the change of terms 1 and 3. It is expected that x^*_{sep} will not correlate precisely with only term 1 and term 3 at the separation location because x^*_{sep} also depends on term 2, which is always zero at x^*_{sep}. Generally, term 2 tends to increase x^*_{sep}, while the other two terms tend to decrease it. For a steam-hydrogen mixture, increasing W_- from 0 to approximately 0.1 results in an increase of the second derivative at the interface at the separation location. Additional increase in W_- results in decreasing of the effective adverse pressure gradient at the separation location. This trend follows closely the trend of change of the buoyant force described earlier.

In order to show the change in x^*_{sep} compared to $\mu_i\left(\frac{\partial^2 u}{\partial y^2}\right)_i$ and $(\rho_i - \rho_-)$, Figure 6.11 was plotted. In that figure x^*_{sep} decreases with different rate as W_- increases from 10^{-5} to about 0.15, while for the same W_- range the values of $\mu_i\left(\frac{\partial^2 u}{\partial y^2}\right)_i$ and $(\rho_- - \rho_i)$ increase. This trend is explained by the fact that for the very small values of W_-, term 2 is dominant

and any decreasing of its magnitude extends the separation point. As W_- keeps increasing, the density difference (buoyant force) also increases, and when combined with an additional reduction in the magnitude of term 2, results in a more rapid decline of x^*_{sep}. This decline is evident for the interval of W_- between 0.001 and 0.15. In other words, the increase in the effective adverse pressure gradient is primarily due to an increase in the buoyant force and a decrease in the second inertia term (term 2). It was already shown that term 1 has an insignificant influence on the variation of x^*_{sep}.

For higher values of W_- (greater than 0.15), Figure 6.11 shows that $\mu_i\left(\frac{\partial^2 u}{\partial y^2}\right)_i$ starts to decrease rapidly. For the same interval of W_- the figure shows that $(\rho_- - \rho_i)$ also decreases while x^*_{sep} increases. This trend was explained by the fact that $\rho_i u_i\left(\frac{\partial u}{\partial x}\right)_i$ is very small (Figure 6.7) and that $\rho_i v_i\left(\frac{\partial u}{\partial y}\right)_i$, for these values of W_-, approaches zero at a higher rate (Figure 6.8), so the only dominant term is $g(\rho_i - \rho_-)$. This term reaches a maximum and then decreases, which causes a reduction of the effective adverse pressure gradient and an increase in x^*_{sep}.

In general, the upper limit for W_∞ is only restricted by T_{wall}. However, calculation of x^*_{sep} for higher values of W_∞ caused considerable problems related to convergence for mercury-air mixtures. The problem required more adjustment of the grid and convergence parameters and significantly more CPU time. Since the main features of x^*_{sep} curves are illustrated for W_∞ up to 0.6, that was considered to be the upper limit in the presentation of the results.

The previous presentation of the separation results in the form of plots (Figures 6.4 to 6.6) required one diagram for each free stream temperature. In order to reduce the number of graphs, an additional collapsing of the curves was done through the elimination of ΔT as a separate parameter. To accomplish the additional collapsing, x^*_{sep} was multiplied by Jakob number raised to the exponent m. The three curves in Figure 6.4 were merged into one curve plotted for $T_\infty = 353.15\ K$ in Figure 6.12. The same procedure was repeated for the two other free stream temperatures studied. In this procedure the most important step was to define the value of the exponent m so that the error which was introduced is as small as possible. The value of the exponent m was obtained by collapsing pairs of curves with different values of ΔT. From Figure 6.4, for one value of W_∞ and two values of ΔT (for example, ΔT=5 K and ΔT=15 K) two values of x^*_{sep} were obtained. One Jakob number corresponds to each ΔT. Using the following equation:

$$x^*_{sep,1} Ja_1^{m_1} = x^*_{sep,2} Ja_2^{m_1} \qquad (6.6)$$

the value of m_1 was calculated. This exponent was used to collapse curves $\Delta T = 5$ K and $\Delta T = 15$ K at a specified W_-. The same procedure was repeated for other values of W_- within the range. Repeating the calculation for another pair of curves, values for two other exponents were obtained. For curves with $\Delta T = 5$ K and $\Delta T = 30$ K, the exponent was m_2, and for curves with $\Delta T = 15$ K and $\Delta T = 30$ K, the exponent was m_3. Taking the average of the three exponents, a final value of m was obtained. This exponent m corresponds to the fixed T_- and covers temperature differences from $\Delta T = 5$ K to $\Delta T = 30$ K. Since the three exponents m_1, m_2 and m_3 are not exactly the same, a plot of $x^*_{sep,1}Ja_1^m$, $x^*_{sep,2}Ja_2^m$, and $x^*_{sep,3}Ja_3^m$ does not give only one curve. Another approximation method involved taking an average of $x^*_{sep,1}Ja_1^m$, $x^*_{sep,2}Ja_2^m$, and $x^*_{sep,3}Ja_3^m$ and plotting the average as $x^*_{sep}Ja^m$ versus W_-. The collapsed curves for the three values of T_- are shown in Figure 6.12, while the values of the exponent m are shown in Figure 6.13. The error introduced by taking the averaged m was calculated for the points for which x^*_{sep} and ΔT were known. Calculation showed that the relative error for x^*_{sep} is less than 10% for the whole range of W_- and for all three values of T_- compared to x^*_{sep} obtained numerically. A comparison of the approximated x^*_{sep} and the numerically obtained x^*_{sep} is shown in Figure 6.14, and it includes all values of x^*_{sep} which were used in the second procedure for collapsing the data. The error may be higher if a separation distance is needed for a value of T_- which is located between the specified values, and an interpolation is required. In these calculations the specific heat used to calculate Jakob number was evaluated at the

wall temperature and the latent heat of vaporization was evaluated at the interface temperature.

6.2.2 Heat Transfer Results for Steam-Hydrogen Mixtures

The heat transfer results are presented in terms of $Nu_x / \mathrm{Re}_x^{1/2}$ versus x^*. Results plotted in this form are independent of u_∞ and θ. Unlike the separation results, the heat transfer results include the limiting cases of horizontal forced convection. In Figure 6.15, the values of $Nu_x / \mathrm{Re}_x^{1/2}$ are given for $T_\infty = 393.15$ K, $T_{wall} = 373.15$ K and for four different values of W_∞. In all four cases the curves approach the limiting case of the horizontal forced convection condensation at lower values of x^*. As x^* increases, the behavior of the curves becomes different for different values of W_∞. For $W_\infty = 0$ and higher values of x^*, the rate of heat transfer increases due to the gravity force which accelerates the film causing the film to become thinner compared to the case of horizontal forced convection condensation. As W_∞ increases, the rate of increase of $Nu_x / \mathrm{Re}_x^{1/2}$ with x^* becomes smaller. Furthermore, the inhibiting effect of hydrogen produces a small change in the rate of heat transfer for $W_\infty = 0.1$, which leads to an almost constant value of $Nu_x / \mathrm{Re}_x^{1/2}$. It can be seen that the value of $Nu_x / \mathrm{Re}_x^{1/2}$ for $W_\infty = 0.01$ reaches a maximum and starts to decrease in the vicinity of the separation point. For higher values of W_∞ this behavior is repeated, but it is not as pronounced as in the case for $W_\infty = 0.01$. This phenomenon is

typical for the condensation of a vapor in the presence of lighter gases and can be attributed to deceleration of the mixture boundary layer.

Figure 6.16 shows the effect of ΔT on Nu_x / $\mathrm{Re}_x^{1/2}$ at $T_\infty = 393.15$ K and $W_\infty = 0.01$. It can be observed that an increase in ΔT does not change the trend shown in Figure 6.15. The magnitude of Nu_x / $\mathrm{Re}_x^{1/2}$ decreases with increasing ΔT because the heat transfer coefficient was defined as $h_x = \dfrac{q_x}{T_\infty - T_{wall}}$ and the rate at which the heat flux increases is lower than the rate at which ΔT increases. Regardless of the lower values for Nu_x / $\mathrm{Re}_x^{1/2}$, the heat flux at the wall increases with increasing ΔT. Because different scales were used in Figures 6.15 and 6.16, the change in the slope of Nu_x / $\mathrm{Re}_x^{1/2}$ curves is more emphasized in the latter figure.

Figures 6.17 to 6.19 show the results for the dimensionless liquid film thickness, gas concentration at the interface, and the film Reynolds number, respectively. Figure 6.17 shows that the value of δ^* follows the expected trends: it decreases with increasing W_∞ because of a lower condensation rate, and it increases along the plate. Increasing of the liquid film thickness along the plate reduces the rate of heat transfer to the wall. From Figure 6.18, it can be seen that the interfacial gas concentration W_i changes very little along the plate for higher gas concentration, while for the small values of W_∞, the value of

W_i increases considerably with x^*. In each case, at low values of x^*,the value of W_i approaches a constant value corresponding to the limiting case of horizontal forced convection condensation.

The value of the film Reynolds number can be found in Figure 6.19. This value is important because it was used as the criterion for determining whether the flow is laminar or not. For $W_\infty = 0$ the film Reynolds number increases along the plate at the highest rate, while for $W_\infty = 0.1$ it remains approximately constant. The value of $Re_\delta\ Re_x^{-1/2}$ is lower for higher values of W_∞ because the condensation rate decreases as W_∞ increases.

6.3 Comparison of the Heat Transfer Rates for Steam-Air and Steam-Hydrogen

Comparison of the normalized heat flux at the wall for steam-hydrogen and steam-air mixtures is shown in Figure 6.20. The heat flux at the wall was normalized with the value of heat flux for the case of pure vapor condensation and results are reported for the cases of horizontal and vertical plates. Since the condensation on the horizontal plate is characterized by an absence of the buoyant force, the solution obeys similarity and the ratio $q\ /\ q_0$ is constant along the plate. In this case the difference in the rate of heat transfer between the two mixtures is due to the different properties of gases and the

difference in the binary diffusion coefficients. The comparison was made for T_∞ =373.15 K, T_{wall} = 363.15 K, W_∞ = 0.03, and u_∞ = 0.3 m/s. Because of the difference in the molecular weight between air and hydrogen, the total pressure was different between the two mixtures. The value of q / q_0 for the steam-air mixture is always greater than q / q_0 for the steam-hydrogen mixture. The greater reduction in heat transfer for steam-hydrogen mixtures has already been explained (Siddique et al., 1989) by the fact that, for the same mass fraction, hydrogen has greater number of moles in the mixture than air.

For the vertical plate case, a decrease of q / q_0 along the plate is seen for both mixtures. The ratio between two results, however, is not constant. At the beginning of the plate the ratio is approximately the same as it was for the horizontal case, but at the end it increases to 3.4. This large ratio does not mean that the buoyant force alone reduced the rate of heat transfer almost twice; it is also the result of the decreasing magnitude of q / q_0 along the plate. Therefore, it is not possible to completely isolate and to demonstrate the effect of the buoyant force only on the reduction of heat transfer. In order to show more information on the behavior, the first derivative of q with respect to x was calculated and plotted in Figure 6.21. The purpose of this graph is to show the rate of change of q along x instead of the value itself. In addition, the rate of change of q for pure steam was plotted in order to compare with those obtained for steam-air and steam-hydrogen mixtures. Figure 6.21 shows that for x < 0.018 m, $\frac{dq}{dx}$ for steam-hydrogen decreases

faster in magnitude than $\frac{dq}{dx}$ for steam-air. At approximately x = 0.02 m, the value of $\frac{dq}{dx}$ for steam-hydrogen starts to increase in magnitude due the buoyancy force, while for steam-air it keeps decreasing toward zero. This means that the value of q for steam-air is approaching an asymptotic value. For steam-hydrogen, however, q in the vicinity of the separation point continues to decrease because the effect of flow deceleration is most pronounced near the separation point. A careful examination of the q / q_0 curve for steam-hydrogen shows this change in the trend for x between 0.02 and 0.023 m. Also, it seems that this drop in the rate of heat transfer due to the buoyant force is relatively small compared to the reduction caused by different properties of mixtures seen in the horizontal plate case. Results obtained for other two free stream temperatures T_∞ = 348.55 K and T_∞ = 393.15 K showed similar trends. For T_∞ = 348.55 K, q / q_0 for the steam-air mixture is 1.56 times greater than steam-hydrogen, while for T_∞ = 393.15 K, this ratio is 1.47. An additional increase of T_∞ caused a small reduction in the value of q / q_0 for the two mixtures.

6.4 Freon12-Air Mixtures

Presentation of the results for Freon12-air mixtures follows the procedure seen with steam-hydrogen mixtures. The first group of results correlate the separation length to the input parameters, and the second group gives heat transfer results for a particular set of input parameters. Generally, the results obtained for Freon12-air mixtures follow the

trends obtained for steam-hydrogen mixtures. Therefore, the results will not be described in as much detail as was done with the previous mixture.

6.4.1 Separation Results for Freon12-Air Mixtures

Results were obtained for three free stream temperatures: $T_\infty = 288.15$ K, $T_\infty = 315.15$ K, and $T_\infty = 333.15$ K. These values correspond to saturation pressures (with zero gas concentration) of 0.5 bar, 1 bar, and 2 bars, respectively. At each free stream temperature, three values of ΔT were used: $\Delta T = 5$K, $\Delta T = 15$ K, and $\Delta T = 30$K. In each case, the free stream gas concentration was varied from 10^{-5} to 0.6.

The procedure used to produce results related to the location of the mixture boundary layer separation was exactly the same as that used for the steam-hydrogen mixtures. The collapsing method used to eliminate the effects of the plate inclination and free stream velocity (described in Section 6.1) was also applied to the Freon12-air mixtures. The limitations on u_∞ and θ applied in the analysis of steam-hydrogen were the same for the analysis of Freon12 - air mixtures.

The dimensionless separation length versus W_∞ is shown in Figures 6.22 to 6.24. Curves in each of the figures correspond to one free stream temperature. Examination of those diagrams shows that all curves exhibit the same trend within the range of W_∞ tested. In other words, as W_∞ increases x^*_{sep} decreases until a minimum value is reached, after which

x^*_{sep} gradually increases. This trend is the same as that seen for steam-hydrogen. The rate at which x^*_{sep} changes depends on ΔT and W_-.

To confirm further that the same physical processes occurred in this case as in the steam-hydrogen case, all four terms in the Equation (6.5) were plotted as before and presented in Figures 6.25 to 6.28. For the first three terms: $\rho_i u_i \left(\frac{\partial u}{\partial y}\right)_i$, $\rho_i v_i \left(\frac{\partial u}{\partial y}\right)_i$, and $g(\rho_i - \rho_-)$, there is no change in the trend compared to steam-hydrogen. However, the magnitudes and the rates of change are different. Figure 6.28 shows that the value of $\mu_i \left(\frac{\partial^2 u}{\partial y^2}\right)_i$ at the separation location increases as W_- increases up to a maximum and then decreases with further increase in W_-.

A plot of x^*_{sep}, $\mu_i \left(\frac{\partial^2 u}{\partial y^2}\right)_i$ and $(\rho_i - \rho_-)$ versus W_- for a Freon12-air mixture is shown in Figure 6.29. It is evident that the trend of $\mu_i \left(\frac{\partial^2 u}{\partial y^2}\right)_i$ (which represents the effective adverse pressure gradient) is a good indicator of the change in x^*_{sep} because an increase in the effective pressure gradient decreases x^*_{sep} and vice versa. One reason for such a trend lies in the small magnitude of the first inertia term when compared to the second inertia term. This is not always the case, as will be seen later in the results for a mercury-air

mixture. For higher values of W_-, the buoyant force term becomes dominant and $\mu_i\left(\frac{\partial^2 u}{\partial y^2}\right)_i$ follows the change of that term.

Figure 6.30 was obtained following the second data collapsing procedure, described earlier. It gives the variation of $x^*_{sep}Ja^m$ versus W_- for three values of T_-. Again, the value of the exponent m is plotted on a separate figure (Figure 6.31). A detailed examination of Figure 6.30 shows that the curves of $x^*_{sep}Ja^m$ have a maximum and a minimum. The changes of the sign of the slope are the result of the chosen value of the exponent m and the change of x^*_{sep}. The value of m, shown in Figure 6.31, is higher for W_- less than 0.01. Between $W_- = 0.01$ and 0.03, m reaches a minimum, then gradually increases, which corresponds to the minimum x^*_{sep}, and finally decreases as x^*_{sep} increases.

Figures 6.30 and 6.31 show overlapping of $x^*_{sep}Ja^m$ and m curves. This is the result of minimizing the error during the second data collapsing procedure. The main objective in the procedure was to reach the smallest relative error between x^*_{sep} obtained using diagrams 6.30 and 6.31 and the numerically calculated value. The relative error was less than 5% for $W_- < 0.1$ and less than 10% for $W_- < 0.6$. This means that for any of the defined T_- in Figures 6.30 and 6.31 the approximate x^*_{sep} is not more than 10% from x^*_{sep} obtained using the computer program. Figure 6.32 is a comparison of the numerical and approximate values of For all values of x^*_{sep} for all values of T_- and ΔT used. The good

agreement between the approximate and computer code predicted values of x^*_{sep} is evident in Figure 6.32.

6.4.2 Heat Transfer Results for Freon12-Air Mixtures

Heat transfer results are again presented as a plot of $Nu_x/\mathrm{Re}_x^{1/2}$ versus x^*. In Figure 6.33 values of $Nu_x/\mathrm{Re}_x^{1/2}$ are plotted for $T_\infty = 315.15$ K and $\Delta T = 30$ K, for four values of W_∞. All four curves approach a constant value at small x^*, which represents the limiting case of forced convection condensation on a horizontal plate. The value of $Nu_x/\mathrm{Re}_x^{1/2}$ increases along the plate with a rate which is a maximum for $W_\infty = 0$. At $W_\infty = 0.1$, the value of $Nu_x/\mathrm{Re}_x^{1/2}$ has the maximum value at $x^* \approx 1.5$. For lower values of W_∞, the curves of $Nu_x/\mathrm{Re}_x^{1/2}$ keep increasing along the plate until the separation occurs (no a maximum value was detected).

Figure 6.34 shows the effect of ΔT on $Nu_x/\mathrm{Re}_x^{1/2}$ at $T_\infty = 315.15$ K and $W_\infty = 0.01$. The values of ΔT that were used are 5 K, 15 K, and 30 K. Again, the value of $Nu_x/\mathrm{Re}_x^{1/2}$ decreases as ΔT increases because ΔT increases at a greater rate than the heat flux at the wall. However, the heat flux increases as ΔT increases.

Plots of δ^* versus x^* are shown in Figure 6.35. All curves show an increase in the film thickness along the plate. Differences in δ^* are almost negligible for $W_- < 0.01$, except near the separation location. At $W_- = 0.1$, the film is thinner but with almost the same rate of increase with x^* as for $W_- < 0.01$.

Figures 6.36 and 6.37 are plots of the gas concentration at the interface along the plate. In Figure 6.36 the effect of different W_- on W_i can be seen. It is interesting to observe that W_i is constant at small values of x^*, which again corresponds to the limiting case of forced convection condensation on a horizontal plate, and then increases along the plate at a rate which is higher for lower W_-. Figure 6.37 shows the effect of ΔT on W_i while T_- and W_- are constant. An increase in ΔT causes an increase in W_i which is independent of x^* for the horizontal force convection limit. At higher values of x^*, W_i increases above the forced convection value with similar behavior seen in all three cases.

The liquid film Reynolds number normalized with the local Reynolds number is plotted in Figure 6.38 versus x^* for four values of W_- between 0 and 0.1. Again the $W_- = 0$ was included in order to provide a datum. The diagram shows that the value of $\mathrm{Re}_\delta/\mathrm{Re}_x^{1/2}$ changes more rapidly for smaller W_-. At the limiting case of the forced-convection

condensation on a horizontal plate, the value of $Re_\delta/Re_x^{1/2}$ becomes constant with respect to x^*.

6.5 Mercury-Air Mixtures

Following the calculation procedure applied in the previous two sections, results obtained for mercury-air mixtures are presented in this section. As earlier, the first group of results shows the dimensionless separation length, and the second gives the heat transfer and some related results for a particular set of input parameters. Typical velocity, gas concentration and temperature profiles along the plate and at the separation location are also given. The profiles shown are typical of the results for all three vapor-gas combinations.

6.5.1 Separation Results for Mercury-Air Mixtures

Results were obtained for three free stream temperatures: $T_\infty = 666.67$ K, $T_\infty = 750$ K and $T_\infty = 880$ K. Those temperatures correspond to a total system pressure (with zero gas concentration) of 2 bar, 6 bar and 25 bar. The free stream gas concentration was varied from 10^{-5} to 0.4. A narrower range of W_∞ was used in this case because of the significant CPU time that was required for calculations with higher gas concentrations and because the selected range covers the main features of the curves. Following the same procedure

described for steam-hydrogen, curves of x^*_{sep} versus W_∞ were plotted. For three free stream temperatures, the results are shown in Figures 6.39 to 6.41. From those figures it can be seen that all the curves exhibit the same trends. Unlike the previously described trends, in this case increasing W_∞ at low values (up to approximately 10^{-3}) increases x^*_{sep} until it reaches a maximum value, after which x^*_{sep} gradually decreases to a minimum. At higher values of W_∞ (above 0.2), the value of x^*_{sep} increases again.

In all the mercury-air cases studied, as W_∞ approaches zero, x^*_{sep} reaches a maximum and then rapidly decreases. The value of W_∞ for which the curves have a maximum generally decreases as T_∞ and ΔT decrease. For example, at $T_\infty = 666.67$ K and $\Delta T = 5.55$ K, x^*_{sep} has a maximum at $W_\infty = 5 \times 10^{-4}$, while at $T_\infty = 880$ K and $\Delta T = 30$ K x^*_{sep} has a maximum at $W_\infty = 2.5 \times 10^{-3}$.

In order to make sure that physically unreasonable phenomena did not occur, an examination of some important parameters at the liquid-mixture interface was made over a large number of cases. Figures 6.42 to 6.47 show the change of δ, u_i, $\dot{m}^*_i$, W_i, T_i and q / q_{Nu} for $T_\infty = 666.67$ K, $T_{wall} = 661.11$ K, and $u_\infty = 0.03$ m/s. The values of all the parameters were plotted versus the distance along the plate, and each curve shows the real (dimensional) separation distance. The value of W_∞ was varied from 6×10^{-5} up to 5×10^{-3}. At $W_\infty = 5 \times 10^{-4}$, the separation distance has a maximum value. Values of

$W_\infty = 9.64 \times 10^{-5}$ and $W_\infty = 1.455 \times 10^{-3}$ were chosen because they gave the same separation location on the plate. When observed separately, all the parameters change monotonically with W_∞. Furthermore, each change has an expected and reasonable trend.

Figure 6.42 shows the change of the liquid film thickness along the plate. Increasing the free stream gas concentration reduced the condensation rate, and the liquid film thickness decreased, which is an expected trend. The change of the interface velocity along the plate is shown in Figure 6.43. It can be observed that as W_∞ increases, u_i decreases. During that monotonic decrease in u_i, however, the separation distance first increases, and then decreases. The change of the mass flux, $\dot{m}_i^{"}$ at the interface is shown in Figure 6.44. The graph shows a decrease of $\dot{m}_i^{"}$ with an increase of W_∞ as expected. Figures 6.45 and 6.46 show the change of interface gas concentration and temperature, respectively. Both plots show that W_i and T_i changes are monotonic and that there are no unexpected behaviors. Finally, Figure 6.47 shows the change along the plate of the normalized heat flux at the wall. The heat flux decreases both with increased W_∞ and along the plate. Those two trends are typical for condensation in the presence of a noncondensable gas. Therefore, the results shown in Figures 6.42 to 6.47 indicate that there are no physically unreasonable phenomena that occur when W_∞ is changed that could correspond to a maximum in x_{sep}^*. These trends provide no explanation for the exhibited change in x_{sep}^*. In addition, it should be emphasized that further checks were

performed to confirm that the momentum balance within the mixture boundary layer was satisfied for any control volume as well as for a set of control volumes at any station.

An explanation for the existence of the maximum x^*_{sep} can be obtained by calculating the four terms in Equation (6.5) and plotting them versus distance along the plate. That was done for T_∞ = 880 K, T_{wall} = 850 K, u_∞ = 0.03 m/s, and $\theta = 0$. The gas concentration was varied from 0.001 to 0.4.

Figure 6.48 shows the variation of $\rho_i u_i \left(\frac{\partial u}{\partial x}\right)_i$ (term 1 in Equation(6.5)) with x. The rate at which this term increases as W_∞ decreases is significant. For a change in W_∞ from 0.1 to 0.4, this term changes from 1.05 to 0.15, while for W_∞ between 0 and 0.001 it changes from 300 to 30. This rate of change at very low values of W_∞ appears to be only a characteristic of a mercury-air mixture because the values seen for the other mixtures studied are much lower.

Figure 6.49 shows the variation of $\rho_i v_i \left(\frac{\partial u}{\partial y}\right)_i$ (term 2 in Equation (6.5)) with x. The vertical scale was adjusted again so that only the region around zero was shown. The

value of $\rho_i v_i \left(\frac{\partial u}{\partial y}\right)_i$ changes in the same way as it did for steam-hydrogen and Freon12-air. In other words, as the gas concentration increases, the magnitude of this term decreases.

The behavior of term 3 in Equation (6.5) is shown in Figure 6.50. The characteristic behavior which was not seen before is the high rate at which this term increases in magnitude as W_- first increases from zero. This means that adding a small gas concentration, for example $W_- = 0.001$, decreases the mixture density at the interface such that the buoyant force at the interface reaches a magnitude which changes only a few percent if gas concentration further increases to 0.1. Other than the high rate of change of this term, Figure 6.50 exhibits the same increase in magnitude and subsequent decreases as seen for the other mixtures studied.

Figure 6.51 shows the change along x of $\mu_i \left(\frac{\partial^2 u}{\partial y^2}\right)_i$ (term 4 in Equation (6.5)) calculated using the finite difference approximation. For a mercury-air mixture, increasing W_- from 10^{-5} to 0.002 results in a decrease of the second derivative at the interface. This means that regardless of the higher condensation rate or the larger suction velocity, the influence of the $\rho_i u_i \left(\frac{\partial u}{\partial x}\right)_i$ term is significant. More precisely, as W_- approaches zero, the first inertia term (term 1) grows at the rate which is large enough to reduce the influence of the $\rho_i v_i \left(\frac{\partial u}{\partial y}\right)_i$ term. This behavior causes the effective adverse pressure gradient to increase

at the separation locations. This trend is fundamentally different from the trends observed with the two other vapor-gas combinations.

In order to relate the change in x^*_{sep} to the changes in $\mu_i\left(\frac{\partial^2 u}{\partial y^2}\right)_i$ and $(\rho_\infty - \rho_i)$, Figure 6.52 was plotted. From the figure we can see that x^*_{sep} increases as W_- increases from 10^{-5} to 0.002 (region 1 in the figure). At the same time $\mu_i\left(\frac{\partial^2 u}{\partial y^2}\right)_i$ decreases and $(\rho_\infty - \rho_i)$ increases. Overall, the effective adverse pressure gradient at the separation location was defined by the sum of term 1 and term 3. Within region 1 the buoyant term (term 3) increases (which increases the effective pressure gradient), but the rate at which this term increases is lower than the rate at which the first inertia term decreases. Because of the trend in these two terms, the value of $\mu_i\left(\frac{\partial^2 u}{\partial y^2}\right)_i$ decreases in region 1. Further, from Figure 6.49 it can be seen that curves of $\rho_i v_i\left(\frac{\partial u}{\partial y}\right)_i$ for $W_- = 0$ and $W_- = 0.001$ have approximately the same slope, which suggests that the decrease in this term (term 2) was not significant between these two cases of different gas concentrations. Because of the small changes in the value of $\rho_i v_i\left(\frac{\partial u}{\partial y}\right)_i$ and because of the decrease in the combined sum of terms 1 and 3, the value of the separation length increases within region 1.

The interval of W_- between 0.002 and 0.2 (denoted as region 2 in the figure) shows a very gradual decrease of $\mu_i\left(\frac{\partial^2 u}{\partial y^2}\right)_i$, while at the same time the value of x^*_{sep} decreases considerably. This may be explained by the change of $\rho_i v_i\left(\frac{\partial u}{\partial y}\right)_i$ for different values of W_- in this region. Figure 6.49 shows that the magnitude of this term decreases more rapidly as W_- increases. Since the rate of change of the two other terms (1 and 3) causes a very small change in the value of $\mu_i\left(\frac{\partial^2 u}{\partial y^2}\right)_i$, the decrease in x^*_{sep} was primarily caused by a decrease in $\rho_i v_i\left(\frac{\partial u}{\partial y}\right)_i$ as W_- increases. In other words, reducing suction velocity increases the curvature of the velocity profile along the plate. The variations of parameters in this region indicates that the value of $\mu_i\left(\frac{\partial^2 u}{\partial y^2}\right)_i$ at the separation location cannot be directly correlated to the x^*_{sep} because of the effect of term 2.

The change of all parameters in region 3 has the same form as those seen with the other two mixtures at high gas concentration.

Results of the second data collapsing procedure are shown in Figures 6.53 and 6.54. The first figure shows the values of $x^*_{sep}Ja^m$ plotted versus W_-. Using these results along with the exponent m plotted in Figure 6.54, it is possible to estimate the separation distance for

given ranges of T_∞, ΔT and W_∞. Restrictions on θ and u_∞ defined in Section 6.2 are also applicable in this case. The error introduced by taking the averaged m and $x^*_{sep}Ja^m$ is less than 6% for the whole range of W_∞ and for all three values of T_∞ compared to the x^*_{sep} obtained numerically. A comparison of approximated x^*_{sep} and numerically obtained x^*_{sep} is plotted in Figure 6.55 for all values of x^*_{sep} which were used in the procedure for collapsing the data. Again, the specific heat used to calculate Jakob number was evaluated at the reference temperature (Equation 6.3), and the latent heat of vaporization was evaluated at the interface temperature.

6.5.2 Velocity, Temperature and Gas Concentration Profiles

Figures 6.56 to 6.58 show typical profiles for u, T and W across the mixture boundary layer. The numbered curves show the profiles at particular locations along the plate. The profiles for T and W are typical for a vapor-noncondensable gas mixture boundary layer, while velocity profiles are characteristic of a vapor-lighter gas mixture boundary layer. Figure 6.56 shows that as the distance along the plate increases, the velocity gradient at the interface decreases until it becomes equal to zero at the separation location. Since the velocity gradient is also zero at the free stream, an inflection point exists between the interface and free stream. This kind of profile (profile 4 in Figure 6.56) is the characteristic profile for a boundary layer flow with an adverse pressure gradient (Chang,

1970). The values of T and W at the interface show very little change along x in the cases plotted. In this respect they are not typical of the other mixtures (for example, Figure 6.18 and 6.36).

6.5.3 Heat Transfer Results for Mercury-Air Mixtures

The variation of $Nu_x / \mathrm{Re}_x^{1/2}$ versus x^* is plotted in Figure 6.59. The results are presented for $T_\infty = 666.67$ K, $T_{wall} = 636.67$ K and four different values of W_∞. In all four cases the curves approach the limiting case of horizontal forced convection condensation at low values of x^*. For $W_\infty = 0$, the rate of heat transfer increases as x^* increases, as reflected by the magnitude of $Nu_x / \mathrm{Re}_x^{1/2}$. For higher values of W_∞, the curve of $Nu_x / \mathrm{Re}_x^{1/2}$ remains fairly flat at the limiting value for horizontal forced convection condensation. In the vicinity of the separation point, the value of $Nu_x / \mathrm{Re}_x^{1/2}$ starts to decrease for $W_\infty \geq 0.01$, actually dropping the value of $Nu_x / \mathrm{Re}_x^{1/2}$ below the limiting case of horizontal forced convection condensation. Generally, the small change of $Nu_x / \mathrm{Re}_x^{1/2}$ along the plate is characteristic of liquid metals only, while the decrease in the vicinity of the separation point for higher values of W_∞ is the result of the adverse pressure gradient.

Figure 6.60 shows the effect of ΔT on Nu_x / $Re_x^{1/2}$ at $T_\infty = 666.67$ K and $W_\infty = 0.01$. It can be observed that the increase of ΔT does not change the trend shown in Figure 6.59. The magnitude of Nu_x / $Re_x^{1/2}$ decreases with increasing of ΔT due to same reasons described regarding condensation of steam-hydrogen.

Figures 6.61 to 6.63 show the changes with x^* of the dimensionless liquid film thickness, the gas concentration at the interface, and Re_δ / $Re_x^{1/2}$. All parameters follow the expected trends. A comparison with similar results obtained for the other two mixtures shows that the change in δ^* with W_∞ is much more pronounced for mercury-air. Also, the gas concentration at the interface (Figure 6.62) and Re_δ / $Re_x^{1/2}$ (Figure 6.63) for mercury-air are nearly unchanged with x^* unlike the behavior of the other two mixtures where the changes of these two parameters were considerable along x^*.

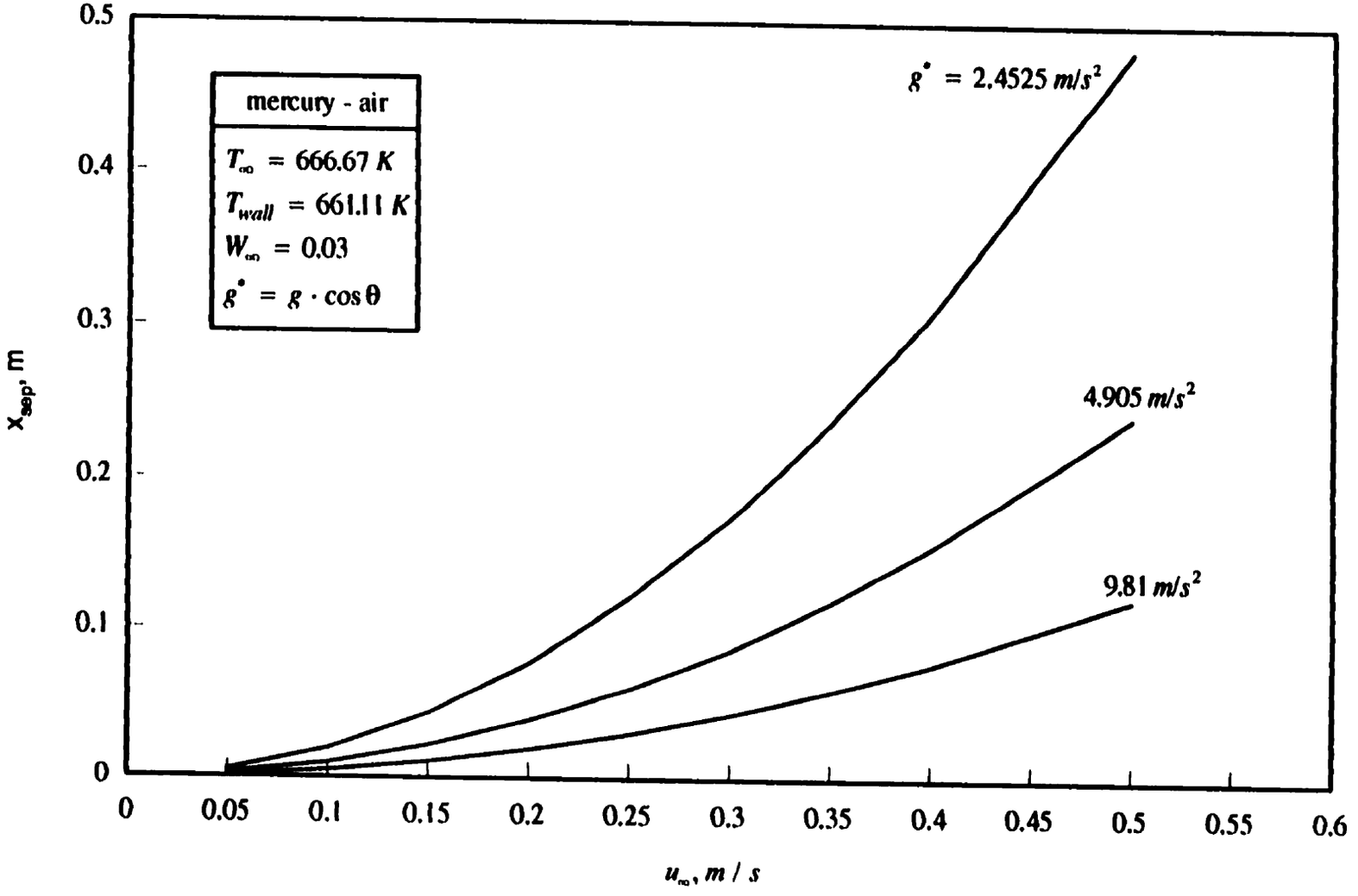

Figure 6.1: Effect of θ and u_∞ on x_{sep} for a mercury - air mixture at T_∞ = 666.67 K

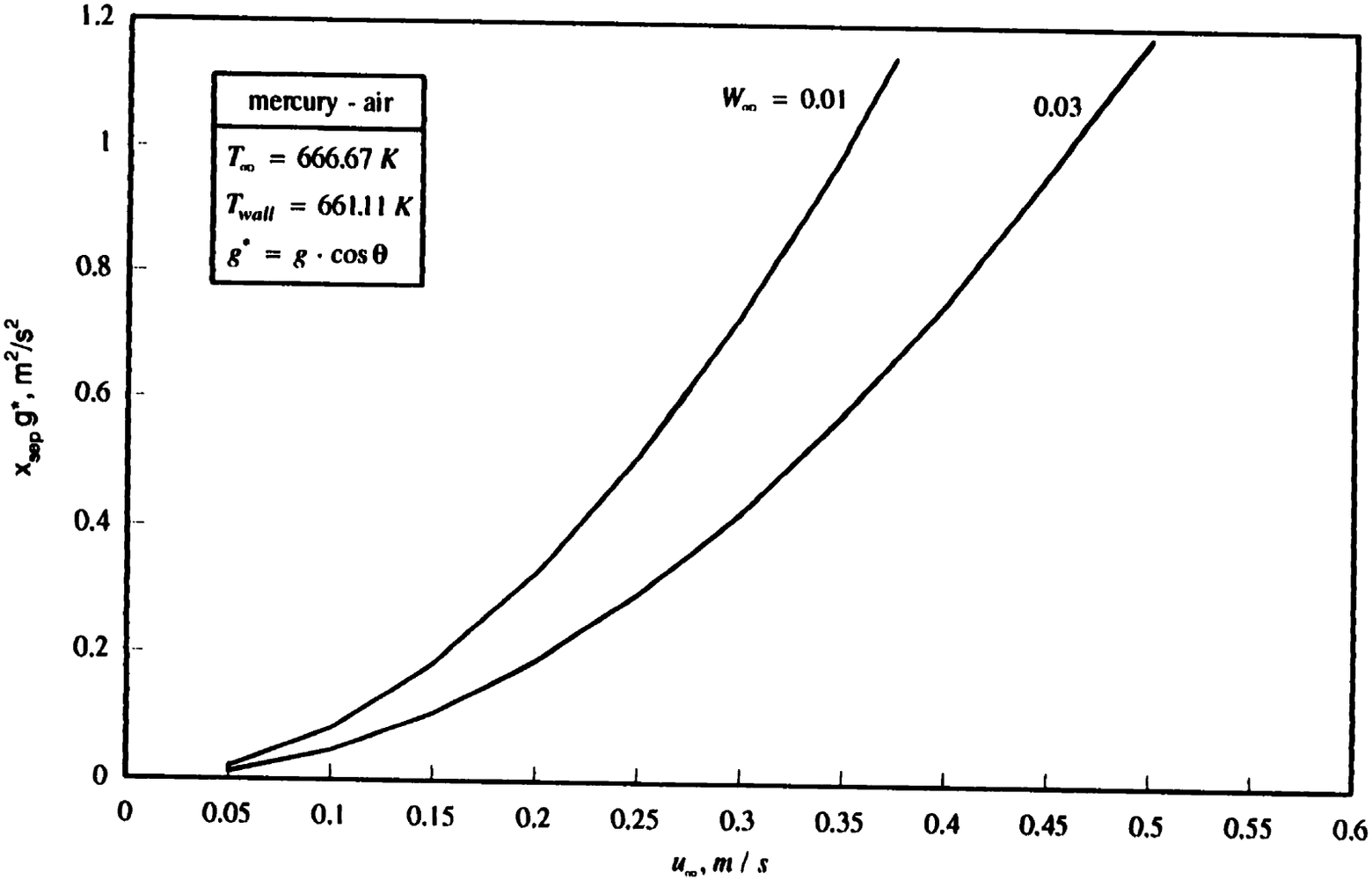

Figure 6.2: Effect of W_∞ and u_∞ on $x_{sep}g^*$ for a mercury - air mixture at T_∞ = 666.67 K

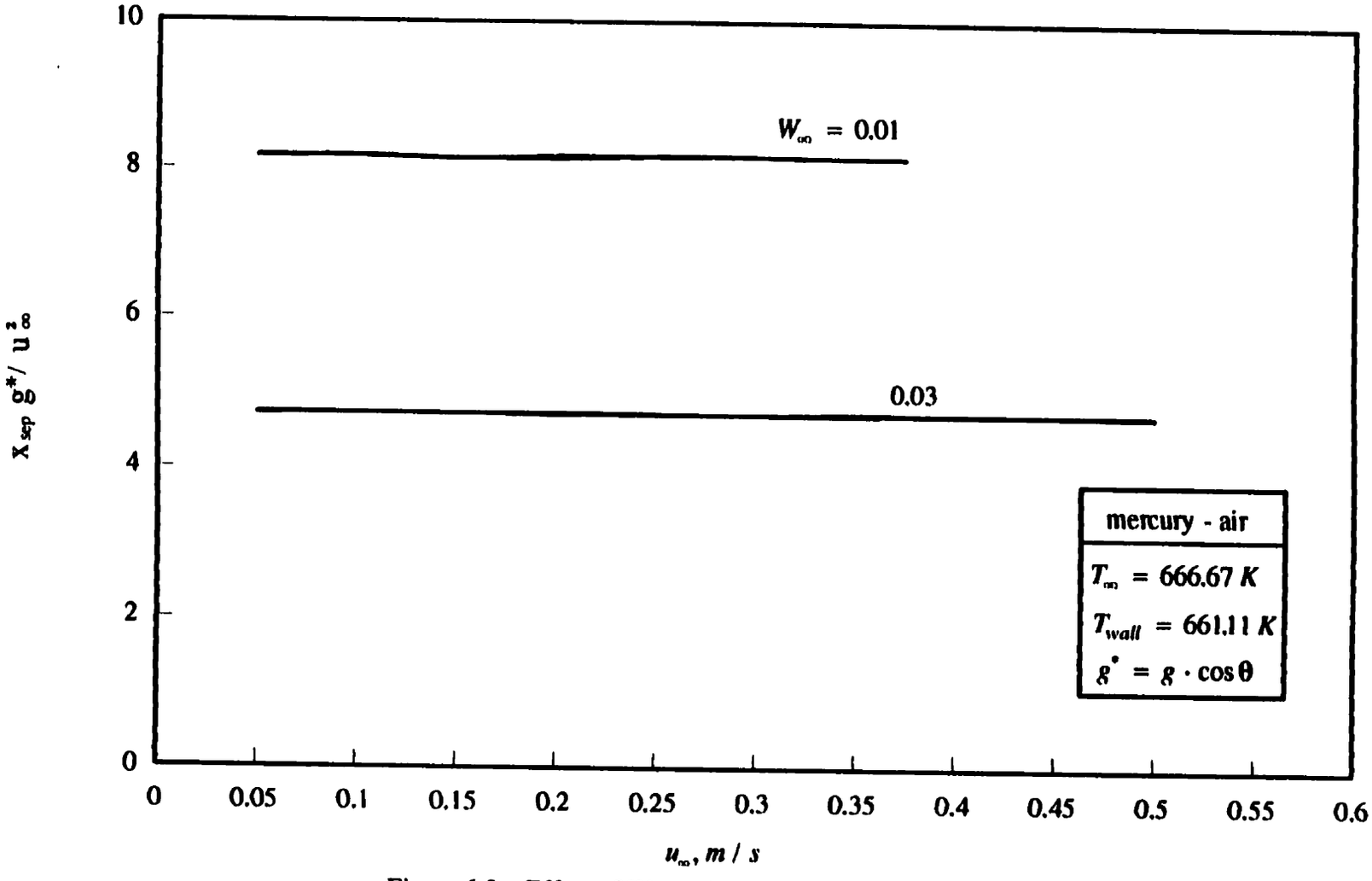

Figure 6.3: Effect of W_{∞} and u_{∞} on the dimensionless separation length for a mercury - air mixture at T_{∞} = 666.67 K

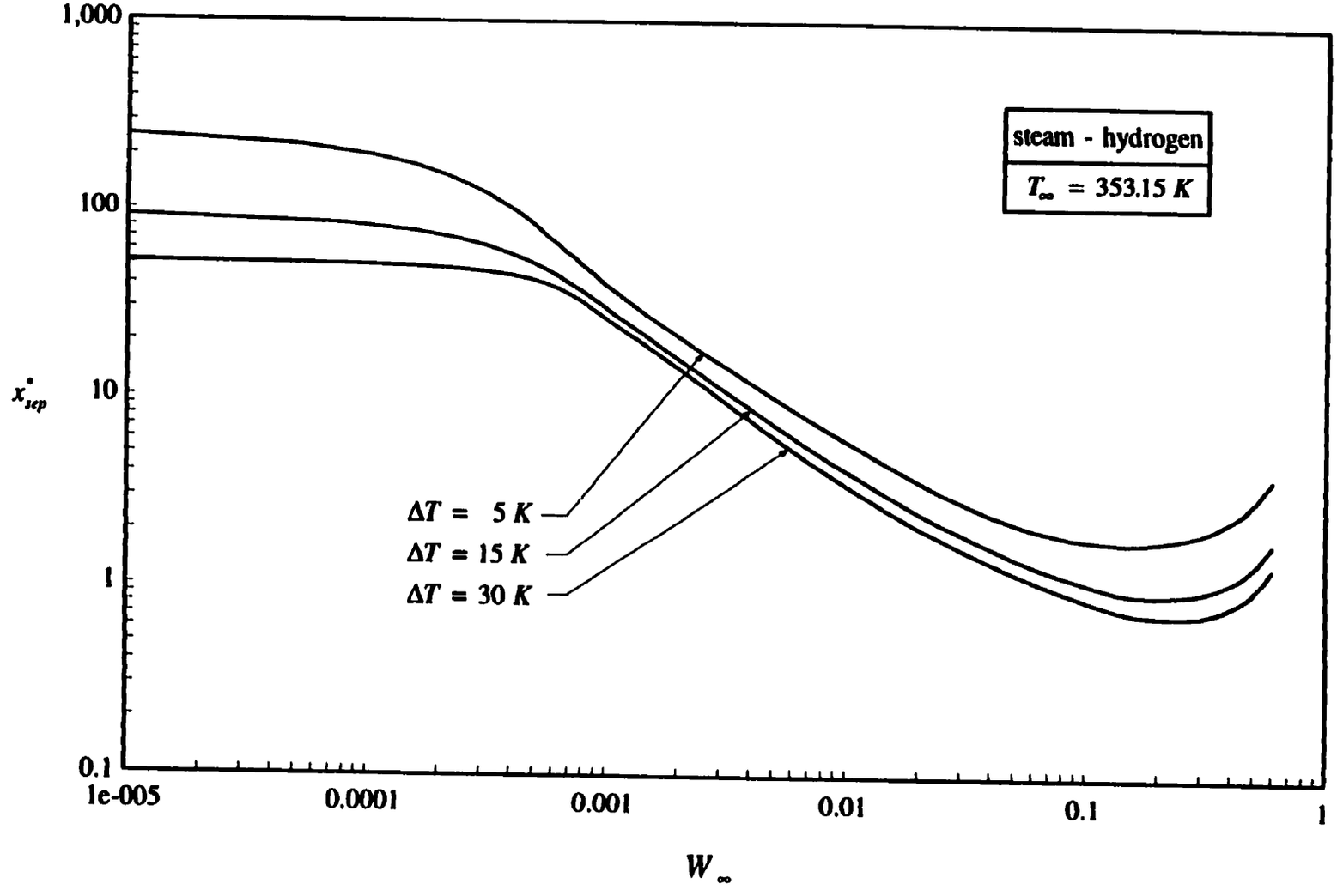

Figure 6.4: Dimensionless separation length for a steam - hydrogen mixture, T_∞ = 353.15 K

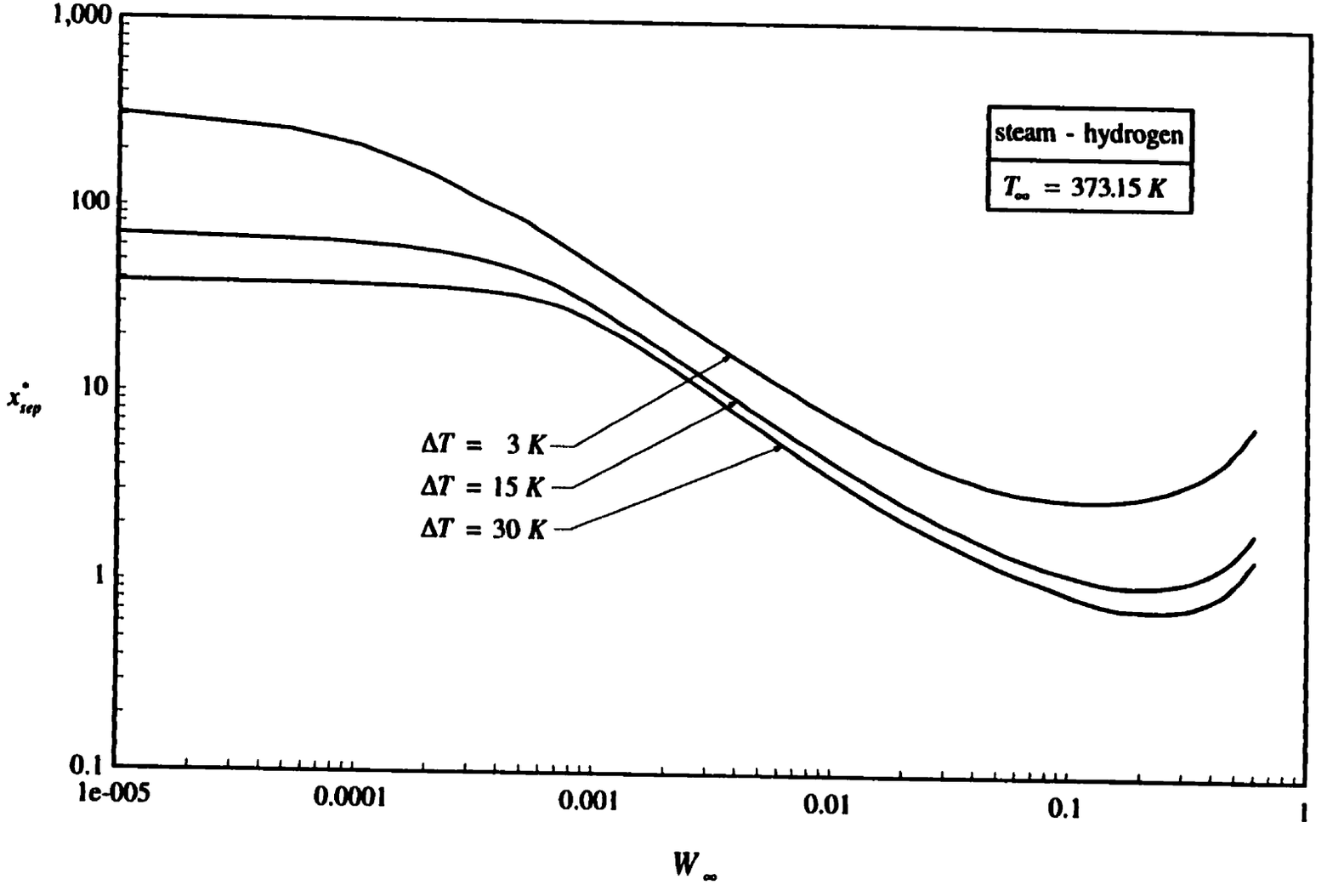

Figure 6.5: Dimensionless separation length for a steam - hydrogen mixture, T_∞ = 373.15 K

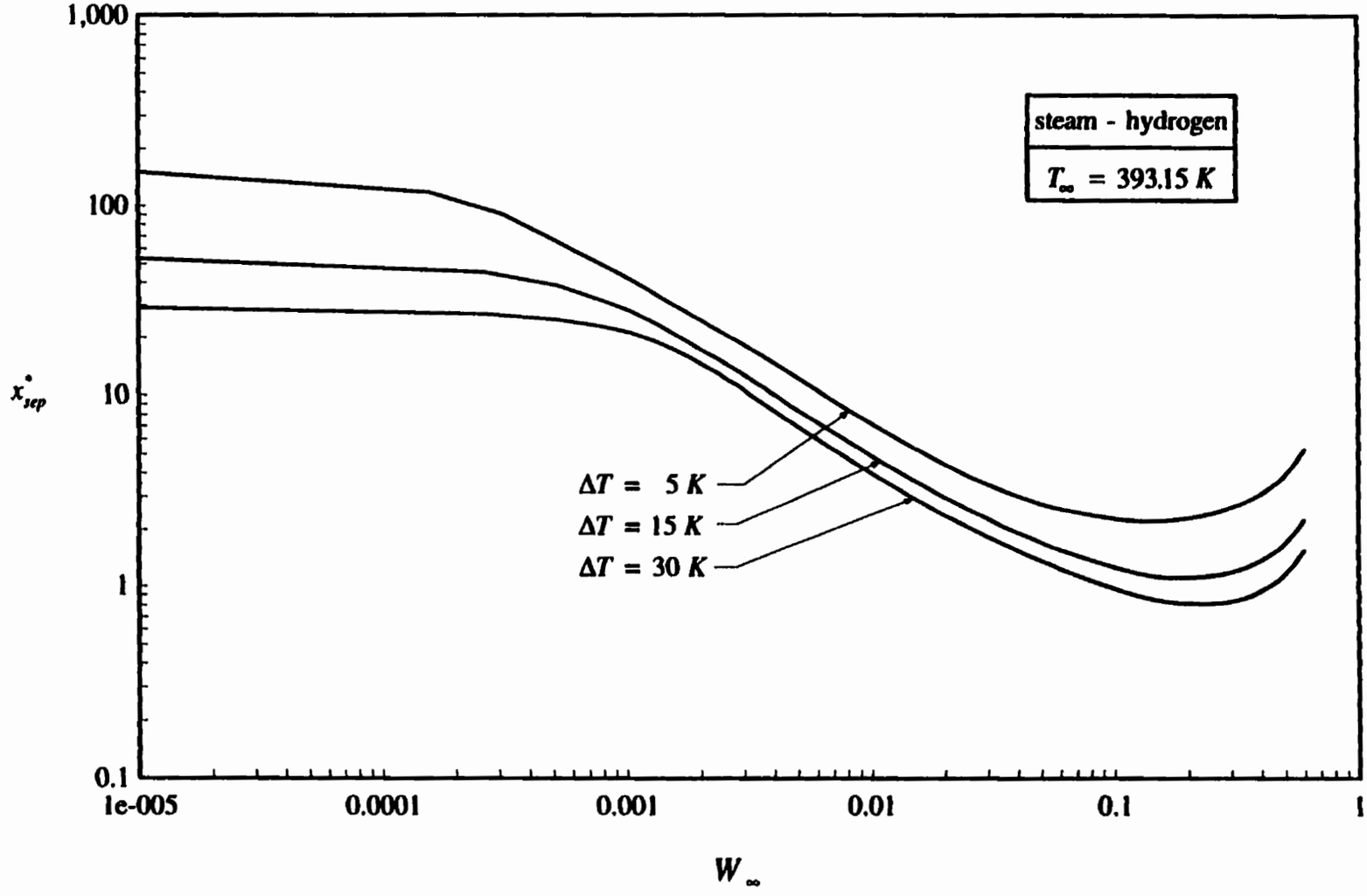

Figure 6.6: Dimensionless separation length for a steam - hydrogen mixture, T_∞ = 393.15 K

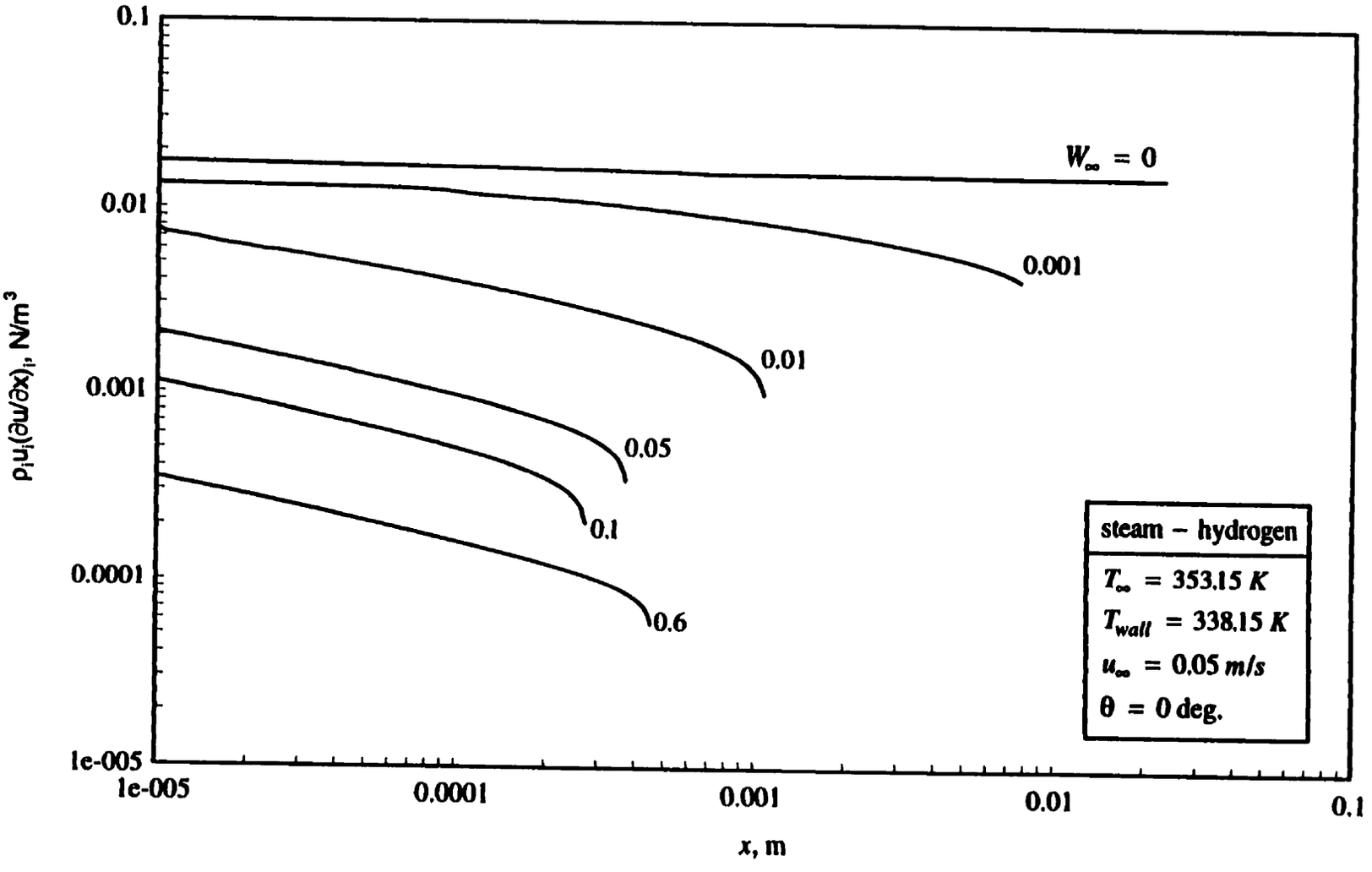

Figure 6.7: Variation of $\rho_i u_i \left(\frac{\partial u}{\partial x}\right)_i$ along the vertical plate for different values of W_∞ for a steam - hydrogen mixture at T_∞ = 353.15 K, ΔT = 15 K and u_∞ = 0.05 m/s

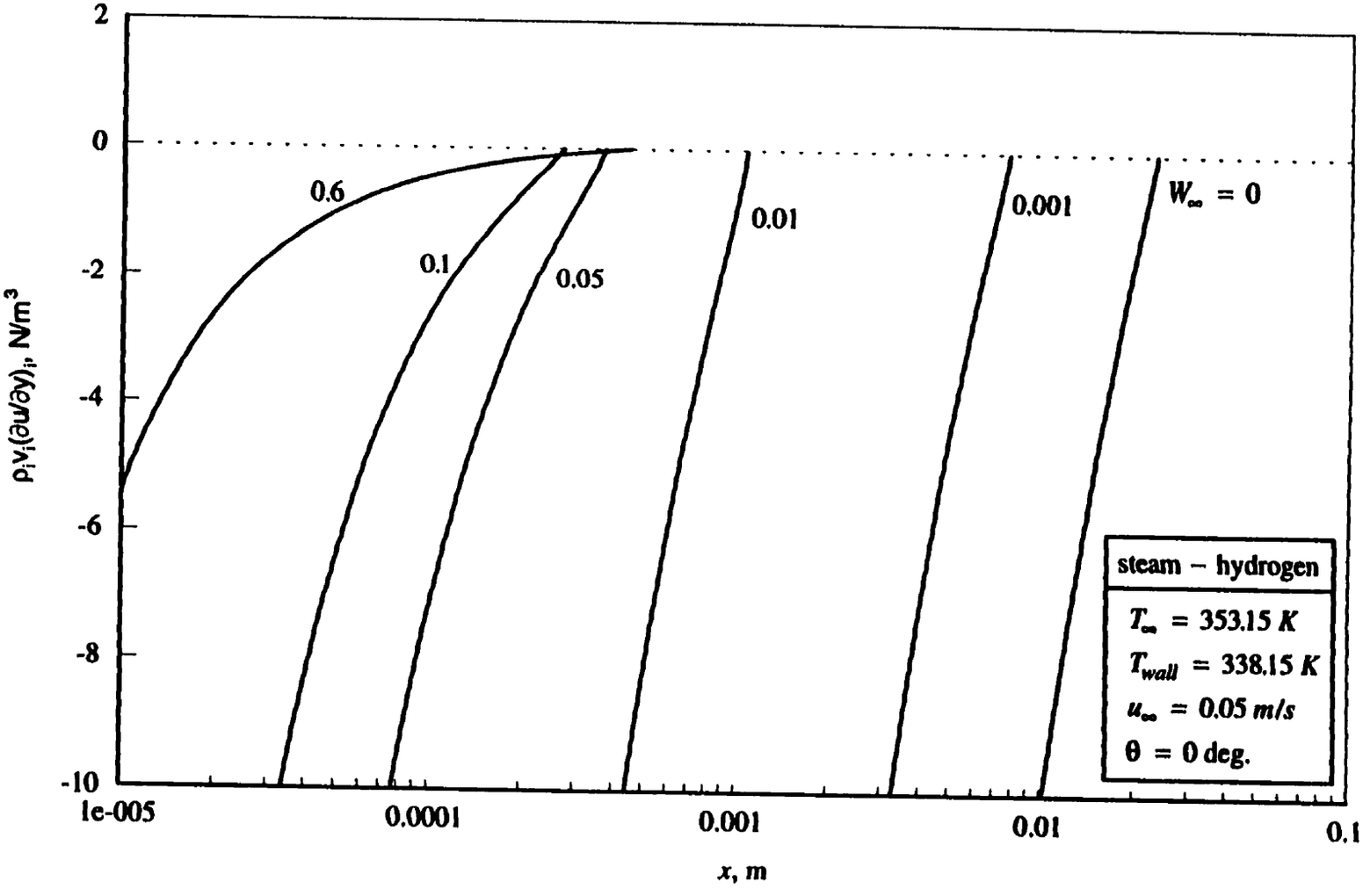

Figure 6.8: Variation of $\rho_i v_i \left(\frac{\partial u}{\partial y}\right)_i$ along the vertical plate for different values of W_∞ for a steam - hydrogen mixture at $T_\infty = 353.15\ K$, $\Delta T = 15\ K$ and $u_\infty = 0.05\ m/s$

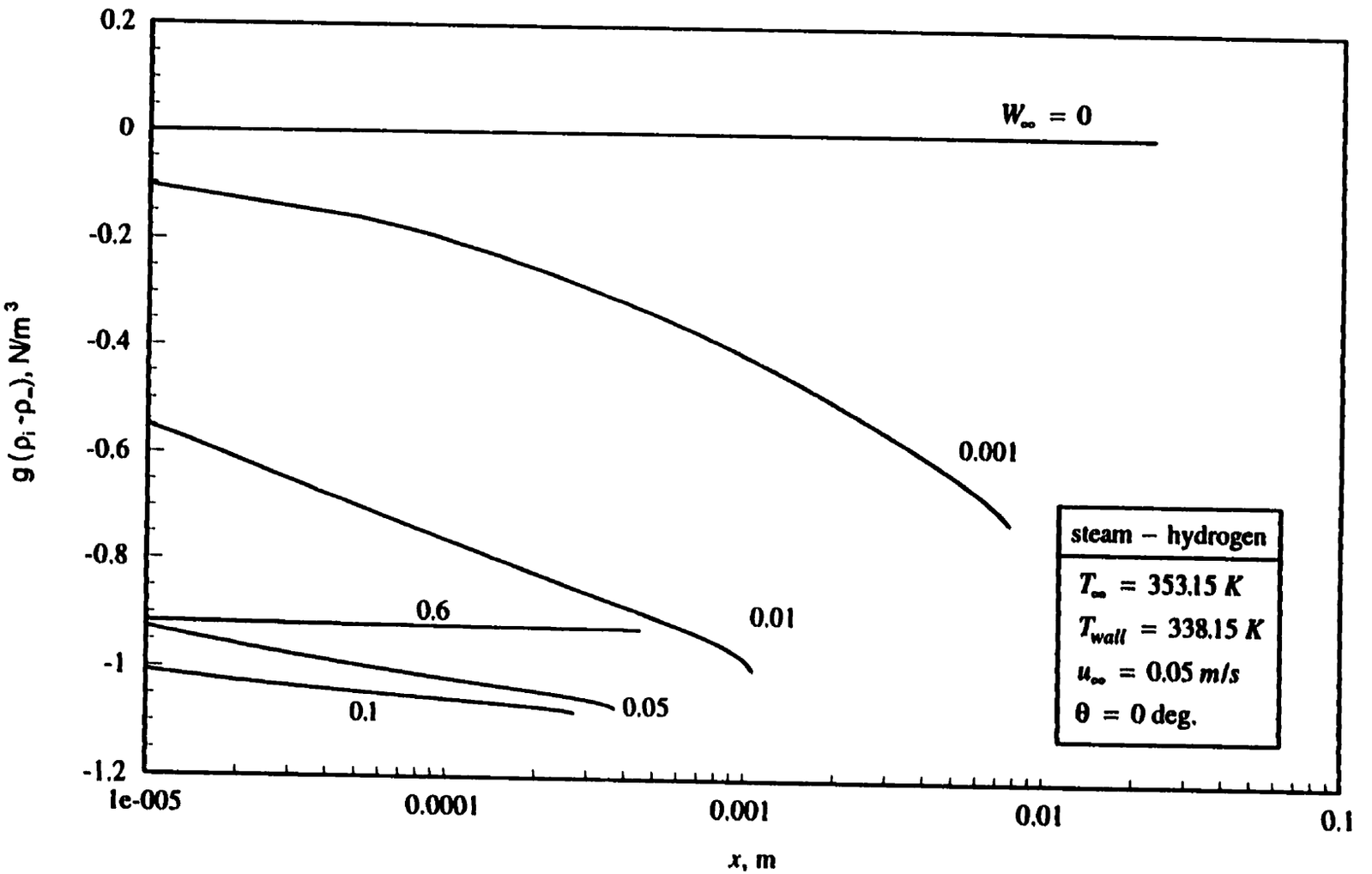

Figure 6.9: Variation of g ($\rho_i - \rho_\infty$) along the vertical plate for different values of W_∞ for a steam - hydrogen mixture at $T_\infty = 353.15\ K$, $\Delta T = 15\ K$ and $u_\infty = 0.05\ m/s$

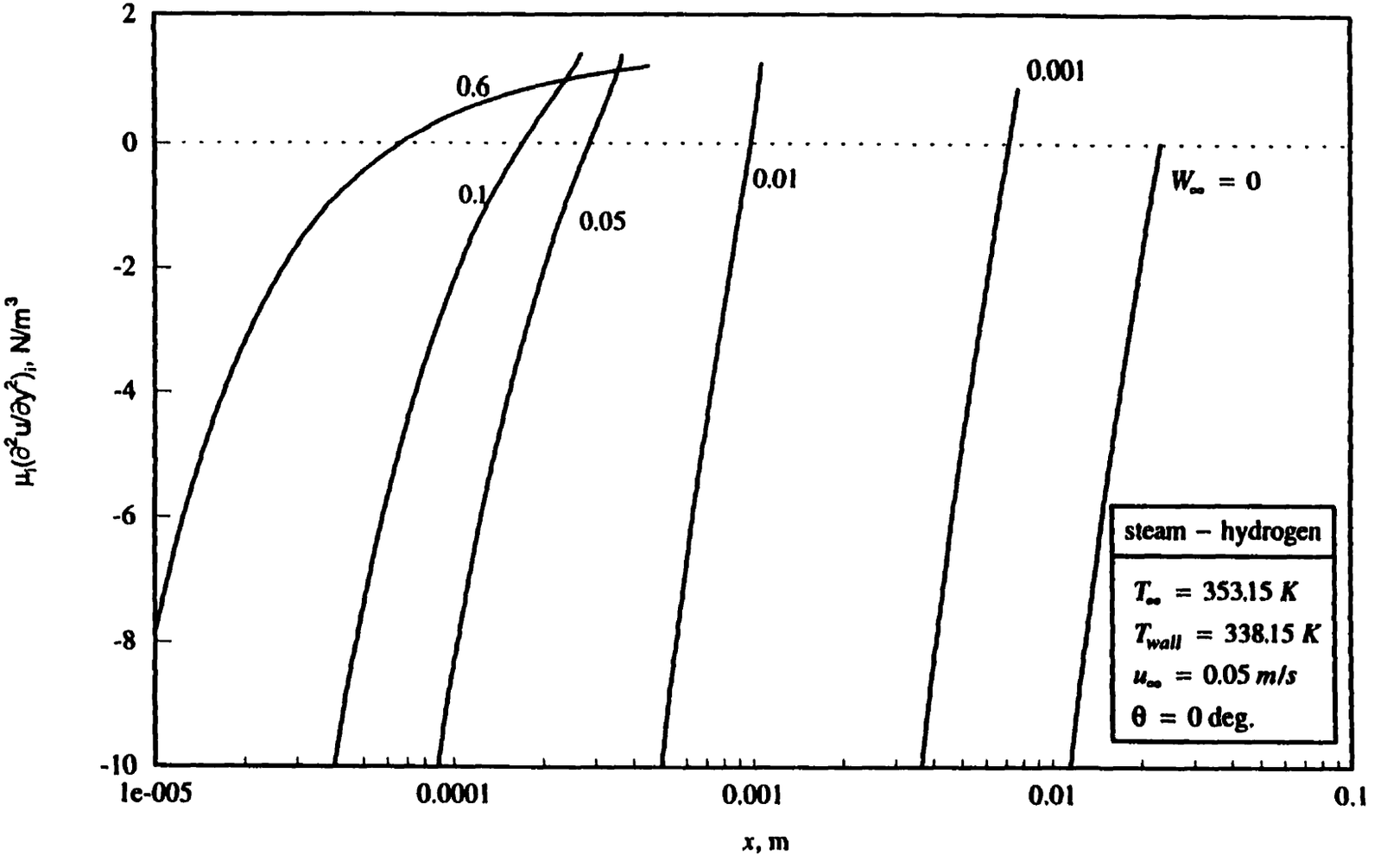

Figure 6.10: Variation of $\mu_i\left(\frac{\partial^2 u}{\partial y^2}\right)_i$ along the vertical plate for different values of W_∞ for a steam - hydrogen mixture at $T_\infty = 353.15\ K$, $\Delta T = 15\ K$ and $u_\infty = 0.05\ m/s$

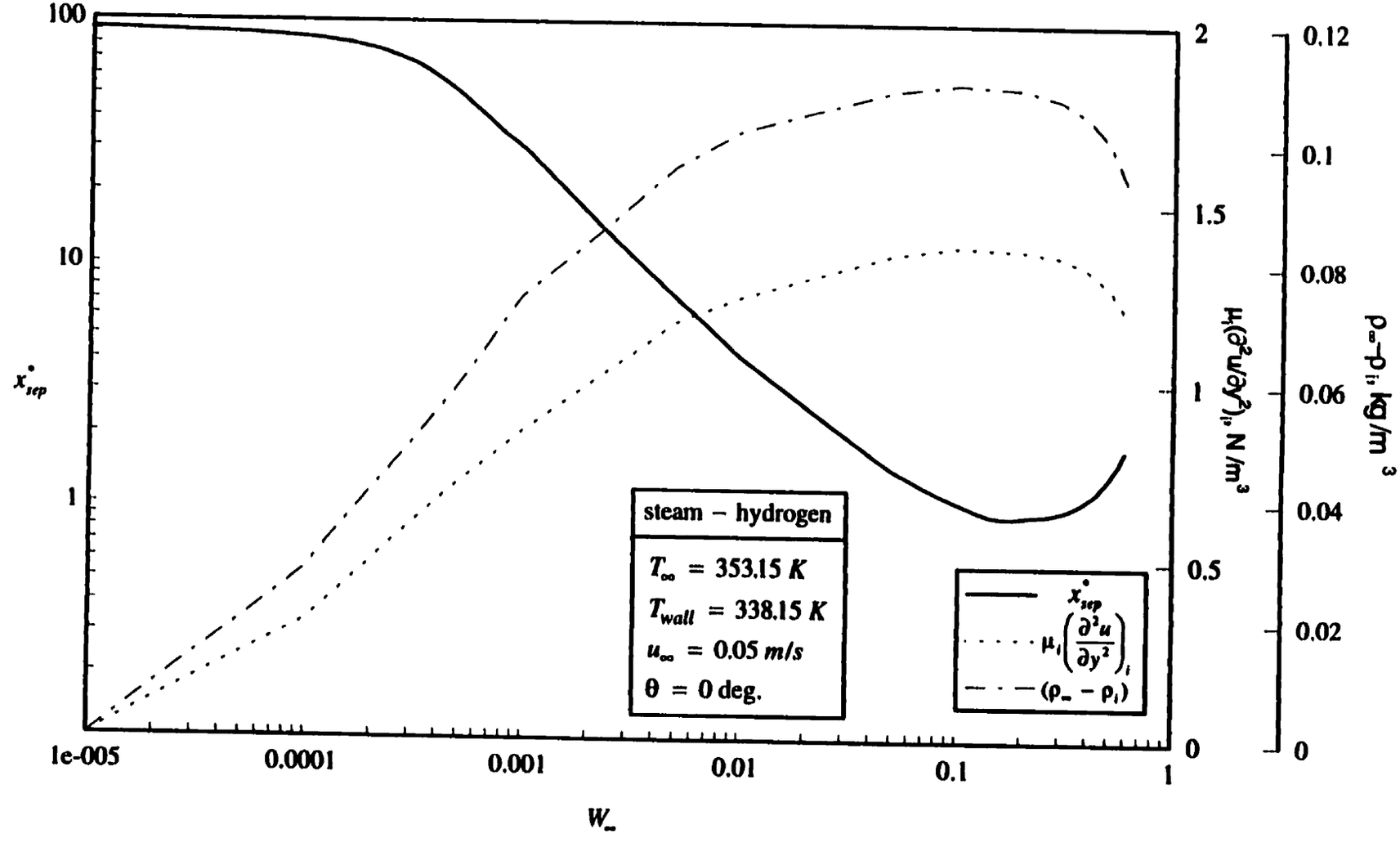

Figure 6.11: Variation of x^*_{sep}, $\mu_i\left(\frac{\partial^2 u}{\partial y^2}\right)_i$ and $(\rho_\infty - \rho_i)$ with W_∞ for a steam - hydrogen mixture at $T_\infty = 353.15\ K$, $\Delta T = 15\ K$ and $u_\infty = 0.05\ m/s$ on a vertical plate

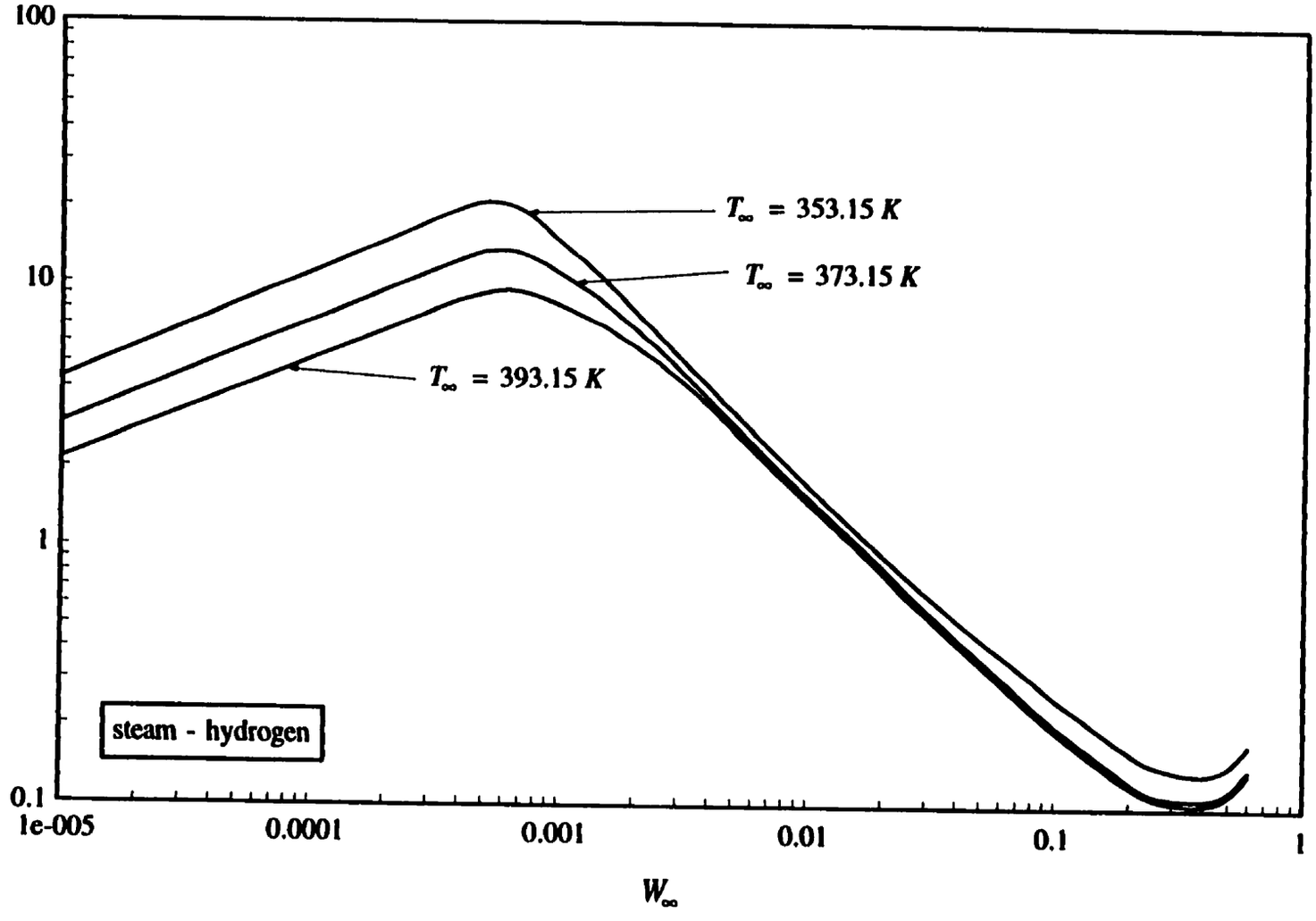

Figure 6.12: Value of $x^*_{sep}Ja^m$ for a steam - hydrogen mixture

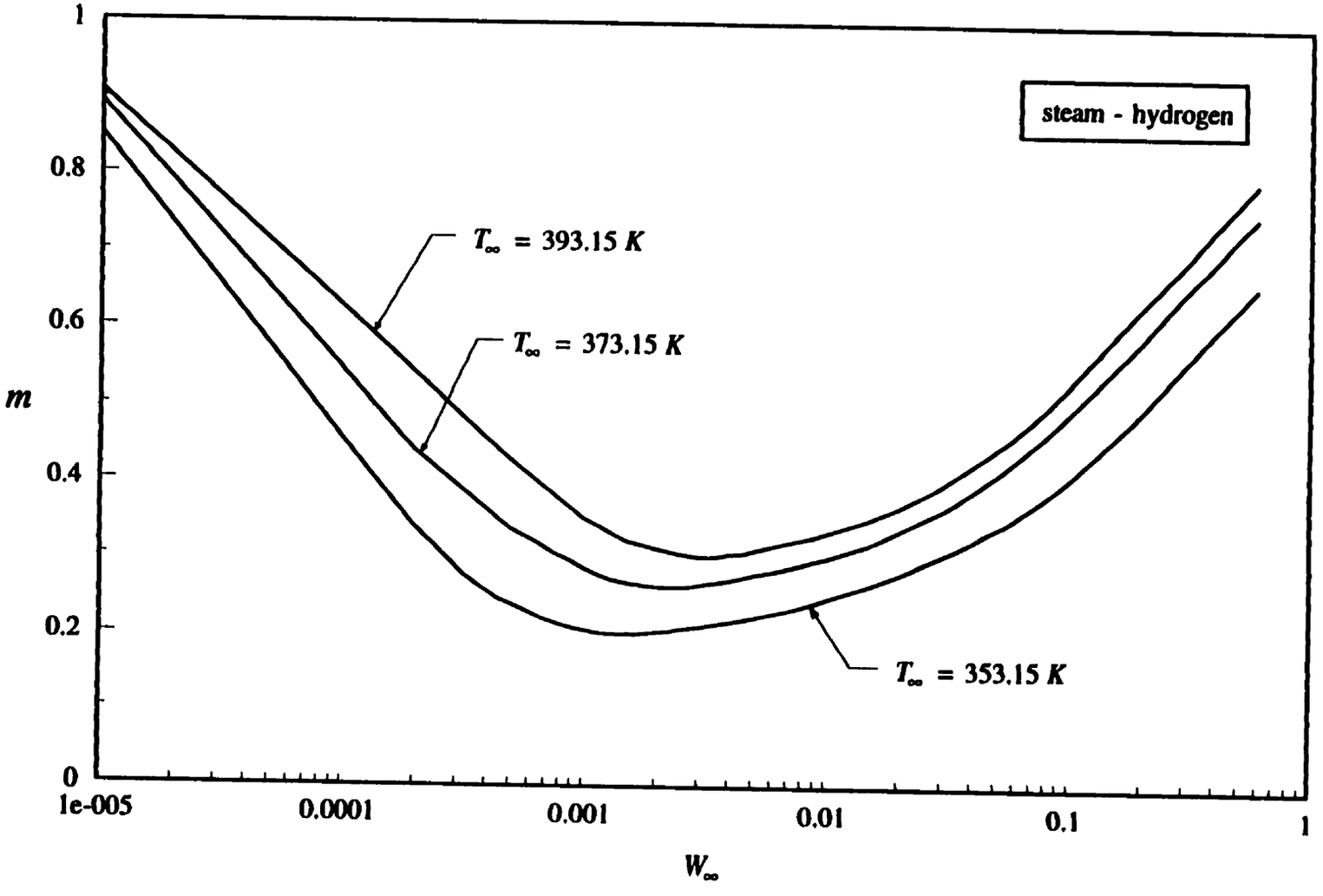

Figure 6.13: Value of the exponent m for a steam - hydrogen mixture

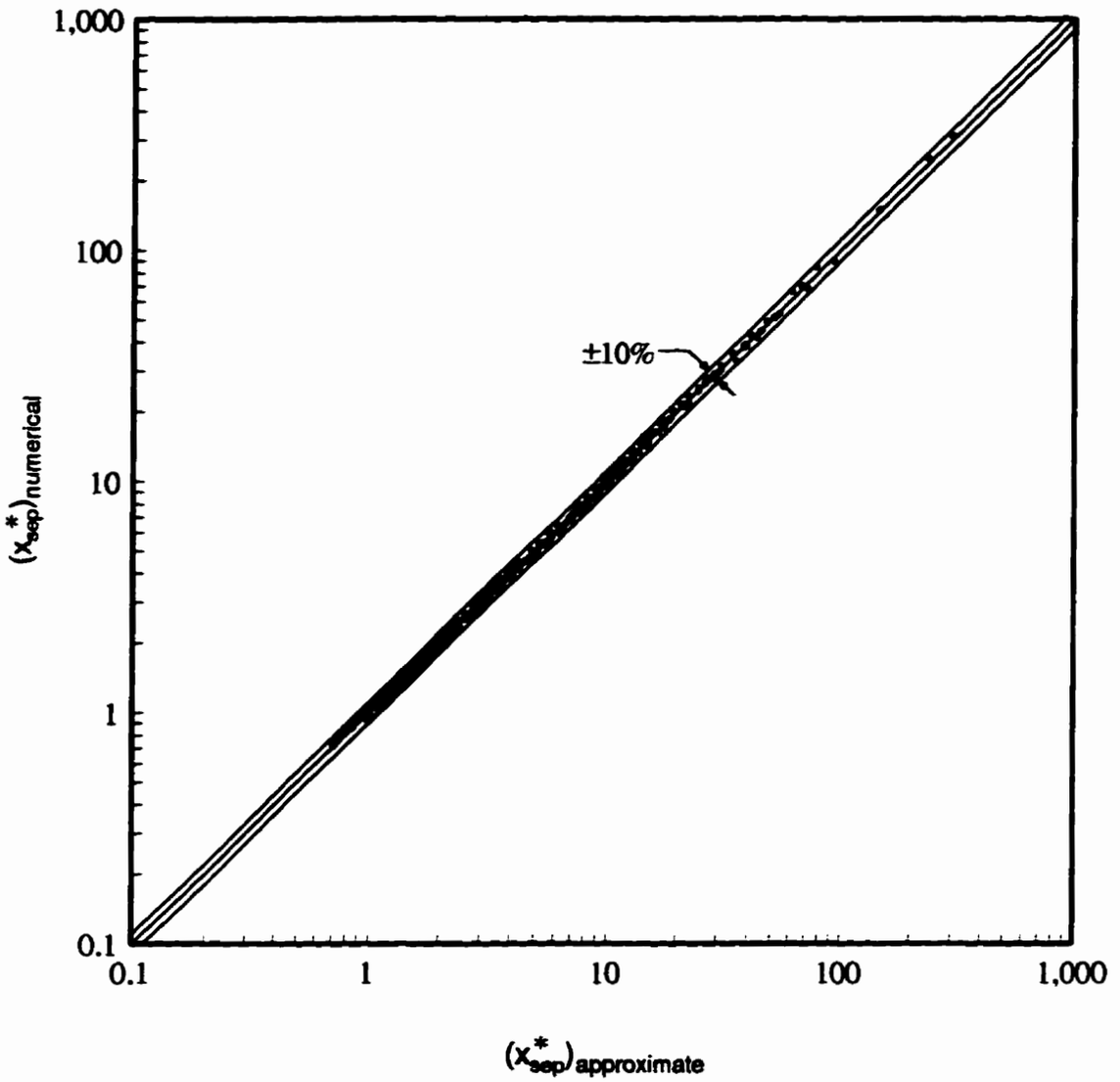

Figure 6.14: Comparison of approximate x^*_{sep} and numerically obtained x^*_{sep} for a steam-hydrogen mixture

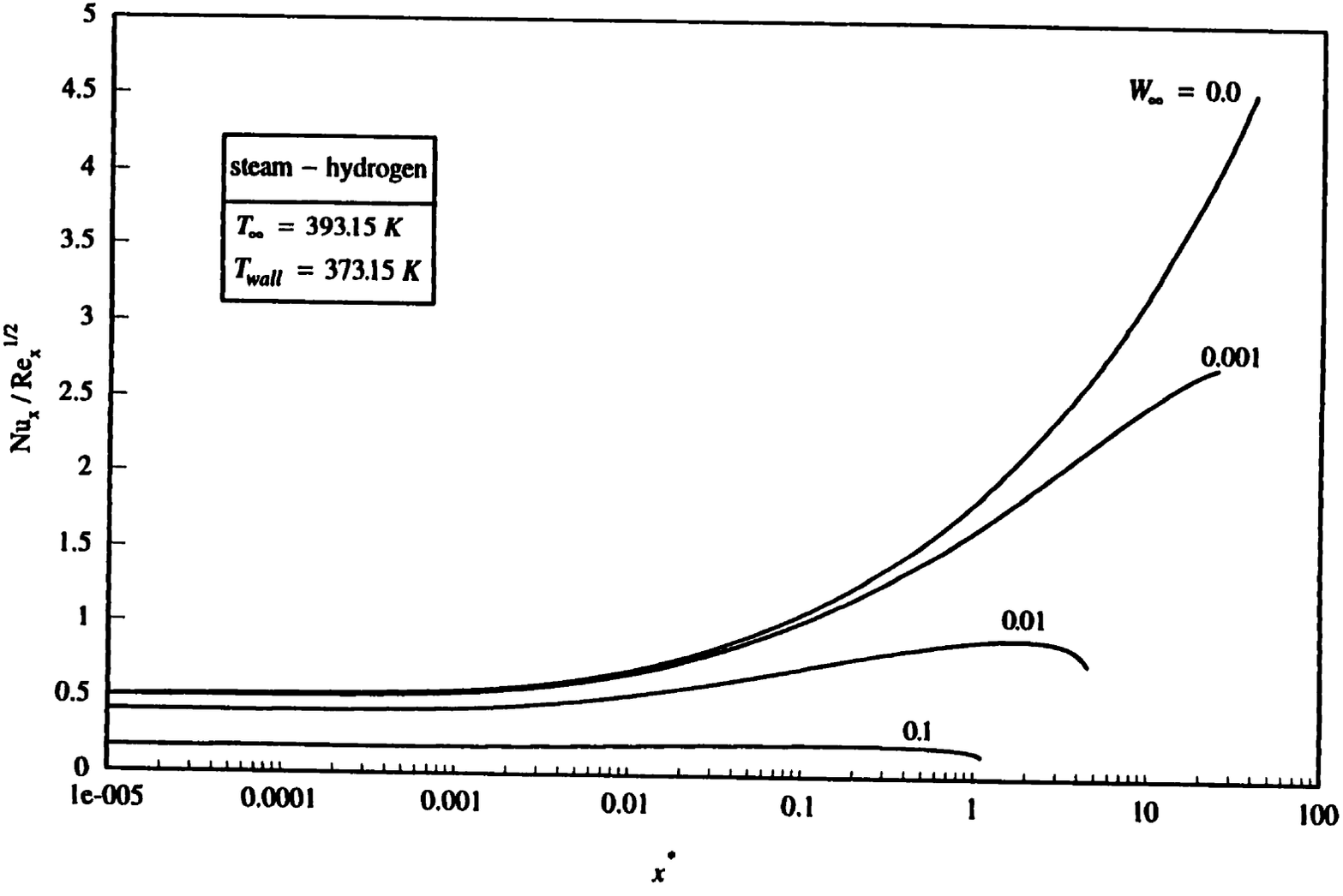

Figure 6.15: Effect of W_∞ on Nu_x / $Re_x^{1/2}$ for a steam - hydrogen mixture at T_∞= 393.15*K* and T_{wall}= 373.15*K*

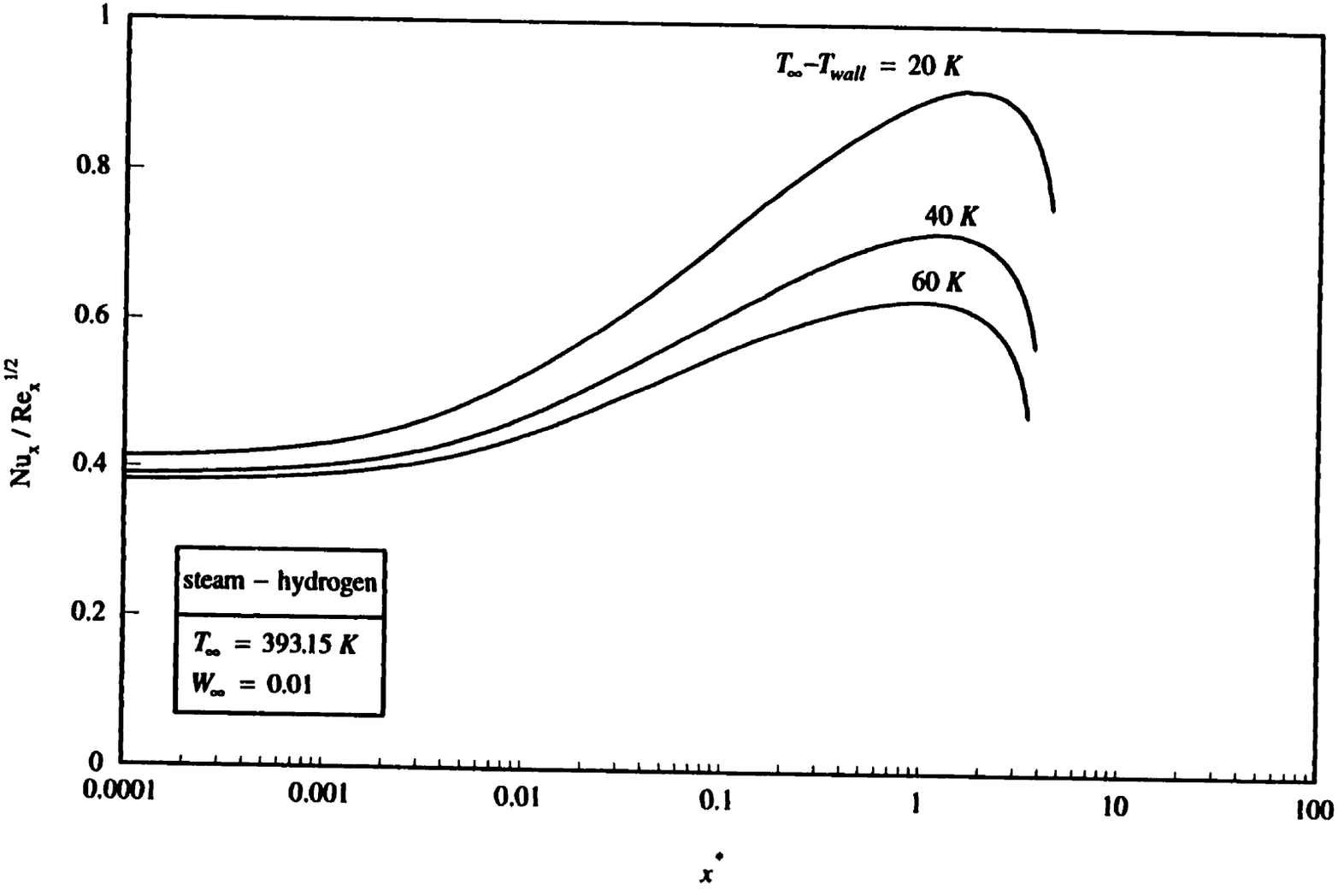

Figure 6.16: Effect of $(T_\infty - T_{wall})$ on Nu_x / $Re_x^{1/2}$ for a steam-hydrogen mixture at T_∞= 393.15K and W_∞= 0.01

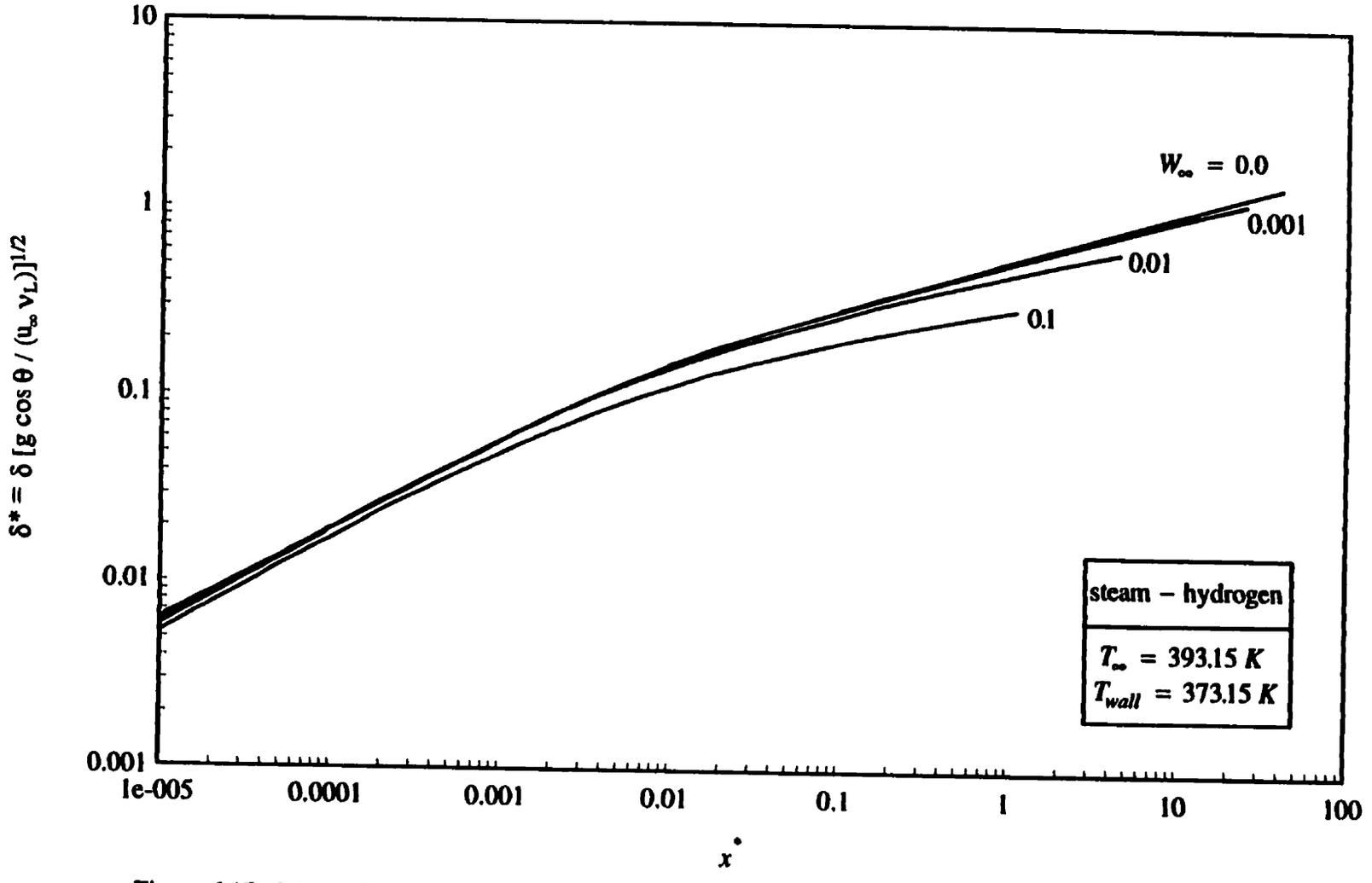

Figure 6.17: Dimensionless liquid film thickness for a steam-hydrogen mixture at $T_\infty = 393.15K$ and $T_{wall} = 373.15K$

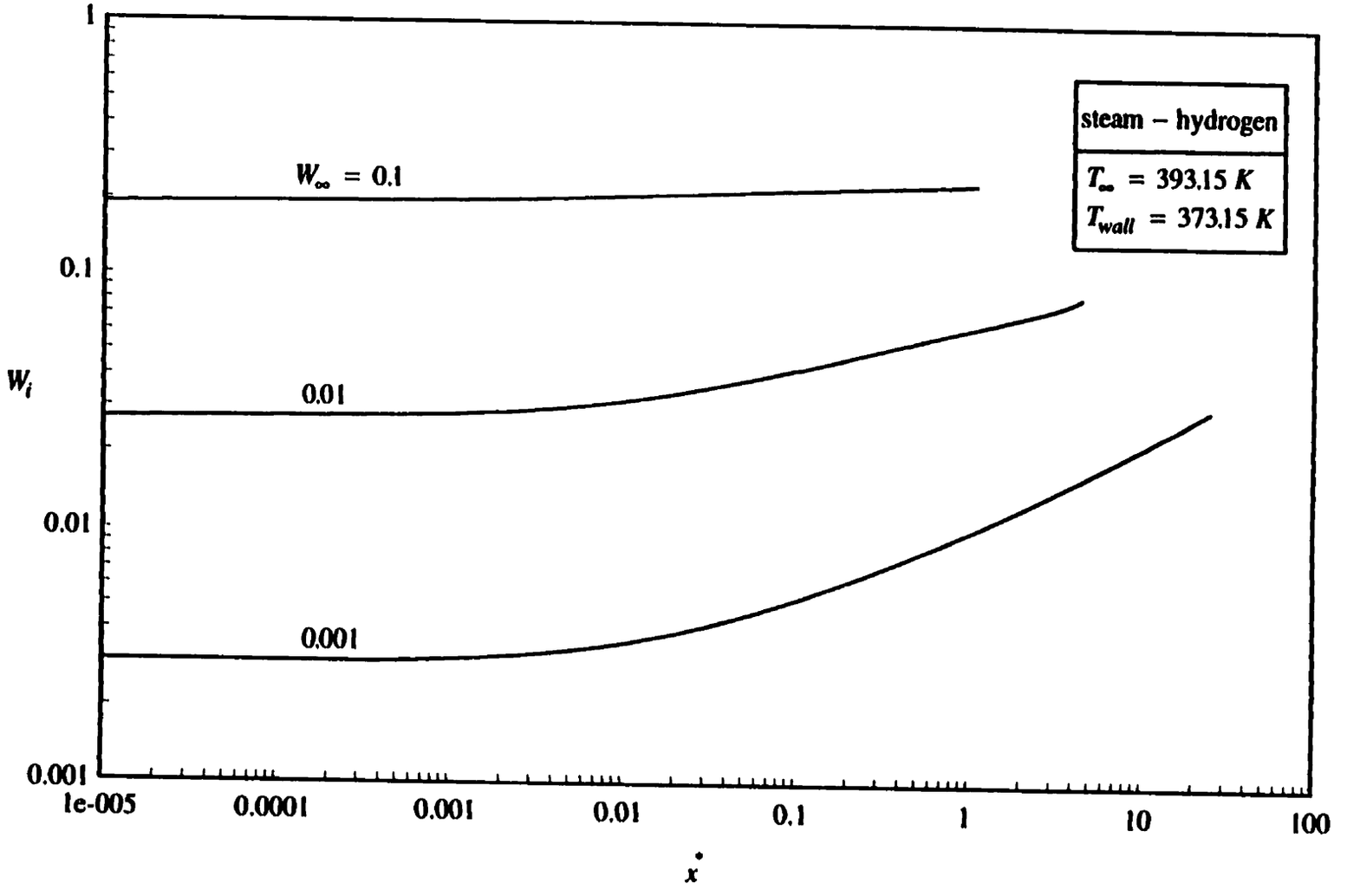

Figure 6.18: Interfacial gas concentration for a steam - hydrogen mixture at T_∞= 393.15K and T_{wall}= 373.15K

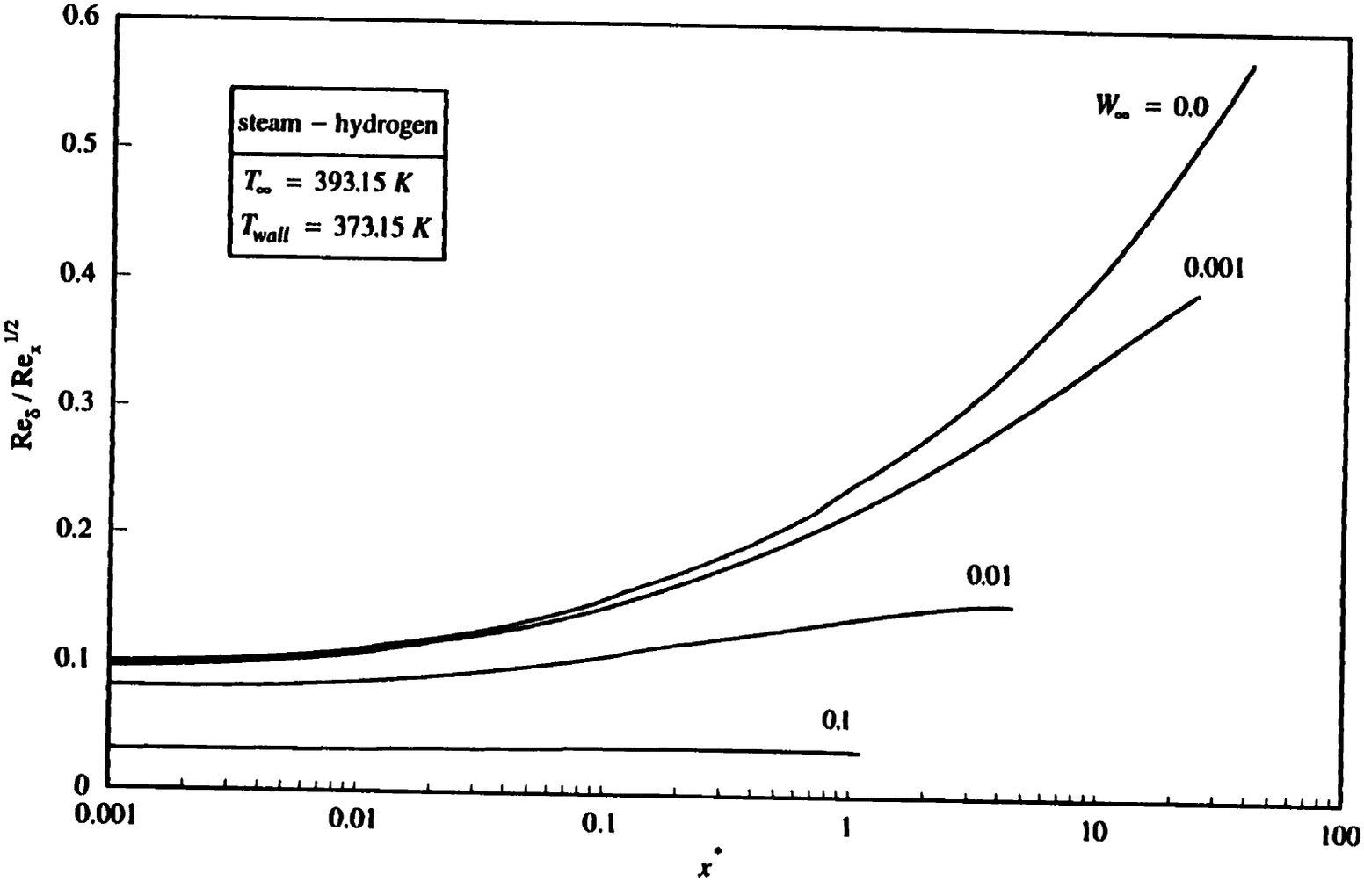

Figure 6.19: Values of Re_δ / $Re_x^{1/2}$ for a steam-hydrogen mixture at T_∞=393.15K and T_{wall}=373.15K

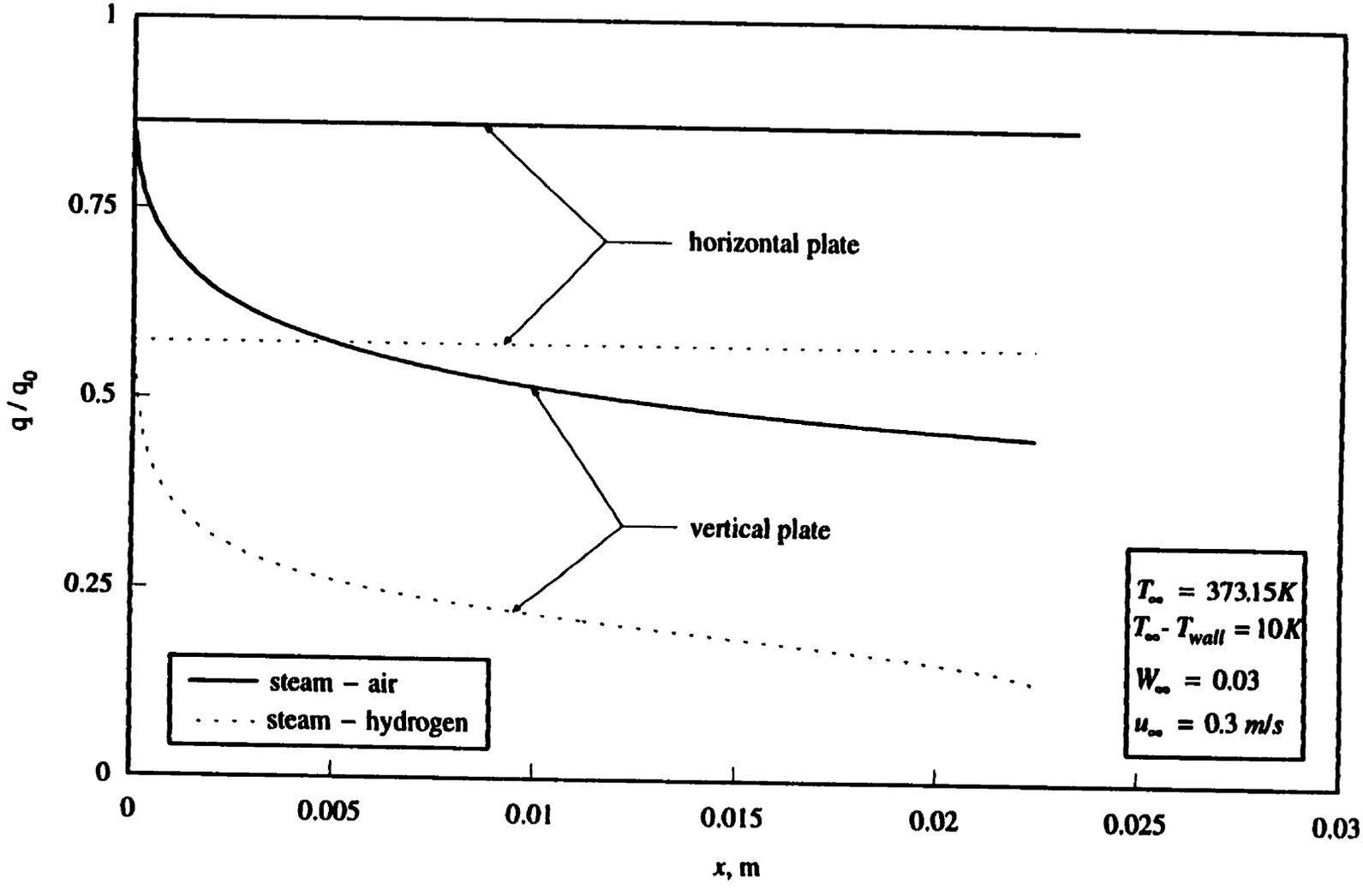

Figure 6.20: Comparison of the rate of heat transfer for steam - air and steam - hydrogen mixtures at T_∞ = 373.15K and W_∞ = 0.03

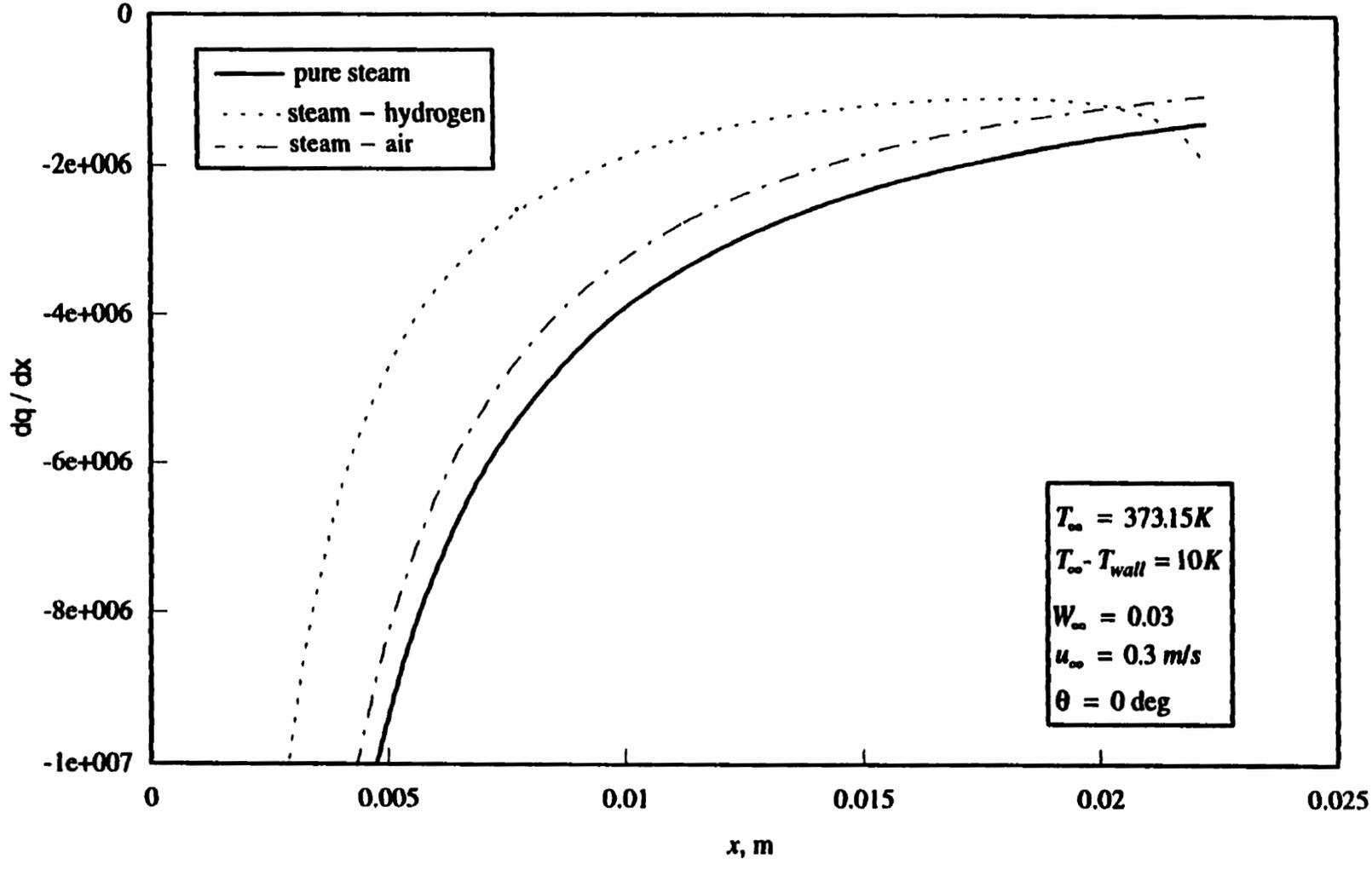

Figure 6.21: Values of $\frac{dq}{dx}$ along the plate for pure steam, steam - air and steam - hydrogen mixtures at T_∞ = 373.15K and W_∞ = 0.03

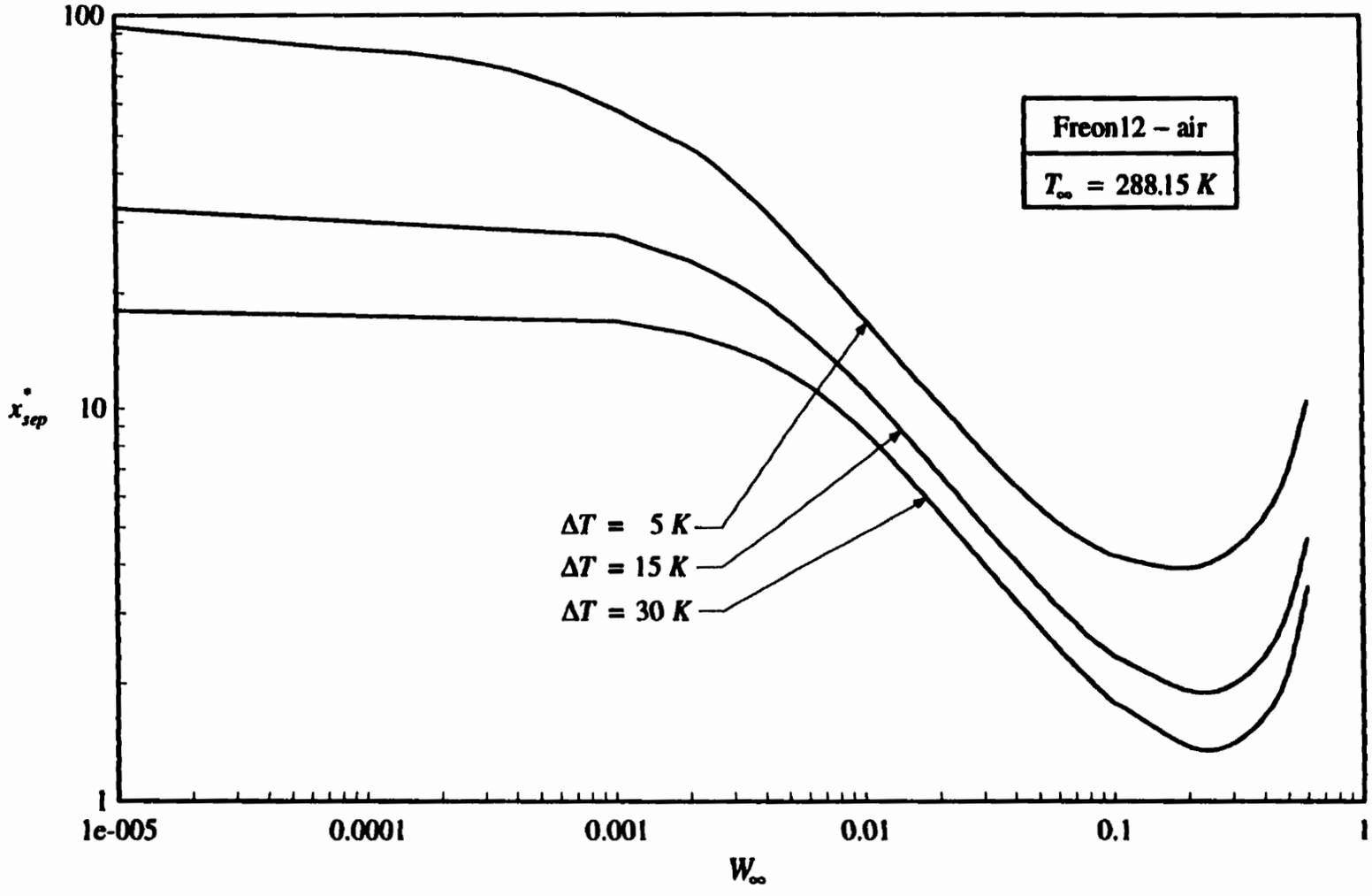

Figure 6.22: Dimensionless separation length for a Freon12 - air mixture at T_∞ = 288.15 K

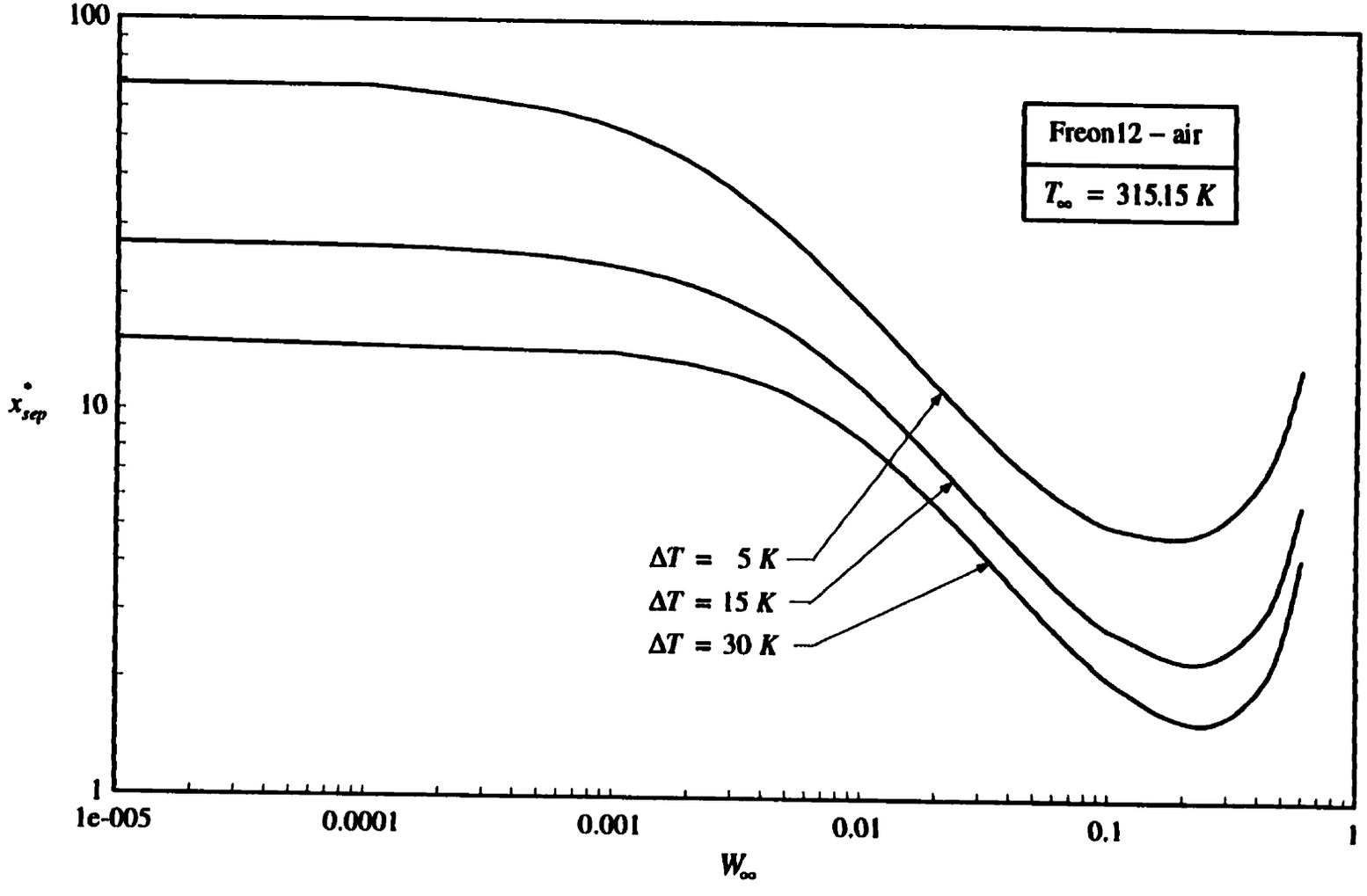

Figure 6.23: Dimensionless separation length for a Freon12 - air mixture at T_∞ = 315.15 K

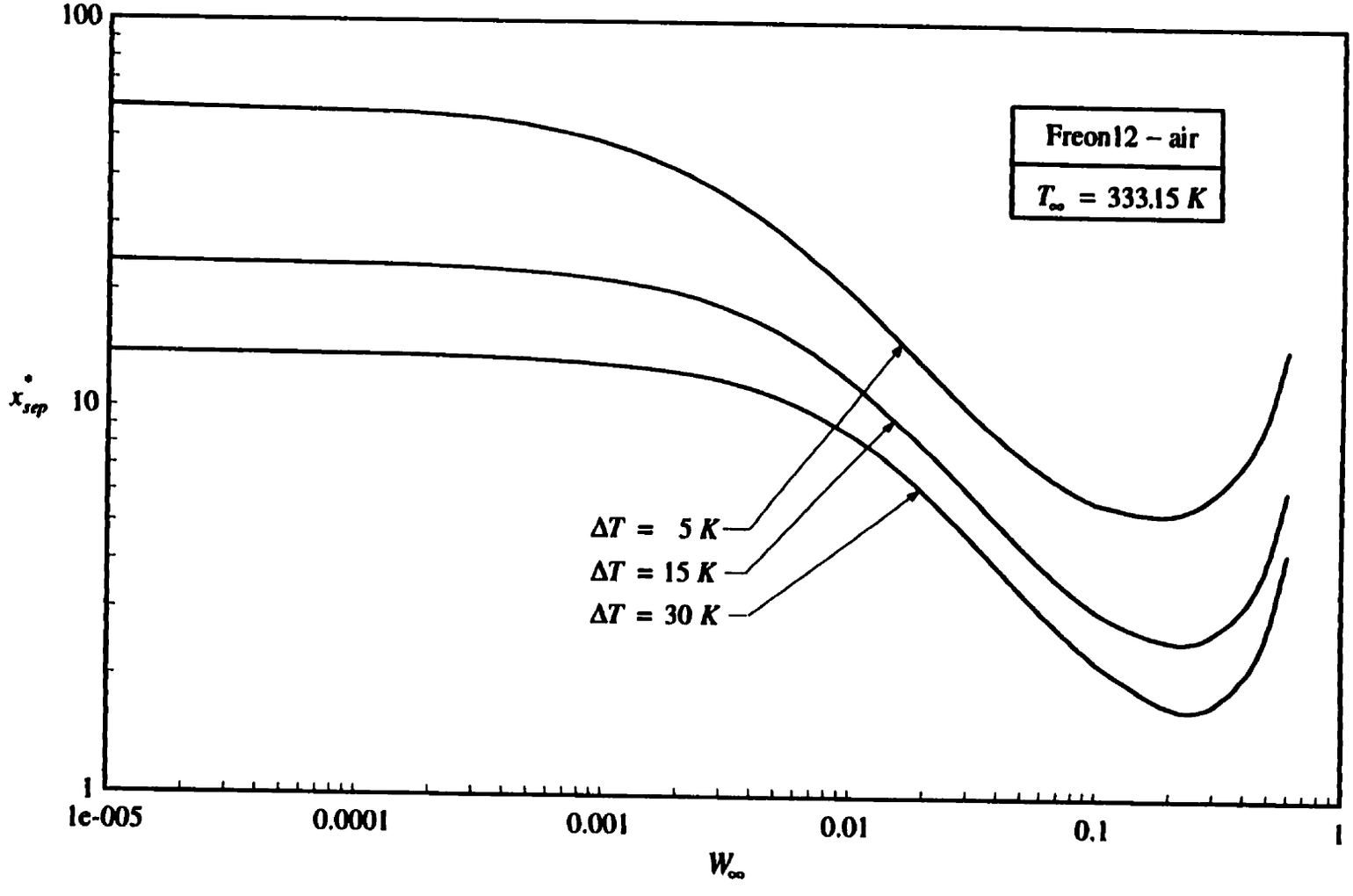

Figure 6.24: Dimensionless separation length for a Freon12 - air mixture at T_∞ = 333.15 K

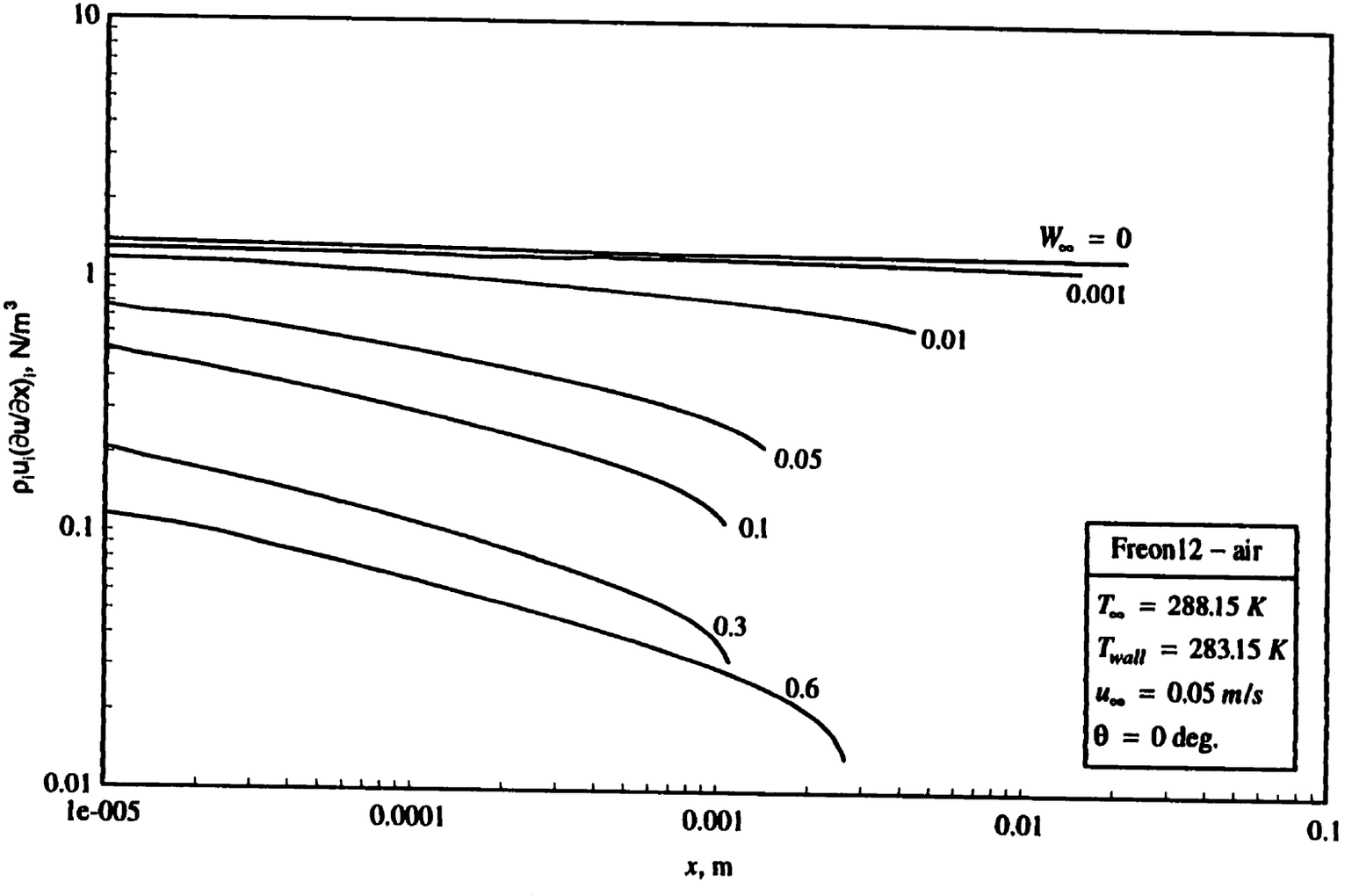

Figure 6.25: Variation of $\rho_i u_i \left(\frac{\partial u}{\partial x}\right)_i$ along the vertical plate for different values of W_∞ for a Freon12 - air mixture at $T_\infty = 288.15\ K$, $\Delta T = 5\ K$ and $u_\infty = 0.05\ m/s$

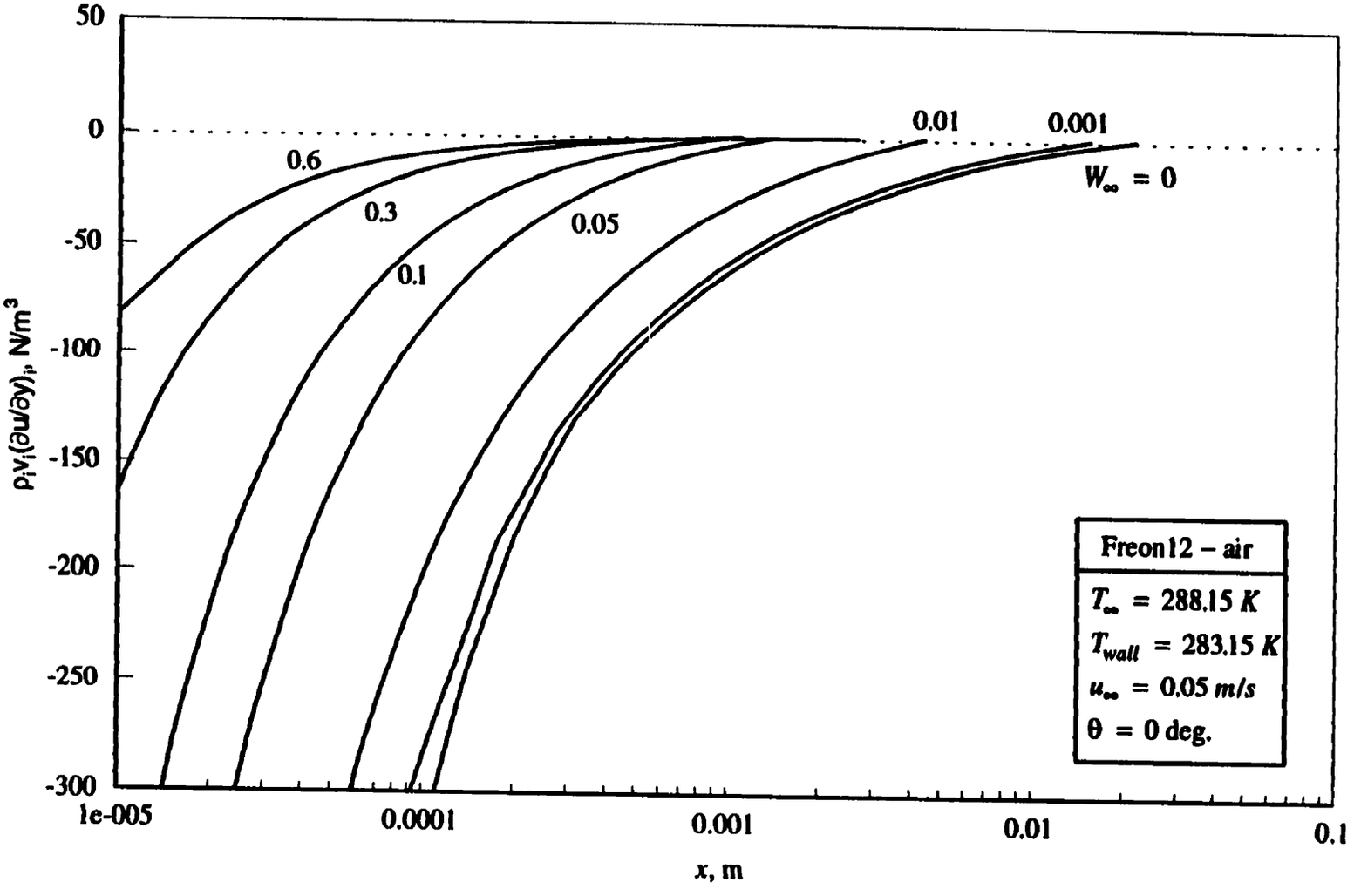

Figure 6.26: Variation of $\rho_i v_i \left(\frac{\partial u}{\partial y}\right)_i$ along the vertical plate for different values of W_∞ for a Freon12 - air mixture at $T_\infty = 288.15\ K$, $\Delta T = 5\ K$ and $u_\infty = 0.05\ m/s$

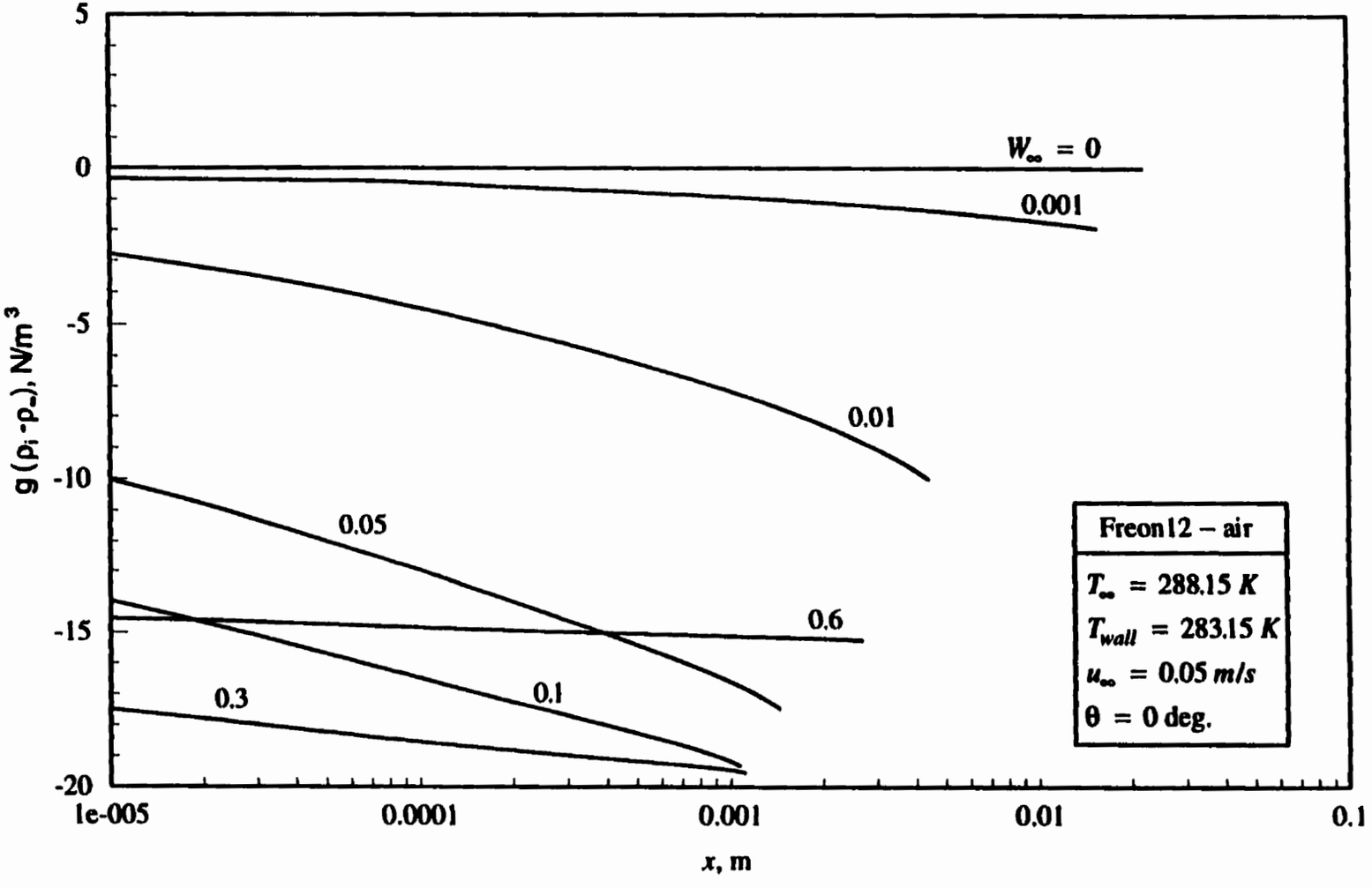

Figure 6.27: Variation of g ($\rho_i - \rho_\infty$) along the vertical plate for different values of W_∞ for a Freon12 - air mixture at $T_\infty = 288.15\ K$, $\Delta T = 5\ K$ and $u_\infty = 0.05\ m/s$

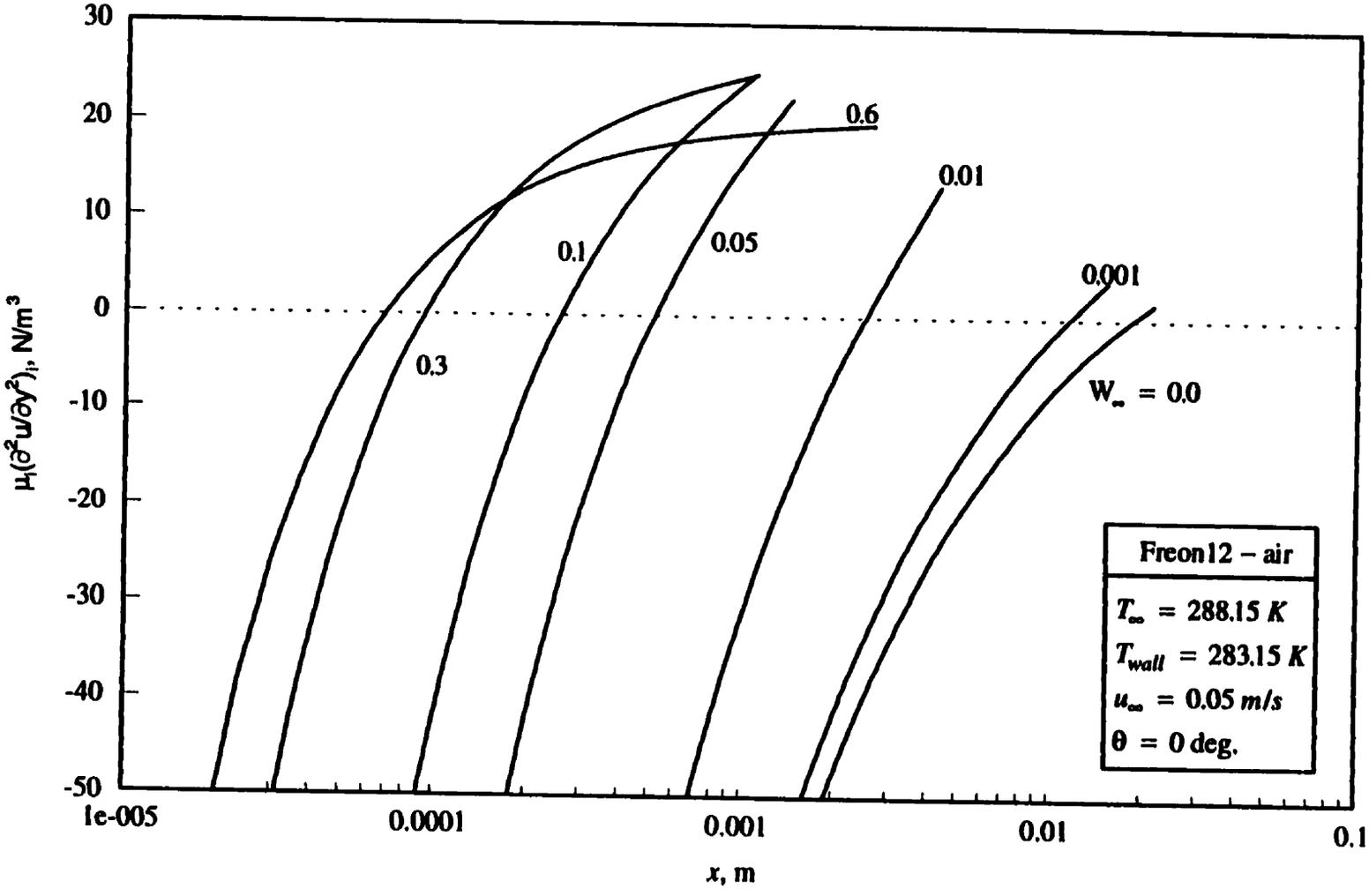

Figure 6.28: Variation of $\mu_i\left(\frac{\partial^2 u}{\partial y^2}\right)_i$ along the vertical plate for different values of W_∞ for a Freon12 - air mixture at $T_\infty = 288.15\ K$, $\Delta T = 5\ K$ and $u_\infty = 0.05\ m/s$

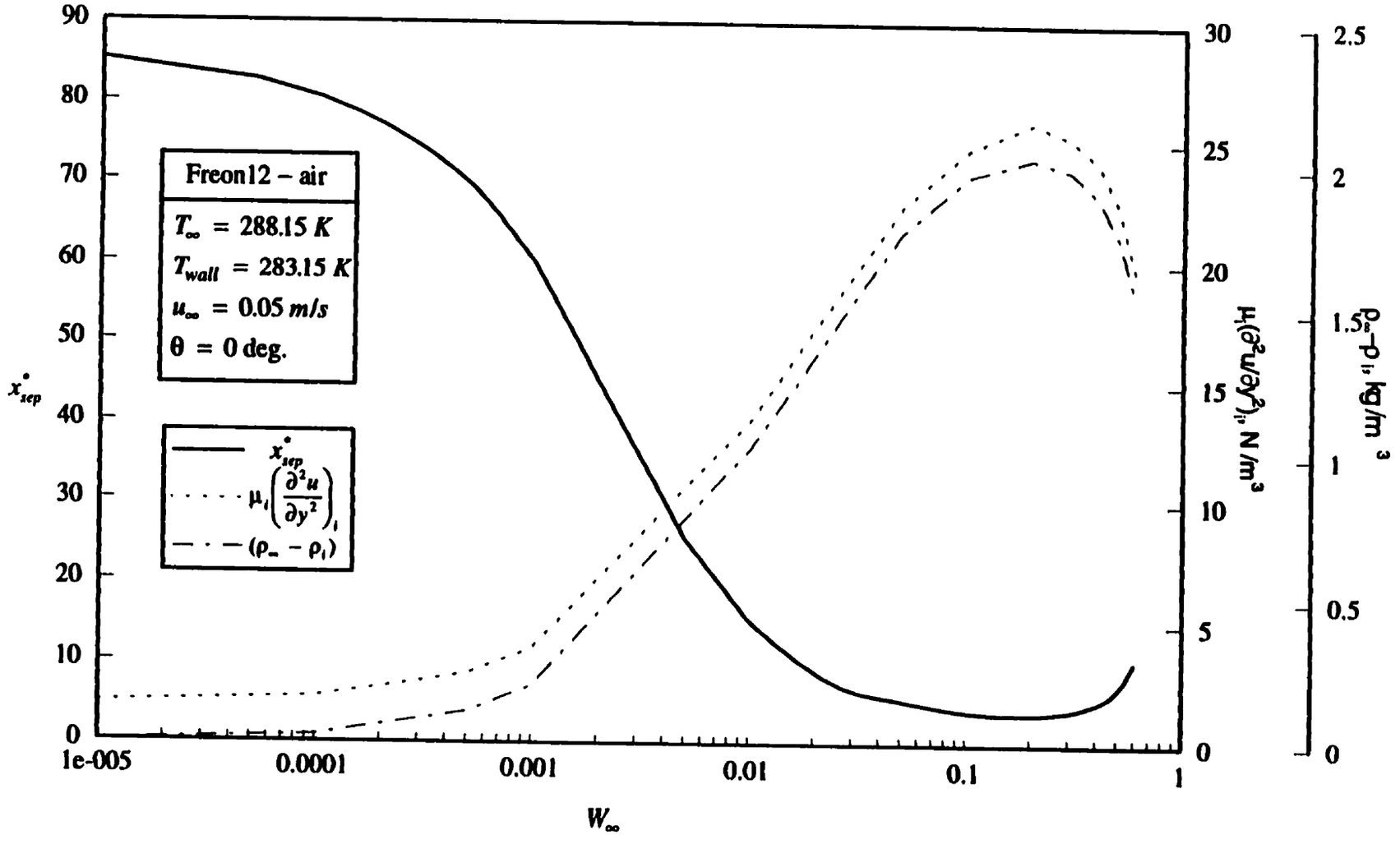

Figure 6.29: Variation of x^*_{sep}, $\mu_i\left(\frac{\partial^2 u}{\partial y^2}\right)_i$ and $(\rho_\infty - \rho_i)$ with W_∞ for a Freon12 - air mixture at T_∞ = 288.15 K, ΔT = 5 K and u_∞ = 0.05 m/s

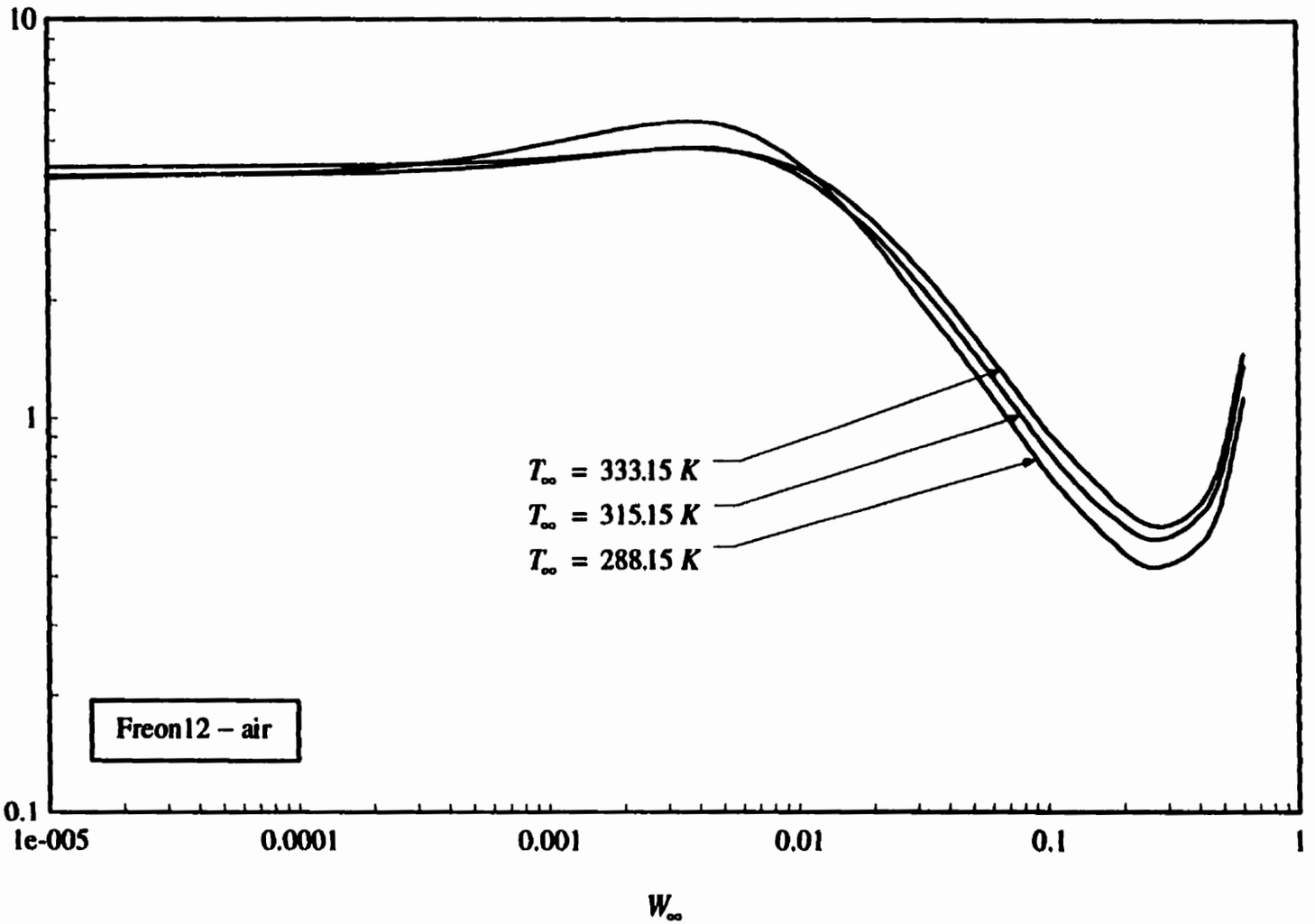

Figure 6.30: Value of $x^*_{sep}Ja^m$ for a Freon12 - air mixtures

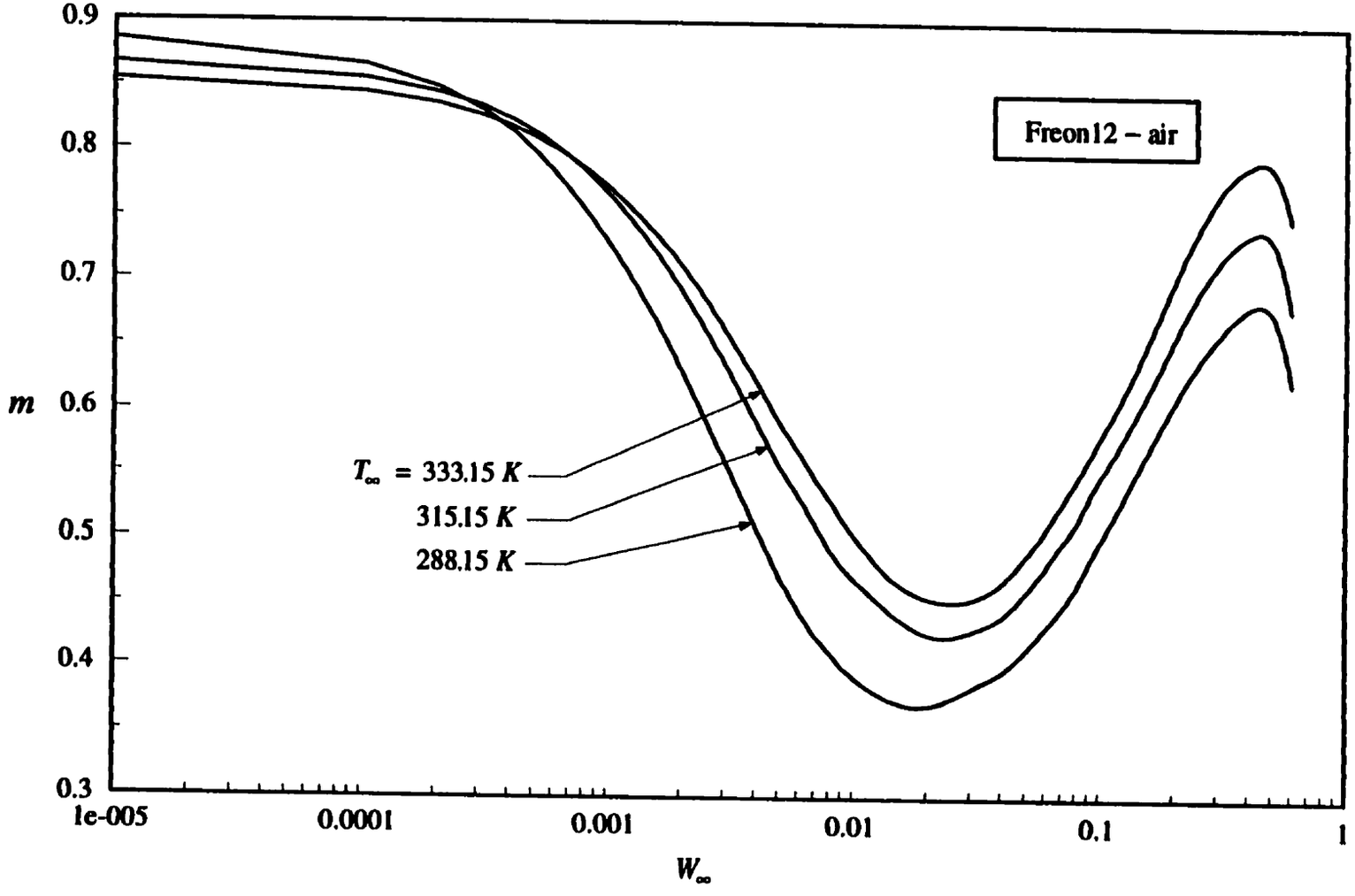

Figure 6.31: Value of the exponent m for a Freon12 - air mixtures

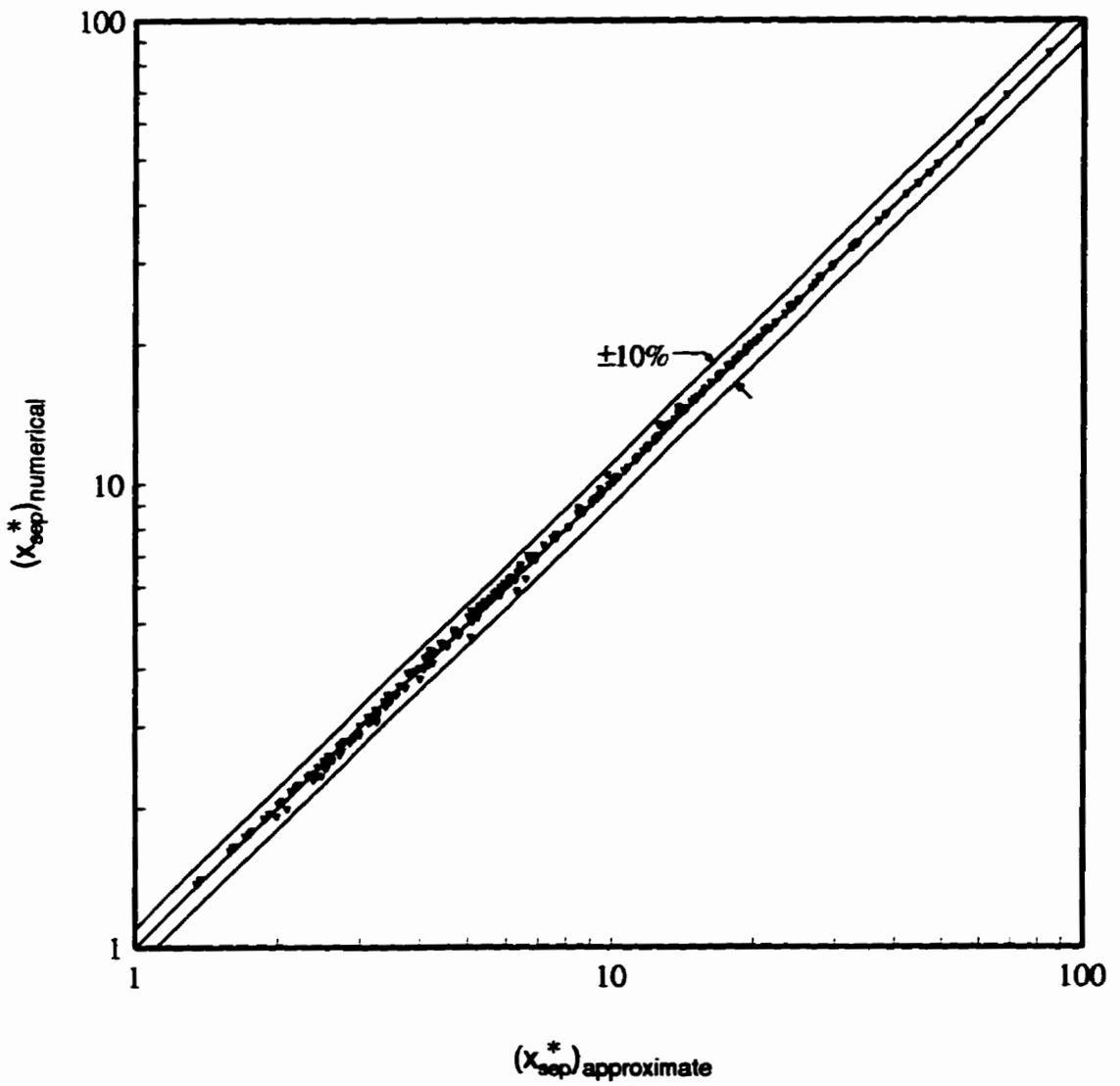

Figure 6.32: Comparison of approximate x^*_{sep} and numerically obtained x^*_{sep} for a Freon12-air mixture

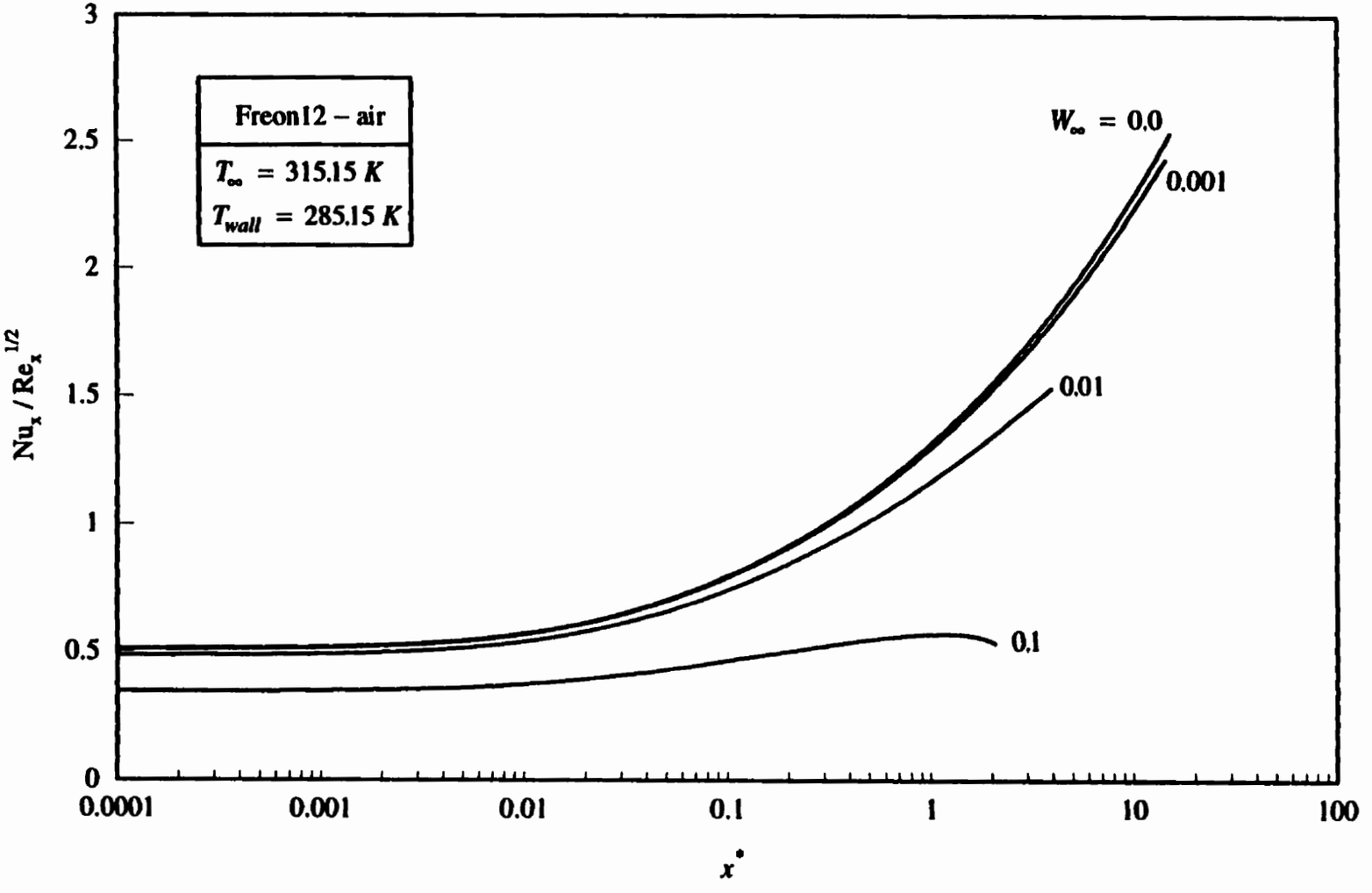

Figure 6.33: Effect of W_∞ on Nu_x / $Re_x^{1/2}$ for a Freon12-air mixture at T_∞= 315.15K and T_{wall}= 285.15K

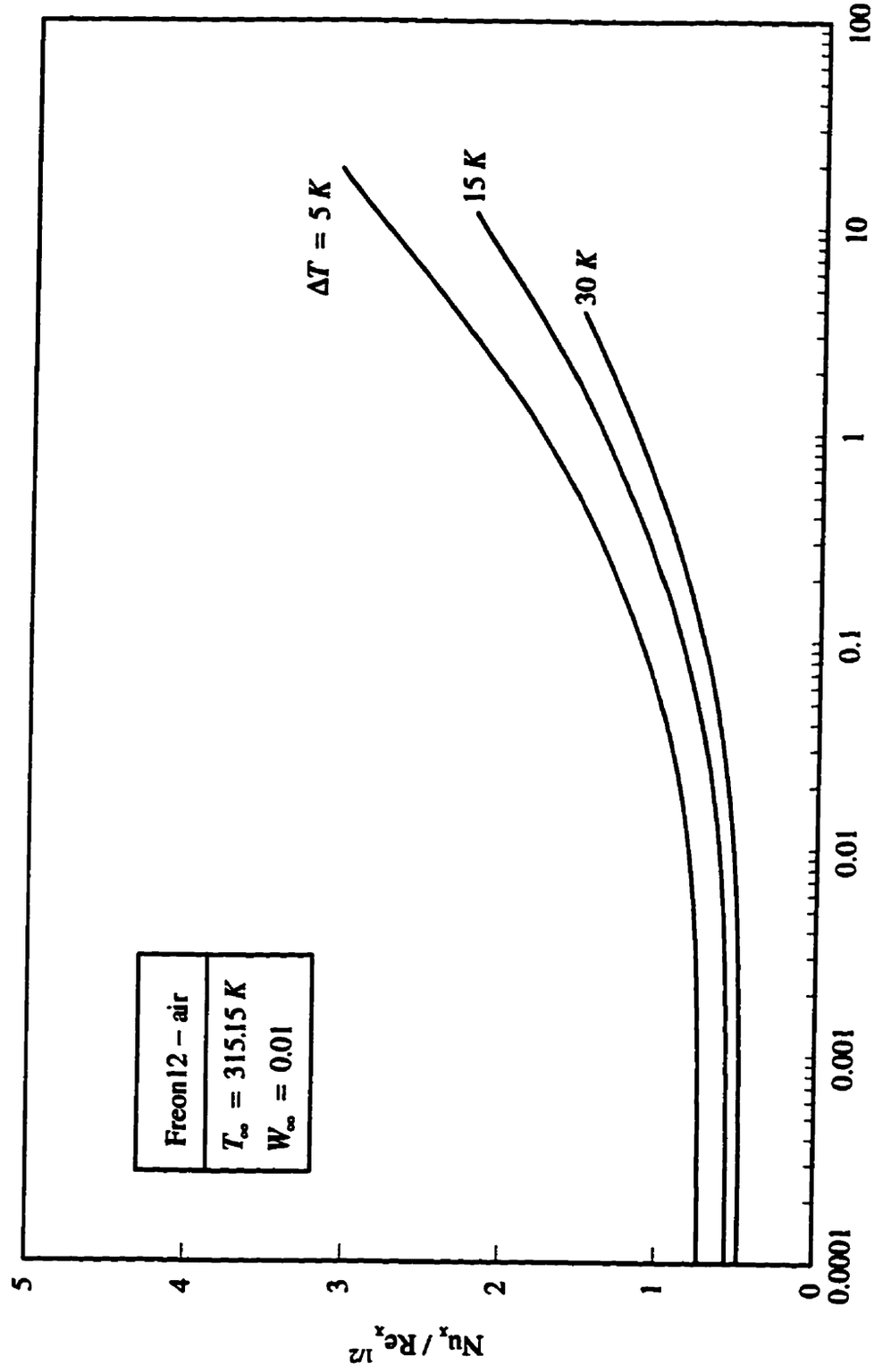

Figure 6.34: Effect of $(T_\infty - T_{wall})$ on Nu_x / $Re_x^{1/2}$ for a Freon12 - air mixture at T_∞ = 315.15K and W_∞ = 0.01

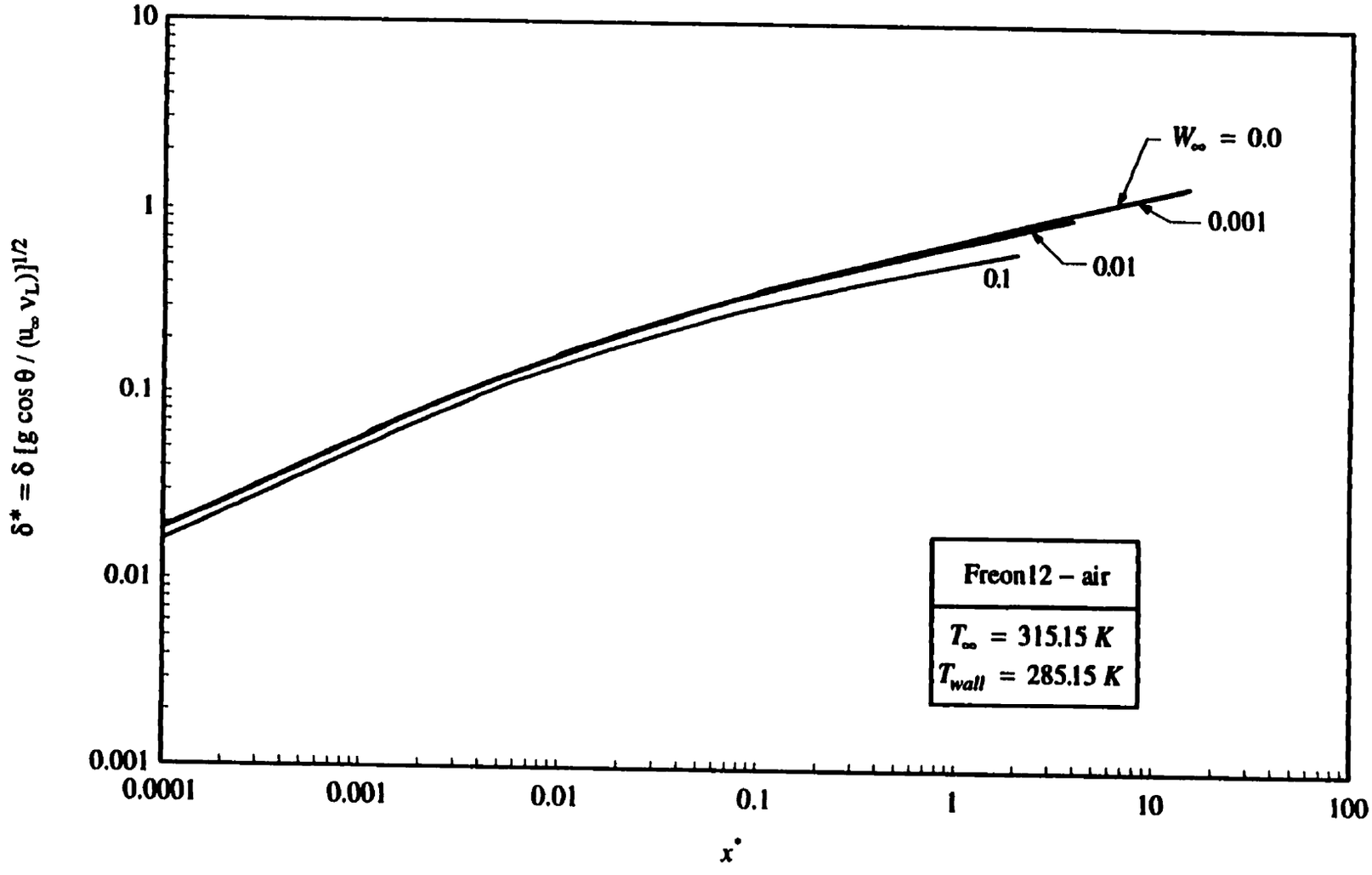

Figure 6.35: Dimensionless liquid film thickness for a Freon12 - air mixture at T_∞= 315.15K and T_{wall}= 285.15K

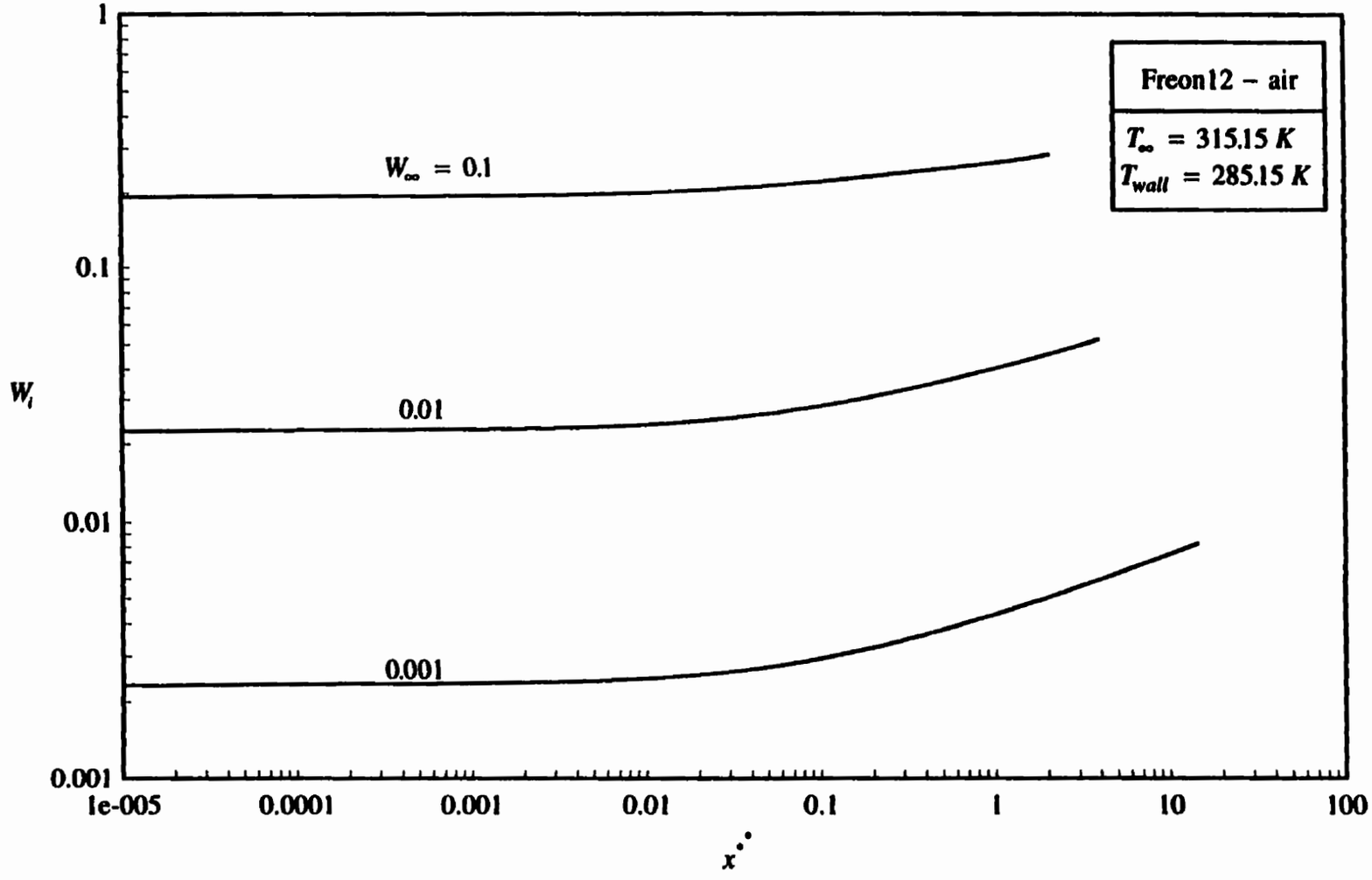

Figure 6.36: Interfacial gas concentration for a Freon12 - air mixture at T_∞= 315.15*K* and T_{wall}= 285.15*K*

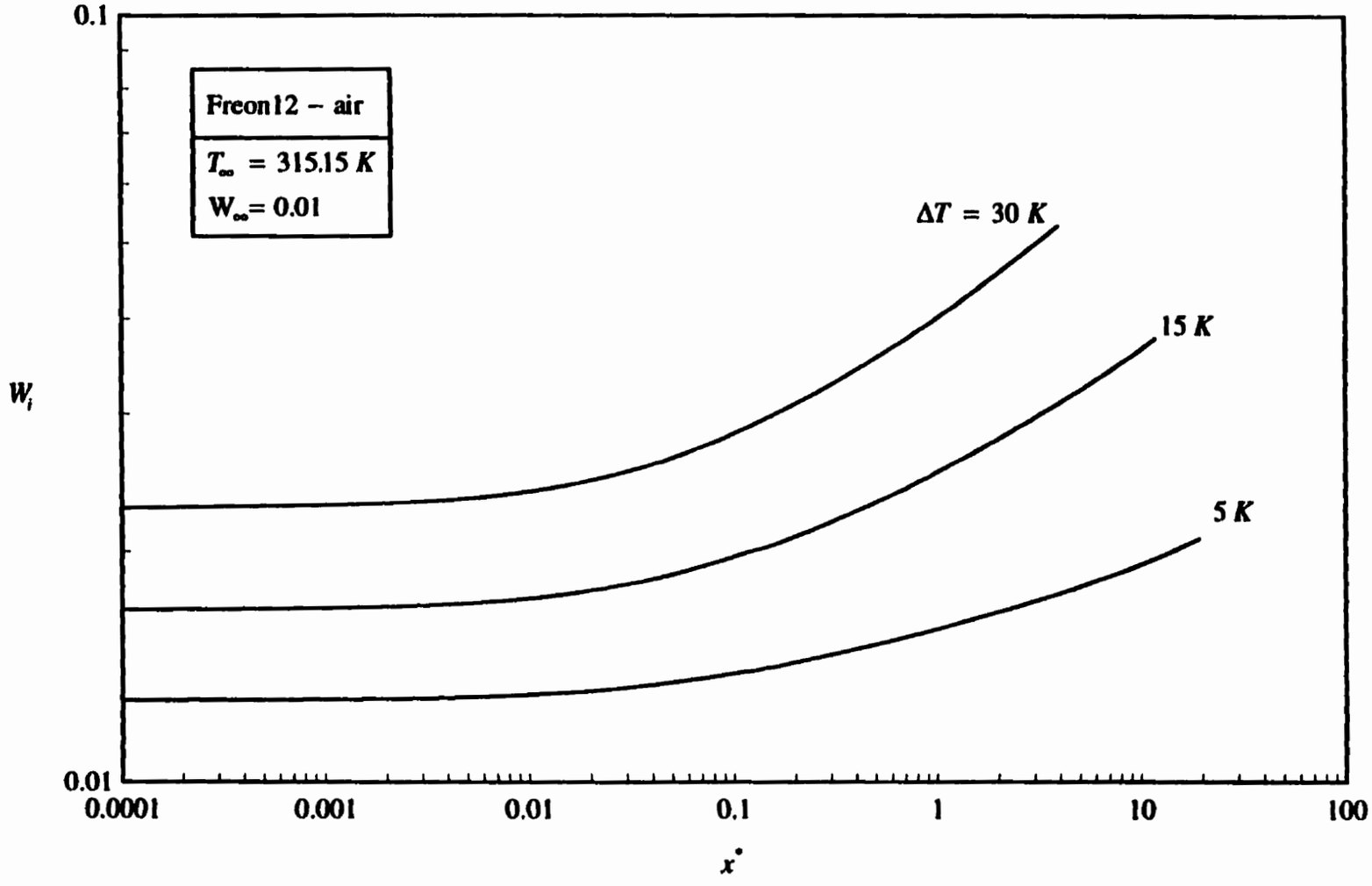

Figure 6.37: Interfacial gas concentration for a Freon12 - air mixture at T_∞= 315.15K and W_∞= 0.01

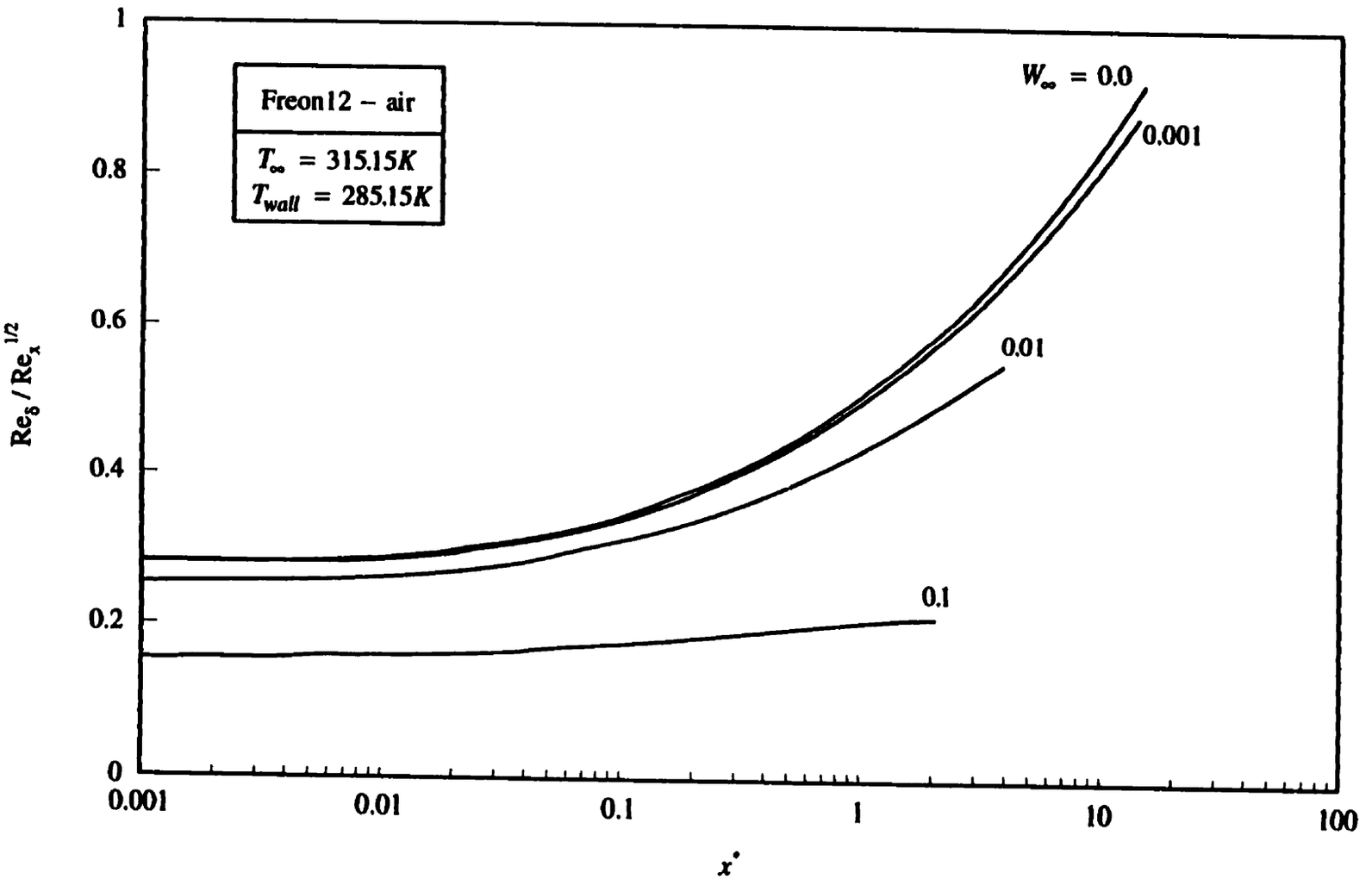

Figure 6.38: Value of Re_δ / $Re_x^{1/2}$ for a Freon12 - air mixture at T_∞= 315.15K and T_{wall}= 285.15K

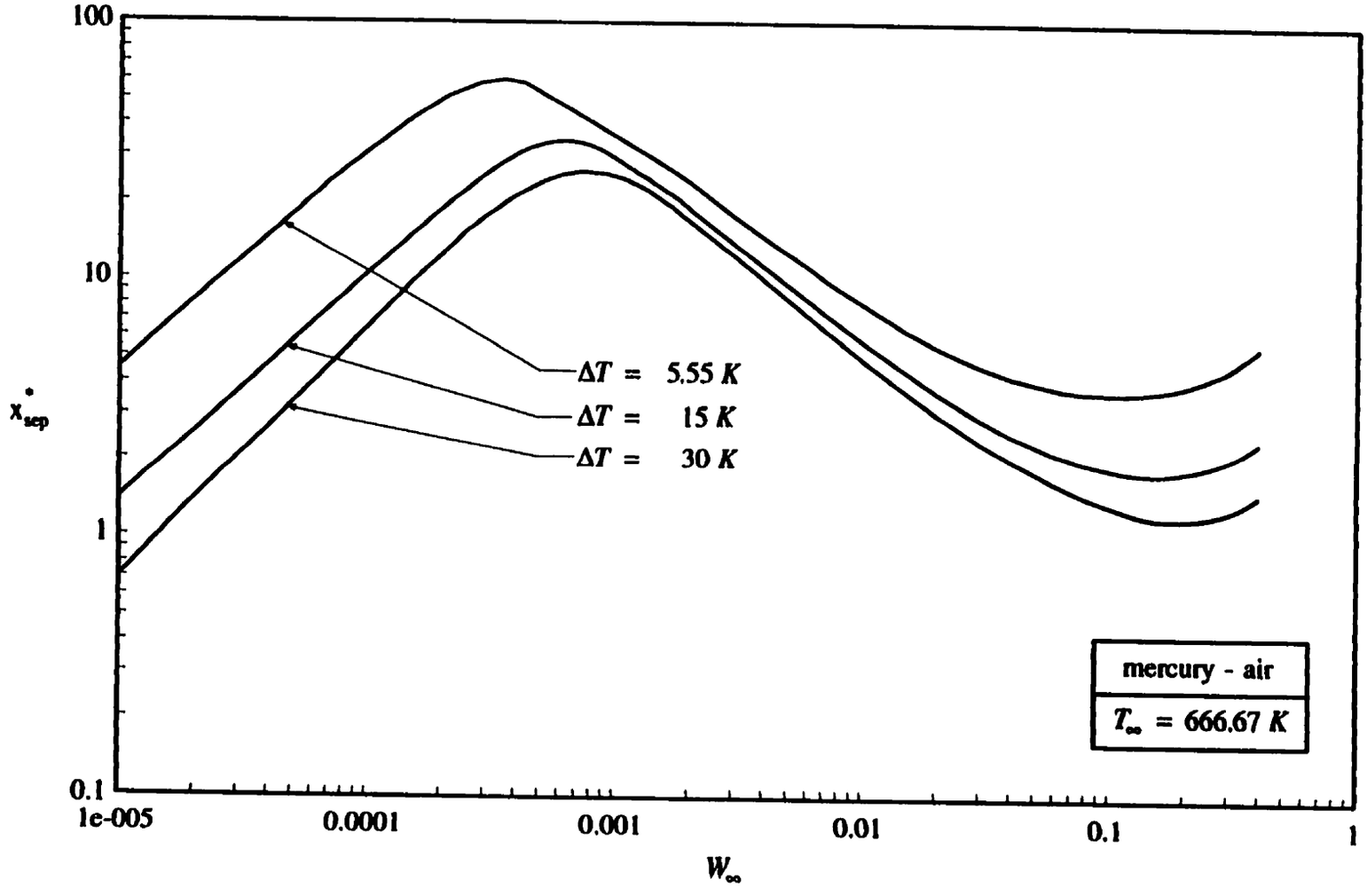

Figure 6.39: Dimensionless separation length for a mercury - air mixture at T_∞ = 666.67 K

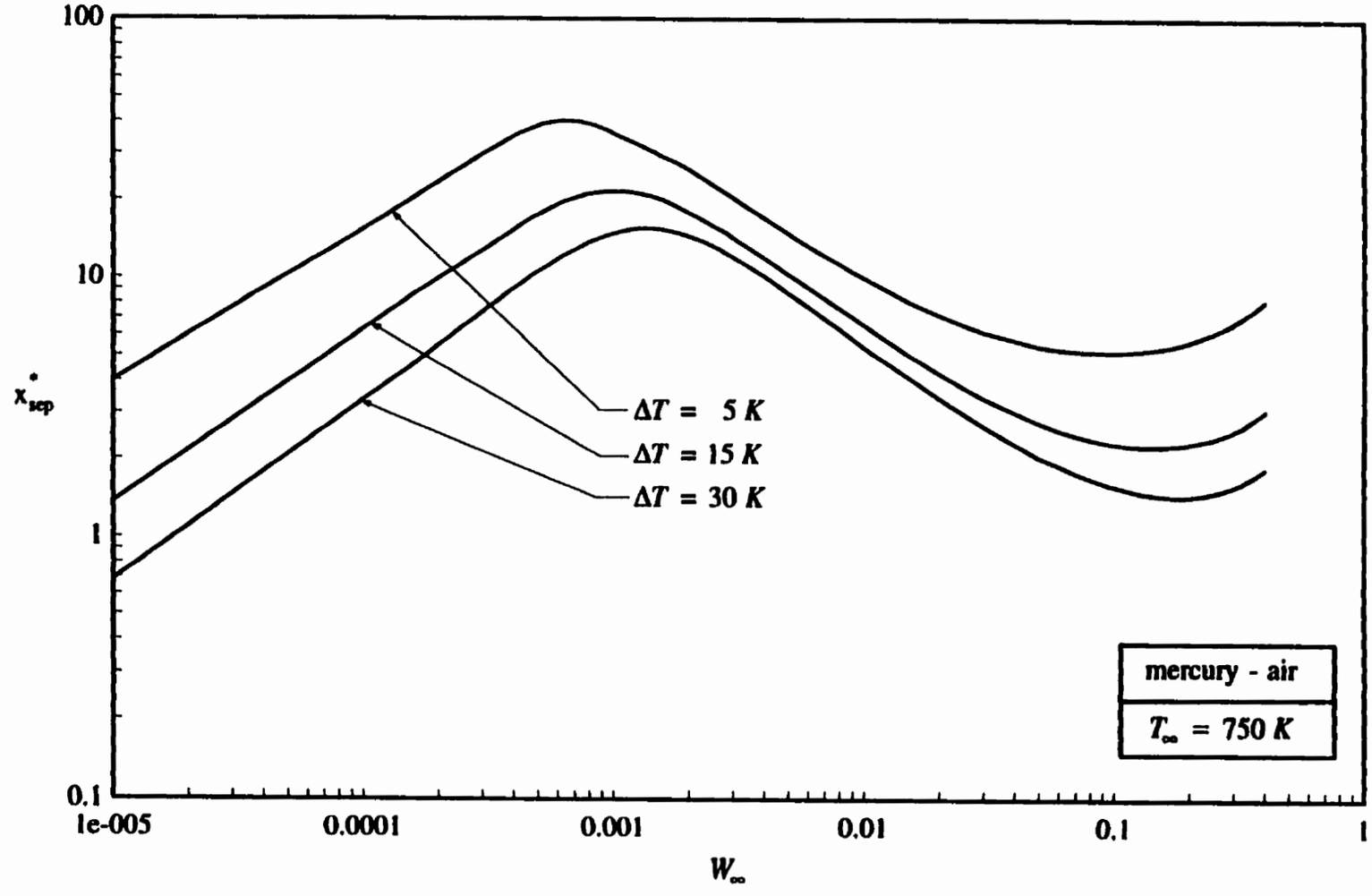

Figure 6.40: Dimensionless separation length for a mercury - air mixture at T_∞ = 750 K

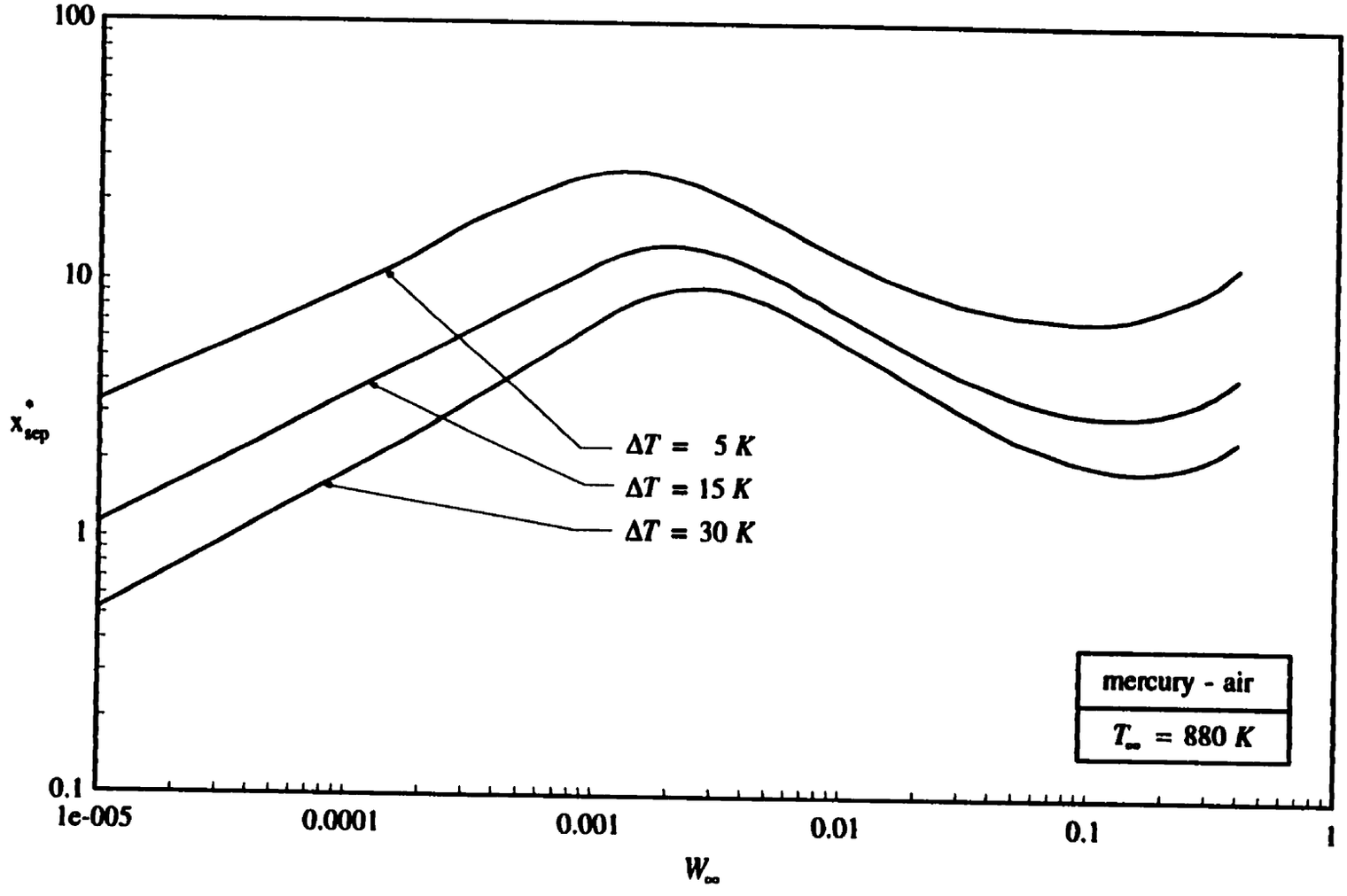

Figure 6.41: Dimensionless separation length for a mercury - air mixture at T_∞ = 880 K

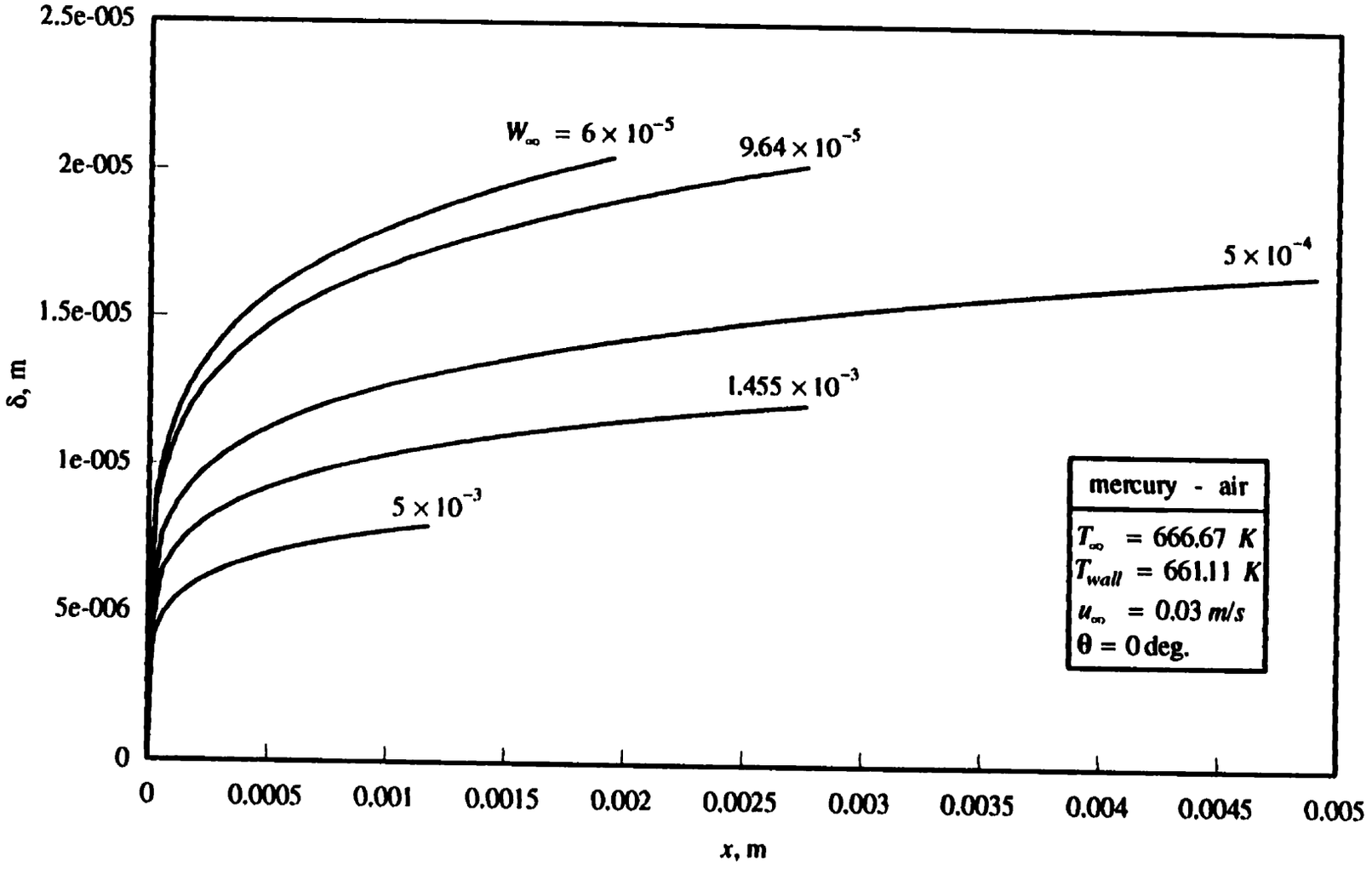

Figure 6.42: The liquid film thickness for a mercury - air mixture at $T_\infty = 666.67\ K$

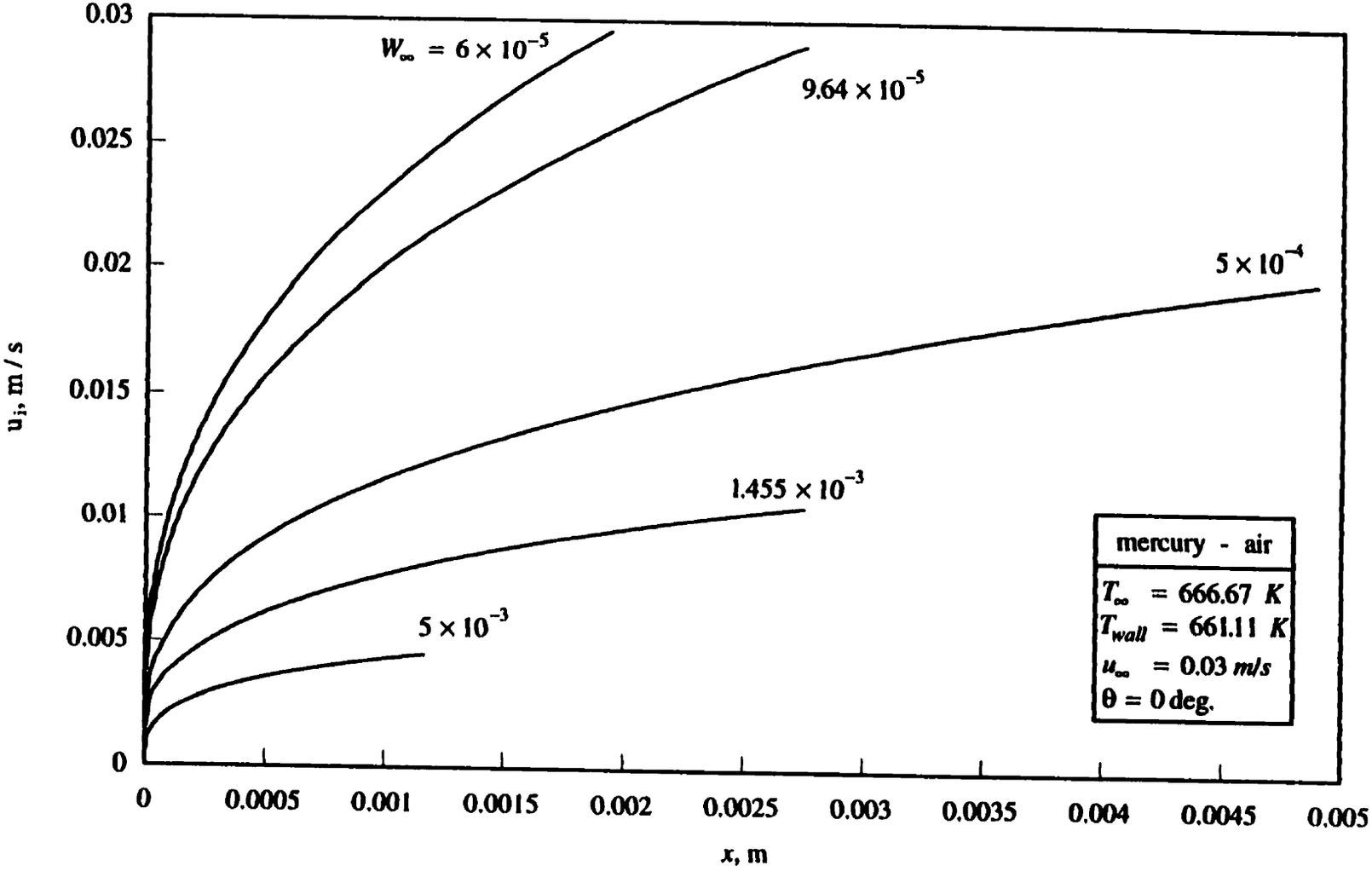

Figure 6.43: Interface velocity for a mercury - air mixture at $T_\infty = 666.67\ K$

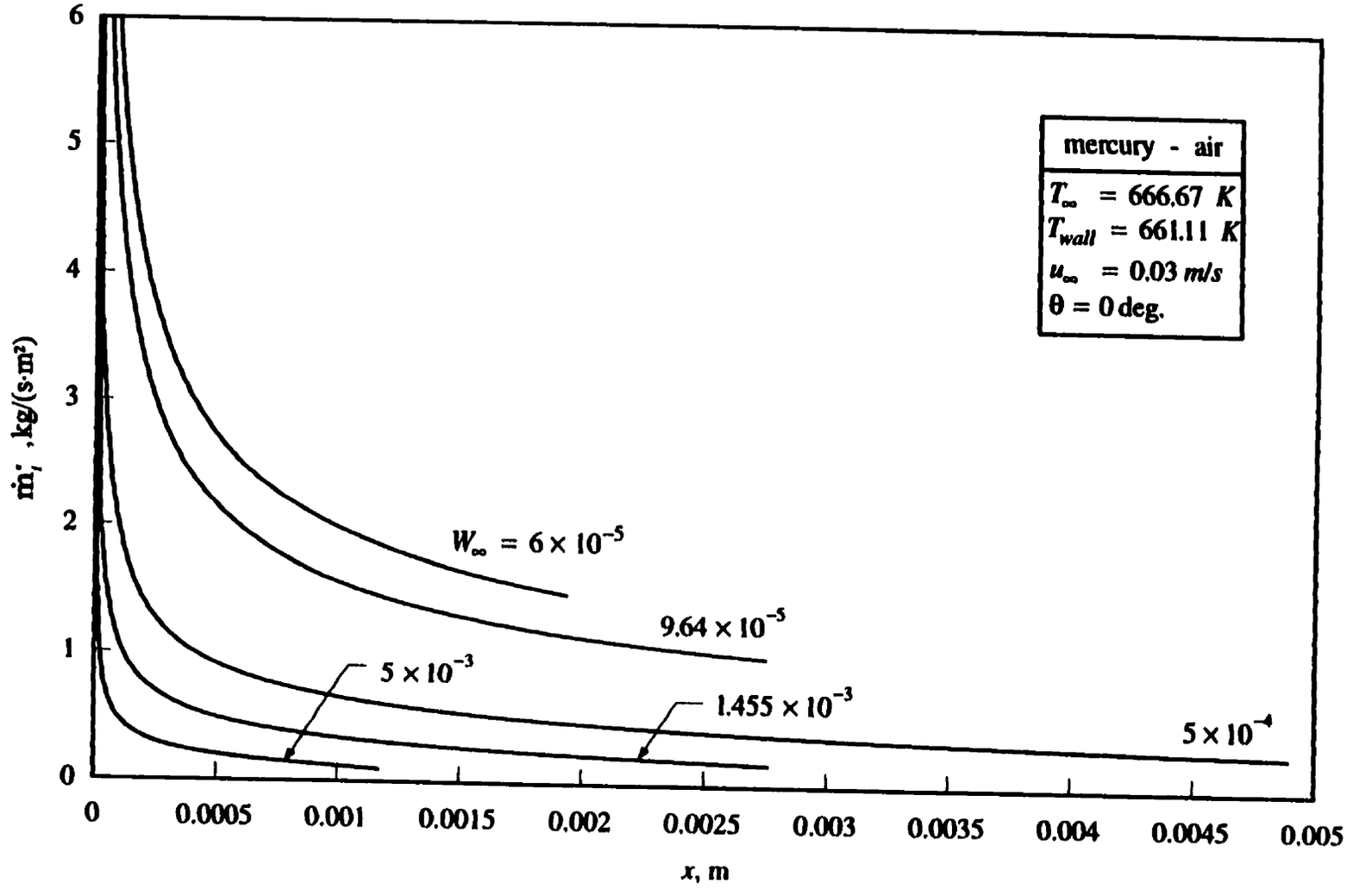

Figure 6.44: The mass flux at the interface for a mercury - air mixture at T_∞ = 666.67 K

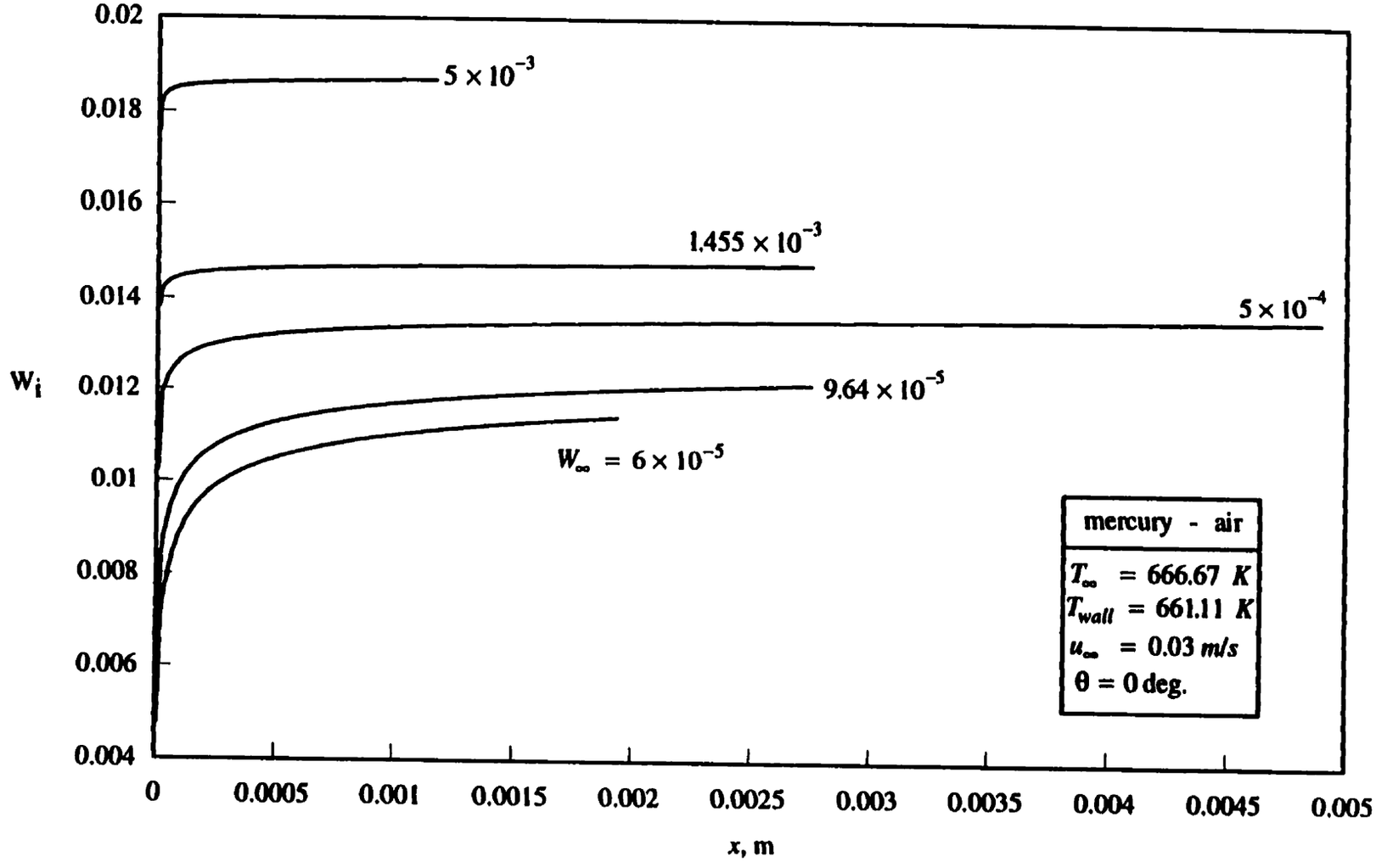

Figure 6.45: Gas concentration at the interface for a mercury - air mixture at $T_\infty = 666.67\ K$

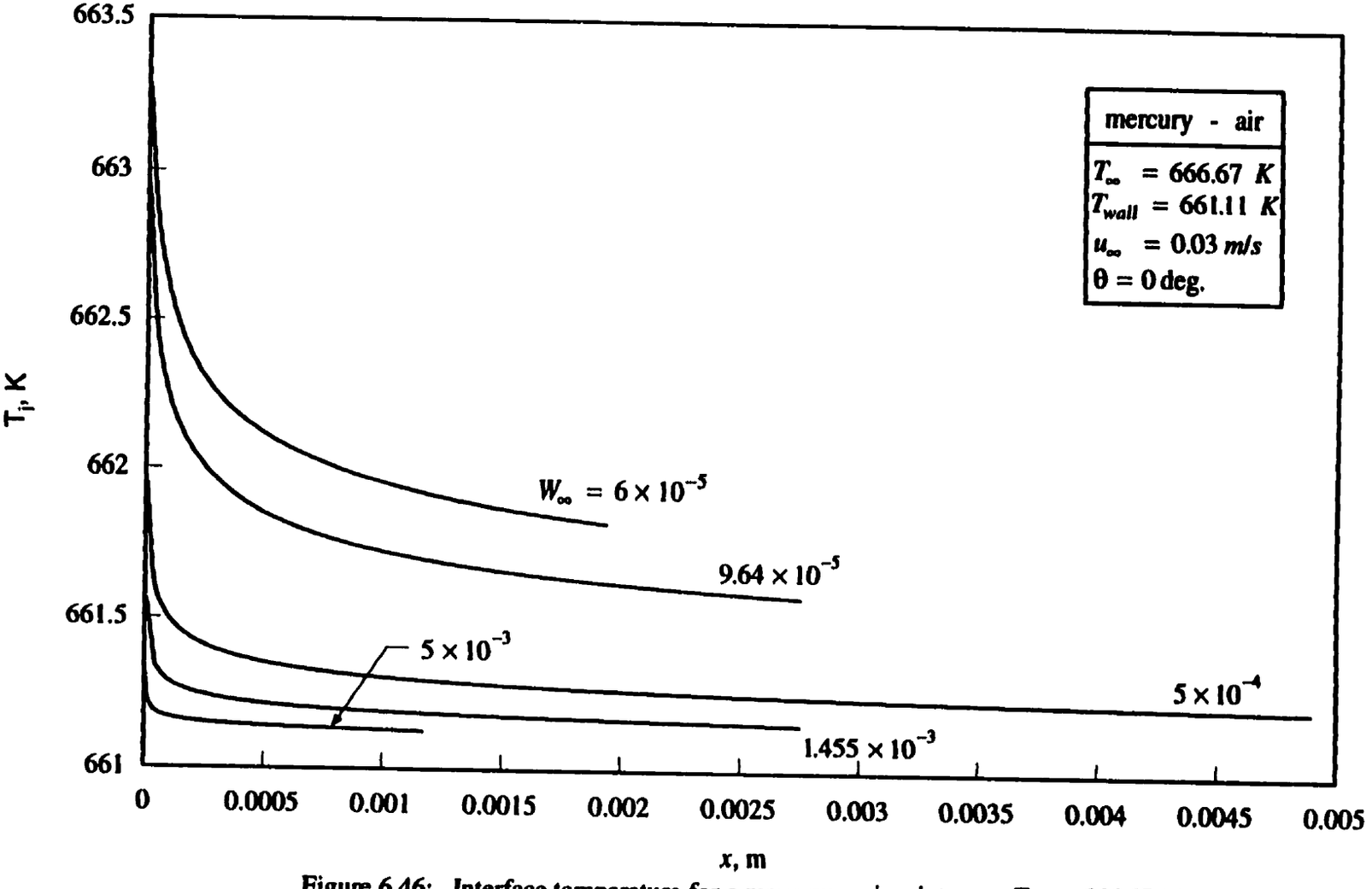

Figure 6.46: Interface temperature for a mercury - air mixture at T_∞ = 666.67 K

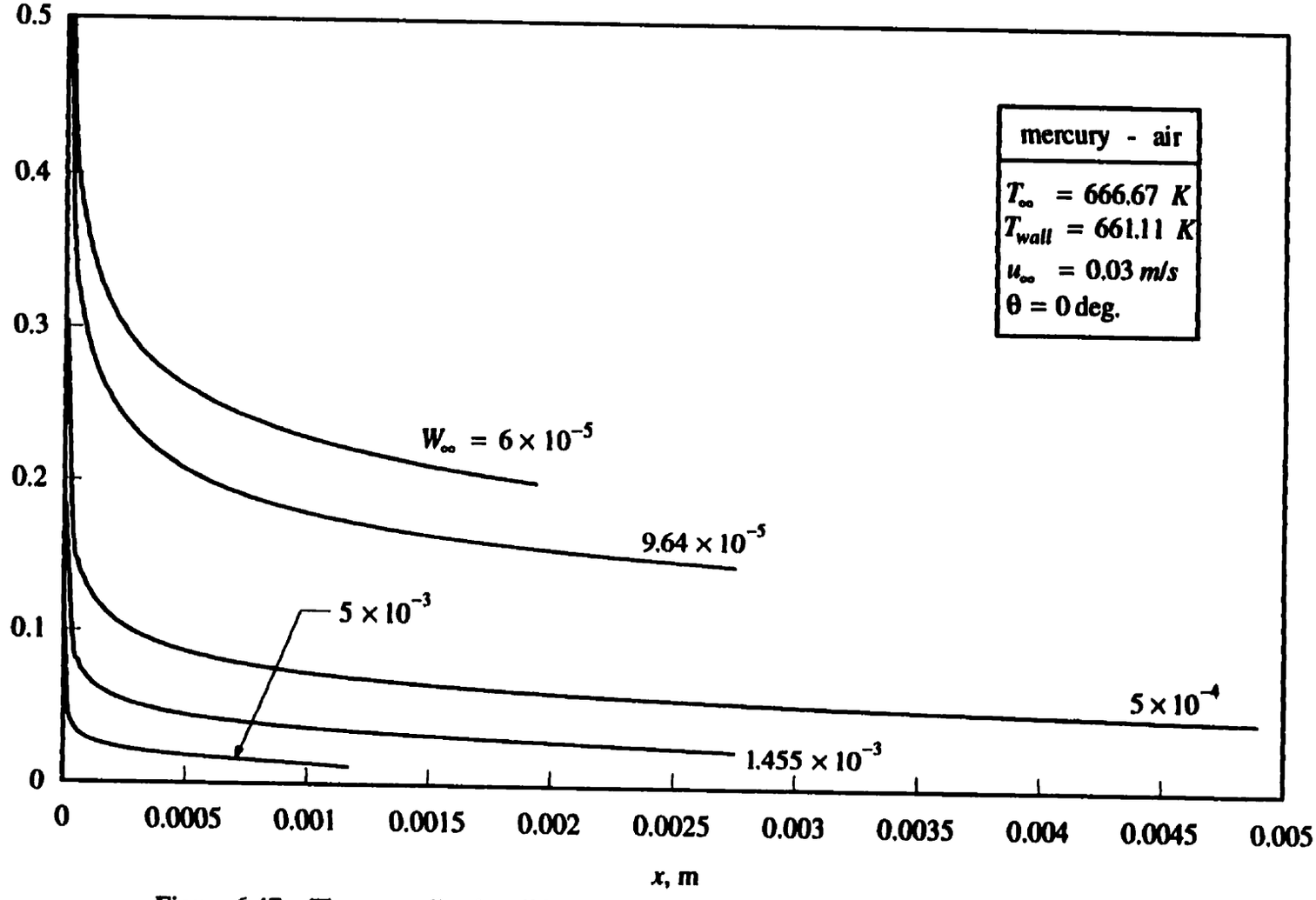

Figure 6.47: The normalized wall heat flux for a mercury - air mixture at T_∞ = 666.67 K

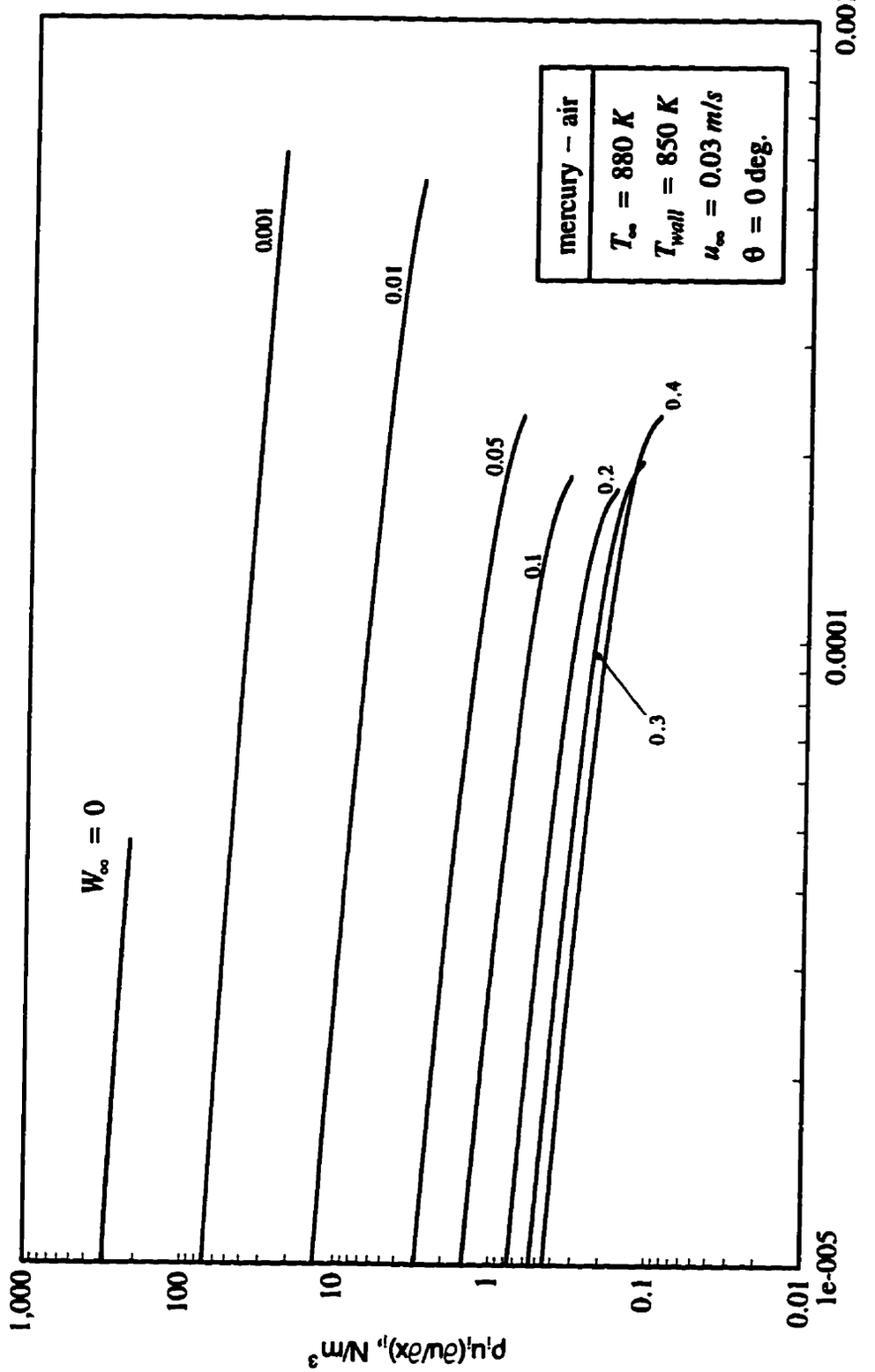

Figure 6.48: Variation of $\rho_i u_i \left(\frac{\partial u}{\partial x}\right)_i$ along the vertical plate for different values of W_∞ for a mercury - air mixture at T_∞ = 880 K, ΔT = 30 K and u_∞ = 0.03 m/s

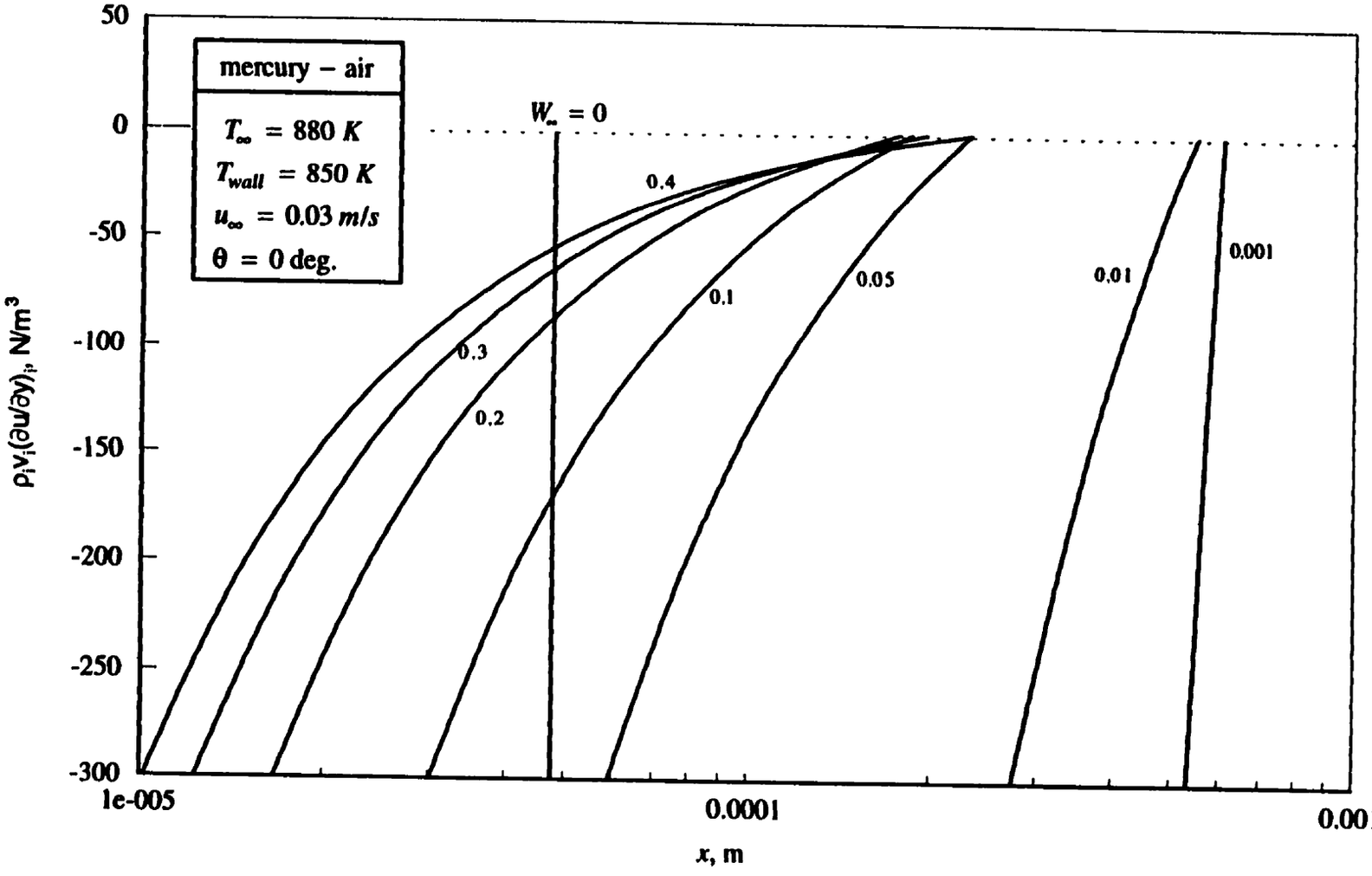

Figure 6.49: Variation of $\rho_i v_i \left(\frac{\partial u}{\partial y}\right)_i$ along the vertical plate for different values of W_∞ for a mercury - air mixture at T_∞ = 880 K, ΔT = 30 K and u_∞ = 0.03 m/s

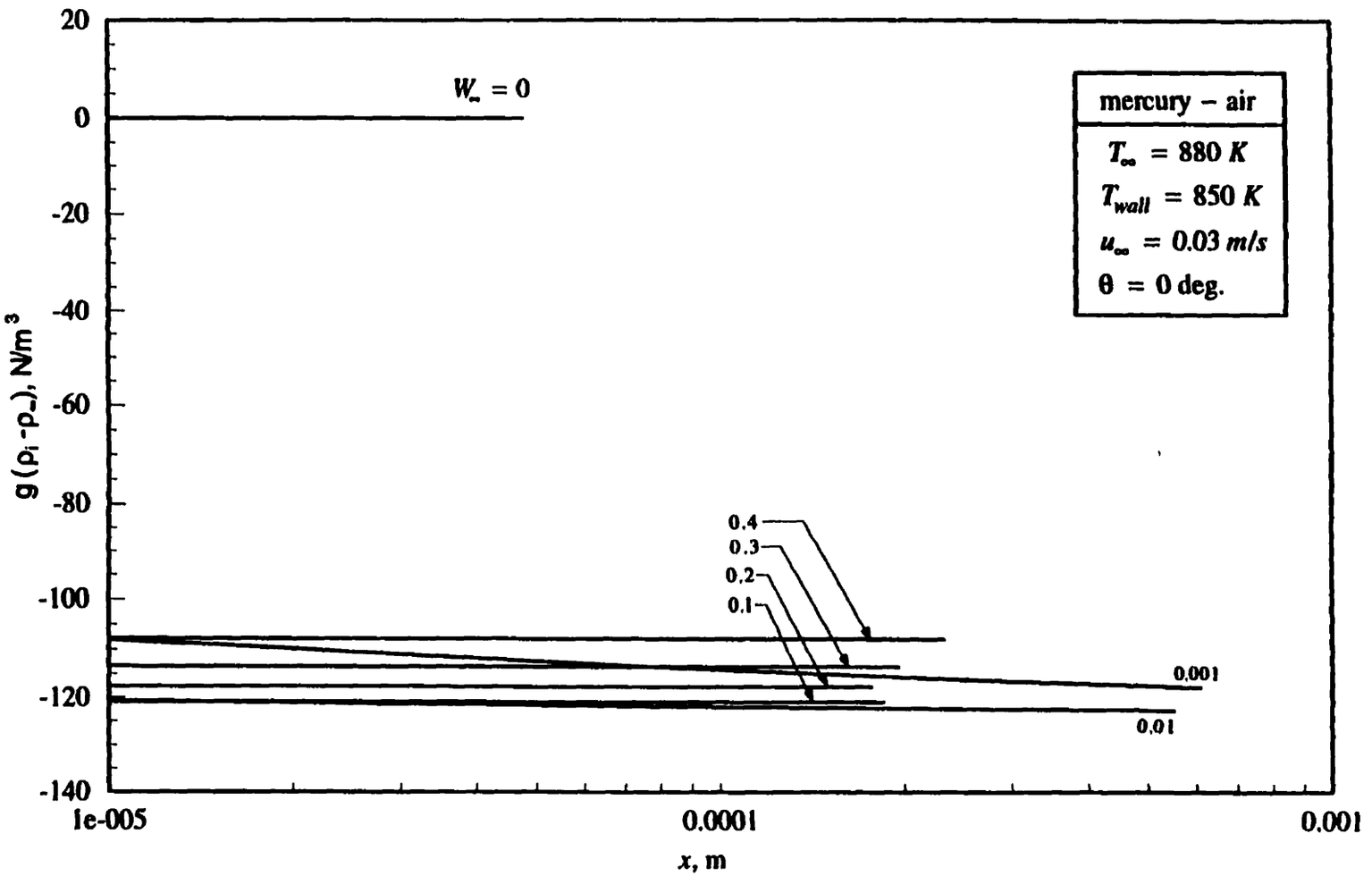

Figure 6.50: Variation of $g(\rho_i - \rho_\infty)$ along the vertical plate for different values of W_∞ for a mercury - air mixture at $T_\infty = 880\ K$, $\Delta T = 30$ K and $u_\infty = 0.03\ m/s$

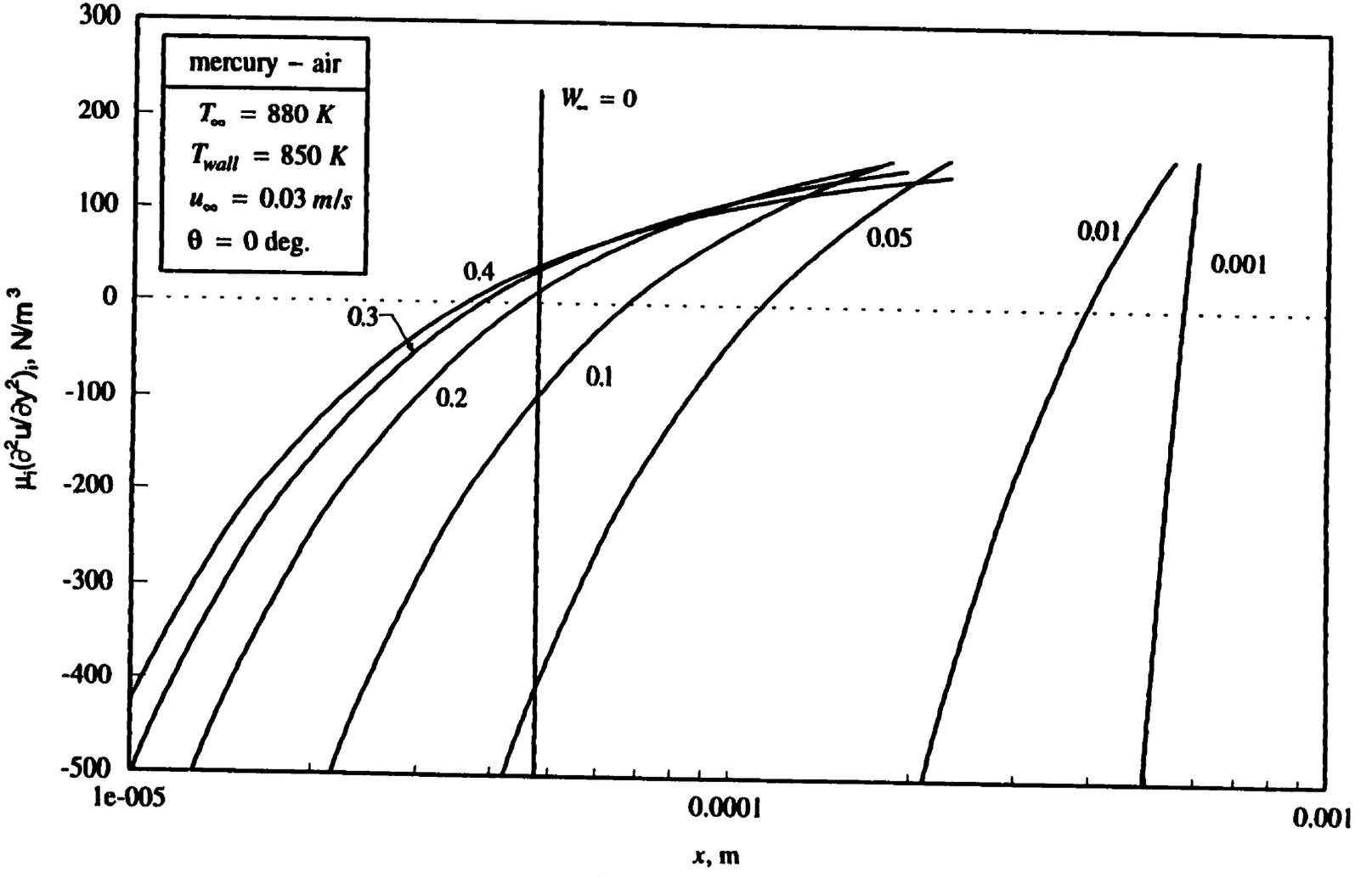

Figure 6.51: Variation of $\mu_i\left(\frac{\partial^2 u}{\partial y^2}\right)_i$ along the vertical plate for different values of W_∞ for a mercury - air mixture at T_∞ = 880 K, ΔT = 30 K and u_∞ = 0.03 m/s

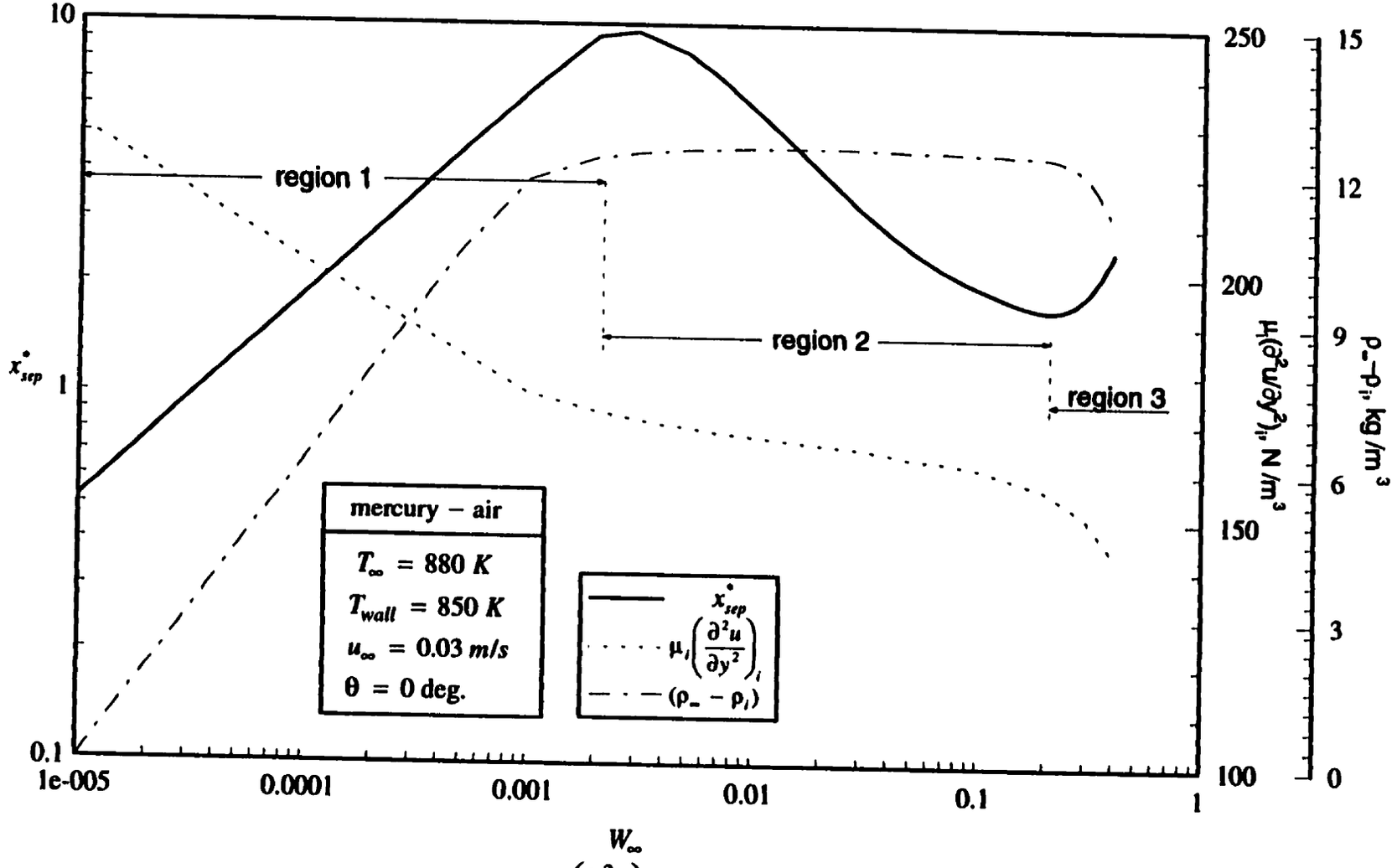

Figure 6.52: Variation of x^*_{sep}, $\mu_i\left(\frac{\partial^2 u}{\partial y^2}\right)_i$ and $(\rho_\infty - \rho_i)$ with W_∞ for a mercury - air mixture at T_∞ = 880 K, ΔT = 30 K and u_∞ = 0.03 m/s

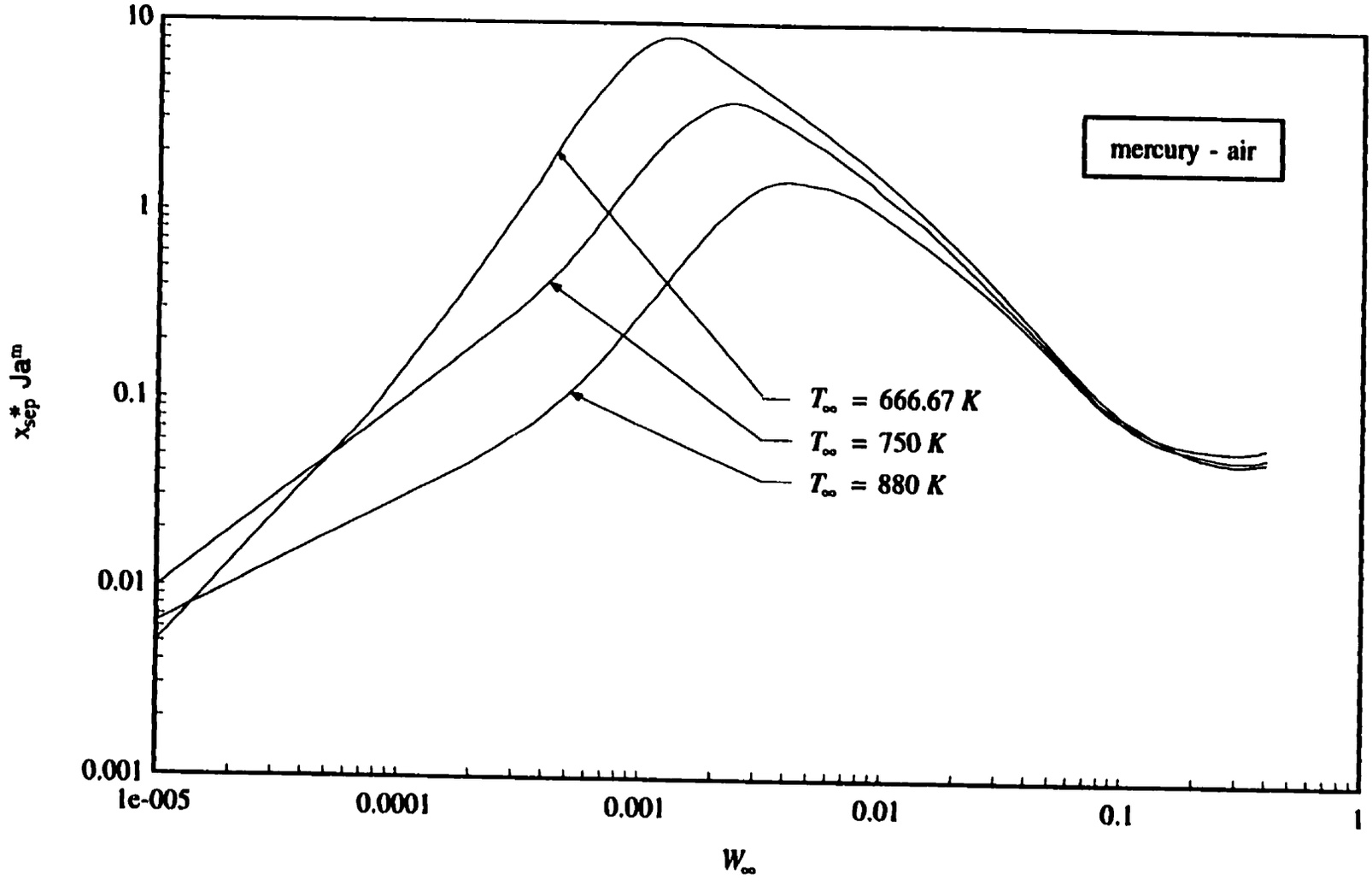

Figure 6.53: Variation of $x^*_{sep}Ja^m$ with W_∞ for a mercury - air mixture

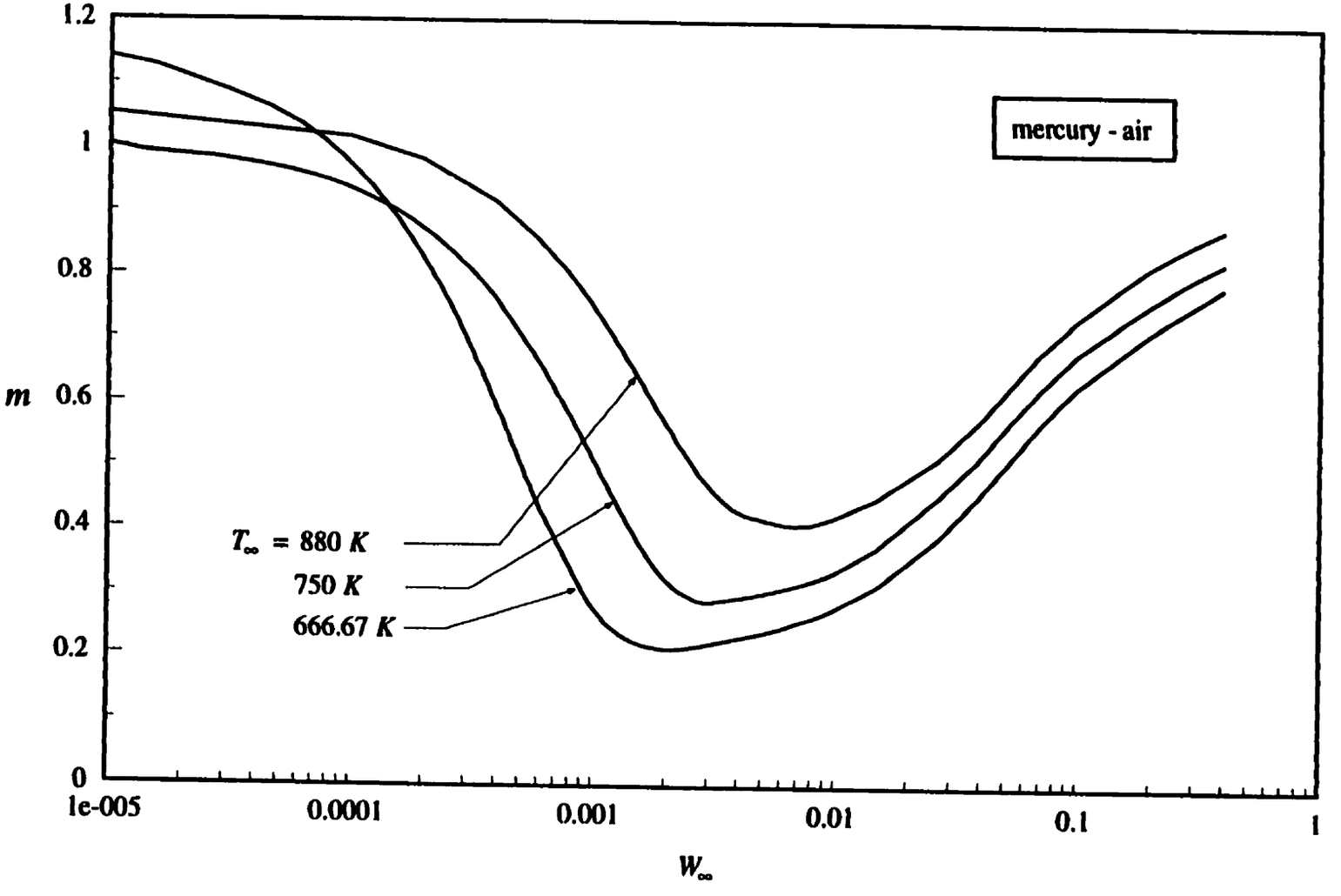

Figure 6.54: Value of the exponent m for a mercury - air mixture

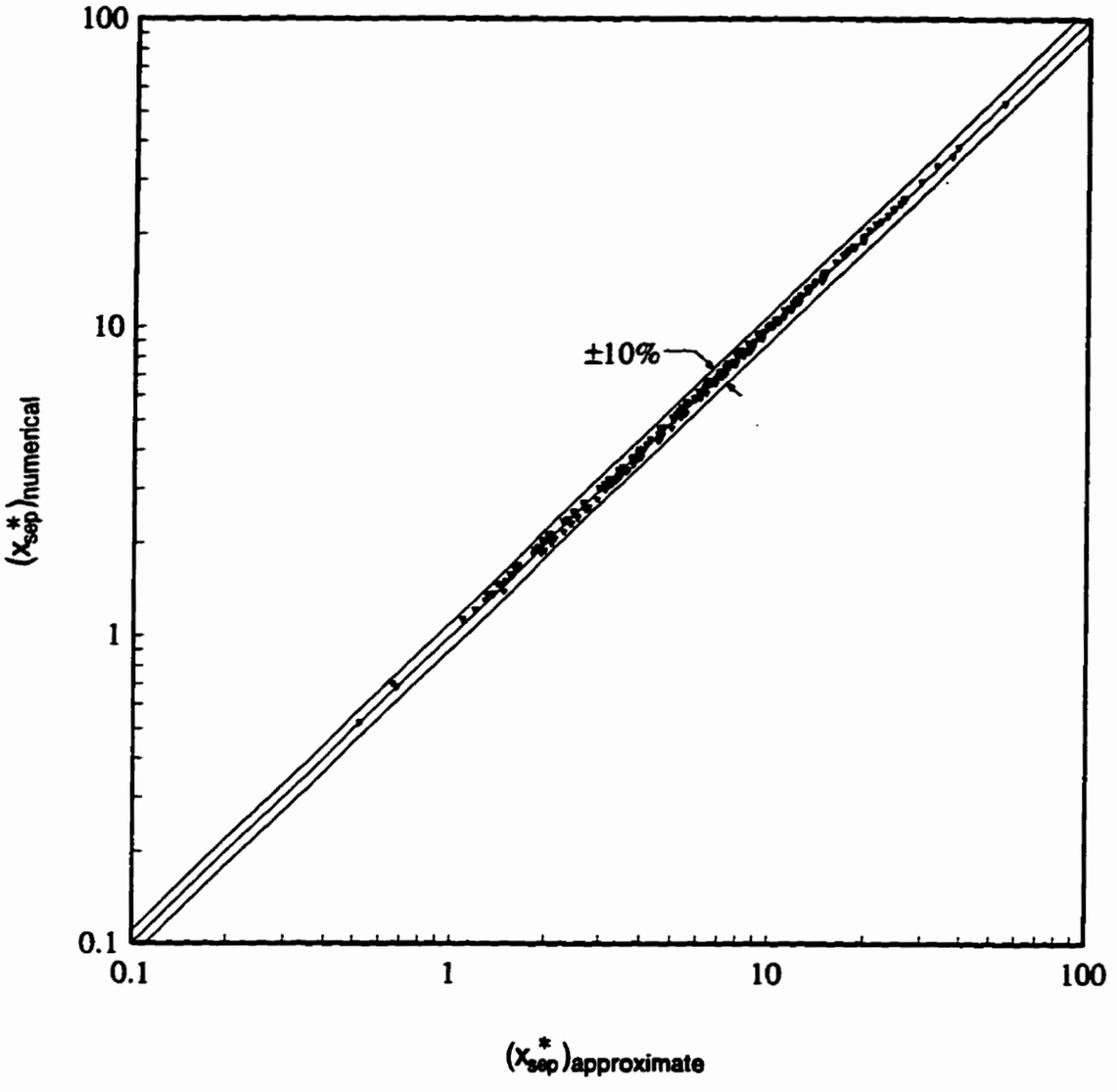

Figure 6.55: Comparison of approximate x^*_{sep} and numerically obtained x^*_{sep} for a mercury - air mixture

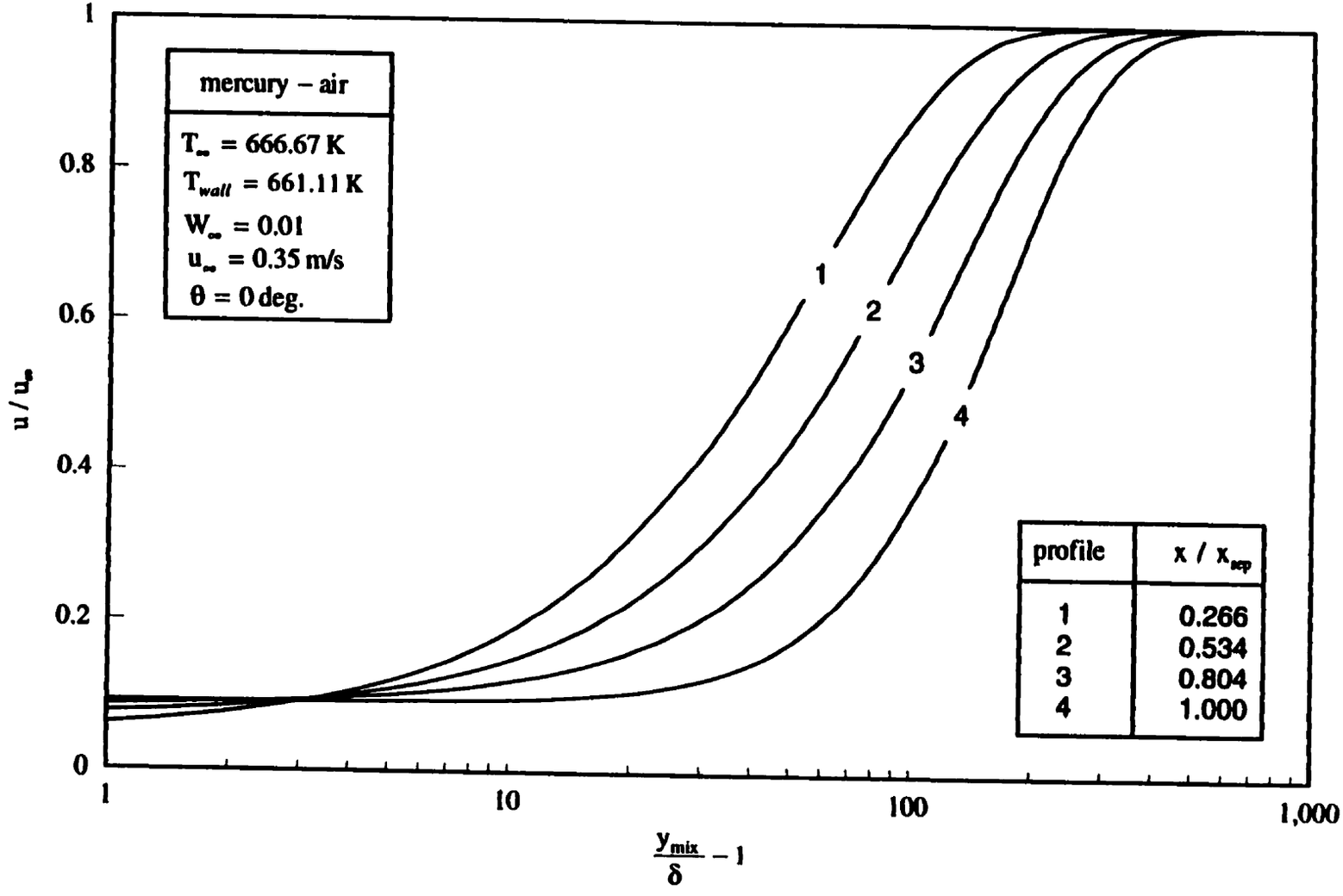

Figure 6.56: Velocity profiles along the plate for a mercury - air mixture at T_∞ = 666.67 K

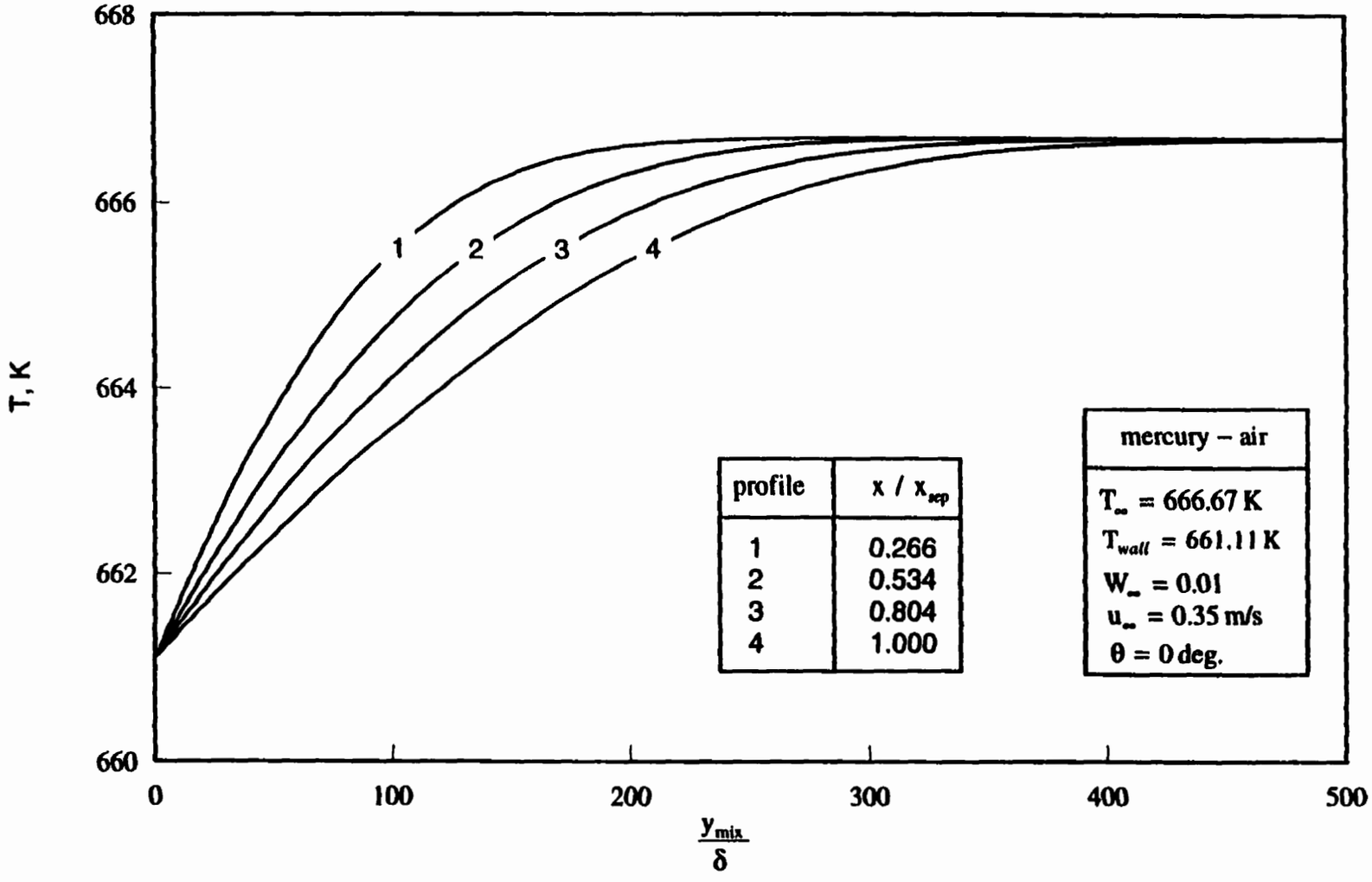

Figure 6.57: Temperature profiles along the plate for a mercury - air mixture at T_∞ = 666.67 K

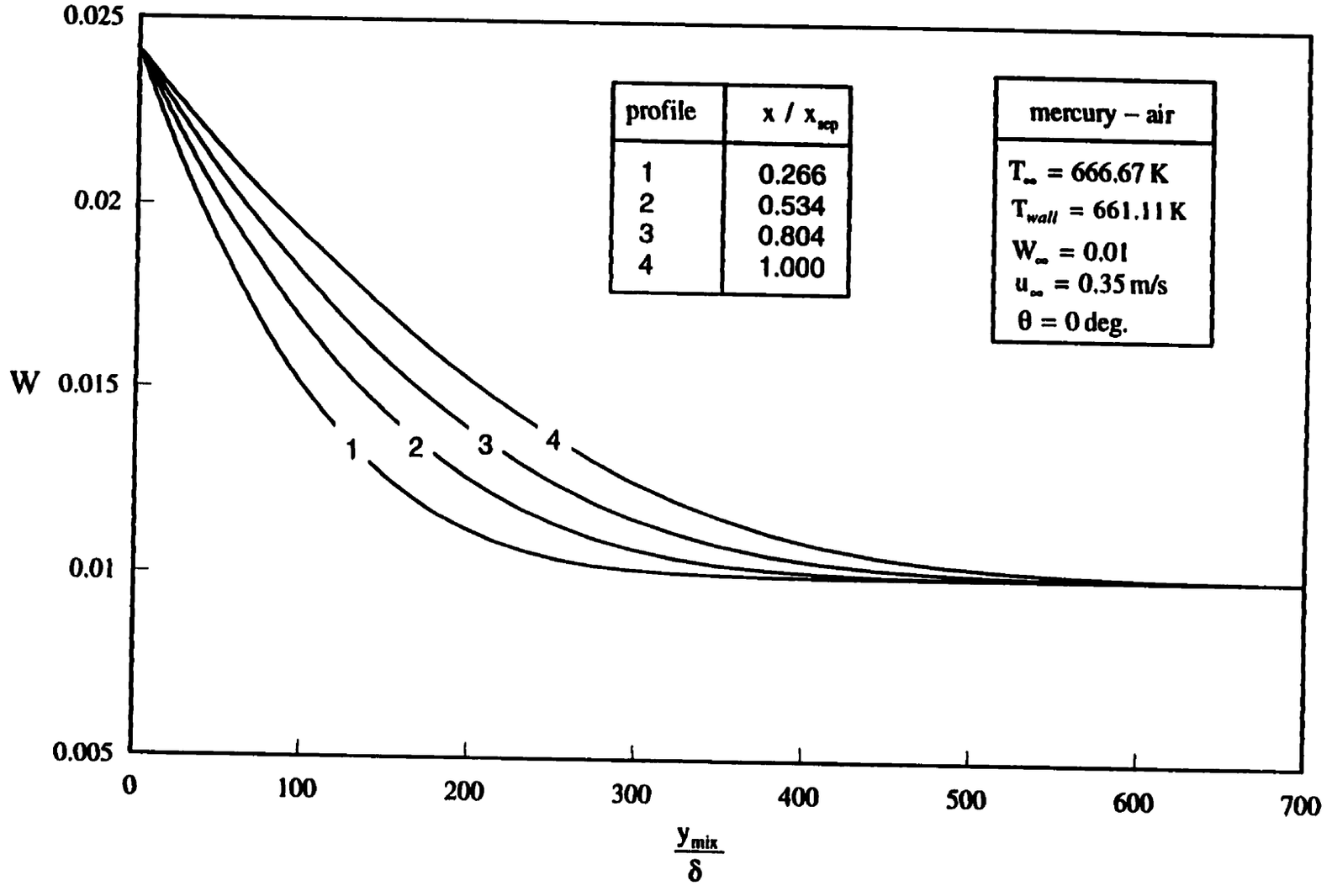

Figure 6.58: Concentration profiles along the plate for a mercury - air mixture at T_∞ = 666.67 K

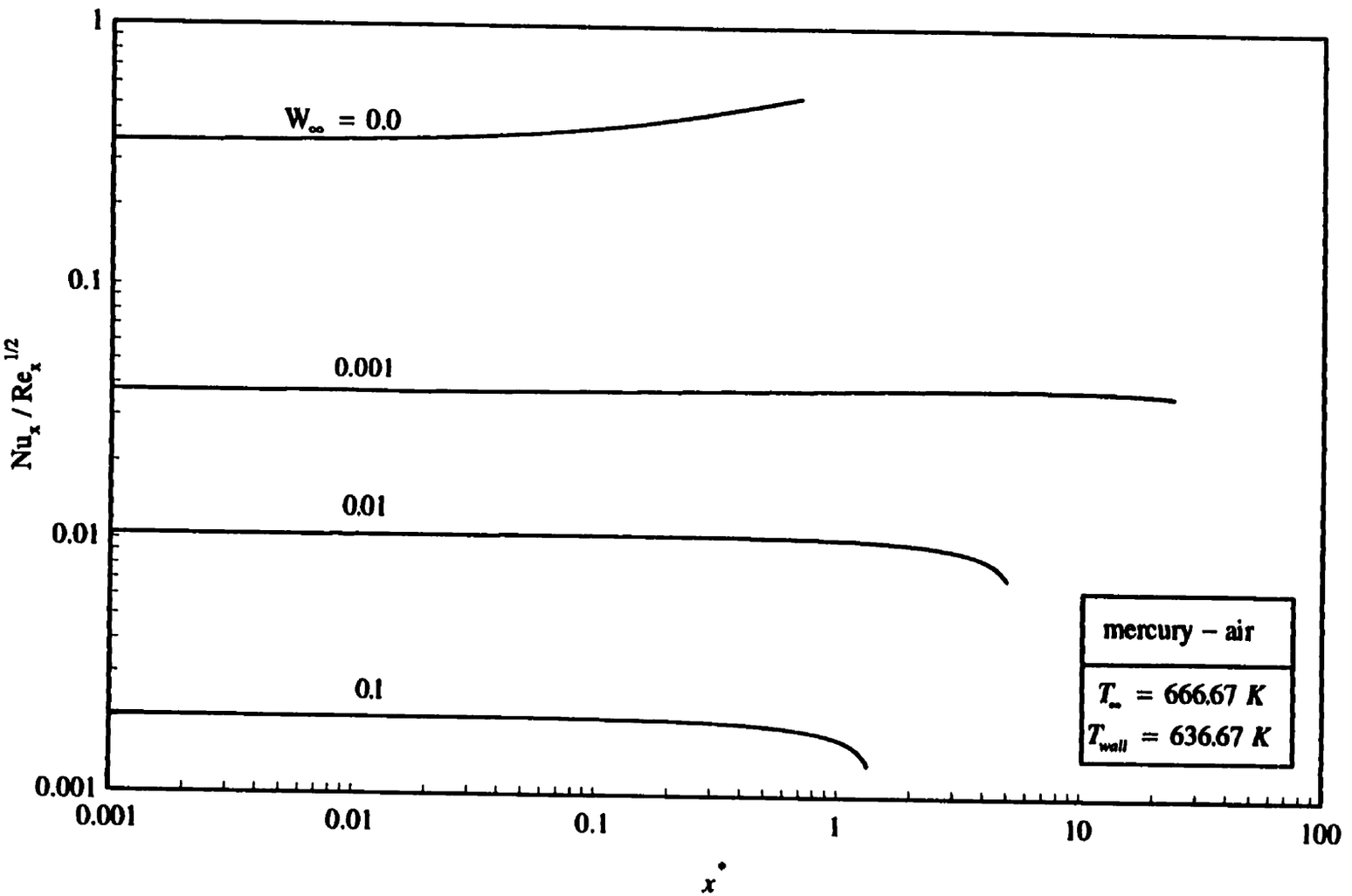

Figure 6.59: Effect of W_∞ on $Nu_x / Re_x^{1/2}$ for a mercury-air mixture at $T_\infty = 666.67K$ and $T_{wall} = 636.67K$

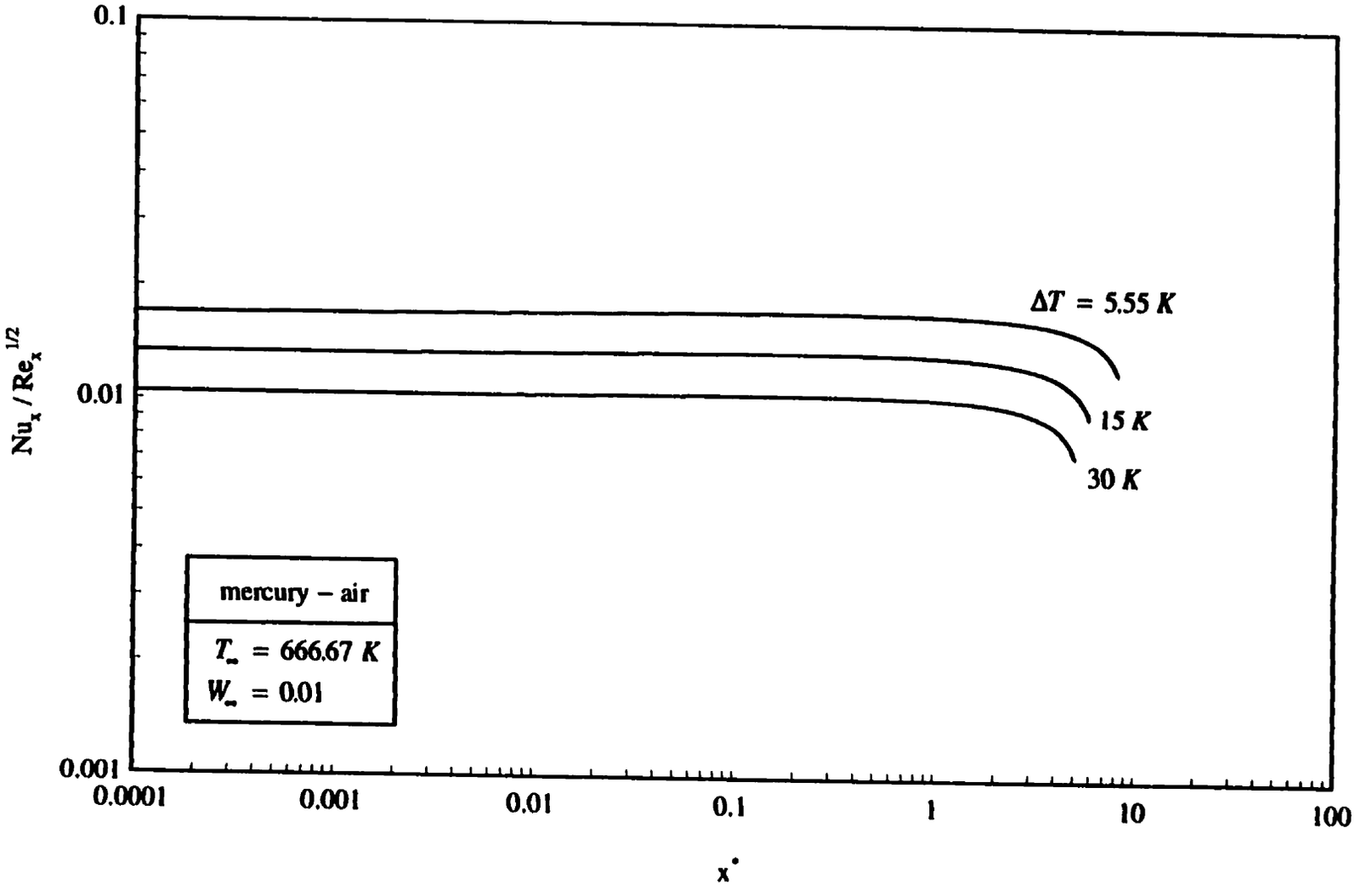

Figure 6.60: Effect of $(T_\infty - T_{wall})$ on Nu_x / $Re_x^{1/2}$ for a mercury-air mixture at T_∞ = 666.67K and W_∞ = 0.01

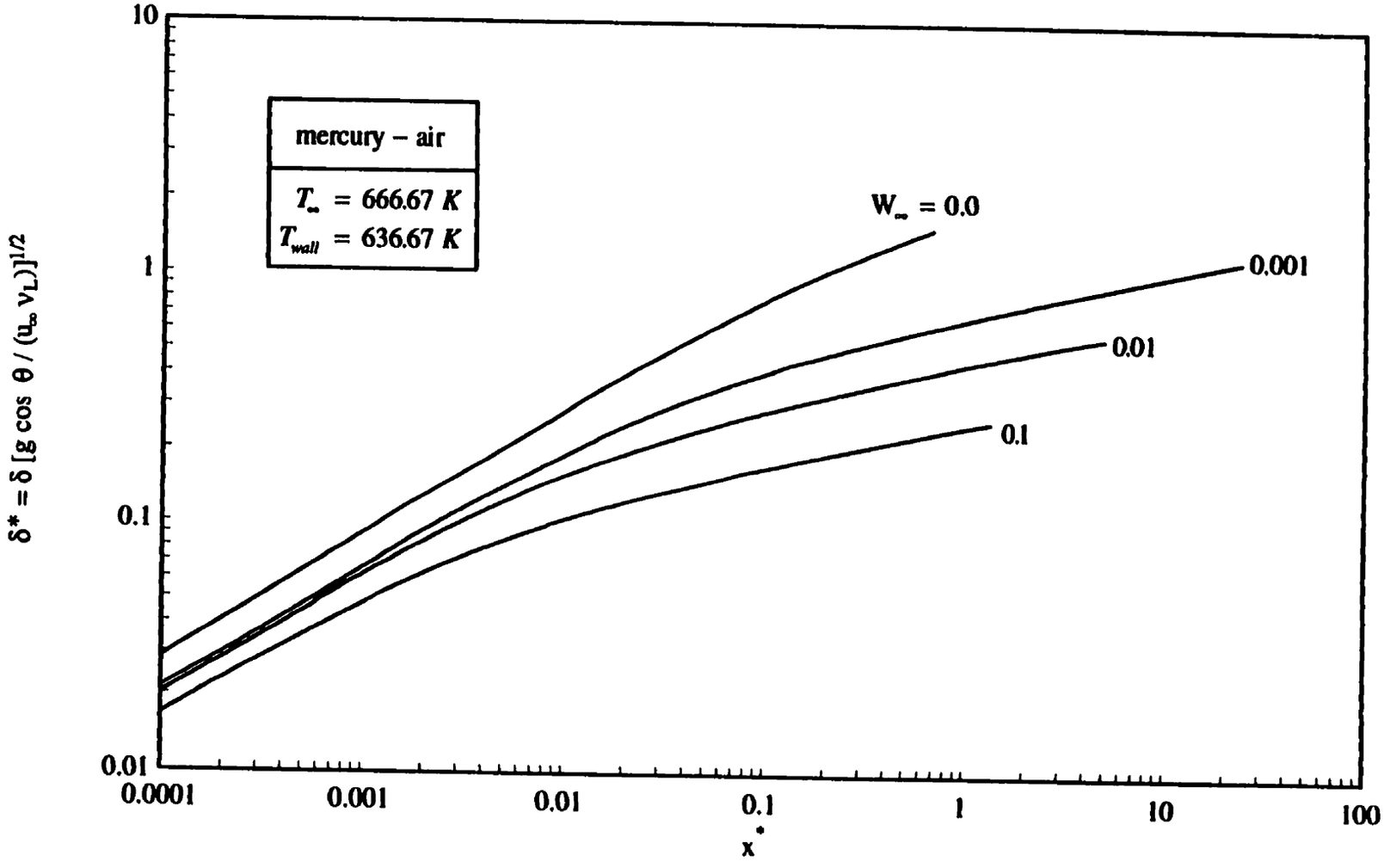

Figure 6.61: Dimensionless liquid film thickness for a mercury-air mixture at T_∞ = 666.67K and T_{wall} = 636.67K

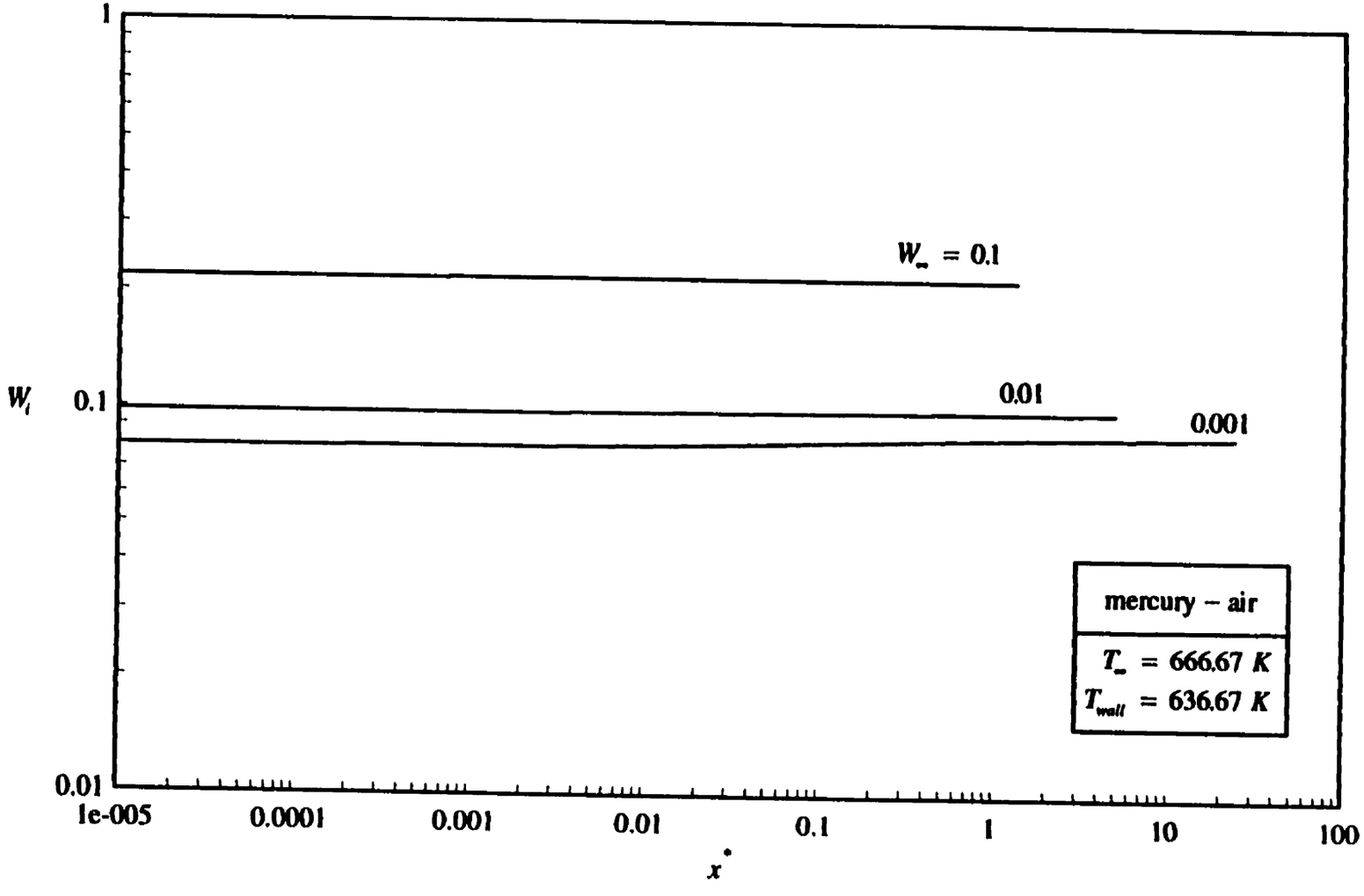

Figure 6.62: Interfacial gas concentration for a mercury-air mixture at $T_\infty = 666.67K$ and $T_{wall} = 636.67K$

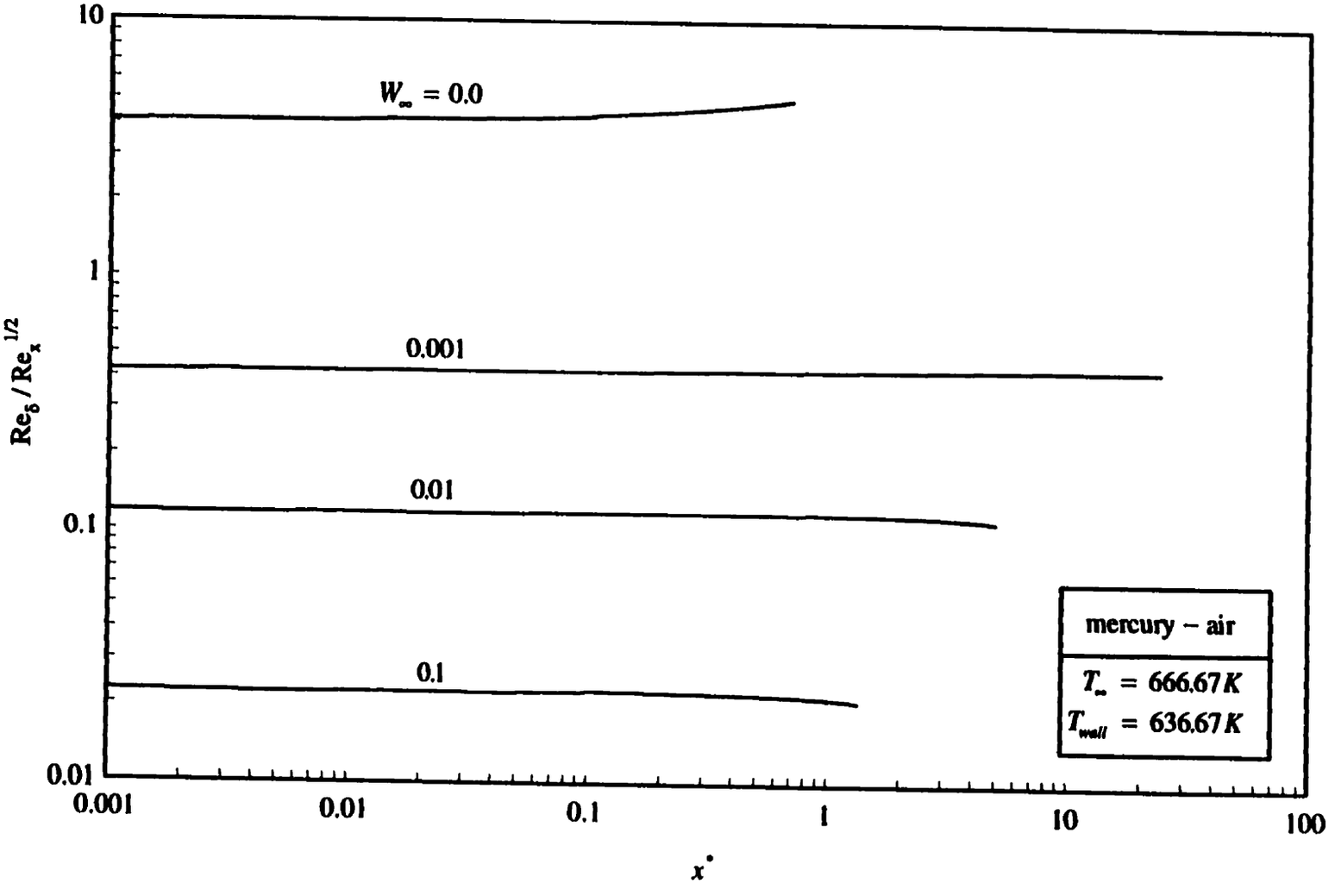

Figure 6.63: Value of Re_δ / $Re_x^{1/2}$ for a mercury - air mixture at T_∞= 666.67K and T_{wall}= 636.67K

Chapter 7

CONCLUDING REMARKS

7.1 Overview

The influence of a lighter gas on laminar film condensation on a vertical or inclined plate has been presented for steam-hydrogen, Freon12-air and mercury-air mixtures. The physical model was described with two sets of the complete boundary layer equations for the liquid film and the mixture. A finite volume method was applied in the solution procedure. Results were focused on the mixture boundary layer separation and on the change in the rate of heat transfer due to the presence of a lighter noncondensable gas. By applying two simple collapsing procedures, the number of independent parameters was reduced. It was found that dependence on the free stream velocity and the plate inclination can be eliminated by introducing the dimensionless separation length, x^*_{sep}. Also, a reasonably good approximation was obtained introducing the Jakob number, which enabled presentation of the results in a more concise form. This second collapsing procedure produced the results in x^*_{sep} that are within 10% compared to the x^*_{sep} obtained numerically. The results related to the separation distance are summarized in two graphs for each vapor-gas combination, which can be used to estimate the separation location for a specified range of input parameters.

The three main factors that affect the separation distance are the buoyant force and the two inertia terms in the momentum equation for the mixture boundary layer. The buoyant force is the result of a density difference across the mixture layer. It was found that the this force reaches a maximum value over the free stream gas concentration range studied. Further increasing of W_∞ reduces the buoyant force, which extends the separation location. For very low gas concentration the buoyant force becomes insignificant due to the very small density difference between the interface and the free stream. The inertia term which includes the v-velocity is always negative at the interface and it increases the separation distance. In most cases this term is significant along the plate except in the vicinity of the separation point where it becomes equal to zero. The influence of the other inertia term (due to the film interface velocity acceleration), depends on the vapor-gas mixture. Computations show that this term had a fundamentally different effect on x^*_{sep} for small values of W_∞ in the case of mercury-air compared with the other two mixtures. This term changes, however, with W_∞ in the same way for all three vapor-gas combinations. The inertia terms and the buoyant term change, in general, along the plate at a rate that depends on the free stream gas concentration. The combined effect of all three terms determines the separation distance.

In terms of heat transfer for small values of W_∞ the change of the Nu_x / $\mathrm{Re}_x^{1/2}$ along x^* is similar to the case of a vapor-heavier gas mixture under similar conditions. The essential difference between the cases of lighter and heavier gas on Nu_x / $\mathrm{Re}_x^{1/2}$ becomes evident in the vicinity of the separation point for higher values of a gas concentration. Near that

point, the value of $Nu_x / \mathrm{Re}_x^{1/2}$ for the lighter gas case reaches a maximum and then decreases sharply. This was directly correlated to the deceleration of the mixture boundary layer , which reduces the rate of heat transfer to the wall. As x^* approaches zero, the value of $Nu_x / \mathrm{Re}_x^{1/2}$ asymptotically approaches a constant value, which corresponds to the limiting case of pure forced convection condensation on a horizontal plate. This behavior is typical of all vapor-gas combinations that were considered and for all values of W_-. The changes of other parameters such as gas concentration at the interface, liquid film thickness and the film Reynolds number (normalized with the local Reynolds number) are not qualitatively different from those seen during condensation from a mixture with a heavier noncondensable gas.

7.2 Observations Regarding the Steam-Hydrogen Mixture

A characteristic of the separation point results for this mixture is that x^*_{sep} keeps increasing as W_- approaches zero. The reason for this was found to be due to the small magnitude of $\rho_i u_i \left(\frac{\partial u}{\partial x}\right)_i$ as well as in a small rate at which this term increases as W_- approaches zero. This suggests that there is no other term which can counter the effect of the $\rho_i v_i \left(\frac{\partial u}{\partial y}\right)_i$ term. The other part of the x^*_{sep} versus W_- curves, for higher values of W_-, follows the trend of the change of x^*_{sep}, which is common for all three mixtures: decreasing to a minimum and then increasing.

A comparison of the axial change of q_{wall}/q_0 for steam-air and steam-hydrogen on a horizontal plate shows that the value of q_{wall}/q_0 for steam-hydrogen is 33% lower than that for steam-air. The detrimental effect of a lighter gas (hydrogen) is even more pronounced on a vertical plate, due to the buoyant force. The rate of change of q_{wall}/q_0 showed that the effect of the buoyant force appears to be the highest near the separation location where the rate of q_{wall}/q_0 starts to increase in magnitude, unlike the rate for steam-air which asymptotically approaches zero.

7.3 Observations Regarding the Freon12-Air Mixture

Qualitatively, a comparison of the results obtained for Freon12-air mixture with those obtained for steam-hydrogen mixture does not show a significance difference. The value of x^*_{sep} keeps increasing as W_∞ is reduced, while for higher values it follows the pattern seen in other two mixtures.

A maximum value of $Nu_x / \mathrm{Re}_x^{1/2}$ was detected for $W_\infty = 0.1$ while for lower gas concentration, and for pure vapor condensation, the values of $Nu_x / \mathrm{Re}_x^{1/2}$ keep increasing along the plate, which is similar to the change of vapor-heavier gas heat transfer coefficient. The ratio between the normalized Nusselt number for $W_\infty = 0$ and $W_\infty = 0.1$ at the separation location is more than five, which indicates the strong detrimental effect of a lighter gas compared to a pure vapor condensation.

7.4 Observations Regarding the Mercury-Air Mixture

The most outstanding feature related to a mercury-air mixture is the decrease of x^*_{sep} as W_∞ approaches zero. Although the buoyant force is almost zero and the second inertia term (which includes the suction velocity) becomes large as W_∞ approaches zero, both the rate at which $\rho_i \mu_i \left(\frac{\partial u}{\partial x}\right)_i$ increases and its magnitude are large enough to reduce the value of x^*_{sep}. This effect was found to be primary reason for the decrease in x^*_{sep} as W_∞ approaches zero. This behavior is the opposite of the behavior seen for other two mixtures.

The local Nusselt number (normalized with the local Reynolds number) changes very little except when $W_\infty = 0$ and in the vicinity of the separation point. This small change occured only for liquid metals. Other parameters of interest including dimensionless film thickness, gas concentration at the interface and $\mathrm{Re}_\delta / \mathrm{Re}_x^{1/2}$, also showed very little change along the plate.

7.5 Recommendations

In order to investigate further the effect of inertia terms on separation during the liquid-metal vapor condensation it would be useful to set up a new vapor (liquid metal)-lighter gas combination. The calculation done on all three mixtures showed that all characteristic

phenomena related to the mixture boundary layer separation were noticeable on all total pressure levels that were used in this work, so it is sufficient to choose the total pressure range between 0.5 bar and 2 bars. However it is very important to vary the gas concentration over a wide range (for example, between 10^{-6} and 0.5 or higher). The criterion for the lower value of free stream velocity should be the magnitude of the value of x_{sep}, or as an alternative, the deviation of x^{*}_{sep} from its constant value. No standard recommendations related to the grid parameter or convergence criteria can be made because those parameters are highly dependent on the particular vapor-gas mixture used.

One of the limitations of the solution procedure is slow convergence particularly at the higher values of W_{∞}. A coupling between the momentum equations and the gas conservation equation, or between all governing equations could improve convergence and reduce CPU time.

The present model is based on laminar film condensation and it is limited to small free stream velocities. Defining a new model for turbulent flow would offer much greater opportunity in further investigations.

REFERENCES

Acrivos, A., 1958, "Combined Laminar Free- and Forced-Convection Heat Transfer in External Flows", *A.I.Ch.E. Journal*, Vol. 4, No. 3, pp. 285-289.

Beaton, C.F., Hewitt, G.F., 1989, *Physical Property Data for the Chemical and Mechanical Engineer*, Hemisphere Publishing Corporation, New York.

Chang, P.K., 1970, *Separation of Flow*, Pergamon Press, Oxford.

Cess, R.D., 1960, "Laminar Film Condensation on a Flat Plate in the Absence of a Body Force", *Z. Angew. Math. Phys.*, Vol. 11, pp. 426-433.

Chin, Y.S., 1995, Numerical Solution of the Complete Two-Phase Model for Laminar Film Condensation With a Noncondensable Gas, M.Sc. Thesis, The University of Manitoba.

Denny, V.E., and Mills, A.F., 1969, "Nonsimilar Solutions for Laminar Film Condensation on a Vertical Surface", *Int. J. Heat Mass Transfer*, Vol. 12, pp. 965-979.

Denny, V.E., Mills, A.F., and Jusionis, V.J., 1971, "Laminar Film Condensation From a Steam-Air Mixture Undergoing Forced Flow Down a Vertical Surface", *Journal of Heat Transfer*, Vol. 93, pp. 297-304.

Denny, V.E., and Jusionis, V.J., 1972, "Effects of Noncondensable Gas and Forced Flow on Laminar Film Condensation", *Int. J. Heat Mass Transfer*, Vol. 15, pp. 315-326.

Fujii, T., and Uehara, H., 1972, "Laminar Filmwise Condensation on a Vertical Surface", *Int. J. Heat Mass Transfer*, Vol. 15, pp. 217-233.

Incropera, F.P., DeWitt, D.P., 1985, *Fundamentals of Heat and Mass Transfer*, 2nd ed., John Wiley & Sons, New York, pp. 767-775.

Irvine, T.F. Jr., and Liley, P.E., 1984, *Steam and Gas Tables with Computer Equations*, Academic Press, London.

Jacobs, H.R., 1966, "An Integral Treatment of Combined Body Force and Forced Convection in Laminar Film Condensation", *Int. J. Heat Mass Transfer*, Vol. 9, pp. 637-648.

Kakac, S.,Shah, R.K.,Aung, W., 1987, *Handbook of Single-Phase Convective Heat Transfer*, John Wiley & Sons, New York.

Koh, J.C.Y., 1962, "Film Condensation in a Forced-Convection Boundary-Layer Flow", *Int. J. Heat Mass Transfer*, Vol. 5, pp. 941-954.

Launder, B.E., 1964, "An Improved Pohlhausen-Type Method of Calculating the Two-Dimensional Laminar Boundary Layer in a Pressure Gradient", *Journal of Heat Transfer*, Vol. 86, pp. 360-364.

Lucas, K., 1976, "Combined Body Force and Forced Convection in Laminar Film Condensation of Mixed Vapours—Integral and Finite Difference Treatment", *Int. J. Heat Mass Transfer*, Vol. 19, pp. 1273-1280.

Mills, A.F., 1992, *Heat Transfer*, Richard D. Irwin Inc., Homewood, Boston.

Minkowycz, W.J., Sparrow, E. M., 1966, "Condensation Heat Transfer in the Presence of Noncondensables, Interfacial Resistance, Superheating, Variable Properties and Diffusion", *Int. J. Heat Mass Transfer*, Vol. 9, pp. 1125-1144.

Nusselt, W., 1916, "Die Oberflächenkondensation des Wasserdampfes", *Zeitschr. Ver Deutsch. Ing.*, Vol. 60, pp. 541-546 and pp. 569-575.

Patankar, S.V., 1980, *Numerical Heat Transfer and Fluid Flow*, Hemisphere Publishing Corporation, New York.

Pohlhausen, K., 1921, "Zur Näherungsweisen Integration der Differential-Gleichung der Laminaren Reibungsschicht", *Z. Agnew. Math. Mech.*, Vol. 1, pp. 252-268.

Reid, R.C., Prausnitz, J.M., and Sherwood, T.K., 1977, *The Properties of Gases and Liquids*, Third Ed., McGraw-Hill, New York.

Rohsenow, W.M., Webber, J.H., and Ling, A.T., 1956, "Effect of Vapor Velocity on Laminar and Turbulent-Film Condensation", *Transaction of the ASME*, Vol. 78, pp. 1637-1643.

Rose, J.W., 1980, "Approximate Equations for Forced-Convection Condensation in the Presence of a Non-condensing Gas on a Flat Plate and Horizontal Tube", *Int. J. Heat Mass Transfer*, Vol. 23, pp. 539-546.

Rose, J.W., 1988, "Fundamentals of Condensation Heat Transfer: Laminar Film Condensation", *JSME International Journal*, series II, Vol. 31, No. 3, pp. 357-375.

Rose, J.W., 1989, "A New Interpolation Formula for Forced-Convection Condensation on a Horizontal Surface", *Journal of Heat Transfer*, Vol. 111, pp. 818-819.

Rutunaprakarn, O., and Chen, C.J., 1975, "Effect of Lighter Noncondensable Gas on Laminar Film Condensation Over a Vertical Plate", *Int. J. Heat Mass Transfer*, Vol. 18, pp. 993-996.

Schichting, H., 1979, *Boundary-Layer Theory*, McGraw Hill, New York.

Shekriladze, I.G., and Gomelauri, V.I., 1966, "Theoretical Study of Laminar Film Condensation of Flowing Vapour", *Int. J. Heat Mass Transfer*, Vol. 9, pp. 581-591.

Siddique, M., Golay, M.W., and Kazimi, M.S., 1989, "The Effect of Hydrogen on Forced Convection Steam Condensation", *A.I.Ch.E. Journal*, Vol. 85, pp. 211-216.

Sparrow, E.M., Minkowycz, W.J., and Saddy, M., 1967, "Forced Convection Condensation in the Presence on Noncondensables and Interfacial Resistance", *Int. J. Heat Mass Transfer*, Vol. 19, pp. 1829-1845.

Sucec, J., 1995, "The Double Integral Method Applied to Separation Calculation", *Int. J. Heat Mass Transfer*, Vol. 38, No. 15, pp. 2771-2777.

Thomas, L.C., and Amminger, W.L., 1988, "A Practical One-Parameter Integral Method for Laminar Incompressible Boundary Layer Flow With Transpiration", *Journal of Applied Mechanics*, Vol. 55, pp. 474-481.

Thomas, L.C., and Amminger, W.L., 1990, " Two-Parameter Integral Method for Laminar Transpired Thermal Boundary-Layer Flow", *AIAA Journal*, Vol. 28, No. 2, pp. 193-200.

Turner, R.H., Mills, A.F., and Denny, V.E., 1973, "The Effect of Noncondensable Gas on Laminar Film Condensation of Liquid Metals", *Journal of Heat Transfer*, Vol. 95, pp. 6-11.

Volkov, V.N., 1965, "A Refinement of the Karman Pohlhausen Integral Method in Boundary-Layer Theory", Inzh. Fiz. Zh., Vol 9, pp. 583-588 (English translation in J. Engn. Phys., Vol 9, pp. 371-374).

Zien, T.F., 1971, "A New Integral Calculation of Skin Friction on a Porous Plate", *AIAA Journal*, Vol. 9, No. 7, pp. 1423-1425.

Zien, T.F., 1976, "Approximate Analysis of Heat Transfer in Transpired Boundary Layers With Effects of Prandtl Number", *Int. J. Heat Mass Transfer*, Vol. 19, pp. 513-521.

APPENDIX A

Transport and Thermal Properties

A.1 Introduction

The properties of vapors and gases which were used in the analysis are specified in this appendix. Each property, for either vapor or gas, was defined in the computer program in the form of a subroutine with standardized input-output parameters so that the main program does not have to be modified if a different set of vapor-gas properties are used. In this work the preferred references for properties were those which contained all vapor or gas properties. For steam and air, correlations provided by Irvine and Liley were used to define the following: steam saturation temperature and pressure, latent heat of vaporization of steam, liquid density, and all the air properties. Following Chin (1995), a linear interpolation with property table values was used to evaluate the specific heat, thermal conductivity, and viscosity of steam. Mercury vapor and liquid properties were taken from Kakac et al. (1987) and the data in tabulated form were fitted using the least square method. Properties for Freon12 were found in Beaton et al. (1989), and the same method was used to fit tabulated data as used for mercury properties. Hydrogen properties were obtained from Incropera and DeWitt (1985). Mixtures properties, calculated from the vapor and gas properties, are defined at the end of the appendix.

The parameters that are important for the calculation procedure as well as for the evaluation of some properties are: free stream pressure and partial pressures of vapor and gas. Making the assumption that the vapor is at saturation state at the free stream, it is possible to calculate the free stream pressure for given W_∞ and T_∞:

$$P_\infty = P_{sat}(T_\infty)\left[\frac{M_g + W_\infty(M_v - M_g)}{M_g - W_\infty M_g}\right] \qquad \text{(A.1)}$$

Assuming that the free stream pressure is the total system pressure and that it is constant across the mixture boundary layer, the partial pressures of gas and vapor for any gas concentration W were calculated from:

$$P_g = P_\infty\left[\frac{WM_v}{M_g + W(M_v - M_g)}\right] \qquad \text{(A.2)}$$

and

$$P_v = P_\infty - P_g \qquad \text{(A.3)}$$

respectively.

A.2 Water Properties

Molecular weight: $M_v = 18.015\ kg\ /\ kmol$

Saturation Temperature, Pressure and Pressure Gradient of Steam

Source: Irvine and Liley (1984), page 21

Saturation temperature as a function of saturation pressure is given by:

$$T_{sat} = A + \frac{B}{\ln(P_{sat}) + C}, \qquad \text{(A.4)}$$

where constants A, B, and C are given for two pressure or temperature ranges:

$0.611\ kPa \le P_{sat} < 12.33 \times 10^3\ kPa$ $\quad 12.33 \times 10^3\ kPa \le P_{sat} \le 22.10 \times 10^3\ kPa$

$273.16\ K \le T_{sat} < 600.0\ K$ $\quad 600.0\ K \le T_{sat} < 647.3\ K$

$A = 0.426776 \times 10^2$ $\quad A = -0.387592 \times 10^3$

$B = -0.389270 \times 10^4$ $\quad B = -0.125875 \times 10^5$

$C = -0.948654 \times 10^{1}$ $C = -0.152578 \times 10^{2}$

Although an expression for P_{sat} as a function of T_{sat} was given in the same source, an inverse of Equation (A.1) was used to calculate P_{sat} because it gives a unique pair of P_{sat} and T_{sat}. The equation which is used to calculate P_{sat} is:

$$P_{sat} = \exp\left(\frac{B}{T_{sat} - A} - C\right), \tag{A.5}$$

where constants A, B, and C are the same as before.

The pressure derivative with respect to the temperature was obtained from Equation (A.2).

$$\frac{dP_{sat}}{dT_{sat}} = \frac{-B\,P_{sat}}{(T_{sat} - A)^2} \tag{A.6}$$

Latent Heat of Vaporization

Source: Irvine and Liley (1984), page 23

The equation was given for the temperature range: $273.16\ K \le T < 647.3\ K$

$$h_{fg} = 2.5009 \times 10^{3}\left[A + BT_c^{1/3} + CT_c^{5/6} + DT_c^{7/8} + \sum_{N=1}^{5} E(N)T_c^{N}\right] \tag{A.7}$$

where:

$$T_c = \frac{647.3 - T}{647.3}$$

$A = 0.0$
$B = 7.79221 \times 10^{-1}$
$C = 4.62668$
$D = -1.07931$
$E(1) = -3.87446$
$E(2) = 2.94553$
$E(3) = -8.06395$
$E(4) = 1.15633 \times 10^{1}$

$$E(5) = -6.02884$$

Steam Density

Steam was considered to be an ideal gas, and the ideal gas equation of state was used to calculate density:

$$\rho_v = \frac{P_v M_v}{\overline{R} T}, \qquad \text{(A.8)}$$

where:

P_v is the partial pressure of the vapor

$\overline{R} = 8.3145\ kJ/kmol K$ is universal gas constant

Steam Viscosity, Thermal Conductivity and Specific Heat

Source: Incropera and DeWitt (1985), page 774

To evaluate μ_v, k_v and C_{P_v} at the arbitrary temperature within given range, a linear interpolation was used. It was assumed that μ_v, k_v and C_{P_v} are at the saturation values.

Table A.1: Saturated water vapor properties

T_v (K)	μ_v (Pas×10^6)	k_v (W/mK × 10^3)	C_{P_v} (kJ/kgK)
273.15	8.02	18.2	1.854
275.0	8.09	18.3	1.855
280.0	8.29	18.6	1.858
285.0	8.49	18.9	1.861
290.0	8.69	19.3	1.864
295.0	8.89	19.5	1.868
300.0	9.09	19.6	1.872
305.0	9.29	20.1	1.877
310.0	9.49	20.4	1.882
315.0	9.69	20.7	1.888
320.0	9.89	21.0	1.895

Table A.1: Saturated water vapor properties(continued)

T_v (K)	μ_v (Pas×10^6)	k_v (W/mK × 10^3)	C_{P_v} (kJ/kgK)
325.0	10.09	21.3	1.903
330.0	10.29	21.7	1.911
335.0	10.49	22.0	1.920
340.0	10.69	22.3	1.930
345.0	10.89	22.6	1.941
350.0	11.09	23.0	1.954
355.0	11.29	23.3	1.968
360.0	11.49	23.7	1.983
365.0	11.69	24.1	1.999
370.0	11.89	24.5	2.017
373.15	12.02	24.8	2.029
375.0	12.09	24.9	2.036
380.0	12.29	25.4	2.057
385.0	12.49	25.8	2.080
390.0	12.69	26.3	2.104
400.0	13.05	27.2	2.158
410.0	13.42	28.2	2.221
420.0	13.79	29.8	2.291
430.0	14.14	30.4	2.369
440.0	14.50	31.7	2.46
450.0	14.85	33.1	2.56
460.0	15.19	34.6	2.68
470.0	15.54	36.3	2.79
480.0	15.88	38.1	2.94
490.0	16.23	40.1	3.10
500.0	16.59	42.3	3.27
510.0	16.95	44.7	3.47
520.0	17.33	47.5	3.70
530.0	17.72	50.6	3.96
540.0	18.1	54.0	4.27
550.0	18.6	58.0	4.64
560.0	19.1	63.7	5.09
570.0	19.7	76.7	5.67
580.0	20.4	76.7	6.40
590.0	21.5	84.1	7.35
600.0	22.7	92.9	8.75

Table A.1: Saturated water vapor properties(continued)

T_v (K)	μ_v (Pas×10^6)	k_v (W/mK × 10^3)	C_{P_v} (kJ/kgK)
610.0	24.1	103.0	11.1
625.0	27.0	121.0	18.3
630.0	28.0	130.0	22.1
635.0	30.0	141.0	27.6
640.0	32.0	155.0	42.0
645.0	37.0	178.0	1.0e+10
647.3	45.0	238.0	1.0e+10

Liquid (Water) Density

Source: Irvine and Liley (1984), page 22

Temperature range: $273.16K \leq T_L \leq 647.3K$

$$\rho_L = \frac{1}{3.155\times10^{-3}\left[A + BT_c^{1/3} + CT_c^{5/6} + DT_c^{7/8} + \sum_{N=1}^{5} E(N)T_c^N\right]} \quad \text{(A.9)}$$

where: $T_c = \dfrac{647.3 - T_L}{647.3}$

$A = 1.0$
$B = -1.9153882$
$C = 1.2015186\times10^{1}$
$D = -7.84664025$
$E(1) = -3.888614$
$E(2) = 2.0582238$
$E(3) = -2.0829991$
$E(4) = 8.218\times10^{-1}$
$E(5) = 4.7549742\times10^{-1}$

Liquid (Water) Viscosity, Thermal Conductivity and Specific Heat

Source: Incropera and DeWitt (1985), page 774

To evaluate μ_v, k_v and C_{P_v} at temperature T, a linear interpolation was used and properties were assumed to be at the saturation values.

Table A.2: Saturated liquid water properties

T_v (K)	μ_v (Pas×10^6)	k_v (W/mK × 10^3)	C_{P_v} (kJ/kgK)
273.15	1750.0	569.0	4.217
275.0	1652.0	574.0	4.211
280.0	1422.0	582.0	4.198
285.0	1225.0	590.0	4.189
290.0	1080.0	598.0	4.184
295.0	959.0	606.0	4.181
300.0	855.0	613.0	4.179
305.0	769.0	620.0	4.178
310.0	695.0	628.0	4.178
315.0	631.0	634.0	4.179
320.0	577.0	640.0	4.180
325.0	528.0	645.0	4.182
330.0	489.0	650.0	4.184
335.0	453.0	656.0	4.186
340.0	420.0	660.0	4.188
345.0	389.0	668.0	4.191
350.0	365.0	668.0	4.195
355.0	343.0	671.0	4.199
360.0	324.0	674.0	4.203
365.0	306.0	677.0	4.209
370.0	289.0	679.0	4.214
373.15	279.0	680.0	4.217
375.0	274.0	681.0	4.220
380.0	260.0	683.0	4.226
385.0	248.0	685.0	4.232
390.0	237.0	686.0	4.239
400.0	217.0	688.0	4.256
410.0	200.0	688.0	4.278
420.0	185.0	688.0	4.302
430.0	173.0	685.0	4.331
440.0	162.0	682.0	4.36
450.0	152.0	678.0	4.40

Table A.2: Saturated liquid water properties (continued)

T_v (K)	μ_v (Pas×10^6)	k_v (W/m·K × 10^3)	C_{P_v} (kJ/kgK)
460.0	143.0	673.0	4.44
470.0	136.0	667.0	4.48
480.0	129.0	660.0	4.53
490.0	124.0	651.0	4.59
500.0	118.0	642.0	4.66
550.0	97.0	580.0	5.24
560.0	94.0	563.0	5.43
570.0	91.0	548.0	5.68
580.0	88.0	528.0	6.00
590.0	84.0	513.0	6.41
600.0	81.0	497.0	7.00
610.0	77.0	467.0	7.85
620.0	72.0	444.0	9.35
625.0	70.0	430.0	10.6
630.0	67.0	412.0	12.6
635.0	64.0	392.0	16.4
640.0	59.0	367.0	26.0
645.0	54.0	331.0	90.0
647.3	45.0	238.0	1.0e+10

A.3 Air Properties

Molecular weight: $M_v = 28.97\ kg\ /\ kmol$

Air Density

Air is considered to be an ideal gas, and its density was calculated using:

$$\rho_g = \frac{P_g M_g}{\bar{R}T} \tag{A.10}$$

where P_g is partial pressure of the gas.

Air Viscosity

Source: Irvine and Liley (1984), page 113

Temperature range: $250K \leq T \leq 600K$

The expression for viscosity is given in the polynomial form:

$$\mu_g = 10^{-6} \sum_{N=0}^{4} B(N) T^N , \qquad \text{(A.11)}$$

where:

$$B(0) = -9.8601 \times 10^{-1}$$
$$B(1) = 9.081025 \times 10^{-2}$$
$$B(2) = -1.17635575 \times 10^{-4}$$
$$B(3) = 1.2349703 \times 10^{-7}$$
$$B(4) = -5.7971299 \times 10^{-11}$$

Thermal Conductivity

Source: Irvine and Liley (1984), page 114

Temperature range: $250K \leq T \leq 1050K$

The expression for thermal conductivity is given as follow:

$$k_g = \sum_{N=0}^{5} C(N) T^N , \qquad \text{(A.12)}$$

where:

$$C(0) = -2.27650 \times 10^{-3}$$
$$C(1) = 1.2598485 \times 10^{-4}$$
$$C(2) = -1.4815235 \times 10^{-7}$$
$$C(3) = 1.73550646 \times 10^{-10}$$
$$C(4) = -1.066657 \times 10^{-13}$$
$$C(5) = 2.47663035 \times 10^{-17}$$

Specific Heat

Source: Irvine and Liley (1984), page 97

Temperature range: $250K \leq T \leq 2000K$

The expression for specific heat is given in the polynomial form:

$$C_{P_g} = \sum_{N=0}^{4} A(N)T^N, \qquad \text{(A.13)}$$

where:

$A(0) = 0.103409 \times 10^{1}$
$A(1) = -0.284887 \times 10^{-3}$
$A(2) = 0.7816818 \times 10^{-6}$
$A(3) = -0.4970786 \times 10^{-9}$
$A(4) = 0.1077024 \times 10^{-12}$

A.4 Mercury Properties

Molecular weight: $M_v = 200.51\ kg\ /\ kmol$

Saturation Temperature of Mercury

Source: Kakac et al. (1987), page 22-19

Temperature range: $260K \leq T \leq 1000K$

Saturation temperature as a function of saturation pressure is given by:

$$T_{sat} = \frac{1}{\sum_{N=1}^{3} A(N)\left[\frac{Log_{10}(P_{sat})}{1000}\right]^{N-1}}, \qquad \text{(A.14)}$$

where:

A(1) = $2.228646730815123 \times 10^{-3}$
A(2) = $-3.180533006020381 \times 10^{-1}$
A(3) = $-9.462506996387053 \times 10^{-1}$

Saturation Pressure of Mercury

Saturation pressure of mercury was calculated using the Newton-Raphson root search of Equation (A.14), as presented by Chin (1995). For a given T_{sat} an initial guess of P_{sat} was found using a polynomial expression, and that value was used as the initial value in the Newton-Raphson root search. The polynomial expression for the P_{sat} as a function of T_{sat} was defined as:

$$P_{sat,guess} = 10^{a}, \tag{A.15}$$

where: $$a = 1000\sum_{N=1}^{3} A_i(N)\frac{1}{T_{sat}^{N-1}}$$

$A_i(1) = 6.861356058571274 \times 10^{-3}$
$A_i(2) = -3.012456507914288$
$A_i(3) = -29.702694295999220$

Introducing variables $y = \frac{1}{T_{sat}}$ and $x = \frac{Log_{10}(P_{sat})}{1000}$ Equation (A.14) can be written as follows:

$$f(x) = \sum_{N=1}^{3} A(N)\,x^{N-1} - y = 0 \tag{A.16}$$

The first derivative of f with respect to x is:

$$f'(x) = \sum_{N=2}^{3} (N-1)\,A(N)\,x^{N-2} \tag{A.17}$$

For given value of T_{sat}, the value of x_{old} was calculated using Equation (A.15). A new value of x was obtained from:

$$x_{new} = x_{old} - \frac{f(x_{old})}{f'(x_{old})} \tag{A.18}$$

If the two values of x were different then x_{old} was replaced by x_{new} and the iteration was repeated until the relative error, which is defined as $\frac{|x_{new} - x_{old}|}{x_{new}} 100$, was less than 10^{-7}.

Once the value of x was obtained with satisfactory accuracy, pressure was calculated from:

$$P_{sat} = 10^{1000 x_{new}} \tag{A.19}$$

Comparison of tabulated and calculated data for P_{sat} is given in the table below.

Table A.3: Saturated pressure of mercury

$T_{sat}(K)$ tabulated	$P_{sat}(kPa)$ tabulated	$P_{sat}(kPa)$ calculated	% error of calculated P_{sat}
2.60E+02	6.9250E-06	6.838900E-06	1.258974E+00
2.80E+02	5.2960E-05	5.293200E-05	5.289806E-02
3.00E+02	3.0750E-04	3.090811E-04	5.115486E-01
3.20E+02	1.4280E-03	1.437860E-03	6.857344E-01
3.40E+02	5.5160E-03	5.553691E-03	6.786640E-01
3.60E+02	1.8290E-02	1.838659E-02	5.253372E-01
3.80E+02	5.2890E-02	5.349567E-02	1.132177E+00
4.00E+02	1.3940E-01	1.395257E-01	9.008363E-02
4.50E+02	1.0530E+00	1.047607E+00	5.148233E-01
5.00E+02	5.2610E+00	5.216309E+00	8.567464E-01
5.50E+02	1.9490E+01	1.930351E+01	9.660732E-01
6.00E+02	5.7760E+01	5.724593E+01	8.980107E-01
6.50E+02	1.4425E+02	1.432841E+02	6.741134E-01
7.00E+02	3.1530E+02	3.140426E+02	4.003771E-01
7.50E+02	6.1970E+02	6.191425E+02	9.003703E-02
8.00E+02	1.1180E+03	1.120278E+03	2.033333E-01
8.50E+02	1.8820E+03	1.889040E+03	3.726801E-01
9.00E+02	2.9880E+03	3.003943E+03	5.307518E-01
9.50E+02	4.5230E+03	4.547123E+03	5.305093E-01
1.00E+03	6.5740E+03	6.601093E+03	4.104395E-01

Mercury Saturation Curve Derivative

Saturation pressure derivative was obtained from Equation (A.14). Because the pressure gradient was given in Pa / K, the expression for derivative was multiplied by 10^6:

$$\frac{dP_{sat}}{dT_{sat}} = -10^6 P_{sat} \ln(10) \sum_{N=2}^{3} \frac{(N-1)A_i(N)}{T_{sat}^N} \qquad \text{(A.20)}$$

Latent Heat of Vaporization of Mercury

Source: Kakac et al. (1987), page 22-19

Temperature range: $260K \leq T_i \leq 1000K$

An approximate expression for latent heat is given in the polynomial form:

$$h_{fg} = 10^3 \sum_{N=1}^{11} A(N) T_i^{N-1} \qquad \text{(A.21)}$$

where:

A(1) = 347.152340719917300
A(2) = - 4.818400715270975 × 10^{-1}
A(3) = 2.678854889285191 × 10^{-3}
A(4) = - 8.327016074846239 × 10^{-6}
A(5) = 1.316505183579043 × 10^{-8}
A(6) = - 6.062230888858590 × 10^{-12}
A(7) = - 1.124984942131947 × 10^{-14}
A(8) = 1.650997360133698 × 10^{-17}
A(9) = -4.003993979027860 × 10^{-21}
A(10) = -4.667249392037415 × 10^{-24}
A(11) = 2.365815946616059 × 10^{-27}

Comparison between tabulated and computed values of latent heat are given in the following table.

Table A.4: Latent heat of vaporization of mercury

$T_i(K)$ tabulated	$h_{fg}(kJ/kg)$ tabulated	$h_{fg}(kJ/kg)$ calculated	% error of calculated h_{fg}
2.60E+02	3.073100E+05	3.073124E+05	7.872692E-04
2.80E+02	3.065700E+05	3.065640E+05	1.958885E-03
3.00E+02	3.058400E+05	3.058425E+05	8.231285E-04
3.20E+02	3.051400E+05	3.051382E+05	5.810935E-04
3.40E+02	3.044400E+05	3.044458E+05	1.914041E-03
3.60E+02	3.037600E+05	3.037629E+05	9.621369E-04
3.80E+02	3.028200E+05	3.030888E+05	8.867199E-02
4.00E+02	3.024300E+05	3.024232E+05	2.238359E-03
4.50E+02	3.008000E+05	3.007951E+05	1.633097E-03
5.00E+02	2.991900E+05	2.991994E+05	3.127721E-03
5.50E+02	2.975800E+05	2.975902E+05	3.435292E-03
6.00E+02	2.959200E+05	2.959112E+05	2.976404E-03
6.50E+02	2.941700E+05	2.941176E+05	1.779914E-02
7.00E+02	2.920800E+05	2.921861E+05	3.630207E-02
7.50E+02	2.901700E+05	2.900980E+05	2.481158E-02
8.00E+02	2.878100E+05	2.878017E+05	2.880186E-03
8.50E+02	2.851300E+05	2.851756E+05	1.599572E-02
9.00E+02	2.820800E+05	2.820486E+05	1.112171E-02
9.50E+02	2.783600E+05	2.783698E+05	3.505883E-03
1.00E+03	2.746700E+05	2.746688E+05	4.419389E-04

Mercury Vapor Density

Mercury vapor is considered to be an ideal gas, and the ideal gas equation of state was used to calculate density:

$$\rho_v = \frac{P_v M_v}{\bar{R} T}, \qquad \text{(A.22)}$$

where P_v is the partial pressure of the mercury vapor

Mercury Vapor Viscosity

Source: Kakac et al. (1987), page 22-20

Temperature range: $260K \leq T \leq 1000K$

An approximate expression (least square curve fit) for viscosity is given as follow:

$$\mu_v = 10^{-4} \sum_{N=1}^{4} A(N) T^{N-1}, \qquad \text{(A.23)}$$

where:

$A(1) = 5.683366598857462 \times 10^{-2}$
$A(2) = 5.433436554830212 \times 10^{-4}$
$A(3) = 7.188317372958504 \times 10^{-7}$
$A(4) = -3.002012660681679 \times 10^{-10}$

Mercury Vapor Thermal Conductivity

Source: Kakac et al. (1987), page 22-20

Temperature range: $260K \leq T \leq 1000K$

An approximate expression for thermal conductivity is given in the polynomial form:

$$k_v = 10^{-3} \sum_{N=1}^{11} A(N) T^{N-1}, \qquad \text{(A.24)}$$

where:

$A(1) = -34.13243845717039$
$A(2) = 6.547899849090263 \times 10^{-1}$
$A(3) = -5.264704070512250 \times 10^{-3}$
$A(4) = 2.468587207864500 \times 10^{-5}$
$A(5) = -7.212953352378778 \times 10^{-8}$
$A(6) = 1.348199531705186 \times 10^{-10}$
$A(7) = -1.587991558199037 \times 10^{-13}$
$A(8) = 1.099333126724636 \times 10^{-16}$
$A(9) = -3.561829284479875 \times 10^{-20}$
$A(10) = -7.858739084948582 \times 10^{-25}$
$A(11) = 2.553564628287123 \times 10^{-27}$

Mercury Vapor Specific Heat

Source: Kakac et al. (1987), page 22-19

Temperature range: $260K \leq T \leq 1000K$

An approximate expression (least square curve fit) for specific heat is given in the form:

$$C_{P_v} = \sum_{N=1}^{11} A(N)T^{N-1}, \qquad \text{(A.25)}$$

where:

A(1) = 1205.110307437128
A(2) = 12.905408867875090
A(3) = $6.304367134228415 \times 10^{-2}$
A(4) = $-1.633586432054034 \times 10^{-4}$
A(5) = $2.289756820286235 \times 10^{-7}$
A(6) = $-1.309708079506991 \times 10^{-10}$
A(7) = $-7.583413284524297 \times 10^{-14}$
A(8) = $1.711407255860443 \times 10^{-16}$
A(9) = $-1.027848541276225 \times 10^{-19}$
A(10) = $2.082958835944735 \times 10^{-23}$
A(11) = $7.735691672719935 \times 10^{-28}$

Liquid Mercury Density

Source: Kakac et al. (1987), page 22-19

Temperature range: $400K \leq T \leq 1000K$

An approximate expression for the liquid mercury density is given in the polynomial form:

$$\rho_L = \sum_{N=1}^{4} A(N)T^{N-1}, \qquad \text{(A.26)}$$

where:

A(1) = 14289.84177690087
A(2) = -2.700524534055227
A(3) = $6.681706282663574 \times 10^{-4}$
A(4) = $-4.671313282498846 \times 10^{-7}$

Liquid Mercury Viscosity

Source: Kakac et al. (1987), page 22-20

Temperature range: $260K \leq T \leq 1000K$

An approximate expression for the liquid mercury viscosity is given in the polynomial form:

$$\mu_L = 10^{-4} \sum_{N=1}^{9} A(N) T^{N-1}, \qquad \text{(A.27)}$$

where:

A(1) = 162.5593339625174
A(2) = -1.695431455712477
A(3) = $8.745655071128042 \times 10^{-3}$
A(4) = $-2.650106286789457 \times 10^{-5}$
A(5) = $5.057275968165792 \times 10^{-8}$
A(6) = $-6.166486521270661 \times 10^{-11}$
A(7) = $4.668932398106511 \times 10^{-14}$
A(8) = $-2.001473258454851 \times 10^{-17}$
A(9) = $3.713334650282130 \times 10^{-21}$

Liquid Mercury Thermal Conductivity

Source: Kakac et al. (1987), page 22-20

Temperature range: $260K \leq T \leq 1000K$

An approximate expression for the liquid mercury thermal conductivity is given in the polynomial form:

$$k_L = \sum_{N=1}^{3} A(N) T^{N-1}, \qquad \text{(A.28)}$$

where:

A(1) = 3.996461822872357
A(2) = $1.704655307721554 \times 10^{-2}$
A(3) = $-6.349417231970252 \times 10^{-6}$

Liquid Mercury Specific Heat

Source: Kakac et al. (1987), page 22-20

Temperature range: $260K \leq T \leq 1000K$

An approximate expression for the liquid mercury specific heat is given in the polynomial form:

$$C_{P_L} = \sum_{N=1}^{9} A(N) T^{N-1}, \qquad \text{(A.29)}$$

where:

$A(1) = 458.3630993175319$
$A(2) = -5.200761055578581$
$A(3) = 3.775370779788821 \times 10^{-2}$
$A(4) = -1.579003237663987 \times 10^{-4}$
$A(5) = 4.158885678443660 \times 10^{-7}$
$A(6) = -7.157799645691694 \times 10^{-10}$
$A(7) = 8.089064933473153 \times 10^{-13}$
$A(8) = -5.847053723759683 \times 10^{-16}$
$A(9) = 2.517766248561060 \times 10^{-19}$
$A(10) = -5.456776290363734 \times 10^{-23}$
$A(11) = 3.519727914371710 \times 10^{-27}$

A.5 Freon12 Properties

Molecular weight: $M_v = 120.92\ kg\ /\ kmol$

Saturation Temperature of Freon12

Source: Beaton and Hewitt (1989), page 186

Temperature range: $244K \leq T \leq 384K$

Saturation temperature as a function of saturation pressure is given by:

$$T_{sat} = \frac{1}{\sum_{N=1}^{3} A(N)\left[\frac{Log_{10}(P_{sat})}{1000}\right]^{N-1}}, \qquad \text{(A.30)}$$

where:

$A(1) = 5.280768116978539 \times 10^{-3}$
$A(2) = -1.613227971731792 \times 10^{-1}$
$A(3) = -271.9170803416368$
$A(4) = 30807.22776789830$

Saturation Pressure of Freon12

Saturation pressure of Freon12 was calculated using the same algorithm as for mercury.

Only the coefficients are different.

$$P_{sat,guess} = 10^{a} \qquad \text{(A.31)}$$

where: $a = 1000\sum_{N=1}^{4} A_i(N)\frac{1}{T_{sat}^{N-1}}$,

$A_i(1) = 7.648915289382953 \times 10^{-3}$
$A_i(2) = -2.283925148483701$
$A_i(3) = 384.7124480071707$
$A_i(4) = -39648.54848554815$

Introducing variables $y = \frac{1}{T_{sat}}$ and $x = \frac{Log_{10}(P_{sat})}{1000}$ Equation (A.30) was written as:

$$f(x) = \sum_{N=1}^{3} A(N)\, x^{N-1} - y = 0 \qquad \text{(A.32)}$$

The first derivative of $f(x)$ with respect to x is:

$$f'(x) = \sum_{N=2}^{3} (N-1)\, A(N)\, x^{N-2} \qquad \text{(A.33)}$$

For given value of T_{sat}, the value of x_{old} was calculated using Equation (A.31). A new value of x was obtained from:

$$x_{new} = x_{old} - \frac{f(x_{old})}{f'(x_{old})} \tag{A.34}$$

The iterative procedure was repeated until the relative error, which is defined as $\frac{|x_{new} - x_{old}|}{x_{new}} 100$, was less than 10^{-7}. Once the value of x was obtained with satisfactory accuracy, pressure was calculated from:

$$P_{sat} = 10^{1000 x_{new}} \tag{A.35}$$

Comparison of tabulated and calculated data for P_{sat} is given in table below.

Table A.5: Saturated pressure of Freon12

$T_{sat}(K)$ tabulated	$P_{sat}(kPa)$ tabulated	$P_{sat}(kPa)$ calculated	% error of calculated P_{sat}
2.6000E+02	2.000000E+02	1.995073E+02	2.469414E-01
2.7500E+02	3.330000E+02	3.344532E+02	4.345095E-01
2.9000E+02	5.280000E+02	5.272084E+02	1.501487E-01
3.0500E+02	7.930000E+02	7.920069E+02	1.253917E-01
3.2000E+02	1.145000E+03	1.144594E+03	3.548554E-02
3.3500E+02	1.602000E+03	1.602262E+03	1.634481E-02
3.5000E+02	2.183000E+03	2.183919E+03	4.206389E-02
3.6500E+02	2.907000E+03	2.910188E+03	1.095502E-01

Freon12 Saturation Curve Derivative

Saturation pressure derivative was obtained from Equation (A.31). Because the pressure gradient was given in Pa / K, the expression for derivative was multiplied by 10^6:

$$\frac{dP_{sat}}{dT_{sat}} = -10^6 P_{sat} \ln(10) \sum_{N=2}^{4} \frac{(N-1) A_i(N)}{T_{sat}^N} \tag{A.36}$$

Latent Heat of Vaporization of Freon12

Source: Beaton and Hewitt (1989), page 186

Temperature range: $244K \leq T \leq 384K$

An approximate expression for latent heat is given in the polynomial form:

$$h_{fg} = 10^3 \sum_{N=1}^{11} A(N) T_i^{N-1} \qquad \text{(A.37)}$$

where:

A(1) = -1295.870000418633
A(2) = 21.73391354432067
A(3) = $-1.184762216965941 \times 10^{-1}$
A(4) = $2.850148661803296 \times 10^{-4}$
A(5) = $-2.612355060982694 \times 10^{-7}$

The comparison between tabulated and computed values of latent heat are given in the following table.

Table A.6: Latent heat of vaporization of Freon12

$T_i(K)$ tabulated	$h_{fg}(kJ/kg)$ tabulated	$h_{fg}(kJ/kg)$ calculated	% error of calculated h_{fg}
2.4400E+02	1.683000E+02	1.679955E+02	1.812576E-01
2.6000E+02	1.615000E+02	1.615927E+02	5.733927E-02
2.7500E+02	1.547000E+02	1.545679E+02	8.545892E-02
2.9000E+02	1.466000E+02	1.466732E+02	4.987561E-02
3.0500E+02	1.377000E+02	1.377022E+02	1.615234E-03
3.2000E+02	1.272000E+02	1.271315E+02	5.384454E-02
3.3500E+02	1.140000E+02	1.141201E+02	1.052825E-01
3.5000E+02	9.760000E+01	9.750966E+01	9.265097E-02
3.6500E+02	7.580000E+01	7.582429E+01	3.204102E-02

Freon12 Vapor Density

Freon12 vapor is considered to be an ideal gas, and the ideal gas equation of state was used to calculate density:

$$\rho_v = \frac{P_v M_v}{\bar{R} T}, \tag{A.38}$$

where P_v is the partial pressure of the Freon12 vapor

Freon12 Vapor Viscosity

Source: Beaton and Hewitt (1989), page 186

Temperature range: $244K \leq T \leq 384K$

An approximate expression for viscosity is given in the polynomial form:

$$\mu_v = 10^{-6} \sum_{N=1}^{7} A(N) T^{N-1}, \tag{A.39}$$

where:

A(1) = -5933.362287916454
A(2) = 121.3699144272514
A(3) = -1.027652489614548
A(4) = $4.614713401623965 \times 10^{-3}$
A(5) = $-1.158639763710729 \times 10^{-5}$
A(6) = $1.541963912399715 \times 10^{-8}$
A(7) = $-8.495221551670347 \times 10^{-12}$

Freon12 Vapor Thermal Conductivity

Source: Beaton and Hewitt (1989), page 186

Temperature range: $244K \leq T \leq 384K$

An approximate expression for thermal conductivity is given in the form:

$$k_v = 10^{-3} \sum_{N=1}^{9} A(N) T^{N-1}, \tag{A.40}$$

where:

A(1) = -30257.81554051268
A(2) = 524.9461049742886

A(3) = -3.019640930722789
A(4) = $8.690109501043903 \times 10^{-4}$
A(5) = $7.000161992335235 \times 10^{-5}$
A(6) = $-3.640469481462557 \times 10^{-7}$
A(7) = $8.695524153655378 \times 10^{-10}$
A(8) = $-1.046780465462567 \times 10^{-12}$
A(9) = $5.141941472709557 \times 10^{-16}$

Freon12 Vapor Specific Heat

Source: Beaton and Hewitt (1989), page 186

Temperature range: $244K \leq T \leq 384K$

An approximate expression for specific heat is given as:

$$C_{P_v} = \sum_{N=1}^{6} A(N) T^{N-1}, \qquad \text{(A.41)}$$

where:

A(1) = -3291.98
A(2) = 292.435
A(3) = -3.76099
A(4) = 0.0195602
A(5) = -4.59975×10^{-5}
A(6) = 4.08348×10^{-8}

Liquid Freon12 Density

Source: Beaton and Hewitt (1989), page 186

Temperature range: $244K \leq T \leq 384K$

An approximate expression for the liquid Freon12 density is given as:

$$\rho_L = \sum_{N=1}^{8} A(N) T^{N-1}, \qquad \text{(A.42)}$$

where:

A(1) = -416428.4428923179

A(2) = 5200.285445245216
A(3) = -5.337413829345634
A(4) = $-2.325892680863172 \times 10^{-1}$
A(5) = $1.648812753119473 \times 10^{-3}$
A(6) = $-5.023667210900118 \times 10^{-6}$
A(7) = $7.455461653264922 \times 10^{-9}$
A(8) = $-4.412339397531186 \times 10^{-12}$

Liquid Freon12 Viscosity

Source: Beaton and Hewitt (1989), page 186

Temperature range: $244K \leq T \leq 384K$

An approximate expression for the liquid Freon12 viscosity is given in the form:

$$\mu_L = 10^{-6} \sum_{N=1}^{7} A(N) T^{N-1}, \qquad \text{(A.43)}$$

where:

A(1) = 184816.8477050371
A(2) = -3563.976216899797
A(3) = 28.87081781783347
A(4) = $-1.252340737513709 \times 10^{-1}$
A(5) = $3.061469631895338 \times 10^{-4}$
A(6) = $-3.993024791463627 \times 10^{-7}$
A(7) = $2.168066453668025 \times 10^{-10}$

Liquid Freon12 Thermal Conductivity

Source: Beaton and Hewitt (1989), page 186

Temperature range: $244K \leq T \leq 384K$

An approximate expression for the liquid Freon12 thermal conductivity is given in the polynomial form:

$$k_L = 10^{-3} \sum_{N=1}^{8} A(N) T^{N-1}, \qquad \text{(A.44)}$$

where:

A(1) = -31142.94498140129
A(2) = 395.7111926800813
A(3) = $-5.536848250191901 \times 10^{-1}$
A(4) = $-1.593378175492990 \times 10^{-2}$
A(5) = $1.159798963352051 \times 10^{-4}$
A(6) = $-3.552366995938784 \times 10^{-7}$
A(7) = $5.274127904733923 \times 10^{-10}$
A(8) = $-3.116301763143214 \times 10^{-13}$

Liquid Freon12 Specific Heat

Source: Beaton and Hewitt (1989), page 186

Temperature range: $244K \leq T \leq 384K$

An approximate expression for the liquid Freon12 specific heat is given as:

$$C_{P_L} = 10^3 \sum_{N=1}^{7} A(N) T^{N-1}, \qquad \text{(A.45)}$$

where:

A(1) = 1136.370455884202
A(2) = -23.17931780100425
A(3) = $1.964517881559136 \times 10^{-1}$
A(4) = $-8.848302757111981 \times 10^{-4}$
A(5) = $2.233715882606763 \times 10^{-6}$
A(6) = $-2.996567616692175 \times 10^{-9}$
A(7) = $1.669025076029951 \times 10^{-12}$

A.6 Hydrogen Properties

Molecular weight: $M_v = 2.016\ kg / kmol$

Hydrogen Density

Hydrogen is considered to be an ideal gas, and density was calculated using:

$$\rho_g = \frac{P_g M_g}{\bar{R}T} \tag{A.46}$$

where P_g is the partial pressure of the gas.

Hydrogen Viscosity

Source: Incropera and DeWitt (1985), page 769

Temperature range: $100K \leq T \leq 2000K$

An approximate expression (least square curve fit) for the viscosity is given as:

$$\mu_g = 10^{-7} \sum_{N=1}^{11} A(N) T^{N-1}, \tag{A.47}$$

where:

$A(1) = 1.198602158040322$
$A(2) = 5.553650082219447 \times 10^{-1}$
$A(3) = -2.029582995472589 \times 10^{-3}$
$A(4) = 7.023133376731805 \times 10^{-6}$
$A(5) = -1.588042686039259 \times 10^{-8}$
$A(6) = 2.337445477453487 \times 10^{-11}$
$A(7) = -2.254502464822129 \times 10^{-14}$
$A(8) = 1.410700244670514 \times 10^{-17}$
$A(9) = -5.506009036075899 \times 10^{-21}$
$A(10) = 1.216333033476007 \times 10^{-24}$
$A(11) = -1.160108756009459 \times 10^{-28}$

Thermal Conductivity

Source: Incropera and DeWitt (1985), page 769

Temperature range: $100K \leq T \leq 2000K$

An approximate expression (least square curve fit) for thermal conductivity is given as:

$$k_g = \sum_{N=1}^{9} A(N) T^{N-1}, \qquad \text{(A.48)}$$

where:

$$\begin{aligned}
A(1) &= -2.855463408653849 \times 10^{-2} \\
A(2) &= 1.199674673517537 \times 10^{-3} \\
A(3) &= -3.098851592391150 \times 10^{-6} \\
A(4) &= 7.270155507840660 \times 10^{-9} \\
A(5) &= -1.079053206088383 \times 10^{-11} \\
A(6) &= 9.797123462068353 \times 10^{-15} \\
A(7) &= -5.211939690150603 \times 10^{-18} \\
A(8) &= 1.487753709892786 \times 10^{-21} \\
A(9) &= -1.757274462138067 \times 10^{-25}
\end{aligned}$$

Specific Heat

Source: Incropera and DeWitt (1985), page 69

Temperature range: $100K \leq T \leq 2000K$

An approximate expression (least square curve fit) for specific heat is given as:

$$C_{P_g} = 10^3 \sum_{N=1}^{11} A(N) T^{N-1}, \qquad \text{(A.49)}$$

where:

$$\begin{aligned}
A(1) &= 6.015992923464465 \\
A(2) &= 7.223694748760842 \times 10^{-2} \\
A(3) &= -2.320836872427285 \times 10^{-4} \\
A(4) &= 2.981564282723661 \times 10^{-7} \\
A(5) &= 9.692793275123578 \times 10^{-11} \\
A(6) &= -8.346889370034364 \times 10^{-13} \\
A(7) &= 1.211317231532233 \times 10^{-15} \\
A(8) &= -9.141043071001927 \times 10^{-19} \\
A(9) &= 3.942504629858325 \times 10^{-22} \\
A(10) &= -9.211081913760062 \times 10^{-26} \\
A(11) &= 9.066125833119529 \times 10^{-30}
\end{aligned}$$

A.7 Mixture Properties

Diffusion Coefficient for a Mercury-Air Mixture

Source: Reid et al. (1977), Equation (11-3.2)

$$D = 1.858 \times 10^{-3} T^{3/2} \frac{\left[\frac{M_v + M_g}{M_v M_g}\right]^{1/2}}{\frac{P_{atm}}{101.325}\sigma_{vg}^2 \Omega} \times 10^{-4} \qquad \text{(A.50)}$$

where:

$\sigma_{vg} = \frac{\sigma_v + \sigma_g}{2}$, binary value of characteristic length, $\mathring{A}$

$\sigma_v = 2.969\ \mathring{A}$, from Appendix C, page 678 of Reid et al.

$\sigma_g = 3.711\ \mathring{A}$, from Appendix C, page 678 of Reid et al.

Ω is diffusion collision integral, dimensionless, defined by:

$$\Omega = \frac{A}{T^{*B}} + \frac{C}{\exp(DT^*)} + \frac{E}{\exp(FT^*)} + \frac{G}{\exp(HT^*)}$$

$$T^* = \frac{kT}{\varepsilon}$$

k=1.3805×10^{-16} ergs/K, Boltzman's constant

$\varepsilon = \sqrt{\varepsilon_v \varepsilon_g}$, the characteristic energy, Equation (11-3.4) of Reid et al.

$\varepsilon_v / k = 750\ K$, from Appendix C, page 678 of Reid et al.

$\varepsilon_g / k = 78.6\ K$, from Appendix C, page 678 of Reid et al.

$A = 1.06036$	$E = 1.03587$
$B = 0.15610$	$F = 1.52996$
$C = 0.19300$	$G = 1.76474$
$D = 0.47635$	$H = 3.89411$

Diffusion Coefficient for a Freon12-Air and Steam-Hydrogen mixture

Source: Reid et al. (1977), Equation (11-4.1)

$$D = 10^{-4}\left\{\frac{10^{-3}T^{1.75}\left[\frac{M_g + M_v}{M_g M_v}\right]^{1/2}}{\frac{P_\infty}{101.325}\left[(v_g)^{1/3} + (v_v)^{1/3}\right]}\right\} \qquad \text{(A.51)}$$

where v is the atomic diffusion volume. From table 11-1 on page 554 of Reid et al.:

$$v_g = \begin{cases} 20.1, \text{ air} \\ 7.07, \text{ hydrogen} \end{cases}$$

$$v_v = \begin{cases} 114.8, \text{ Freon} \\ 12.7, \text{ steam} \end{cases}$$

Mixture Density

Mixture density was calculated as a sum of the vapor and gas densities:

$$\rho = \rho_v + \rho_g \qquad \text{(A.52)}$$

Mixture Viscosity

Mixture viscosity was calculated following the procedure used by Chin(1995):

$$\mu = \frac{\gamma_g \mu_g}{\gamma_g + \gamma_v \varphi_{gv}} + \frac{\gamma_v \mu_v}{\gamma_v + \gamma_g \varphi_{vg}} \qquad \text{(A.53)}$$

where:

$$\gamma_g = \frac{P_g}{P_\infty}$$

$$\gamma_v = \frac{P_v}{P_\infty}$$

$$\varphi_{gv} = \frac{\left[1 + \left(\frac{\mu_g}{\mu_v}\right)^{1/2}\left(\frac{M_g}{M_v}\right)^{1/4}\right]^2}{\left[8\left(1 + \frac{M_g}{M_v}\right)\right]^{1/2}}$$

$$\varphi_{vg} = \varphi_{gv}\left(\frac{\mu_v}{\mu_g}\frac{M_g}{M_v}\right)$$

Mixture Thermal Conductivity

Mixture thermal conductivity was calculated following the procedure used by Chin(1995):

$$k = \frac{\gamma_g k_g}{\gamma_g + \gamma_v \varphi_{gv}} + \frac{\gamma_v k_v}{\gamma_v + \gamma_g \varphi_{vg}} \qquad \text{(A.54)}$$

where:

$$\gamma_g = \frac{P_g}{P_\infty}$$

$$\gamma_v = \frac{P_v}{P_\infty}$$

$$\varphi_{gv} = \frac{\left[1 + \left(\frac{\mu_g M_v}{\mu_v M_g}\right)^{1/2}\left(\frac{M_g}{M_v}\right)^{1/4}\right]^2}{\left[8\left(1 + \frac{M_g}{M_v}\right)\right]^{1/2}}$$

$$\varphi_{vg} = \frac{\left[1 + \left(\frac{\mu_v M_g}{\mu_g M_v}\right)^{1/2}\left(\frac{M_v}{M_g}\right)^{1/4}\right]^2}{\left[8\left(1 + \frac{M_v}{M_g}\right)\right]^{1/2}}$$

Mixture Specific Heat

Mixture thermal conductivity was calculated following the procedure used by Chin(1995):

$$C_P = WC_{P_g} + (1 - W)C_{P_v} \qquad \text{(A.55)}$$

APPENDIX B

Discretization and Solution of the Interface Boundary Equations

Solution of Equations (3.1) to (3.7) requires the knowledge of the liquid film thickness, the temperature at the interface and the mass flow rate at the interface. These quantities were obtained by solving the following interface boundary condition equations:

- **Interfacial Resistance Equation**

$$\dot{m}_i'' = \frac{\sigma}{\sigma - 0.5}\frac{1}{\sqrt{2\pi RT_i}}\left[P_v - P_{sat}(T_i)\right] \qquad \text{(B.1)}$$

- **Energy Balance Equation**

$$k_L \frac{\partial T_L}{\partial y} = k\frac{\partial T}{\partial y} + \dot{m}_i'' h_{fg} \qquad \text{(B.2)}$$

- **Continuity Equation for Liquid Film**

$$\dot{m}_i'' = \frac{d}{dx}\int_0^{\delta} \rho\, u\, dy \qquad \text{(B.3)}$$

In the system, $\dot{m}_i''$ was assumed to be positive in the negative y direction. Also, it was assumed that all quantities on the west side of the current station are known from the previous station solution. The initial guess for the second station is described in Appendix C.

Using the substitution $\chi = x$ and $\eta = \frac{y}{\delta}$, Equation (B.3) can be written as

$$\dot{m}_i'' = \frac{d}{d\chi}\left(\delta\int_0^1 \rho\, u\, d\eta\right). \qquad \text{(B.4)}$$

The derivative with respect to χ was approximated in terms of the difference between east and west faces

$$\dot{m}_i^{\cdot} = \frac{1}{\Delta\chi}\left[\delta_e\left(\int_0^1 \rho\, u\, d\eta\right)_e - \delta_w\left(\int_0^1 \rho\, u\, d\eta\right)_w\right] \tag{B.5}$$

and it can be written in terms of mass flow rates through east and west face as

$$\dot{m}_i^{\cdot} = \frac{1}{\Delta\chi}\left[\delta_e\, \dot{m}_e^{\cdot} - \delta_w\, \dot{m}_w^{\cdot}\right] \tag{B.6}$$

Temperature derivatives in Equation (B.2) were approximated as follows:

$$\left(\frac{\partial T_L}{\partial y}\right)_{\eta=n-1} \approx \frac{T_i - T_{wall}}{\delta_m} \tag{B.7}$$

$$\left(\frac{\partial T}{\partial y}\right)_{\eta=1} \approx \frac{T(i\text{–}1,2) - T_i}{\delta_m \Delta\eta_+(1)} \tag{B.8}$$

where

$$\delta_m = \frac{\delta(i) + \delta(i\text{–}1)}{2} \tag{B.9}$$

In Equation (B.7) a linear temperature distribution in the liquid film is assumed, and in Equation (B.8) a piecewise linear profile assumption is used for temperature gradient in the vapor at the interface. Replacing δ_e by $\delta(i)$ and δ_w by $\delta(i\text{–}1)$ in Equation (B.6) and substituting of Equations (B.6), (B.7) and (B.8) into Equation (B.2) gives the following equation

$$AT_i = B[\delta(i)]^2 + C\delta(i) + D \tag{B.10}$$

where A, B, C and D are constants defined as follows:

$$A = k_L(x, x) + \frac{k(i,1)}{\Delta\eta_+(1)} \tag{B.11}$$

$$B = \frac{h_{fg}\, \dot{m}_i''}{2\, \Delta\chi(i)} \tag{B.12}$$

$$C = \frac{h_{fg}\,\delta(i\text{-}1)}{2\,\Delta\chi(i)}\left(\dot{m}^{\cdot}_{e} - \dot{m}^{\cdot}_{w}\right) \qquad \text{(B.13)}$$

$$D = k_L\,T_L(i,1) + \frac{k(i,1)\,T(i,2)}{\Delta\eta_{+}(1)} - \delta(i-1)\,\frac{h_{fg}}{2\,\Delta\chi(i)}\,\dot{m}^{\cdot}_{w} \qquad \text{(B.14)}$$

Equating (B.1) and (B.6) and solving for $\delta(i)$ gives

$$\delta(i) = \frac{\Delta\chi(i)}{\dot{m}^{\cdot}_{e}}\left\{\frac{\delta(i-1)}{\Delta\chi(i)}\dot{m}^{\cdot}_{w} + \frac{\sigma}{\sigma - 0.5}\frac{1}{\sqrt{2\,\pi\,R\,T_i}}\left[P_v - P_{sat}(T_i)\right]\right\} \qquad \text{(B.15)}$$

The initial system of equations [Equations (B.1) to (B.3)] was replaced by two equations [Equations (B.10) and (B.15)] in the two unknowns T_i and $\delta(i)$. To solve for the mass flow rate through east face of the control volume, an initial guess for velocity profile was used as follows

$$\dot{m}^{\cdot}_{e} = \int_o^1 \rho_L\,u_L\,d\eta \approx \sum_{j=1}^{n} \rho_{Lj}\,u_{Lj}\,\Delta\eta_j \qquad \text{(B.16)}$$

Also an initial guess for surface temperature must be made.

Equations (B.10) and (B.15) can be written in general form as:

$$T_i = f_1[\delta(i)] \qquad \text{(B.17)}$$

$$\delta(i) = f_2(T_i) \qquad \text{(B.18)}$$

and combining these two an implicit expression can be obtained

$$F \equiv T_i - f_1[f_2(T_i)] = 0 \qquad \text{(B.19)}$$

Function F and its derivatives with respect to T_i can be written in terms of constants A, B, C and D

$$F = T_i - \frac{B}{A}\delta^2(i) - \frac{C}{A}\delta(i) - \frac{D}{A} \tag{B.20}$$

$$\frac{dF}{dT_i} = 1 - \frac{2B}{A}\delta(i)\frac{d\delta(i)}{dT_i} - \frac{C}{A}\frac{d\delta(i)}{dT_i} \tag{B.21}$$

The film thickness derivative with respect to T_i can be obtained from Equation (B.15)

$$\frac{d\delta(i)}{dT_i} = \frac{\Delta\chi(i)}{\dot{m}''_e}\frac{\sigma}{\sigma - 0.5}\left\{\frac{-\pi R}{(2\pi RT_i)^{3/2}}[P_v - P_{sat}(T_i)] + \frac{1}{\sqrt{2\pi RT_i}}\left(-\frac{dP_{sat}}{dT}\right)_{T=T_i}\right\} \tag{B.22}$$

Now, Equation (B.19) can be solved by Newton's iteration method as described below:

1. Guess T_i between T_{wall} and T_∞ (usually the interface temperature at the previous station)
2. Calculate $\delta(i)$ and $\frac{d\delta(i)}{dT_i}$ using Equations(B.15) and (B.22)
3. Calculate F and $\frac{dF}{dT_i}$ using Equations (B.20) and (B.21)
4. Calculate $T_i^{new} = T_i - \frac{F}{F'}$, where $F' = \frac{dF}{dT_i}$
5. If $\left|\frac{T_i^{new} - T_i}{T_i^{new}}\right| \cdot 100 \le \varepsilon$ then convergence was obtained and the new interface temperature as $T(i,1) = T_i^{new}$. The liquid film thickness was known from Equation (B.15). The convergence criterion used in this work was $\varepsilon = 10^{-5}$. The number of

iterations needed depends on the initial guess for T_i, and in the program it was limited to 100. If more than 100 iterations were needed for convergence, then the grid was refined in the input file and the calculation was repeated.

6. If the condition from step 5 is not satisfied, then $T_i = T_i^{new}$ and steps 2 to 5 are repeated until convergence is obtained.

Functions $P_{sat}(T)$ and $\frac{dP_{sat}(T)}{dT}$ were described separately for each vapor in Appendix A.

APPENDIX C

Initial Solution Field for the Second Station

The initial solution field was based on Nusselt's analysis (as described in Mills (1992)). If the interfacial resistance is included in the model then the standard Nusselt analysis was extended so that it includes the effect of interfacial resistance. For all three vapor-gas combinations used in this work the same procedure was used. Further details of the analysis are given in Mills (1992).

The film layer thickness was obtained by solving following equation:

$$\frac{Ja_L}{\mathrm{Pr}_L}\bar{x} = \frac{\delta^{*4}}{4} + \frac{\delta^{*3}}{3Nu_i} \tag{C.1}$$

where

$$\frac{Ja_L}{\mathrm{Pr}_L} = \frac{k_L(T_{sat} - T_{wall})}{\mu_L h_{fg}} \tag{C.2}$$

$$\bar{x} = \frac{x}{\left(\nu_L^2/g\right)^{1/3}} \tag{C.3}$$

$$Nu_i = \frac{h_i\left(\nu_L^2/g\right)^{1/3}}{k_L} \tag{C.4}$$

$$h_i = \left(\frac{2}{\pi \bar{R} T_{sat}}\right)^{1/2} \frac{\rho_v h_{fg}^2}{T_{sat}} \tag{C.5}$$

$$\delta^* = \frac{\delta}{\left(\nu_L^2/g\right)^{1/3}} \tag{C.6}$$

In the Equation (C.1) the only unknown is δ^* (or δ). Liquid properties were evaluated at T_{wall}, and mixture properties were evaluated at T_∞. Temperature T_{sat} corresponds to the partial pressure of the vapor at the interface.

Equation (C.1) can be solved by a Newton-Raphson iterative procedure as follows.

After rearranging, Equation (C.1) becomes

$$f = \delta^{*4} + a\delta^{*3} + b = 0 \qquad \text{(C.7)}$$

and

$$f' = \frac{df}{d\delta^*} = 4\delta^{*3} + 3a\delta^{*2} \qquad \text{(C.8)}$$

where

$$a = \frac{4}{3Nu_i}$$

$$b = -\frac{4\bar{x}Ja_l}{\mathrm{Pr}}$$

As the initial guess, δ^* was taken to be 1, and new δ^* was calculated from:

$$\delta^*_{new} = \delta^* - \frac{f}{f'} \qquad \text{(C.9)}$$

Iterations are repeated until $\left(\frac{\delta^*_{new} - \delta^*}{\delta^*}\right) \cdot 100 < \varepsilon$, where ε is defined as the maximum relative error. Using the value of 10^{-5} for ε, convergence was usually obtained after 10 to 15 iterations.

If interfacial resistance was not included, then the film layer thickness was calculated using the standard formula:

$$\delta(i) = \left[\frac{4k_l\mu_l(T_\infty - T_{wall})x_b(i)}{h_{fg}g\rho_L^2}\right]^{1/4} \qquad \text{(C.10)}$$

Once the liquid film thickness was calculated then velocity and temperature profiles within the liquid were calculated as:

$$u_L(j_L) = \delta^2(i)\left[\frac{0.5\rho_L g}{\mu_L}\right]\left[2\eta_L(j_L) - \eta_L^2(j_L)\right] \qquad \text{(C.11)}$$

$$T_L(j_L) = (T_i - T_{wall})\eta_L(j_L) + T_{wall} \qquad \text{(C.12)}$$

Within the mixture layer, velocity, concentration and temperature were initiated at:

$$u(j) = u_\infty \qquad \text{(C.13)}$$

$$W(j) = W_\infty \qquad \text{(C.14)}$$

$$T(j) = T_\infty \qquad \text{(C.15)}$$

Equations (C.11) to (C.15) were used for both type of calculations (with and without interfacial resistance). The only difference is the calculation procedure for the liquid film thickness.